

**Experimental and Numerical Investigations of Vortex-Induced Vibration for a  
Single Cylinder**

Von der Fakultät für Ingenieurwissenschaften, Abteilung Maschinenbau und  
Verfahrenstechnik der

Universität Duisburg-Essen

zur Erlangung des akademischen Grades

eines

Doktors der Ingenieurwissenschaften

Dr.-Ing.

genehmigte Dissertation

von

Mohamed Youssef

aus

Ägypten

Gutachter: Univ.-Prof. Dr.-Ing. Bettar Ould el Moctar

Univ.-Prof. Dr.-Ing. Wojciech Kowalczyk

Tag der mündlichen Prüfung: 4. November 2021

# DuEPublico

Duisburg-Essen Publications online

UNIVERSITÄT  
DUISBURG  
ESSEN

*Offen im Denken*

ub | universitäts  
bibliothek

Diese Dissertation wird via DuEPublico, dem Dokumenten- und Publikationsserver der Universität Duisburg-Essen, zur Verfügung gestellt und liegt auch als Print-Version vor.

**DOI:** 10.17185/duepublico/75382

**URN:** urn:nbn:de:hbz:465-20220301-145436-3

Alle Rechte vorbehalten.

*For my family,*

*“If anyone deserves to be rewarded for this work, you must be. Thank you for taking all this pressure until we get that moment”*

*Jan.2021*

# Acknowledgment

First of all, thank Allah S.W.T for the strength in completing this study.

Secondly, I would like to express my sincere gratitude to my supervisor Prof. Dr.-Ing. Bettar Ould el Moctar for his supervision associated with all work related to this thesis. I am grateful for his continuous guidance and motivational support that inspired me to achieve this goal during huge stresses and time limitations less than three years ago. Besides, I want to thank Dr. Thomas Schellin for critically reviewing research work associated with this thesis.

I was fortunate to have contact with my all departmental colleagues. I had many fruitful discussions and always an enjoyable time at the institute. Acknowledgments go to all of them for sharing their expertise and for their help and support over the years. Special thanks to Mrs. Claudia for being always helpful and understanding.

Last but not least, I'm grateful for the support my family gave me during my work here in Germany. They understood my absence during important family occasions and motivated me to obtain my Ph.D. Words cannot express how grateful I am.

# Abstract

Vortex-induced vibration (VIV) of cylindrical structures in fluid flow is a well-explored topic that is relevant to many fields of engineering. In particular, it is a classical topic within fluid-structure interaction (FSI). In offshore engineering, VIV often causes fatigue in slender structures, such as risers, mooring lines, and pipelines. Recently, VIV has been a key issue in wind turbine tower design. Turbine towers can be subject to VIV when exposed to stream flow because the shedding of vortices downstream of the structure induces forces on the structure that may cause vibrations. A detailed understanding of this FSI phenomenon and efficient estimation of such self-excited and self-sustained oscillations are required for the reliable prediction of the fatigue damage and the development of VIV suppression techniques. The study of this problem is hampered by a lack of high-quality measurements and a lack of reliable models to predict the response and the fluid loading on towers undergoing VIV.

In the present study, experimental and numerical investigations on a cantilever cylinder with free end boundary conditions have been studied. Methods of eliminating or reducing vortex-induced oscillations are by varying structural or aero/hydro-dynamics behavior. Structural methods, such as those that involve altering damping, mass, or natural frequency, however, aerodynamic/hydrodynamic techniques, such as those that change the flow pattern using alternative methods.

A series of experiments were performed in an enclosed towing tank to investigate the response amplitudes, hydrodynamic forces, lock-in region, Strouhal number, and frequency response while varying the locations of different newly developed angular-position fin plates. The experiments were conducted in a uniform current flow with cylinder models below the critical mass value and allowed to oscillate in two degrees of freedom in the inline and transverse directions. The results demonstrated the disappearance of the synchronization features when the models approached their natural frequencies, which led to a significant reduction in the response amplitudes. Interestingly, strong suppression of over 90% and 75% was observed for the inline response and transverse response, respectively. This trend is also apparent for the lift and drag forces when compared with the measuring data of the smooth cylinder, demonstrating a potential solution for these mitigation tools.

A further experimental investigation was performed in a wind tunnel to examine VIV behavior in an attempt to understand the free end effect with a high Reynolds number and a rigid installation without adding storing elements. Wind tunnel experiments were conducted at Reynolds numbers ranging from  $3.6 \times 10^4$  to  $3.26 \times 10^5$ . The current study produced several important results. The study showed that the response amplitude with vortex shedding was finite, even at the synchronization point. It increased with flow velocity and affected synchronization behavior. The lock-in region was reduced to a certain point. Results suggested that nonlinearities occurred when vortices were shed due to the influence of the free end conditions and the higher Reynolds numbers. The present study focused on aspects that have not been fully addressed by previous studies, such as end-cell induced vibration. The end-cell-induced vibration that occurred at a high wind speed was not influenced by the high damping ratio of the model, while the amplitude response of the ordinary VIV decreased significantly.

Generally, the use of computational fluid dynamics (CFD) has added value in supporting decisions surrounding the risk management of operating assets. Regarding the numerical investigations of the VIV of a cantilever cylinder, the new models for suppressing VIV were examined. The effect of these tools was tested numerically using CFD simulation, which is an attractive and cost-effective alternative to model tests. Numerical simulations were carried out for a low mass ratio cylinder model subjected to uniform flow.

The present numerical model was first verified for different grid resolutions and validated by comparison with published experimental data, and the results indicate that the outcome was satisfactory. The supercritical to upper transition flow regime around a 3D smooth circular cylinder at a Reynolds number range of 4,000 to 14,000 was examined numerically using standard 3D detached-eddy simulation approaches. The objective of the present study was to evaluate whether the models are applicable for further experiments and engineering design within these flow regimes. The simulation results also demonstrated the feasibility of these devices and encourage further experimental studies.

Over the past decades, VIV has been extensively studied, and the majority of literature consists of experiments or semi-empirical modeling. In contrast, FSI simulations, by combining CFD and computational structural dynamics solvers, have received less attention. One of the objectives of this thesis was to investigate the VIV of elastically mounted rigid cylinders and flexible cylinders using fully 3D FSI simulations. The results from 3D simulations were close to previous experimental results. The solid stress tool coupled with a morphed mesh was utilized within StarCCM+ to test their ability to simulate such cases. Finally, further experimental investigations and CFD simulations regarding the effect of group arrangements of the towers and the effectiveness of suppression measures are proposed for future research.

# Declaration

Parts of the work described in this dissertation were previously published or are under review in the following publications:

- The following paper was published :  
“Experimental Investigation of the Tip Vortex Influence on VIV of a Circular Cylinder at High Reynolds Numbers”, Proceedings of the ASME 2020 39th International Conference on Ocean, Offshore and Arctic Engineering. Volume 6A: Ocean Engineering. Virtual, Online. August 3–7, 2020. V06AT06A018. ASME. <https://doi.org/10.1115/OMAE2020-19133>.
- A journal paper entitled “Experimental and Numerical Investigations of Fluid-Structure Interaction for a Fully Submerged Oscillating” has been accepted and is in proceeding to International Journal of Offshore and Polar Engineering ISSN 1053-5381.
- A paper entitled “Two Turbulence Models for URANS Simulations of a Circular Cylinder subject to vortex-induced vibration” has been published in the proceeding of “The 31<sup>st</sup> International Ocean and Polar Engineering Conference” ISOPE,2021-TPC-0147.
- A paper entitled “Experimental and Numerical Investigation of Vortex induced vibration for a Fully Submerged Oscillating Circular Cylinder in a Water Circulation Channel” has been published in proceeding of “The 31<sup>st</sup> International Ocean and Polar Engineering Conference” ISOPE2021-TPC-0143
- The following paper has been submitted to “Ocean Engineering”  
“Passive Flow Control of Vortex-Induced Vibrations of a Low Mass Ratio Circular Cylinder Oscillating in Two degrees-of-freedom”
- The following paper is still under preparation to be submitted  
“Suppression of Vortex-Induced Vibrations of A Single Circular Cylinder: Numerical Investigation”

# Contents

<b>Contents .....</b>	<b>vi</b>
<b>List of Figures .....</b>	<b>viii</b>
<b>1. Introduction .....</b>	<b>1</b>
1.1 Problem Statement.....	1
1.2 Aims of the Research .....	2
1.3 Thesis Layout .....	3
<b>2. Theoretical background and Literature review.....</b>	<b>5</b>
2.1 Theoretical Background.....	5
2.2 Literature Review.....	11
<b>3. Experimental Methods.....</b>	<b>26</b>
3.1 Water Tank Tests .....	26
3.1.1 Water tank facility .....	26
3.1.2 Test model.....	27
3.1.3 Experimental setup and instrumentation .....	28
3.1.4 Test procedure and data analysis.....	31
3.2 Wind Tunnel Tests.....	34
3.2.1 Wind tunnel facility.....	34
3.2.2 Test model.....	35
3.2.3 Experimental setup and instrumentation .....	36
3.2.4 Test procedure and data analysis.....	37
<b>4. Numerical Methods .....</b>	<b>41</b>
4.1 Flow Model .....	41
4.1.1 Governing equations .....	42
4.1.2 Pressure-velocity coupling.....	43
4.1.3 Finite volume method .....	44



4.1.4 Turbulence model.....	47
4.2 Structural Model .....	52
4.2.1 Governing equations .....	53
4.2.2 Finite element method .....	54
4.2.3 Fluid-structure interaction .....	56
<b>5. Experimental Results.....</b>	<b>60</b>
5.1 Water Tank Tests Results .....	60
5.1.1 Smooth cylinder.....	60
5.1.2 Cylinder with attached fins.....	63
5.2 Wind Tunnel Tests Results.....	74
5.2.2 Summary and discussion .....	83
<b>6. Numerical Simulations and Results .....</b>	<b>85</b>
6.1 Turbulence Model Assessment .....	86
6.1.1 Computational domain.....	86
6.1.2 Grids and boundary conditions .....	87
6.1.3 Numerical verification and validation .....	88
6.1.4 The DES turbulence model .....	93
6.1.5 Comparative flow characteristics .....	94
6.2 Suppressing Using Attached Structures .....	99
6.2.1 Models description.....	101
6.2.2 Attached structures results .....	103
6.3 Numerical Validation of FSI Test .....	112
6.3.1 Problem description.....	112
6.3.2 Fluid and structure properties.....	115
6.3.3 Results and discussion.....	115
<b>7. Conclusions .....</b>	<b>126</b>
<b>8. Bibliography .....</b>	<b>130</b>

# List of Figures

<b>Figure 1</b> Definition sketch illustrated boundary layer and wake region around cylinder [17] .....	6
<b>Figure 2</b> Regimes of flow around a smooth, circular cylinder in a steady current [14] 7	
<b>Figure 3</b> Relation between the Strouhal number and the Reynolds number [162].....	8
<b>Figure 4</b> Examples of structural damage due to VIV .....	9
<b>Figure 5</b> VIV Characteristics vs. the product $StU_r$ .....	11
<b>Figure 6</b> Amplitude response for high (a) and low (b) mass/damping parameters [27] .....	13
<b>Figure 7</b> Vortex flow patterns in the wake of the circular cylinder [29] .....	14
<b>Figure 8</b> Cylinder orbits at varying frequency ratios [35] .....	15
<b>Figure 9</b> Transverse response ratio of four cylinders of different mass ratio [38].....	17
<b>Figure 10</b> Transverse response ratio of a cylinder for six different damping ratios [43] .....	18
<b>Figure 11</b> Transverse response ratio at high Reynolds number and high damping [48] .....	20
<b>Figure 12</b> Circular cylinder fitted with helical strakes [55] .....	21
<b>Figure 13</b> Different sectional models tested by Gartshore et al. [59]. .....	22
<b>Figure 14</b> Tested cylinder models parameters at radial positions of (a) 90 deg fin position, (b) 80 deg fin position, and (c) 110 deg fin position from its front stagnation point.....	27
<b>Figure 15</b> Arrangement of eight fin plates attached symmetrically along with cylinder length.....	28
<b>Figure 16</b> Accelerometer sensor cables location .....	29
<b>Figure 17</b> Schematic of the experimental setup including a typical configuration of the experiment tools .....	29
<b>Figure 18</b> Time series for the smooth cylinder without fins in air (A) and in water (B) and corresponding PSD of the lateral acceleration in air (E) and water (F), time series of the cylinder with fins positioned at 110 deg in air (C) and in water (D) and corresponding PSD of the lateral acceleration in air (G) and water (H), time series of the cylinder with fins positioned at 90 deg in air (I) and in water (G) and	

corresponding PSD of the lateral acceleration in air (M) and in water (N), and time series of the cylinder with fins positioned at 80 deg in air (K) and in water (L) and corresponding PSD of the lateral acceleration in air (O) and in water (P), where the acceleration is measured in G and equal to (m/s<sup>2</sup>). ..... 32

**Figure 19** Schematic of the wind tunnel ..... 35

**Figure 20** Calibration curve for the velocity Sensor ..... 37

**Figure 21** plan view (a) and side view (b) of the experimental setup ..... 37

**Figure 22** Experimental setup and the coordinate systems of sensors ..... 38

**Figure 23** Recorded data from decay test no. 0126 ..... 40

**Figure 24** Analyzing data for a decay test No. 0126 in x-direction; left, Time series output; right, The fitting analysis ..... 40

**Figure 25** 2D-view of control volumes with different neighboring cells, C, N, W, E, and S with the interfaces w, e, n, and s ..... 45

**Figure 26** Energy cascade and different length scales of turbulence ..... 48

**Figure 27** Original concept sketch of DES [133] ..... 51

**Figure 28** Major families of elements Used for FEM discretization ..... 54

**Figure 29** Flow chart of the FSI solution algorithm ..... 58

**Figure 30** Example of the interface between non-conformal grids ..... 59

**Figure 31** Root mean square (r.m.s.) values of measured normalized stream-wise (x/D) and lateral (y/D) top-end displacement amplitudes (and the associated trajectories) vs. reduced velocity ( $U_r$ ) for the smooth cylinder ..... 60

**Figure 32** Motion trajectories of the smooth cylinder's top in flows at different velocities (left), black lines represent trajectories over the entire duration of the experiments; red lines, trajectories obtained over one cycle, and the plot of normalized lateral shedding frequency vs. reduced velocity (right) ..... 61

**Figure 33** Drag and lift forces coefficients versus the reduced velocity ..... 62

**Figure 34** Comparative r.m.s. amplitudes of normalized lateral top-end amplitude response vs. reduced velocity for the smooth cylinder and the finned cylinder models ..... 64

**Figure 35** Comparative r.m.s. amplitudes of normalized inline amplitude response vs. reduced velocity for the finned cylinder models and the smooth cylinder ..... 65

**Figure 36** Comparative r.m.s. amplitudes of stream-wise (top) and lateral forces (bottom) vs. reduced velocity  $U_r$  acting on the smooth cylinder and on the cylinders fitted with fin plates positioned at 80 and 110 degrees. .... 67

<b>Figure 37</b> Comparative r.m.s. values of stream-wise (top) and lateral force coefficients (bottom) vs. reduced velocity for the smooth cylinder and for the cylinders fitted with fin plates at 80 and 110 degrees .....	69
<b>Figure 38</b> Comparative shedding frequency ratio vs. reduced velocity for the smooth cylinder and for the cylinders fitted with fin plates positioned at 80, 90, and 110 degrees.....	70
<b>Figure 39</b> Comparative power spectral density distributions of lateral acceleration (left) and the lateral velocity of the wake behind the cylinder (right) fitted with 110 deg fin plates of $x/D = 5$ and .....	71
<b>Figure 40</b> Comparative time series of normalized inline and transverse cylinder displacements and the associated power spectral densities of r.m.s. amplitudes for the smooth cylinder and the cylinders fitted with fins at 80, 90, and 110 degrees for the reduced flow velocity of $U_r = 4.81$ .....	72
<b>Figure 41</b> Structural fatigue damage of the smooth cylinder.....	73
<b>Figure 42</b> Normalized maximum amplitude vs. Scruton number [111].....	74
<b>Figure 43</b> r.m.s. Values of normalized streamline (x) and lateral (y) top-end motion amplitudes Vs. reduced velocity ( $U_r$ ) .....	75
<b>Figure 44</b> Time series and frequency plots of inline (X) and transverse (Y) accelerations and forces at a flow velocity of 9.00 m/s.....	76
<b>Figure 45</b> r.m.s. Values of drag force ( $F_x$ ) and transverse force ( $F_y$ ) (a), and of lift and drag coefficients (b) VS. reduced velocity ( $U_r$ ).....	77
<b>Figure 46</b> Power spectral densities (PSD) of transverse accelerations at the bottom-end of the cylinder .....	78
<b>Figure 47</b> Dominant frequencies from lift spectra, nondimensionalized by flow speed, $U$ , and diameter, $D$ , Vs. Reynolds number (a) and dominant frequency ratio obtained from lift force spectra Vs. reduced velocity (b).....	79
<b>Figure 48</b> Drag force frequencies from drag force spectra Vs. reduced velocity.....	79
<b>Figure 49</b> Phase angle between the transverse force and transverse motion of the cylinder Vs. flow velocity.....	80
<b>Figure 50</b> Evaluation of the 2C mode in time during one cycle of the tested pivoted cylinder [122] .....	81
<b>Figure 51</b> Visualizations of a variety of vortex formation patterns observed in the wake of the tested cylinder at flow velocities of 5 m/s (a), 10 m/s (b), 17m/S (c), 19 m/s (d), and 25m/s (e) .....	82

<b>Figure 52</b> Top view of the computational domain .....	87
<b>Figure 53</b> Top view (top) and side view (bottom) of the computational mesh 2 on the medium grid.....	88
<b>Figure 54</b> Time histories of the drag force coefficients calculated from different grids .....	91
<b>Figure 55</b> Residuals of computed flow quantities vs. number of iterations; full-time calculations (a), zoom in (b).....	93
<b>Figure 56</b> Time series of lift coefficient obtained with the SST k- $\omega$ (top) and the DES (bottom) turbulence model.....	95
<b>Figure 57</b> Time-averaged streamlines on the horizontal mid-span plane of the cylinder obtained with the SST k- $\omega$ (top) and the DES (bottom) turbulence models	96
<b>Figure 58</b> Time-averaged streamlines on the cylinder's vertical symmetry plane obtained with the SST k- $\omega$ (top) and the DES (bottom) turbulence model.....	97
<b>Figure 59</b> Mean pressure coefficient vs. angular position around the cylinder's circumference obtained with the SST k- $\omega$ (top) and the DES (bottom) turbulence models .....	98
<b>Figure 60</b> Shear stress distribution on the cylinder wall obtained with the SST k- $\omega$ (top) and the DES (bottom) turbulence models .....	99
<b>Figure 61</b> Drag coefficients for the bare cylinder compared with data from published work by Khalak and Williamson 1996. ....	100
<b>Figure 62</b> Time-averaged streamlines and pressure contours on the horizontal midspan plane for the plain cylinder .....	100
<b>Figure 63</b> Schematics of the cylinder with attached fin plates in frontal view; and the cross-sectional view of different tested model; (A) straight fin plates, (B) 90 deg fin plates, (C) 80 deg fin plates, and (D) asymmetric straight fin plates model .....	101
<b>Figure 64</b> Top view of the computational meshes for each study case; a) total computational domain, b) 80 deg fins, c) straight fins, d) 90 deg fins.....	103
<b>Figure 65</b> Time-averaged streamlines on the horizontal midspan plane presented the variation of the vortex formation length and vortex thickness for each case at the same time step; model 1 (a), model 2 (b), model 3 (c), model 4 (d), model 5 (e), model 6 (f) .....	104
<b>Figure 66</b> pressure contours on the horizontal midspan plane variation for each case at the same time step; model 1 (a), model 2 (b), model 3 (c), model 4 (d), model 5 (e), model 6 (f) .....	105

<b>Figure 67</b> Time-averaged streamlines on the vertical symmetry plane and the skin friction coefficients for different cases; bare cylinder (top), mode 2 (a), model 3 (b), model 1 (c), model 5 (d), model 4 (e), model 6 (f) .....	106
<b>Figure 68</b> Time series and frequency plots for for different tested cases; bare cylinder (top), mode 1 (a), model 2 (b), model 3 (c), model 4 (d), model 5 (e), model 6 (f) .....	108
<b>Figure 69</b> The mean Drag coefficients and r.m.s. Lift Coefficient for the case study of model 6 in comparison with numerical and experimental results for the bare cylinder .....	109
<b>Figure 70</b> Time-averaged streamlines on the horizontal midspan plane of model 6 at $Re = 10^4$ .....	110
<b>Figure 71</b> Dominant frequencies from lift force (FFT), nondimensionalized by flow speed, $U$ , and diameter, $d$ for bare and case study numerical data.....	110
<b>Figure 72</b> Top view (top) and side view (bottom) of the computational mesh 2 on the fine grid.....	113
<b>Figure 73</b> Time histories of the force coefficients on a stationary cylinder calculated from the different grid meshes .....	114
<b>Figure 74</b> Comparison of amplitude response curves between the present simulation and the experimental data measurements.....	116
<b>Figure 75</b> Comparison of amplitude response curves between the experimental data measurements (top) and the present simulation (bottom) at $U_r = 2.27$ .....	117
<b>Figure 76</b> Comparison of amplitude response curves between the experimental data measurements (top) and the present simulation (bottom) at $U_r = 4.27$ .....	118
<b>Figure 77</b> Comparison of amplitude response curves between the experimental data measurements (top) and the present simulation (bottom) at $U_r = 4.81$ .....	118
<b>Figure 78</b> Power Spectrum Density (PSD) for the flow velocity transverse flow velocity at $U_r = 2.27$ measured by LDV.....	119
<b>Figure 79</b> Shedding frequency normalized by natural frequency against reduced velocity.....	120
<b>Figure 80</b> Forces time histories ( medium grids) at $U=1.6$ m/s; drag force, top; lift force, bottom.....	121
<b>Figure 81</b> Direct comparison between the stream-lines of the mean velocity, at the midspan, between the and rigid cylinder (left) and the flexible cylinder (right), in an x-y plane(top), and, in an x-z plane (bottom) .....	122

**Figure 82** Instantaneous mean velocity at different z-position: a) at  $U=0.85$  m/s, b) at  $U=1.6$  m/s, and c) at  $U=1.8$  m/s..... 124

**Figure 83** Average Courant- Friedrichs-Lewey (CFL) number for numerical calculations at  $U=0.85$  ..... 125

**Figure 84**  $y^+$  ranges on the cylinder for the numerical calculations at  $U= 1.6$ ..... 125

# 1. Introduction

## 1.1 Problem Statement

The phenomenon of vortex-induced vibration (VIV) has been a well-known and widely explored topic since ancient times. However, the modeling of VIV for engineering purposes presents several challenges due to the complexity of the phenomena involved. VIV is a complex phenomenon that is relevant in various disciplines, including fluid mechanics, structural mechanics, vibrations, complex techniques for data analysis, and numerical methods applied to fluid dynamics and solid mechanics. At a practical level, circular cylinders exist in many engineering and industrial applications, such as offshore platforms, power lines, bridge supports, and heat exchangers. In the design of these structures, knowledge is needed regarding the forces involved, frequencies, heat transfer, and flow behavior.

It is well known that the fluid-induced forces on cylindrical structures are strong enough to set the body into oscillatory motion due to the wake vortex shedding flow. If a flexible or elastically mounted rigid cylinder is placed in a fluid flow, the dynamic fluid force induces the vibration of the cylinder, which in turn modifies the flow and leads to a fully coupled fluid-structure interaction (FSI). When VIV occurs, the material is subject to cyclic bending stresses, and the structure starts to oscillate. These oscillations are of great interest for structural engineers, not only because of the large oscillation amplitude but also due to the long-term cyclic loads, which can cause significant fatigue stress and crack growth over time, eventually leading to fracture. The highly non-linear interaction between the fluid flow and the structure response needs to be studied by complex experimental techniques or computational fluid dynamics (CFD).

Further challenges emerge when the cylinder is standing in a flat-plate boundary layer, as a more complex 3D flow field develops. Besides, a horseshoe vortex formed at the cylinder wall junction has practical importance in applications, and hence it has been the focus of numerous studies. Thus, there is an added complexity when the cylinder has a free end exposed to the flow.

The subject of VIV for a finite cylinder is of practical interest in many fields of engineering. For example, marine risers in petroleum production influence the dynamics of riser tubes bringing oil from the seabed to the surface. The subject is also important to the design of civil engineering structures such as bridges and chimney stacks, as well as to the design of marine and land vehicles, and VIV can cause large-amplitude vibrations of tethered structures in the ocean. The offshore industry has been at the forefront of interest in FSI for many decades.

Currently, wind energy research and development programs are being created to advance the global wind industry and increase the share of energy from renewables. In the offshore wind industry, the risk of VIV becomes greater as the size of the towers increases. It is a phenomenon of significant importance because of the fatigue damage on the wind turbine towers. The possible reduction of their service lifetime can be critical for the fatigue design; hence, they must be carefully designed to avoid environmental and economic catastrophes. In addition, maximum loads due to VIV events can be crucial for the design of the quayside foundation frames and sea fastenings. Owing to the above features, suppression, reduction, prediction, and control of VIV are primary objectives and require an understanding of the physics involved in



VIV. An understanding of VIV is critical to safely design many common engineering structures, yet there is still much to learn regarding VIV.

VIV research can follow multiple approaches, experimentally, laboratory tests are the best way of producing high-quality data because all the system input parameters are under control. However, in experiments, the required degree of certainty is not possible to be achieved. On the other hand, in a laboratory, it is very difficult to achieve realistic fluid and structural parameters such as the Reynolds number (Re), aspect ratios, and mass ratios. Numerical simulations that take advantage of enhanced numerical algorithms and increased computational power have become an important and valuable tool for solving this kind of problem, and more benchmarks have become possible within the last decade. As a subclass of FSI problems, VIV problems mainly focus on the understanding of the complex physics of the flow surrounding a moving bluff body and the associated vortex shedding process. Generally, for large, unsteady flow-induced structural deformations, a tightly coupled FSI approach is required in which structural and fluid governing equations are simultaneously satisfied. This can be accomplished by solving iteratively at each time step until a specified tolerance is met. A tightly coupled FSI approach typically requires far more computing resources than loosely coupled FSI approaches, where the governing equations are not simultaneously satisfied, or CFD-only simulations (one-way coupling).

Due to this difficulty, in VIV research, many FSI simulations have used 2D fluid domains such as those by Wanderley et al. [1] and Zhao et al. [2]. The efficient numerical simulation of FSI is essential to realistically simulate the related flow problems. To the author's knowledge, only a limited number of studies dealing with the flow past a bluff body have used a series of methods to investigate the FSI effects on the structure. Studies [3], [4], and [5] treated the structure as a mass-spring system; [5] described it as a discrete structural simplification. Although better computers are gradually becoming available to researchers, they are still extremely expensive to use because of their time consumption. Several numerical models have been proposed to analyze and predict the fatigue life caused by such a topic. The methods for predicting the VIV range from simple modal analysis to fully coupled analysis of the FSI by solving the Navier-Stokes equations.

## 1.2 Aims of the Research

The main aim of the study is to investigate the VIV of a cylindrical structure in steady flow through extensive experimental tests and numerical simulations and to validate the numerical code with experimental data. Finding a practical solution and presenting suppression tools are the intended contributions of the present study. This thesis focuses on the VIV of a cylinder, including the VIV of a rigid cylinder flexibly mounted with two degrees of freedom (2DOF), and tools to suppress the VIV of a stationary cylinder and flexible cylinder with 2DOF. The main objectives of this thesis are as follows:

- Understand the mechanism of VIV and its characteristics at different parameters and conditions by carrying out experimental investigations of the VIV of a cylinder in a water recirculating tank and a wind tunnel. Newly developed attached configurations of fins have been provided.
- Through experimental investigations, illustrate the effectiveness of the three different fin allocations in suppressing VIV, even with one additional challenge: that the cylinder model has a mass below the critical value allowed to oscillate in transverse and in-line directions.

- Conduct numerical investigations of the 3D flow around a stationary cylinder subjected to newly developed attached structures to examine its effect on suppressing VIV.
- As FSI simulations of the VIV of cylindrical structures are still quite limited, provide a challenging and well-defined validation test case for the FSI of the smooth cylinder in turbulent flow to close a gap in the literature.
- Understand the correlation and difference between the shedding frequency and the structure oscillating frequency in the transverse direction obtained from experimental measurements and numerical calculations.

### 1.3 Thesis Layout

This thesis is organized as follows. First, it introduces the nature and significance of the research. It next presents a literature review and background information before establishing the research methodology. An extensive discussion of the results and elaboration of the research outcomes follow. Recommendations for future studies are suggested so that the objectives achieved in this study may be further developed. The detailed organization of the thesis is as follows:

#### **Chapter One: Introduction**

This chapter introduces the research topic and thesis objectives. Besides, it outlines the motivation and objectives of the research.

#### **Chapter Two: Theoretical Background and Literature Review**

This chapter presents a brief theoretical background on the flow around a circular cylinder. In addition, the literature review discusses the significance of the VIVs of circular cylinders, flow around stationary circular cylinders, and the importance of vortex shedding and parameters for the analysis of vortex shedding. VIV of a flexible cylinder with one DOF (1DOF) and 2DOFs, including describing the differences between free and forced oscillation experiments, VIV and galloping, and VIV suppression tools that have been created through experiments and numerical investigations.

#### **Chapter Three: Experimental Investigation**

Chapter 3 summarizes the experimental methods used in the present study. It explains the details of the experimental apparatus and procedure for the 2DOF experiments. In addition, models description and parameters are then covered in this chapter.

#### **Chapter Four: Numerical Method**

Chapter 4 includes fundamental equations of fluid dynamics and approximations of different terms. It covers the basic equations for flows together with the numerical methods used to solve them. Beginning from the Navier–Stokes equations, models to deal with turbulent flows yield additional equations of conservation. Components of the finite volume method (FVM) used to discretize and solve these equations are described, and a linear algebraic system of equations is obtained. Following a pressure-velocity coupling approach. Furthermore, brief details about the numerical method used for the structure solver and the technique used to couple the governing equations of the fluid and structure are described.

#### **Chapter Five: Experimental Results**

Chapter 5 presents the experimental results, discussion, and comparison with previous literature. The first part demonstrates the cylinder test cases performed in the Re range  $1.9 \times 10^4$  to  $7.2 \times$

$10^4$  at the towing tank. In the second section of the chapter, wind tunnel experiments conducted at Re values ranging from  $3.6 \times 10^4$  to  $3.26 \times 10^5$  are presented.

### **Chapter Six: Numerical Simulations and Results**

Chapter 6 investigates the VIV of a single cylinder. Following the numerical simulation, a grid- and time-independent study, validation, and comparison of numerical results are included. The study focuses on the forces applied to the cylinder models and the corresponding frequencies and responses. Velocity and pressure are also presented. In the first section, CFD analysis is performed for a fixed-cylinder case using two turbulence models: unsteady Reynolds-averaged Navier–Stokes (URANS) simulations and detached-eddy simulations (DESs). Then, various newly developed structures attached to the smooth cylinder surface are examined to illustrate their influence in suppressing VIV. Finally, a 3D numerical FSI validation test case is presented. The results from 3D simulations are close to previous experimental results.

### **Chapter Seven: Conclusions**

In this chapter, conclusions are provided based on findings from the numerical and experimental results of this work, and possible recommendations for future studies are proposed.

## 2. Theoretical background and Literature review

Bodies subjected to fluid flow are classified as being streamlined or bluff depending on their overall shape. Bluff bodies are characterized by flow separation along a large section of the structure's surface [6], in which they generate separated flow over a substantial proportion of their surface. The flow structure around bluff bodies is characterized by a region of disturbed flow behind the body designated by the wake. Within the near-wake zone, various forms of flow instabilities may be triggered and amplified. These instabilities are manifested by the generation of unsteady flow structures and eventually lead to turbulence as the  $Re$  is progressively increased (see Fig. 2). The stable street of alternating vortices in the wake has been noted by Von Kármán, following Benard, who, in 1908, related the wake's periodicity to the vortices. Circular cross-section bodies such as cylinders are classified as bluff bodies since, as a result of their shape, they generate particularly large and typically unsteady flow separation structures [7].

The velocity field around a circular cylinder is associated with the characteristic pressure distribution around the cylinder. The flow past a circular cylinder causes maximum pressure at the front stagnation point, minimum pressure at its sides, and pressures that increase toward the aft stagnation point. The measured pressure is expressed via a non-dimensional parameter designed by pressure coefficient:

$$C_p = \frac{p - p_\infty}{0.5\rho U^2} \quad (1)$$

where  $\rho$  is the fluid density,  $p$  is the local pressure on the surface,  $p_\infty$  is the free-stream static pressure and  $0.5\rho U^2$  is the free stream dynamic pressure. The circumferential angle is usually measured from the stagnation point,  $\theta = 0$ , to  $180^\circ$ . For a viscous fluid, friction reduces the kinetic energy of the fluid particles, and these are no longer able to reach the aft stagnation point. The pressure gradient in the boundary layer causes the flow near the body to revert. The fluid then detaches itself from the body and separates the boundary layer from the body surface. This point of detachment is called the "separation point." The reverse motion then creates vortices, which separate from the body and move downstream, forming a von Kármán vortex street.

### 2.1 Theoretical Background

The flow of a uniform flow around a circular cylinder has been extensively studied by King [8], Sarpkaya [9], Skop and Griffin [10], Bearman [6], Norberg [11], and Williamson [12] [13] and reviewed in books by Sumer and Fredsoe [14] and Chen [15]. As mentioned above, due to the pressure gradient, the flow near the body will revert, and there will be a flow away from the body, separating the boundary layer from the body surface. The sketch in Fig. 1 classifies the region around the cylinder, showing the boundary layer with the attached flow and the wake region with the flow separated from the cylinder surface. At the boundary layer, the flow velocity is zero, and shear layers are formed because of the separation of the boundary layer on the cylinder surface. The strength of each shear layer increases away from the cylinder surface, and it continues to grow until a stronger opposing shear layer breaks off the former shear layer

and results in vortex shedding downstream of the cylinder [16]. The mutual interaction between the two separating shear layers is the key factor in the formation of a vortex-street wake.

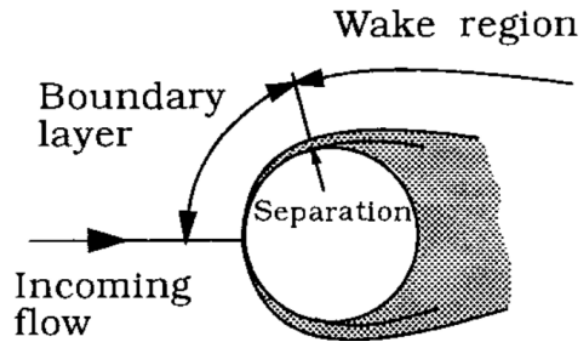











**Figure 1** Definition sketch illustrated boundary layer and wake region around cylinder [17]

A key dimensionless parameter to characterize the flow past a bluff body is the Reynolds number,  $Re$  which defined as:

$$Re = \frac{UD}{\nu} \quad (2)$$

where  $D$  is the cylinder diameter,  $U$  is the flow velocity,  $\nu = \mu/\rho$  is the fluid kinematic viscosity,  $\rho$  is the fluid density, and  $\mu$  is the fluid dynamic viscosity. Figure 2 shows the flow regimes as  $Re$  increases for a smooth circular cylinder.

	Flow characteristic	Reynolds number	Flow regime
(a)		$Re < 5$	Creeping flow
(b)		$5 < Re < 40$	
(c)		$40 < Re < 200$	
(d)		$200 < Re < 300$	
(e)		$300 < Re < 3 \times 10^5$	Sub-critical
(f)		$3 \times 10^5 < Re < 3.5 \times 10^5$	Critical (Lower Transition)
(g)		$3.5 \times 10^5 < Re < 1.5 \times 10^6$	Super-critical
(h)		$1.5 \times 10^6 < Re < 4 \times 10^6$	Upper Transition
(i)		$Re > 4 \times 10^6$	Trans-critical

**Figure 2** Regimes of flow around a smooth, circular cylinder in a steady current [14]

The creeping flow past a cylinder persists without separation up to  $Re \approx 5$ . For  $4-5 < Re < 40$ , a new laminar flow regime starts that is characterized by the separation of the shear layers, asymmetrical pair of vortices is observed behind the body as shown in Fig. 2b. The transverse oscillation begins at the end of the near-wake and initiates a wave along the trail for  $Re > 40$ , where the steady, elongated, and closed near-wake becomes unstable.

Strouhal [18] observed that upon varying the flow velocity  $U$ , the vortex shedding frequency from a cylinder of diameter  $D$  is proportional to  $U/D$ . This constant is the Strouhal number ( $S_t$ ), which is defined by the following equation:

$$S_t = \frac{f_s D}{U} \quad (3)$$

where  $f_s$  is the frequency of the vortex shedding,  $D$  is the characteristic length of the cross-section (cylinder diameter). He found the mean value of the proportionality to be 0.185 for a stationary cylinder. Vortex shedding in the wake of a fixed circular cylinder in a free stream is characterized by the Kármán vortex street, in which vortices are shed periodically in the wake of the cylinder at the Strouhal frequency  $f_s$ . The  $S_t$  value depends on the body shape, roughness of the cylinder, and  $Re$ . Fig. 3 presents the relationship between  $S_t$  and  $Re$ . As depicted in Fig. 3, the upper and lower branches show the difference between a cylinder with a rough and a smooth surface.

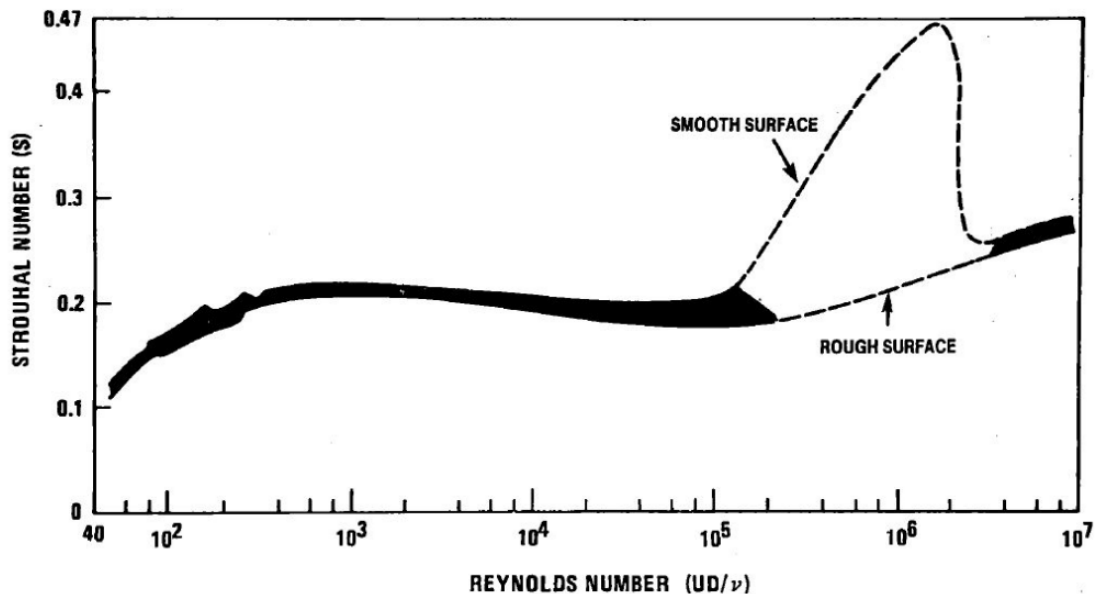


**Figure 3** Relation between the Strouhal number and the Reynolds number [162]

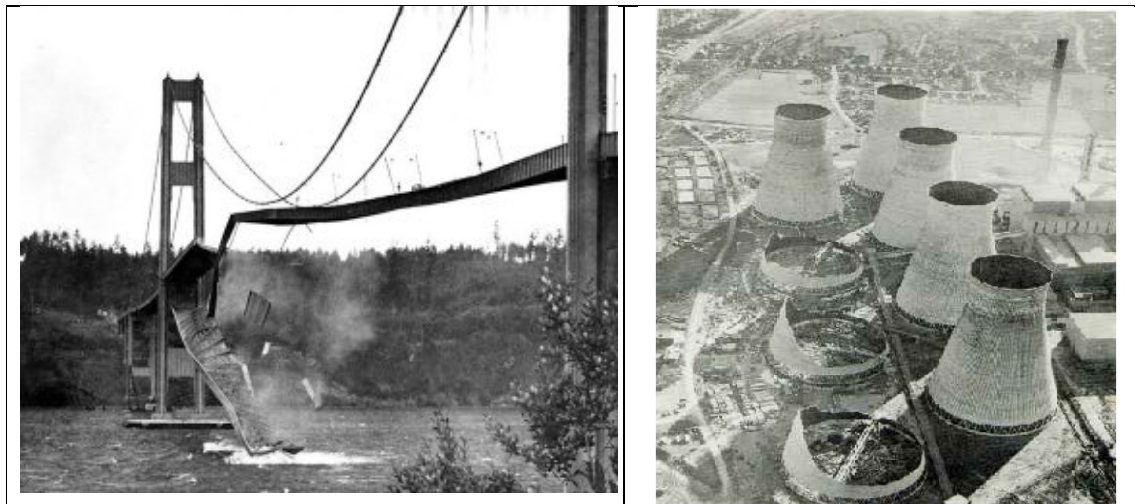
The value of  $S_t \approx 0.2$  in the subcritical range  $Re = 500 \sim 10^5$ , is almost constant; however, in the range  $Re = 10^5 \sim 10^6$ , its value increases. For flexible cylinders or elastically mounted rigid cylinders, the wake behind the cylinder is characterized by the periodic shedding of vortices or groups of vortices, which similarly generates a time-variable pressure over the cylinder that causes periodic forcing on the cylinder in both drag and lift directions.

Forces exerted on the cylinder are a function of this periodic vortex shedding frequency, usually causing large amplitude vibrations [19]. The drag force will consist of a mean value and an oscillating component with a peak frequency at twice the vortex shedding frequency[20]. The lift force will have zero mean and the peak oscillatory component at the vortex shedding frequency.

### Fluid-Structure Interaction

The vortex shedding frequency in Equation 3 refers to a stationary cylinder. The vibration of a flexible structure induced by transverse fluid flow continuously changes the boundary and flow conditions, resulting in more complex phenomena due to the interaction between dynamic flow and cylinder motion. Investigations into VIV have shown that the parameters that affect VIV may be classified as structural parameters or flow parameters. The classical experiment is to adjust the natural frequency of the structure so that it matches the vortex shedding frequency  $f_s$  and thereby create oscillations of the cylinder.

The interaction of fluids and structure can produce a potentially destructive force on the structure itself. The collapse of the Tacoma Narrows Bridge in 1940 is a famous example of this phenomenon. After four months, it was opened to traffic due to wind-induced vibrations [21]. The FSI between the gusts of wind and the bridge triggered large-scale heaving and torsional vibrations, leading to a complex oscillation that eventually reached a severe enough magnitude to cause the dramatic collapse of the bridge [22].



a) The collapse of the Tacoma Narrows Bridge      b) Three collapsed towers in Ferrybridge, UK

**Figure 4** Examples of structural damage due to VIV

In another example, in 1965 [168], three cooling towers, part of a group of eight, collapsed after an hour in Ferrybridge as shown in Fig. 4b. A witness described the motion of the tower as this of a belly dancer.

### Dimensionless parameters

In the literature, different parameters characterize the VIV phenomenon. This section summarizes these expressions and parameters and explains how they are used in this work.

#### **Reynolds number, $Re$**

$Re$  is used to describe the flow regimes of the vortex shedding. It is defined as the ratio between the inertial and the viscous forces. It determines the flow regime and is also of importance for the correlation length in fixed cylinder cases.



### Reduced Velocity, $U_r$

The reduced velocity is the ratio of the path length in the flow direction per cycle to the model width;

$$U_r = \frac{U}{f_n D} \quad (4)$$

where  $U$  is the mean flow velocity and  $f_n$  is the natural frequency of the system. The natural frequency in air and a vacuum is almost the same, but in still water, the natural frequency for normally dense cylinders is significantly reduced due to the added mass effect. Normally, the peak of the normalized amplitude of the VIV phenomenon occurs at  $U_r = 5-6$ . Two versions of the reduced velocity have been used [23]: nominal reduced velocity when the natural frequency in the air is used and true reduced velocity when using the true vibration frequency.

### Strouhal Number, $S_t$

The Strouhal number is related to the shedding frequency of the periodic motion for fixed cylinders as previously discussed. For oscillating elastically mounted cylinders, the  $S_t$  is highly dependent on the natural frequency of the system.

### Damping Ratio, $\zeta$

For any damped system, the damping ratio is defined as the ratio of the damping constant to the critical damping constant:

$$\zeta = \frac{c}{c_c} = \frac{c}{2m\omega_n} \quad (5)$$

where  $c$  is the viscous damping coefficient,  $m$  is the mass of the structure, and  $\omega_n$  is the natural angular frequency.

### Amplitude Ratio, $A^*$

The response amplitude of the structure is presented as the ratio of the vibration amplitude to the diameter of the cylinder ( $D$ ).

### Frequency Ratio, $f^*$

The frequency ratio is defined as the ratio of the vibration and shedding frequency to the natural frequency of the system:  $\frac{f_s}{f_n}$ .

### Mass Ratio, $m^*$

The mass ratio ( $m^*$ ) is the ratio of the total oscillating body mass, which includes the enclosed fluid mass, to the displaced fluid mass:

$$m^* = \frac{m_{osc}}{m_f}; m_{osc} = m + m_a \quad (6)$$

where  $m_f$  is the displaced fluid mass and  $m_a$  is the added fluid mass. The displaced fluid mass is obtained using the following equation:

$$m_f = \frac{1}{4}\pi\rho D^2 L \quad (7)$$

Where  $L$  is the submerged length of the cylinder.

## 2.2 Literature Review

The majority of related studies have focused on cylinders with 1DOF. Typical force models concerned with VIV only consider forces associated with the cross-flow oscillation of the structure that is, with the cylinders vibrating only in the transverse direction of the incident flow. When the cylinder's vibration (or response) frequency,  $f_s$ , approaches the natural frequency of the system,  $f_n$ , large-amplitude (up to the order of the cylinder diameter) vibrations occur. This is the so-called "lock-in" or "synchronization" phenomenon [17]. If at resonance, the flow velocity increases further, the shedding frequency is said to lock into the frequency of the oscillating cylinder. Then, it strongly deviates from the Strouhal law as its shedding frequency is no longer proportional to  $U/D$ . Eventually, at reduced but still high velocities, the shedding frequency again follows the Strouhal law. This lock-in phenomenon causes something like an extended resonance as the wake continues to excite the cylinder at its natural frequency. Instead of VIV occurring only when these frequencies match, they are generated over a relatively wide range of frequencies. Fig. 5a schematically plots the vortex-induced transverse motion amplitude,  $Y$ , versus the product  $S_t U_r$ . Here, the motion amplitude is normalized against the cylinder diameter  $D$ , and  $U_r = U / f_n D$  is the normalized reduced flow velocity. As can be seen, the schematically plotted motion amplitudes remain high even after the flow velocity surpasses the region of pure resonance.

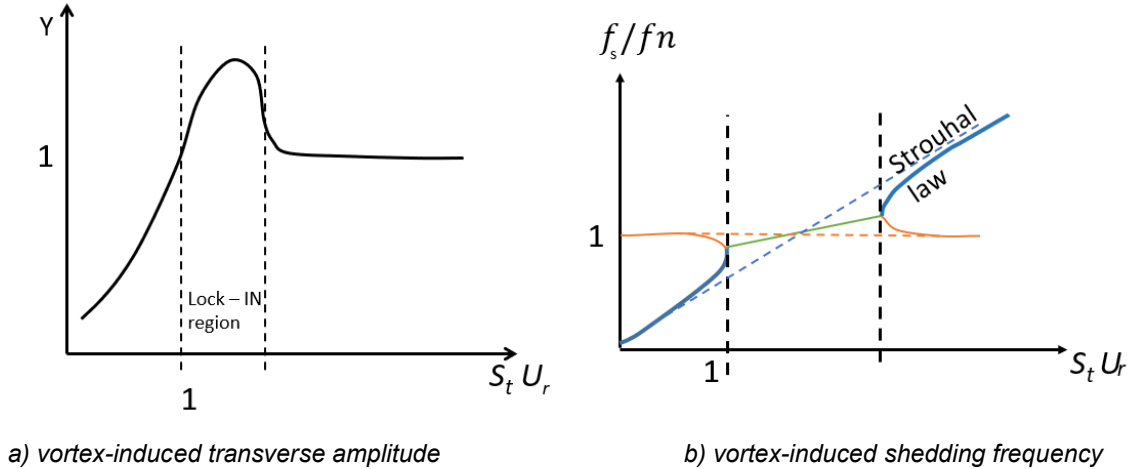


**Figure 5** VIV Characteristics vs. the product  $S_t U_r$

Fig. 5b schematically plots the vortex-induced normalized shedding frequency,  $f_s$ , normalized against the cylinder's natural frequency,  $f_n$ , versus the product  $S_t U_r$ . As seen, at  $S_t U_r = 0$ , where there is no flow, there are two frequencies, one occurring at the natural frequency of the cylinder (at  $f_s/f_n = 1.0$ ), while the other is zero in this case because at  $S_t U_r = 0$  there is no flow and, therefore, no vortices are being shed. As the flow velocity increases, the shedding frequency of the wake first follows the Strouhal law. Then, as the flow velocity increases further, the vortex shedding frequency approaches the cylinder's natural frequency, and these two frequencies collapse into a single lock-in frequency. With further increasing flow velocity that is, at larger values of  $S_t U_r$ , the shedding frequencies separate again, and after the synchronization region, the increasing shedding frequency follows the Strouhal law.

The most significant characteristics of VIV response are the oscillating amplitude, its frequency, and the range of synchronization. The amplitude during lock-in and the band of fluid velocities

over which the lock-in phenomenon exists is strongly dependent on the associated relative damping, usually expressed as the ratio of the damping force and excitation force and the mass of the structure. To illustrate, we shall briefly introduce the single-degree-of-freedom motion equation to represent the vortex-induced vibrations of a cylinder in the (transverse) y-direction perpendicular to the free stream flow

The most significant characteristics of VIV response are the oscillating amplitude, its frequency, and the range of synchronization. The amplitude during lock-in and the band of fluid velocities over which the lock-in phenomenon exists are strongly dependent on the associated relative damping, usually expressed as the ratio of the combined mass and damping of the structure. To illustrate, I shall briefly introduce the single-DOF motion equation to represent the VIV of a cylinder in the (transverse) y-direction perpendicular to the free-stream flow:

$$m\ddot{y} + c\dot{y} + ky = F \quad (8)$$

where  $m$  is the total oscillating structural mass (excluding the hydrodynamic added mass),  $c$  is the structural damping,  $k$  is the restoring force constant, and  $F$  is the fluid force in the transverse direction. When the structure's oscillation frequency is synchronized with the periodic vortex-induced wake frequency, the force,  $F(t)$ , and the response,  $y(t)$ , are given by

$$F(t) = F_0 \sin(\omega t + \phi) \quad (9)$$

and

$$y(t) = A \sin(\omega t) \quad (10)$$

where  $\omega$  is the circular frequency of oscillation, and  $\phi$  is the phase angle between the fluid force and body displacement. The response amplitude ratio,  $A^*$ , and frequency ratio  $f^*$  is derived straightforwardly as follows [24]:

$$A^* = \frac{1}{4\pi^3} \frac{C_y \sin\phi}{(m^* + C_A)\zeta} \left(\frac{U^*}{f^*}\right) f^* \quad (11)$$

$$f^* = \sqrt{\frac{m^* + C_A}{m^* + C_{EA}}} \quad (12)$$

where  $C_A$  is the potential flow added mass coefficient ( $C_A = 1.0$  for a circular cylinder), and  $C_{EA}$  is an effective added-mass coefficient that includes an apparent effect,  $C_y \cos \phi$ , due to total transverse fluid force in phase with the cylinder's acceleration:

$$C_{EA} = \frac{1}{2A^*\pi^3} \left(\frac{U^*}{f^*}\right) 2 C_y \cos \phi \quad (13)$$

This fundamental equation describes the varying response of the peak amplitude,  $A_{max}^*$ , as a function of the mass ratio,  $m^*$ , and damping ratio,  $\zeta$ . Among others, the Scruton number is one of several related parameters that essentially consist of the product of the mass ratio and the damping ratio. Other names used are reduced damping, response parameter, mass damping, and stability parameter, which is defined by [25]:

$$S_c = 4\pi m\zeta / \rho D \quad (14)$$

Recent research considers the relationship between mass, damping, and reduced flow velocity. At high values of the mass/damping parameter  $m^*\zeta$ , only two response branches exist, namely, the initial and the lower branches [26]. Khalak and Williamson [24], by examining the vortex shedding response over a wider range of  $m^*\zeta$  values, demonstrated the existence of three oscillation branches, namely, the initial, the upper, and the lower branches. Of practical

relevance is that ocean structures, such as risers and cables, typically have a structural mass that is relatively close to the displaced mass of the fluid ( $m^* \sim 2.0$ ) and that structural damping is relatively low ( $\zeta < 0.01$ ). By presenting two responses of the vibrating system, Fig. 6 schematically illustrates the effect of a low value and a high value of  $m^*\zeta$  on cylinder response when plotted against the reduced velocity. Graph (a) in this figure plots the transverse response amplitude of a cylinder in an airflow that is, for a high mass/damping parameter ratio at high values of  $m^*\zeta$  showing that the synchronized lock-in range can be divided into an initial branch and a lower branch. Graph (b) plots the response for a low mass/damping ratio at a lower value  $m^*\zeta$ , and a third, upper response branch is presented. The response demonstrates that for the lower value,  $m^*\zeta$  produces two-phase jumps, whereas, in the vibration for a high value of  $m^*\zeta$ , only a single-mode jump is produced.

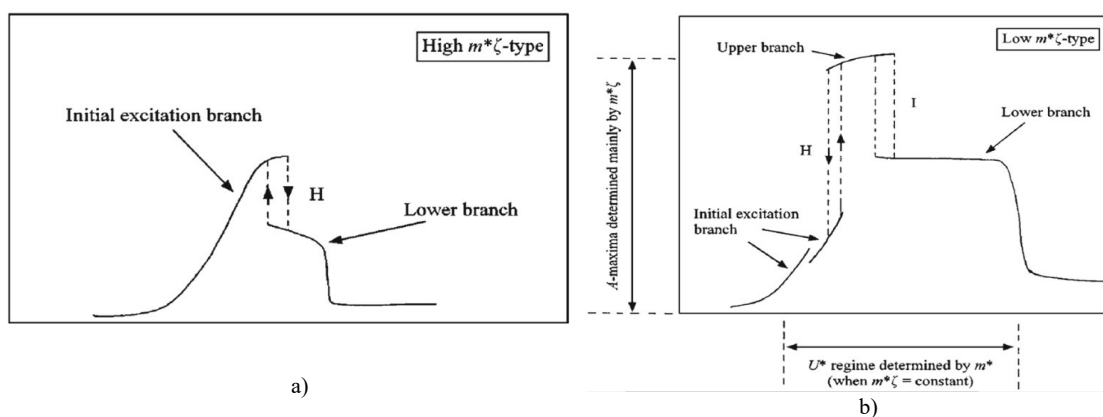


**Figure 6** Amplitude response for high (a) and low (b) mass/damping parameters [27]

Many vortex formation modes correspond to response branches associated with VIV. The first jump (H) signifies the transition of the vortex phase from the initial to the upper branch, and this jump is associated with the changed timing of vortex shedding. The second jump (I) represents the transition of the phase decreasing from the upper to the lower branch, and this jump is not associated with such a switch in the timing of vortex shedding. The initial branch itself seems to be divided into quasi-periodic and purely periodic sub-regimes. In the initial branch, the 2S mode prevailed, with two single vortices shed from the cylinder over one period of vibration. However, in the lower branch, the 2P mode existed, with two pairs of vortices shed from the cylinder in one period of vibration. Khalak and Williamson [24] and Laneville [28] reported that the jump of vibration amplitude from the initial branch to the lower branch corresponds to a vortex shedding pattern changing from 2S to 2P mode. The jumps between the three branches were associated with changes in the phase angle between the cylinder response and the exciting force. The third P + S pattern (one single + one pair of vortices per cycle) appeared initially only in the forced vibrations. Fig. 7 shows the vortex mode map created by Williamson and Roshko [29], which translated a sinusoidal trajectory over a wide range of amplitudes and wavelengths. Their map standardizes the vortex shedding with the oscillation of the cylinder with Y-only motion in the plane ( $\lambda/D$ ,  $A/D$ ). It is possible to observe the map with the different zones corresponding to the vortex pattern shedding into the cylinder transversely to the flow in the function of the oscillation amplitude and wavelength. The shape of the structure also affects the response regime of the reduced velocity [26].

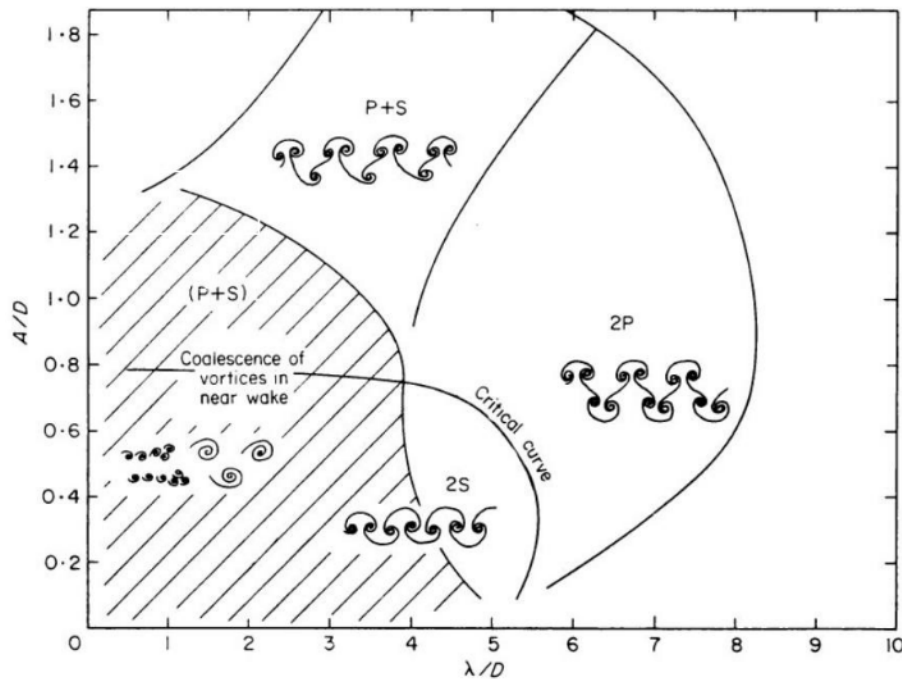


**Figure 7** Vortex flow patterns in the wake of the circular cylinder [29]

Two-DOF VIV (Inline & Transverse motion)

While high attention has been given to studying the 1DOF VIV of a circular cylinder in the transverse direction of the flow, it is logical to assume that the associated oscillating vibrations occur in the streamwise and transverse directions, rather than in the transverse direction only. In reality, vortex-induced forces acting on the cylinder fluctuate in the streamwise and transverse directions. Although the transverse (lift) fluctuation is generally larger than the streamwise (drag) fluctuation, the resultant streamwise vibration must have some effect on the wake [30]. Jauvtis and Williamson [31] carried out studies of vortex-induced cylinder motions where the natural frequencies in the (X) and the cross-flow (Y) directions were precisely the same—that is, where  $f_{ny}/f_{nx} = 1$ . They found a remarkable similarity between inline and cross-flow motion responses, indicating that transverse (cross-flow) response modes are almost unaffected. They observed that when the mass ratio is gradually reduced at a fixed mass-damping, the peak of the transverse amplitude is not affected, and this holds true for a mass ratio as low as  $m^* = 6.0$  [31]. With mass ratios lower than 6, a new response branch with peak amplitudes considerably greater ( $\approx 1.5$  diameters) than that in the 1DOF VIV was found. The super-upper branch interestingly starts and terminates directly above the boundaries of the 2P mode only for the transverse motion. This super-upper branch displays a highly stable, periodic, and hysteretic behavior of the shed vortices, and the in-line and transverse movement of these vortices are strongly coupled. The 2T mode vortex structure meaning that two triplets of vortices are shed from the cylinder in one vibration period was found as the response amplitude reached its maximum value. In the in-line direction, the maximum amplitudes are close to 0.3 diameters.

The authors used digital particle image velocimetry (DPIV) to study the wake vorticity fields for each response branch. Although the experiments of Stappenbelt and Lalji [24] showed that the super-upper response branch occurs in the 2DOF cases up to a mass ratio of 8.76, they

concur with Jauvtis and Williamson [32] that offshore design codes should reflect the significant deviation from the 1DOF VIV data when dealing with the low mass ratios typically encountered in the offshore structure design. The disparity between their results and the work of Jauvtis and Williamson implies that the experiments of Stappenbelt and Lalji were performed with higher damping. Laneville reported that the 2S and 2P vortex shedding modes are influenced by the X–Y motion of the circular cylinder and that the degree of this effect is related to the time derivation of the motions [28]. Govardhan and Williamson [33] carried out experiments for mass ratios of  $m^* = 100$  down to  $m^* = 1.0$  that yielded negligible oscillations: However, with reduced mass, large-amplitude oscillations appear suddenly at a critical mass ratio of 0.542. The Re values for these experiments ranged from 4,000 to 22,000 [34]. In 2003, the authors deduced the following expression for the frequency of the lower-branch vibration at low mass/damping ratios:  $(m^* + CA) \zeta < 0.05$ . Results based on this expression agreed with a wide set of experimental data [33].

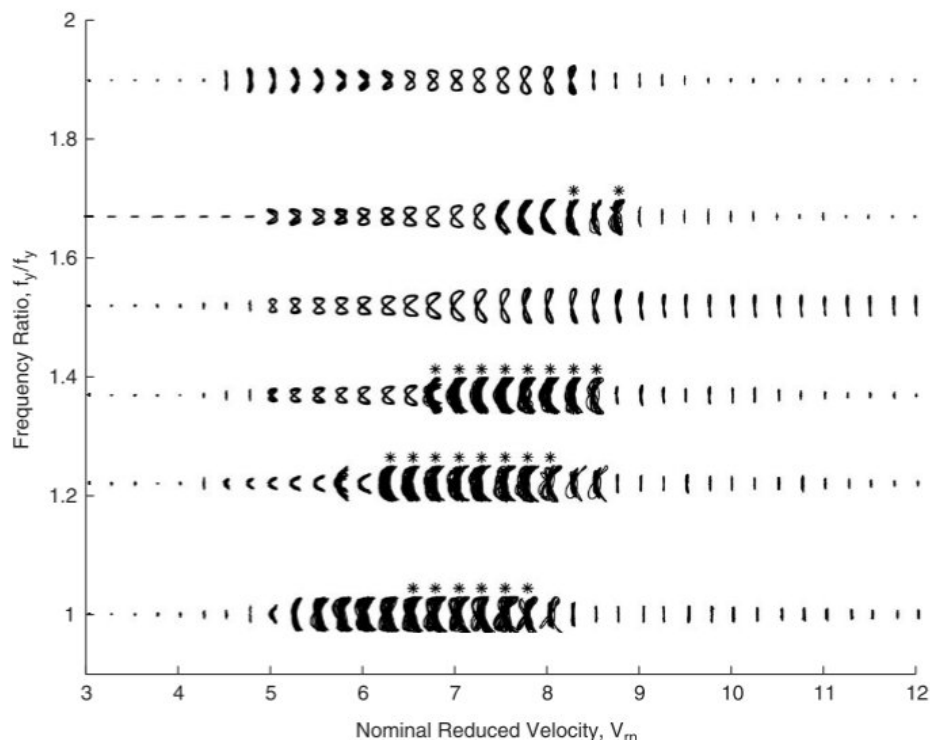


**Figure 8** Cylinder orbits at varying frequency ratios [35]

Another experiment by Morse and Williamson [36] investigated the effect of Re on  $m_{crit}^*$ . They observed that  $m_{crit}^*$  gradually increases from 0.36 to 0.54 over the Re range from 4,000 to 30,000. They predicted the critical mass below which no coherent region exists that is, where a body can resonate over an unlimited range of flow velocities. For the 2DOF cylinder in subcritical tests, Dahl et al. [37] also reported the occurrence of figure-eight orbits. Each time a vortex is shed, a weak fluctuating drag is generated, with the fluid flow inducing inline oscillations. This occurs at a reduced velocity of  $U_r = 1/2St_t$ .

Another form of wake instability was observed for circular cylinders in a range of reduced velocities less than  $1/2St_t$ . Inline oscillations, caused by this effect, have not been observed for bodies in the air; however, serious oscillations may occur in denser fluids of substantially greater mass ratios, such as water. Their measured maximum amplitudes were less than  $1.5D$  and, hence, much smaller than those experienced in vortex-excited cross-flow vibrations.

Fig. 8 presents orbital plots from their experimental investigation, obtained from inline versus cross-flow (transverse) motions at different frequency ratios. With their apparatus, they attained a maximum amplitude ratio of  $A^* = 1.35$ ; however, in some cases, the cylinder reached the end of the guide bearing railing, which in Fig. 8 is indicated by an asterisk (\*). On the other hand, inline motions significantly affect the phase of vortex shedding, and in the wake of the cylinder, this appears as a higher power input.

Jeon and Gharib [30] confirmed this with data obtained from a DPIV system and a strain gauge force balance. They observed that at zero phases, the changing sign of lower frequency oscillations is transferred to the wake, and at the  $-45^\circ$  phase more than 50% higher power gain to the wake when the in-line (streamwise) motion is added. Since the energy transfer between the body and the wake is sensitive to the relative phase between the force and the body motion, the phase of the streamwise motion can control even the sign of energy transfer (wake driving the body or vice versa). It appears that changing the relative phase of shedding causes a corresponding change in the phase of the lift force. As the frequency ratio increases, this peak response shifts to higher reduced velocities, where the drag excitation frequency is closer to the in-line natural frequency. Moreover, the onset of the disappearance of the two pairs of vortices being shed from the cylinder in one period of vibration, the so-called 2P shedding mode, was delayed. That is, the changing energy balance in the relative phase of the streamwise motion caused this 2D response. Interestingly, Blevins and Coughran [38] reported that the 2DOF motions occur over a wider band of entrainment velocities than the transverse-only motions.

Furthermore, the Massachusetts Institute Of Technology (MIT) towing test measurements by Dahl et al. [35] revealed that this kind of motion is characterized by third-harmonic transverse oscillations, a phenomenon related to multi-vortex patterns forming in the wake of the cylinder. They found that the associated large-amplitude lift force components govern first-harmonic components. These dominant third-harmonic lift components occur when the in-line cylinder motions describe a figure-eight shape as the cylinder crosses the centerline of this figure-eight shape. It is worth noting that additional high-frequency harmonics affect the fatigue life of oscillating structures because of their significant influence on the structure's stress level. Thus, large-amplitude third-harmonic oscillations may drastically decrease the fatigue life of long string-like structures, such as marine risers, especially if a large number of natural frequencies are generated. Experiments by Srinil et al. [39] revealed that even a small change of the in-line and transverse structure frequency affects the 2DOF vortex-induced maximum attainable amplitudes. It is worth noting that the in-line response, in particular, may significantly contribute to fatigue because the associated lowest modes generate double-frequency in-line oscillations. Recently, 2DOF vortex-induced cylinder motions have received special attention because the offshore industry must deal with vortex shedding resonance, which is virtually impossible to avoid.

### *Influencing parameters*

A simple dimensional analysis has been used to obtain the parameters of controlling the transverse vortex-induced vibration of a cylinder [9]. As mentioned, parameters that affect vortex-induced vibrations may be classified as structure parameters and flow parameters. The structural one is; structure mass, damping, aspect ratio, surface roughness, and cross-section shape. While the flow parameters are; Reynolds number, end conditions, tip flow, correlation length, flow ratio, turbulence, and flow shear. A simple dimensional analysis has been used to obtain the parameters for controlling the transverse VIV of a cylinder [9]. As mentioned, parameters that affect VIV may be classified as structural parameters or flow parameters. Structural parameters include the structure mass, damping, aspect ratio, surface roughness, end conditions, and cross-section shape, while the flow parameters are the Re value, tip flow,

correlation length, flow ratio, turbulence, and flow shear. The most significant parameters are presented here. More details and an extensive literature review on parameters that affects vortex shedding can be found in the publishing proceeding review paper by Mh. Youssef et. al. (2020).

- Cylinder Mass Ratio

For an elastically mounted cylinder, the oscillation frequency depends primarily on the mass ratio. Khalak and Williamson [19] observed that for a constant value of  $m^*\zeta$ , reducing the mass ratio causes the maximum amplitude of oscillation to remain almost constant over a larger synchronization range. Modir et al. [40] experimentally studied the effect of the mass ratio of an elastically mounted rigid circular cylinder on the maximum amplitude of oscillation and frequency response. The experiments were performed over a wide range of  $Re$  values, ranging from  $1.7 \times 10^4$  to  $7.0 \times 10^4$ . Tests, performed in a towing tank water channel, demonstrated that the amplitude of oscillation tended to decrease at larger mass ratios of the system. By decreasing  $m^*$ , the authors observed that the range of synchronization expanded and shifted to higher  $Re$  values, a process that demonstrates the dependence of VIV on the mass ratio. Furthermore, the range of synchronization expands and shifts to higher  $Re$  values, and the maximum amplitude of oscillation increases as the mass ratio decreases. The range of synchronization strongly depends on the mass ratio. Although these results were obtained by changing the mass ratio, the corresponding damping ratio also changed. These results agreed with those of Blevins and Coughran [38].

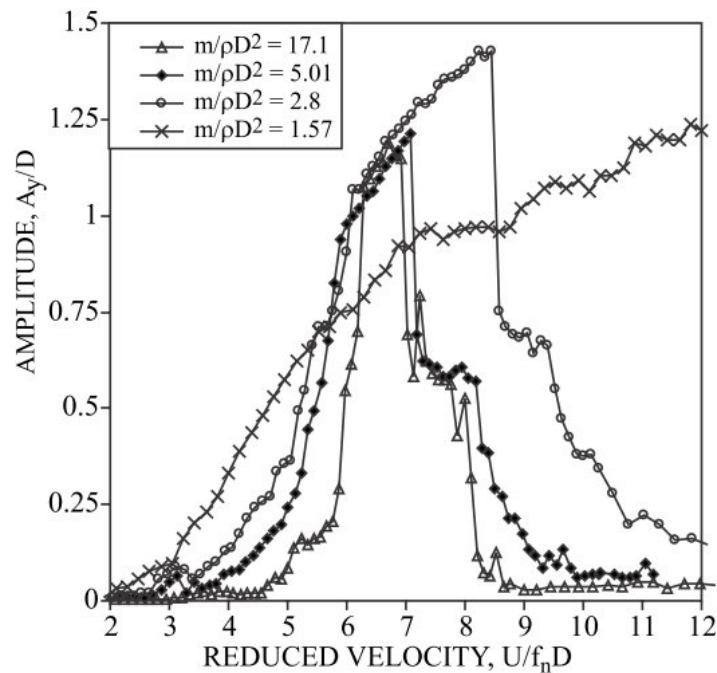


**Figure 9** Transverse response ratio of four cylinders of different mass ratio [38]

Blevins and Coughran performed their experiments with a constantly reduced damping of  $4\pi m\zeta/\rho D^2$ . To illustrate the effect of decreasing the mass ratio, Fig. 9 plots maximum 2DOF cylinder responses as functions of reduced flow velocity for decreasing mass ratios of  $m/\rho D^2 = 17.1, 5.01, 2.80,$  and  $1.57$ , here for the cases with constantly reduced damping of 1.24 and at  $Re$  values up to 150,000. With decreasing cylinder mass ratios, the response increases at higher velocities. For the lowest mass ratio, the synchronization region extends beyond the range of the velocities in the experiments. Furthermore, a steadily increasing linear path appears instead



of a curved path for the upper branch. This observation could have been associated with the effect of the changing  $Re$  and not the mass ratio, as this behavior occurred for the other mass ratios shown in Fig. 11.

- Cylinder damping

Structure damping is useful in the practical VIV response prediction of flexible structures. Venugopal [41] in his doctoral thesis proposed three damping expressions, namely, one for the zero flow case, one for a low flow velocity case, and one for a high flow velocity case. Vikestad et al. [42] revised these expressions because they were too inaccurate. Klamo et al. [43] experimentally investigated the effect of damping on amplitude and frequency. They reported that, for a given  $U_r$ , the value of the amplitude response ratio  $A^*$  decreases as damping is increased. In addition, with increasing damping, the reduced velocity that corresponds to the system entering the desynchronized region decreases, the width of the hysteric jump decreases, and the size of the upper branch decreases because the jump to the upper branch is delayed, as shown in Fig. 10. This figure plots the cylinder response obtained from tests by Blevins and Coughran [38] on a 2DOF oscillating cylinder with a constant mass ratio of  $m^* = 5.02$ , but for the six increasing damping ratios of  $\zeta = 0.006, 0.0015, 0.0026, 0.0051, 0.0085,$  and  $0.0122$ . They observed that similar to the mass ratio, the damping ratio controls not only the maximum amplitude but also the lock-in region of the system. These experimental measurements by Blevins and Coughran [38] documented the same behavior as those of Klamo et al. [43]. Although generally the results of Blevins and Coughran [38] compared favorably to those of Bahmani and Akbari [44], their amplitudes and the associated synchronization range deviated somewhat. This could be due to the lower damping ratios of their tests. As seen in Fig. 10, for all these tests, the upper branch meets the lower branch at a fixed value of  $U_r$ , independent of damping.

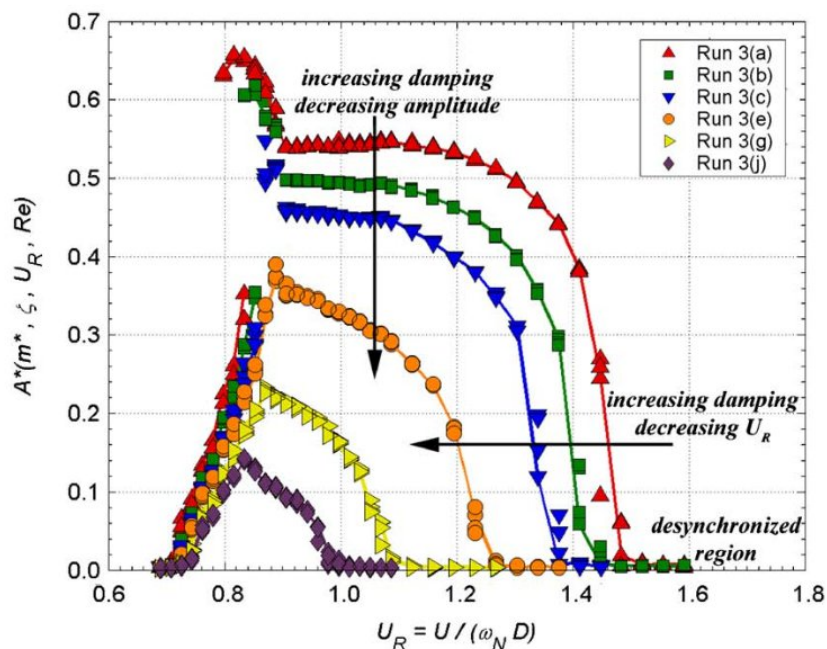


**Figure 10** Transverse response ratio of a cylinder for six different damping ratios [43]

For other systems, this value is different but always independent of damping. Blevins and Coughran [38] performed similar tests for a high damping ratio.

More specifically, Klamo et al. [43] observed that as the velocity is decreased, the jump extending downward from the upper to the initial branch occurs when the amplitude response reaches the 2S/2P boundary. In contrast to the case of increasing flow velocity, for decreasing velocity, the change from the desynchronized region to the lower branch is dramatic and takes the form of a jump discontinuity.

Recently, Vandiver [45] introduced a new damping parameter,  $c^*$ , to replace the damping ratio  $\zeta$ . As long as a periodic cylinder response dominated, he used his damping coefficient to correlate damping and lift. He did so whenever the product of the damping parameter and the non-dimensional amplitude equaled 0.79. Garcis et al. [46] tested this value to obtain the effect of damping on variable added mass. They reported that Vandiver's damping coefficient agreed closely with the maximum lift coefficient of the square root of 0.79. Vandiver and Rao [47] extended the use of the damping parameter  $c^*$  to the analysis of a long flexible cylinder.

- Reynolds Number

The  $Re$  value also affects the response. To obtain an upper branch response, damping must be low enough and the  $Re$  value high enough. Typically, at higher  $Re$  values, the cross-flow amplitude is larger than at lower  $Re$  values. This trend concurs with the results of cylinder response measurements by Dahl et al. [35]. The response profile of a system is controlled by the combination of damping and  $Re$ . The maximum resonant amplitude of lightly damped smooth cylinders increases with  $Re$ . Blevins and Coughran [38] measured an amplitude of 1.75 times the cylinder diameter for a smooth 2DOF cylinder at a  $Re$  of 139,000. This finding demonstrated that the  $Re$  value has a stronger influence on the cylinder response than the mass ratio,  $m^*$ , or the product of the mass ratio and damping ratio,  $m^* \zeta$ . Raghavan and Bernitsas [48] observed that the  $Re$  value rather than  $m^*$  or  $(m^* + CA) \zeta$  dictates high-amplitude VIV. They conducted their experiments for the same mass ratio and nearly the same value of  $(m^* + CA) \zeta$ , but at  $Re$  values between  $10^4$  and  $10^5$ . The increased  $Re$  resulted in increased amplitudes of oscillation and wider ranges of synchronization. Synchronization starts at a higher normalized velocity, the response remains in the 2P regime, and the lower branch disappears as it is overtaken by an extended upper branch. The 2P mode and the higher modes were observed to occur in the upper branch, where, at high  $Re$  values, due to the higher level of velocity fluctuations, the 2P mode becomes more stable and stronger and thus leads to a stronger forcing and larger amplitude of oscillation.

Furthermore, Raghavan and Bernitsas [48] reported no hysteretic response between the initial and upper branches. It seems that there is a critical combination of the  $Re$  and reduced velocity above which a linear and steadily increasing upper branch appears rather than a curving upper branch, as seen for the low  $Re$  cases shown in Fig. 11. A similar response is seen in Fig. 9 over the same  $Re$  range. Tests at higher  $Re$  values need to be examined. It seems that the maximum amplitude of oscillation is determined by the vortex structure that the system can support, which is highly related to the primary factors of the damping, mass ratio, and  $Re$ . Carberry et al. [49] showed that over a small range of subcritical  $Re$  values, the phasing of vortex shedding is only slightly dependent on the  $Re$  value [49]. However, a stronger dependence exists between the magnitude of forces exerted on the cylinder and the  $Re$  value because even a small variation of the shedding point can affect the vortex patterns.

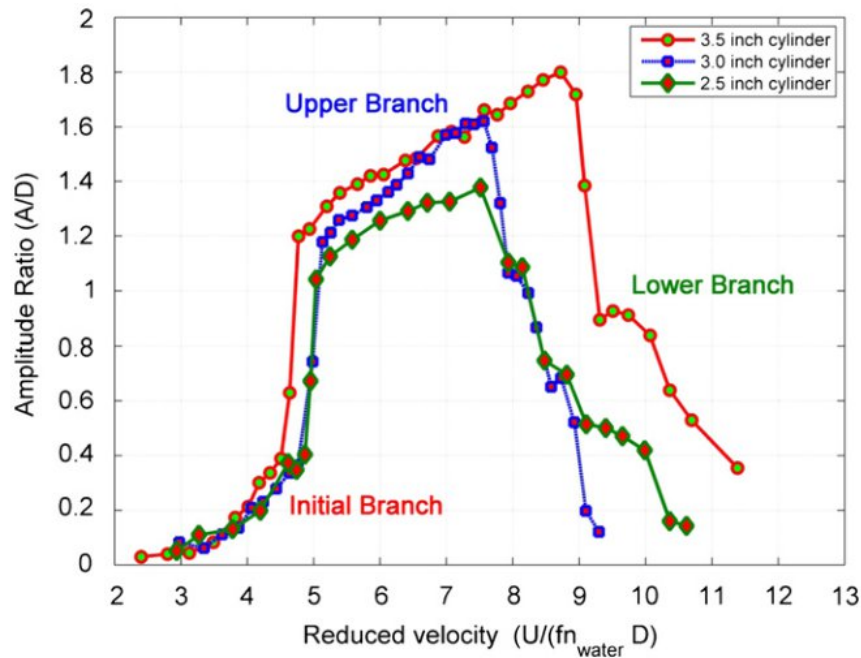


**Figure 11** Transverse response ratio at high Reynolds number and high damping [48]

### Suppressing vortex-induced vibration

Suppressing VIV is no easy undertaking, but there are several ways of reducing the amplitude response. One way to do so during design is to avoid the resonant area completely by changing the natural period of the motion [50] or changing the design of the structure, such as the diameter, to delay the synchronization region. This is possible only when the highest Strouhal frequency for the cross-section is lower than the fundamental natural frequency so that the local reduced velocity will then be less than 5 for all frequencies. An alternative way is to be above the resonant area, which is much more complicated because there will always be a higher natural mode with a frequency that corresponds to the shedding frequency. Vandiver reported that the combination of shear flow and the excitation of the higher modes (above mode number 100) greatly reduces the probability of lock-in [51]. Another way is to increase the mass of the structure and the damping to reduce or avoid the peak amplitudes, but implications for the natural frequency of the motion must be considered. In marine applications, it is seldom possible to increase the damping enough to avoid higher amplitude responses. The most popular way is to modify the pattern of the vortices and their effect on the structure by including protuberances on the surface of the structure. This is a consequence of the modification of the boundary layer around the cylinder. Several techniques have been studied and applied in several fields. There are three categories of passive control devices, according to the Zdravkovich classification, depending on how such a device influences the vortex shedding [52]: (i) surface protrusions (strakes, wires, fins, studs, etc.), which affect separation lines or separated shear layers; (ii) Breaking the flow into many small vortices such as perforated shrouds and axial slats; and (iii) near-wake stabilizers, which affect the switch of the confluence point, preventing the building of the vortex street. Scruton and Walshe [53] first examined helical strakes for suppressing VIV on cylindrical structures. The parameters that affect the effectiveness of the strakes are their number, height, and pitch (see Fig. 12). These results have been confirmed by Vickery and Watkins tests in the water field [54].

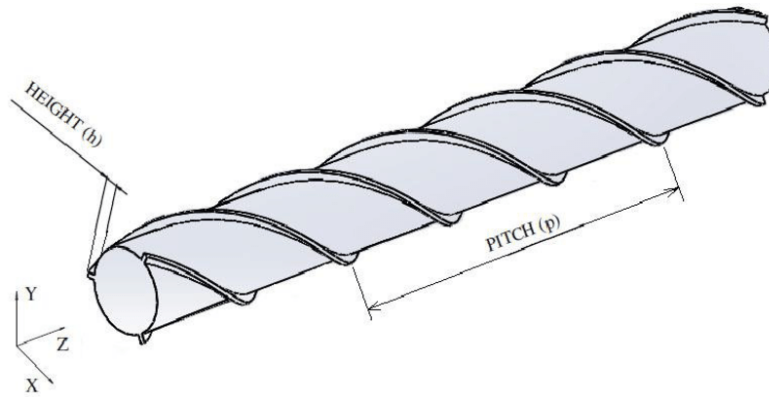


**Figure 12** Circular cylinder fitted with helical strakes [55]

Blevins et al. conducted tests with 5%, 7%, and 13% of diameter high helical strakes. Strakes successfully suppressed large-amplitude VIV; the remaining oscillations were small and irregular. However, to simulate a local strake defect, when one diameter length of 7% high strakes was removed, the oscillation amplitude increased by a factor of four at the worst orientation. This finding suggests that local strake irregularities, such as at pipe joints, strake clamps, access holes, and marine growth, impair the effectiveness of low strakes [38]. Removing one diameter length of the 10% and 13% high strakes did not significantly change the cylinder response.

A rigid splitter plate is one of the most frequently used suppression devices. Roshko (1953) observed that a splitter plate with a length of 5 cylinder diameters attached to a fixed cylinder was sufficient to stop vortex shedding formation completely and increase the base pressure considerably [56]. He found a massive reduction in vortex interaction and a delay in the formation of vortices by extending the separated shear layers downstream of the trailing edge, where the experiment was conducted at a subcritical flow in the  $Re$  of  $1.45 \times 10^4$ . In the range of  $10^4 < Re < 5 \times 10^4$ , Apelt et al. reported the effects of wake splitter plates on circular cylinders. It was found that splitter plates longer than  $2D$  in the wake of a circular cylinder can progressively modify the drag and vortex shedding up to a plate length/diameter ( $L/D$ ) ratio of 3, while no further changes occur with a greater  $L/D$  ratio [57]. Kwon and Choi [58] simulated the laminar vortex shedding behind a circular cylinder using splitter plates attached to the cylinder, confirming the findings of Apelt et al. [57]. In 1980, Gartshore et al. carried out experimental tests on sectional models of a bare circular cylinder and cylinders fitted with different configurations of fins, as shown in Fig. 13.

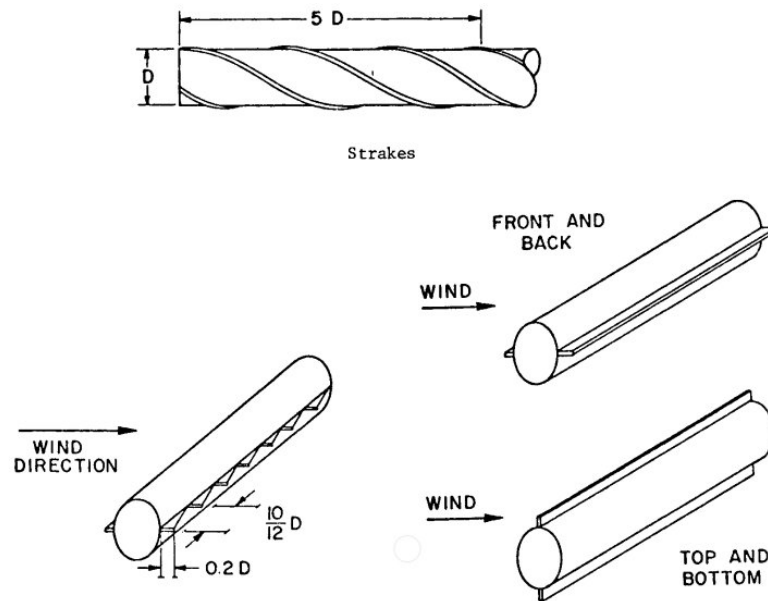


**Figure 13** Different sectional models tested by Gartshore et al. [59].

The results showed that strakes were the most effective of the simple devices tested. The straight fins, whether attached to the front and back or top and bottom, caused an increase in the maximum amplitude of the response [59]. This increase may have been due to sharp edges near the top or bottom of the cylinder causing galloping, which means it would have been due to a combination of galloping and vortex excitation.

Qiu et al. later studied the effect of cylinders with frontal, wake, and bilateral splitter plates on vortex shedding formation with wind flow [60]. They found that vortex shedding from the cylinder can be suppressed effectively by a splitter plate with a length of 3 cylinder diameters in the wake as it isolates the separated shear layers on the side of the cylinder. The application of a splitter plate was investigated experimentally by Ibrahim et al. in 2008; their results contradicted the assumption that the behavior of fixed cylinders with attached splitter plates can be extended to the free-moving case. They found that, rather than suppressing vibration, attachment of a short splitter plate to the riser may amplify the structures' VIV. They observed that splitter plates of lengths greater than 2 cylinder diameters suppressed VIV over the tested range as a result of hydrodynamic damping and a reduction of the interaction of vortices [61]. There was, however, a trend of slightly increasing amplitude, which was reduced as the plate length increased. In recent years, studies have illustrated the flow around a circular cylinder with a flexible plate. After conducting experiments with a flexible splitter plate attached to the cylinder, Liang et al. (2018) reported that the entire synchronization region is postponed and that the shear layers and vortex shedding could be well controlled for a plate length of less than 1.1 cylinder diameters [62]. Strykowski and Sreenivasan reported that at low Re values, vortex shedding behind a cylinder can be controlled by placing another, much smaller cylinder in the near-wake of the main cylinder to alter and suppress the vortex shedding behind it [63]. These results were numerically verified by Dipankar et al. [64]. Hwang and Yang numerically studied drag reduction on a circular cylinder using two splitter plates with the same length [65]. The combined effect of the dual detached splitter plates, where the upstream splitter plate reduces the stagnation pressure by friction and the downstream one increases the base pressure by suppressing vortex shedding, results in significant drag reduction on the cylinder.

It is worth mentioning that such devices increase the cost of the structure model and that they complicate handling during installation. Some devices also reduce the drag coefficient, especially the streamlined fairing, which can reduce the drag coefficient to the order of 0.1 [20]. One essential drawback is the installation of such a mitigation device, which is complicated and costly, especially for cylinders with a low aspect ratio. Spoiler plates are relatively simple to build compared with other passive control solutions. In 2020, Bianchi et al. carried out experiments in a towing tank investigating the effect of spoiler plates along the vertical axis of low aspect ratio (cylinder length to diameter ratio = 1.5). A desynchronization of vortex shedding, reduction of the in-line and transverse responses, and decreasing drag forces occurred for the most improved case [66].

During the past decades, numerous efforts have been made in the study of flow control around the bluff body. Generally, the control of wake flow can be classified into two categories: passive and active. For the category of passive controls, no power input is required; however, for the category of active controls, external power input is generally needed. To date, various forcing devices have been applied to perform active control of vortex shedding behind the bluff body. Examples are a rotary body [67], streamwise and transverse oscillations of a bluff body [68], inflow oscillation, steady and time-periodic blowing suction, distributed and electromagnetic forcing [69], and plasma actuation [70]. For a brief treatise on active control, see the comprehensive review by Choi et al. [71]. Among various active control approaches, the rotational oscillation of the cylinder is used extensively. Gopalkrishnan et al. investigated the feasibility of free shear flow control and energy extraction from the large eddies in a free shear flow. The oncoming vortices of the Kármán street were repositioned, and their strength was changed using the foil model. This resulted in new stable patterns downstream from the plain foil, where three distinct modes were identified [72]. The partial rotation restricted to the upstream part of the cylinder could achieve more drag reduction [73].

### Free vibration and force-excited experiments

Because the amplitude and frequency of the motion can be altered at will, several investigators have conducted forced oscillation experiments rather than free ones. For a freely suspended bluff body oscillating at a steady amplitude, it can be assumed that if the same body is forced to oscillate at a similar amplitude ratio, reduced velocity, and Reynolds number, then the flow patterns will be identical. The available experimental evidence suggests that free and forced vibration flows are the same [74]. It is reported that free vibration tests are performed without using any exciting mechanism for the oscillation either in a wind tunnel or in a water tunnel, mainly for flow visualization reasons. The free oscillation of a cylinder is closer to the true nature of the VIV. The flow velocity increases from low values to higher ones, step by step, measuring the steady-state vibration amplitude for each flow velocity. However, forced oscillation experiments are performed using an excitation mechanism in which the flow velocity is kept constant while the amplitude and frequency of oscillation vary. These tests can regularize and idealize the various aspects of VIV, leading to the extraction of forces from repeated sinusoidal oscillations. For each test, the required driving force for the oscillation is measured throughout a range of reduced velocities  $U_r$ .

The difference between the free and forced oscillation experiments is that, in the former ones, the  $Re$  value varies, while in the latter ones it is constant. Furthermore, there is a two-way coupling in free vibration between the wake and the cylinder motion, which is the driving mechanism. Morse and Williamson reported that with carefully selected conditions, there is very strong agreement with the predictions of critical mass from controlled vibration, and

therefore, the direct measurements from free vibration experiments are obtained similar to forced test [75]. Hover [76] performed other investigations of free and forced oscillation in a water tank, with the amplitude and phase of the lift coefficient extracted in both cases. Although in forced oscillation tests, the force correlation along the span of the cylinder was better, the correspondence of the lifting coefficient in forced and free vibration tests was remarkably close. Although the free and forced vibration cases exhibit many similarities in the wake modes and fluid forcing, there are still major differences in the energy transfer between the fluid and the structure [17]. Dahi et al. (2006) have stated that "Since we cannot control the damping in the system perfectly and the pluck tests do not provide an accurate description of oscillatory damping,  $\epsilon_{\text{error}}$  was not always zero." The power lost to structural damping should equal the power input from the motor so that the average fluid power is zero [35]. In the correlation between end lift forces, however, the forced vibrations yield a completely different view of transition than that seen for the free vibrations, but similar wake properties develop even when the lift forces are drastically different [77].

### *Galloping phenomena and VIV*

Of considerable interest is a dynamic instability triggered by the asymmetric cross-section of the bluff body immersed in a flow. The potential was recently demonstrated for limiting or utilizing the response of quasi-steady galloping oscillations in the plunging mode. The term "galloping" describes the kind of flow-induced vibration that occurs for bodies with non-circular cross-sections. Assi and Bearman [78] showed that classical galloping of non-circular cylinders, such as square cylinders, is caused by fluid dynamic instabilities, where the motion of the cylinder generates forces that increase the vibration response amplitude. Lower frequencies and larger amplitudes than VIV characterize this phenomenon, and these amplitudes increase at higher velocities until the structure fails. Galloping occurs above a critical flow speed and does not depend on vortex formation.

Nakamura et al. [79] were among the first to study a circular cylinder galloping in the presence of a long stationary splitter plate. Recently, Mannini et al. [80] investigated the VIV interface phenomenon of galloping of low-damped rectangular cylinders. Mills et al. [81] suggested that the flow structure and dynamic behavior of vortices could be altered by changing the cylinder's chord-to-thickness ratio. They found that the similarity of the relationship between  $S_t$  and the chord-to-thickness ratio is due to peaks of base suction occurring when the leading-edge vortices pass the trailing edge. It is at this point that the phase of the perturbation cycle (and of the leading-edge shedding cycle) leads to the shedding of trailing-edge vortices. Mannini et al. provided a comprehensive review of the literature on the galloping of a rectangular cross-section cylinder [82]. Galloping could also occur due to marine organisms on marine cables [83]. The galloping response has also been observed in a circular cylinder, free to oscillate, and fitted with three different splitter plates has been investigated by Assi and Bearman [84]. Zheng and Wang numerically studied the galloping oscillation of a circular cylinder combined with different fairing devices [85].

Parkinson and Wawoznek performed an experimental investigation of the interaction between galloping and the Kármán vortex resonance of a square cylinder in a smooth wind flow. They found the instability started at the critical velocity for vortex resonance wind speeds, rather than that predicted by the quasi-steady theory. Furthermore, they reported that a ratio of 2.15 was necessary to separate the two modes of force-induced motion [86]. Below this ratio ( $\approx 2$ ), galloping oscillations with amplitudes increasing linearly with flow velocity were observed between the two resonance velocities of VIV and galloping. The interface phenomenon between

VIV and galloping is important from a practical engineering point of view. This mechanism still requires more investigation to clarify unknown features, such as large-amplitude oscillation inflow speed ranges, for which classical VIV theories are unable to reliably predict excitation-induced galloping.

### *Cylinder model*

Most of the studies were conducted on rigid circular cylinders in which ends were fixed with elastic fixation from one or both ends, allowing a uniform distributed response along the span. There have been only a few studies of a fundamental nature probing the extent to which allowing an elastically mounted body to move in 2DOF will modify the forces, responses, and vorticity dynamics of the body in a flow. There are also very few studies that look into variation in amplitude along the span of cylindrical bodies, such as cantilevers and flexible cables.

The early studies of cantilever cylinders were conducted by Vickery and Watkins [54]. King tested a PVC cantilever cylinder in a water channel [87]. Results show a maximum amplitude followed by a slight decrease and then a linear increase also as the damping ratio decreases [87]. Another cantilever study by Fujarra et al. [88] involved a similar mass ratio and damping ratio as seen for the elastically mounted rigid cylinder [89]. The response of the cantilever appeared to exhibit a single initial branch, which then dropped to a lower branch instead of three branch types for a 2D rigid one. A jump phenomenon was observed, and a high-speed mode of large amplitude response was found outside the principal synchronization regime. Regarding the synchronization behavior in all the research on cantilever cylinders, no lock-in region was found like that found under other conditions. This finding is in agreement with Williamson et al.'s [90] study of a plastic cylinder. Bernitsas et al. found that the tip flow reduces the lift force exerted on a cylinder and narrows the range of synchronization [91]. This behavior did not occur in a cantilever test model by Pesce et al. [88], but their test model was made of aluminum alloy, and thus this outcome was possible due to the vibration behavior of the nonmetallic test model.



## 3. Experimental Methods

Experimental investigation of VIV has a history of around 80 years and still going on to find out more details about the VIV dynamics and methods to suppress. However, a few amounts of work have been performed in parallel with respect to surface-mounted bluff bodies. It is important to investigate flow around the finite circular cylinder of moderated aspect ratio because it is encountered in various engineering applications. Furthermore, it is essential to experimentally investigate VIV suppressing tools to be used as basic data for optimizing structural design.

In order to analyze the VIV for flow past a finite cylinder, the experiments have been performed for different test cases and under different conditions. This chapter describes the details of the experimental investigations performed to illustrate the different characteristics of VIV at the water tank and the wind tunnel with cylinder models below the value of the critical mass ratio, and a high mass ratio model without any added storing elements, respectively. The description for each experiment includes experimental apparatus, experimental rigs, data acquisition, and test procedures to simulate free vibration VIV. The preliminary analyses, including the free decay test in air or/and water, are also presented in this chapter.

### 3.1 Water Tank Tests

#### *VIV Suppressing For Critical Mass Ratio*

In this section, A series of experiments have been undertaken aimed at reducing drag forces and suppressing vortex shedding from circular cylinders. In this work, the newly developed fin plate configuration attached to flexible cylindrical models for suppressing vortex-induced vibration has been experimentally investigated in the regime of Reynolds number range  $Re = 1.4 \times 10^4 - 8.0 \times 10^4$  in the towing tank. These models have been demonstrated numerically as will be discussed in chapter 6. Experimental tests have been carried out on sectional models of a plain circular cylinder, and on cylinders fitted with different newly developed configurations of fins. In order to examine the potential of the used suppressing techniques, a cylinder had a mass ratio of 0.455 below the critical value and an aspect ratio of 18.8 has been tested. Three positions around the cylinder of the fins plate were considered:  $80^\circ$ ,  $90^\circ$ , and  $110^\circ$  from the stagnation point.

#### 3.1.1 Water tank facility

The experiment was carried out in the circulating towing tank of the Institute of Ship Technology, Ocean Engineering, and Transport Systems (ISMT) of the University of Duisburg-Essen, Germany. The main tank dimensions were 6.00m x 1.47m x 0.67m (length x width x depth), and the flow had a maximum velocity of 2.25 m/s with turbulence ( $Tu < 2.2\%$ ) during the tests. Figure 17 illustrates the experiment setup via a schematic diagram for both instrumentation systems in collecting the dynamic response of the vibrating system and the stream flow throughout the test section.

### 3.1.2 Test model

The polyvinyl chloride (PVC) cylinders tested were a smooth cylinder and three cylinders with different fin plate arrangements. All the tested cylinders had an outer diameter of 32mm, a wall thickness of 1.7mm, and an aspect ratio  $L/D$  of 18.75.

The low blockage ratio of 1.95 (less than 6%), defined as the ratio of the water channel's cross-sectional inlet area and a cylinder's cross-sectional area, ensured that the channel walls did not affect vortex shedding frequencies so that the Strouhal number was independent of the blockage ratio and the aspect ratio of the cylinder, therefore, the vortex shedding frequency was independent of these ratios [92]. The models were mounted with a threaded stainless steel pin on a force-torque sensor that was placed underneath the channel's bottom. A 2.0mm gap between the cylinders and the channel's bottom allowed oscillations in the inline and the transverse flow stream directions.

Besides the plain cylinder, three cylinders fitted with fin plates were studied. Eight fins were attached symmetrically to a cylinder at radial positions of 90, 80, and 110 deg from its front stagnation point. Each fin was built out of stainless steel and had a length of 60mm, a breadth of 4mm, and a thickness of 0.5mm as shown in Fig. 14. Table 2 presents the cylinder parameter values for each case tested in the present experiments.

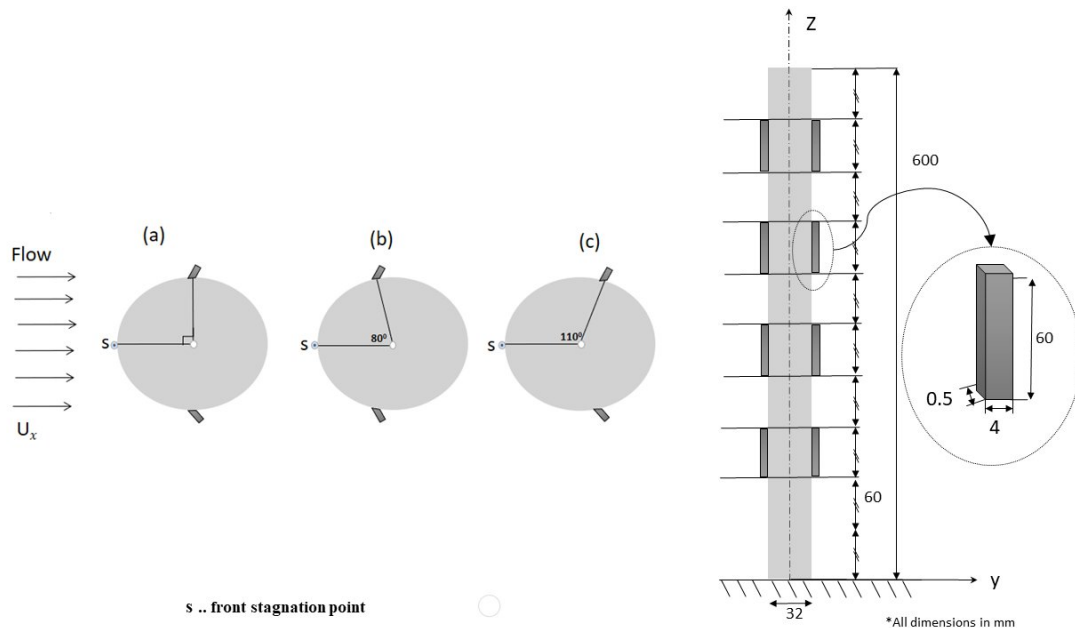


**Figure 14** Tested cylinder models parameters at radial positions of (a) 90 deg fin position, (b) 80 deg fin position, and (c) 110 deg fin position from its front stagnation point

Eight fins were attached symmetrically to the inline flow direction for each arrangement. Each fin was built out of stainless steel and had a length of 60mm, a breadth of 4mm, and a thickness of 0.5mm. Similar to the assembly conducted in section 6.2, the upper fin was placed 60mm below the cylinder's top while the lower fin was situated 120mm from the channel's bottom surface. Furthermore, a gap of 60mm separated each fin. The radial fin positions were 80, 90, and 110deg from the cylinders' front stagnation point. Additionally, all fins were attached at an angle of 45deg relative to the inline flow direction. The fins were glued with flexible silicon to the cylinders' surface. Therefore, a fillet weld was applied between fins and cylinder surface at

the downstream side of the fins. A three-dimensional printed negative form was used to keep the cylinders and their fins in position during gluing. Figures 14 and 15 display the fin arrangements.

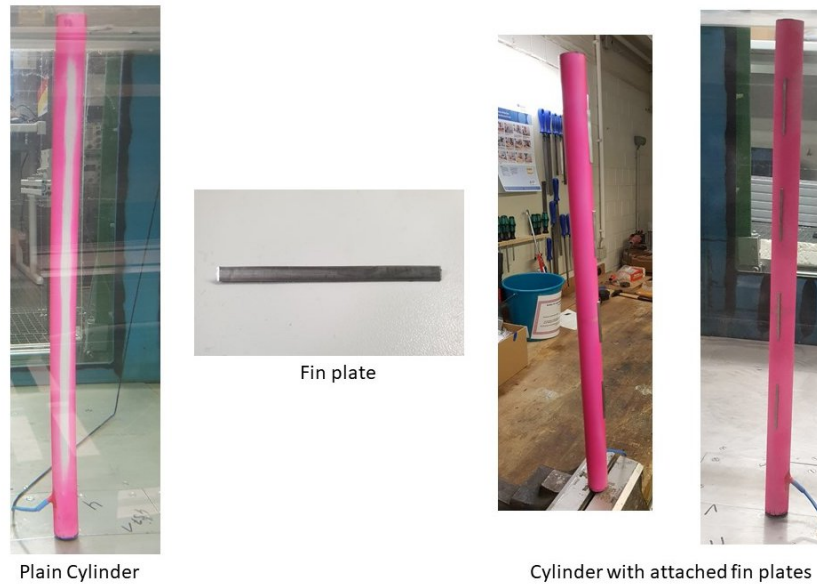


**Figure 15** Arrangement of eight fin plates attached symmetrically along with cylinder length

### 3.1.3 Experimental setup and instrumentation

A Disynet DA 3102-015g accelerometer was placed 5.0mm below the cylinder top to measure the cylinder's inline, transverse, and vertical accelerations. The 15 x 15 x 15mm<sup>3</sup> accelerometer weighed about 15gram, had a measurement uncertainty below 1%. Normally, the accelerometer measured static and dynamic accelerations and was able to measure up to 15g. However, in over-range, it measured up to  $\pm 20g$ , where  $g$  is the earth's gravitational acceleration. The accelerometer was calibrated using the earth gravitation of 1g before starting the measurement campaign. The accelerometer cable trace is kept beside the tank walls and far enough away from the models ( $< 70$  wire diameter) to ensure that its effect could be negligible as shown in Fig. 16.



**Figure 16** Accelerometer sensor cables location

Meanwhile, a force torque-sensor was used to measure simultaneously forces (drag and lift) and moments on the cylinder in six degrees of freedom acting on a cylinder. The six simultaneously recorded signals from the force balance were processed using a balance calibration matrix to obtain time histories of load components acting on a cylinder. These time histories were acquired with a 95% confidence level. Both, acceleration and force-torque measurements were sampled at 2400Hz. In the present study, a right-handed Cartesian coordinate system specified  $x$ -,  $y$ -, and  $z$ -directions corresponding to inline (stream), transverse (cross-stream), and the vertical (axial cylinder) directions, respectively. The  $z$ -direction points up towards the free surface opposite the direction of gravity as indicated in Fig. 17.

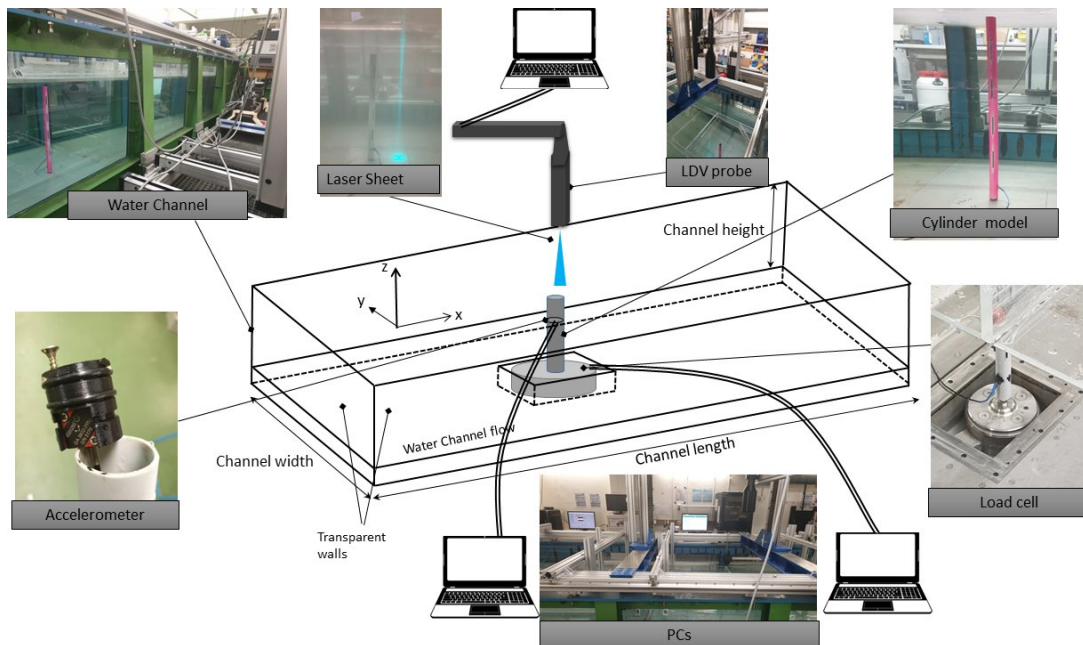


**Figure 17** Schematic of the experimental setup including a typical configuration of the experiment tools

The origin of the Cartesian coordinate system was located at the center of the bottom end of the cylinder. During the experiments, the temperature variation in the water channel test section was kept below 0.5deg Centigrade. In the present tests, a Laser Doppler Velocimetry (LDV) system with an optical fiber probe and a front lens with 800 mm that was mounted vertically over the water channel on a 3D transversing mechanism allows traveling in each direction automatically. LDV is non-intrusive and with no calibration required [93]. For more detail about LDV measurements, refer to N. Shapley (1993) [94]. LDV measurements are based on the Doppler effect that is the two coherent monochromatic laser beams of wavelength  $\lambda$  are intersecting with an angle  $\theta$  to constitute a cigar-like shape probe volume constituted of fringes formed by the interference between the two beams. When the particle is traversing through the probe volume, it diffuses the light in all directions. The light scattered by the traversing particle is received by photo-multipliers. Here, The system was used in backscatter mode so that the probe in both transmitting and receiving signals to measure inline and transverse flow velocities.

The LDV system used a continuous wave Ar-Ion laser. Glass hollow spheres with an outer diameter between 9 and 13 $\mu$ m with a density close to the water density were used as seeding particles. Here, the free flow was captured 10D in front of the cylinder at  $z/L = 0.85$  and  $0.75$ . The obtained inlet velocities were compared with the mean inlet velocities which were measured by the LDV method. Table 1 lists comparative inlet velocities obtained from the water channel control panel and from the LDV system near the inlet section located ten-cylinder diameters ahead of the cylinder at a height of  $z/L = 0.75$ .

Additionally, the wake flow properties were measured at several positions in the cylinder wake to capture vortex shedding frequencies. The locations of the measuring points have been measured at  $x/D = 1, 2, 3, 4,$  and  $5$  downstream of the cylinder, and  $z/D = 0.5$  and  $0.75$ . In this study, the flow velocities were measured along the centerline of the cylinder's wake.

**Table 1 Comparative axial inlet velocities obtained from the water tunnel control panel and from the LDV system**

<i>Axial flow velocity [m/s]</i>		<i>Turbulence intensities [%]</i>
<i>Measured by Tunnel Control Pannel</i>	<i>Measured by LDV system</i>	
2.3	2.187±0.081	1.89±0.24
1.8	1.705±0.076	1.99±0.23
1.6	1.503±0.079	1.99±0.24
1.4	1.303±0.069	2.00±0.20
1.2	1.123±0.051	1.99±0.22
1.0	0.979±0.050	2.03±0.28
0.8	0.789±0.041	2.05±0.26
0.6	0.569±0.002	2.13±0.22
0.4	0.355±0.020	2.25±0.33

### 3.1.4 Test procedure and data analysis

The experimental data were acquired through two data acquisition systems with a sampling rate of 2400 Hz. Three channels were used to record the response data of the cylinder and six-channel for the forces, and moments. The Fast Fourier Transform (FFT) procedure was applied for the raw signals to analyze the frequency content of the measured time-series data to obtain the power spectral density (PSD), describes how the power of the signal is distributed over frequency and measured in ( $G^2/Hz$ ) where the acceleration is measured in G. For the motion of the cylinder, the accelerations were converted to displacements by a double trapezoidal integration method using MATLAB software.

A bandpass filtering operation should be taken to remove the undesirable frequencies. The signal was low-pass filtered at the Nyquist frequency, 100Hz, and high-pass filtered at 1 Hz to remove the low-frequency components that are disproportionately amplified during the integration. As integration reduces high-frequency vibration and amplifies low frequencies, a high pass filter with the same cut-off value is used to attenuate low frequencies after integration [95]. Meanwhile, frequencies higher than 40.0 Hz are cut off to avoid the 50.0 Hz-noise of alternating current (AC) signal. It is sufficiently large to cover the high-order vibration frequencies concerned in this study. All the used sensors have been synchronized with the navigation data to allow combining them. The test duration was approximately ten minutes for each velocity. Repeatability tests are completed to estimate the first-order variable uncertainty for the experiments [96]. The data were processed in a MATLAB environment to obtain a cylinder's response amplitudes, flow velocities, forces acting on the cylinders, and dominant frequencies.

The structural damping and natural frequency were evaluated by hammering free decay tests. The logarithmic decrement method was used to calculate the damping ratio for the underdamped system in the time domain. The damping ratio for the experiments was calculated from the natural log of the ratio of the amplitudes of successive peaks [97]. The damping caused by friction between the internal planes that slip or slide as the material deformed is known as hysteresis or structural damping.

The root mean squares (r.m.s.) values of the displacement amplitudes and forces were computed for comparison to achieve more accurate data analysis [98]. Some analyzed parameters were presented as a function of the reduced velocity,  $U_r$ . The damping coefficient was determined based on the equation:

$$\zeta = \frac{\delta}{2\pi} \quad (15)$$

where the hysteresis logarithmic decrement,  $\delta$ , is defined as follows:

$$\delta = \ln \frac{y_n}{y_{n+1}} \quad (16)$$

Amplitudes  $y_n$  and  $y_{n+1}$  are two successive cycles of the free decay test.

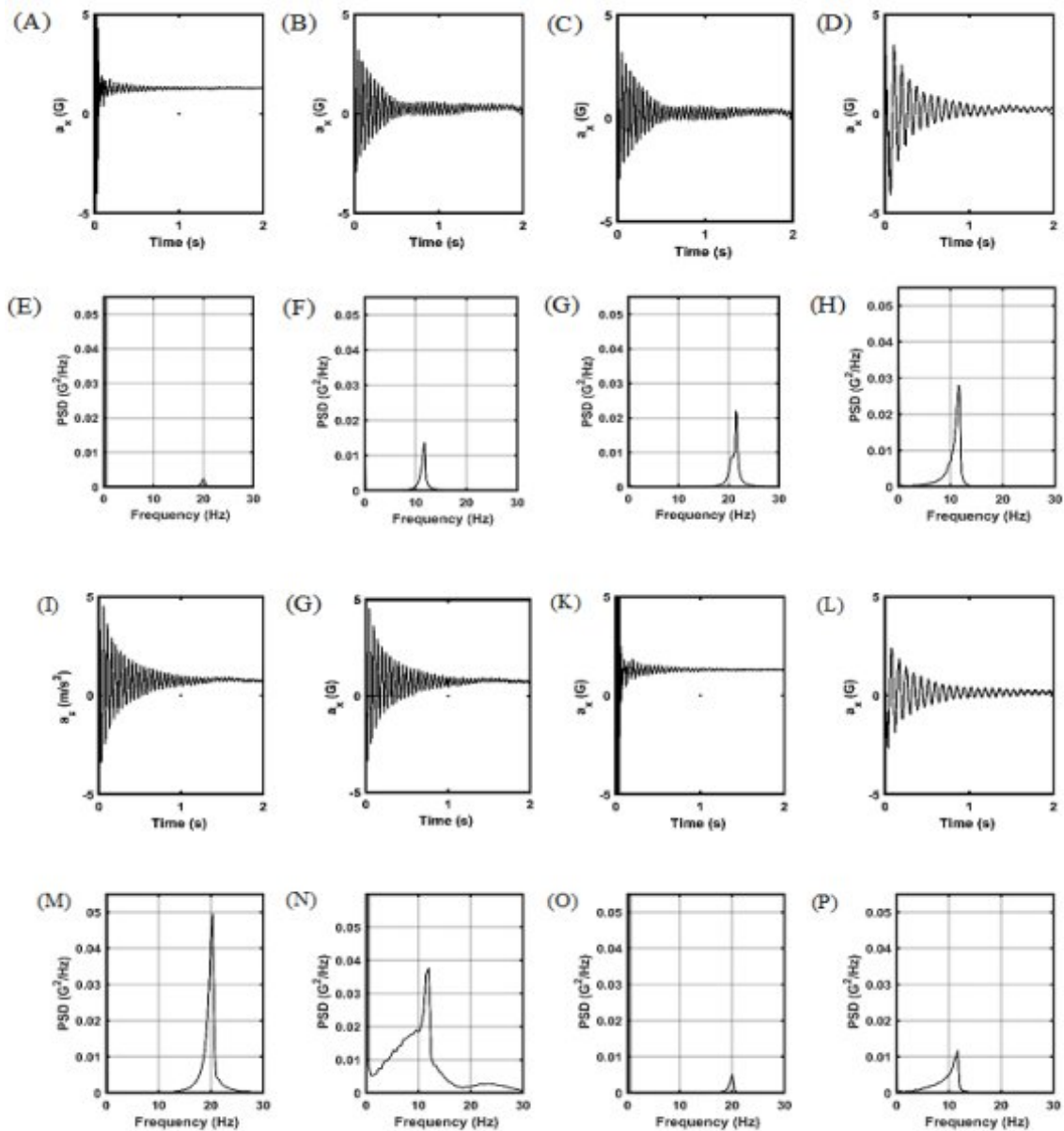


**Figure 18** Time series for the smooth cylinder without fins in air (A) and in water (B) and corresponding PSD of the lateral acceleration in air (E) and water (F), time series of the cylinder with fins positioned at 110 deg in air (C) and in water (D) and corresponding PSD of the lateral acceleration in air (G) and water (H), time series of the cylinder with fins positioned at 90 deg in air (I) and in water (J) and corresponding PSD of the lateral acceleration in air (M) and in water (N), and time series of the cylinder with fins positioned at 80 deg in air (K) and in water (L) and corresponding PSD of the lateral acceleration in air (O) and in water (P), where the acceleration is measured in G and equal to  $(m/s^2)$ .

Examples of the time series of the smooth and fined cylinder cases for free decay test in the air and water, identified as symbols w, are presented in Fig. 18. The free decay test was repeated ten times, and the average values were calculated for each test.

Table 2 lists the parameters of each tested cylinder, comprising mass ratio  $m^*$ , front projected area  $A$ , natural frequencies  $f_{nx}$  and  $f_{ny}$  for the streamline and the lateral flow directions in air, respectively, natural frequencies  $f_{nwx}$  and  $f_{nwy}$  for the streamline and the lateral flow directions in water, respectively, and damping ratios  $\zeta_{wx}$  and  $\zeta_{wy}$  in water as a percentage of critical damping for the streamline and the lateral flow directions, respectively. Cross-sectional areas were measured using a CAD tool; dry and wet frequencies and damping percentages, as well as mass ratios, were calculated based on a cylinder's total weight and the attached fins. The associated experimental measurement uncertainties, estimated to be less than about 4%, were obtained using the method of Moffat (1988) [99].

**Table 2 The structural characteristics for each tested model**

<b>Model</b>	<b><math>m^*</math></b>	<b><math>A</math> (<math>mm^2</math>)</b>	<b><math>f_{nx}</math> [Hz]</b>	<b><math>f_{ny}</math> [Hz]</b>	<b><math>f_{nwx}</math> [Hz]</b>	<b><math>f_{nwy}</math> [Hz]</b>	<b><math>\zeta_{wx}</math> (%)</b>	<b><math>\zeta_{wy}</math> (%)</b>
<i>Smooth Cylinder</i>	0.535	19200	20.01	20.01	11.7	11.7	3.8	3.8
<i>Cylinder with 80 deg. fins</i>	0.535	20233.2	20.70	21.19	11.84	11.90	4.4	5.7
<i>Cylinder with 90 deg. fins</i>	0.537	20319.6	21.03	20.82	11.77	12.13	3.9	7.7
<i>Cylinder with 110 deg. fins</i>	0.537	19974	20.34	20.29	11.26	11.61	3.8	4.9

With the relatively small differences between the characteristics of the four tested cylinders listed in table 2, it is clear that the attached fins did not have any significant changes in the stiffness of the smooth cylinder. Consequently, responses of cylinders fitted with fins that differed from responses of the smooth cylinder would have been expected to be caused by the wake region changes that would raise as a result of using these new fin configurations.



## 3.2 Wind Tunnel Tests

In this section, VIV around a cantilever cylinder at a wind tunnel has been investigated. Flow over the free end of a high mass ratio circular cylinder and flow around the wall junction of the cylinder cause the local flow field and the wake behind the cylinder to become strongly three-dimensional. The flow field is also characterized by a set of time-averaged streamline counter-rotating vortex pairs within the wake near the free end (tip or trailing vortices) associated with a downwash flow on the wake centerline in addition to the familiar Kármán vortex shedding from the sides of the cylinder [109]. Due to the downwash flows behind the free end of the finite cylinder, the three-dimensionality of the wake becomes strong. Few studies addressed the effect of various parameters, such as Reynolds number, aspect ratio, and boundary layer thickness, on the local flow field and how the flow field relates to what happens near the wake region [110]. The early studies of cantilever cylinders were done by Vickery & Watkins [54]. A PVC cantilever cylinder was tested in the water channel by King [13]. Results show a maximum amplitude followed by a slight decrease and then a linear increase also as the damping ratio decreases and as the reduced velocity at which peaks appear decrease [87]. Another cantilever study by Fujarra et. al. [88] had a similar mass ratio and damping ratio as the elastically mounted rigid cylinder [89]. They reported that the response of the cantilever exhibits a single initial branch, which then drops to a lower branch instead of three branch types of responses for a rigid one. A jump phenomenon was observed, and a high-speed mode of large amplitude response was found outside the principal synchronization regime. Regarding the synchronization behavior (when the cylinder's vibration frequency approaches its natural frequency), for all the research on cantilever cylinders mentioned, no lock-in region was found to be similar to that found under other conditions. This phenomenon also agreed with the case of the plastic cylinder of Williamson et. al. [90]. Bernitsas et. al. found that the tip flow reduces the lift force exerted on the cylinder and narrows the range of synchronization [91]. This behavior did not happen for the cantilever test model of Pesce et. al. [88], but their test model was made of aluminum alloy, and one might expect that this was possibly due to the vibration behavior of the nonmetallic test model. With the high mass cantilever cylinder in this study, the same behavior occurred. In the no-lock-in region, with the use of a propylene material, the damping ratio was greater, and, also, the Reynolds number regime was higher.

### 3.2.1 Wind tunnel facility

The experiments were conducted in a subsonic wind tunnel at the Institute of Thermo and Fluid Dynamics, Ruhr University Bochum. It consisted of an open 2.5m long test section of 1.5m width and 1.2m height, and its free stream attained a velocity up to 50m/s with low turbulence of less than 0.2%. The tunnel was powered by a 150kW direct current motor driving a commercial axial flow fan. Figure 19 shows a schematic of the wind tunnel. The test section velocity was calibrated against the pressure difference. The freestream velocity measurement from the wind tunnel control panel was calibrated, and the calibration coefficients acquired from the tests are shown in Fig. 20. The calibration factor was applied to the velocity data, which converted measured volts to meters per second.

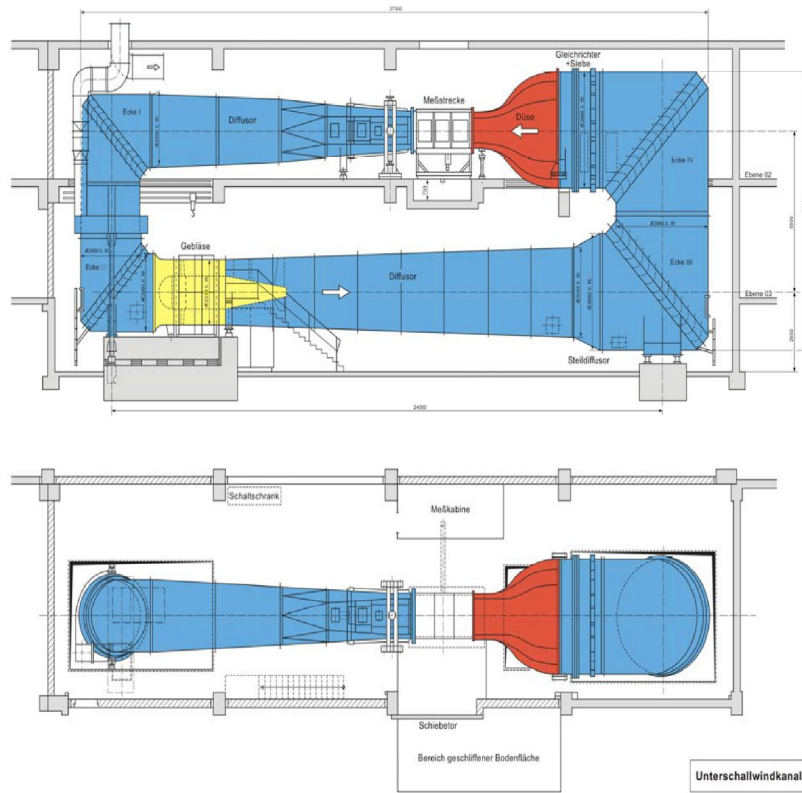


**Figure 19** Schematic of the wind tunnel

### 3.2.2 Test model

The test model was made of a standard propylene circular cylinder. Table 3 lists the material and section properties of the cylinder. To minimize the cylinder blockage, the selected aspect ratio was sufficiently small to guarantee a blockage ratio of less than 6 %. Therefore, the vortex shedding frequency was independent of this ratio [92]. Furthermore, to achieve adequate rigidity and for the purpose of fixation, a 10cm long PVC circular rod was installed inside at the bottom of the cylinder.

**Table 3** Test Model Parameters

<b>Parameter</b>	<b>Value</b>
m ..... Cylinder mass	0.47273 kg
m <sub>total</sub> ... Total model test mass	1.640 kg
D...Outer diameter	0.11 m
t... Thickness	2.7 mm
L....Cylinder Length	1.014 m
L/D.....Aspect ratio	10

$m^*$ .....Mass ratio	747.4
Strouhal no... $S_r$	0.18
Theoretical natural frequency... $f_n$	30.01

### 3.2.3 Experimental setup and instrumentation

In the present work, a separate cylinder set, an accelerometer, a load cell, data acquisition equipment, and a digital camera have been used. Identical accelerometer types with identical technical parameters, used in section 3.1, have been used in wind tunnel experiments. The accelerations were sampled at 2400 Hz for ten minutes. The voltages were converted to acceleration using the unique calibration determined for the accelerometer. The accelerometer was calibrated using the earth gravitation of 1g before starting the measurement campaign. The voltage magnitude was found to depend linearly on the acceleration (see Fig. 20). Details of the acceleration measurement parameters are given in table 4.

**Table 4 Acceleration Measurement Parameters**

<b>Parameter</b>	<b>Value</b>
Sampling frequency	2400 Hz
Sampling time	10 minutes
Accelerometer full-scale range	$\pm 20$ g
Accelerometer Uncertainty	< 1%

Also, a force torque-sensor was used to measure simultaneously forces (drag and lift) and moments on the cylinder in six degrees of freedom. The six signals from the balance were simultaneously acquired at a sampling rate of 2400Hz and were processed through a balance calibration matrix to obtain time histories of load components acting on the model with a 95% confidence level.

The model was placed vertically on a horizontal plane and bolted down to a heavy steel base plate, firmly fastened to another plate connected to a six-axis force/torque load cell, which in turn was connected to the floor of the tunnel's working section by about nine bolts fastened to two other plates. The weight of the connector plates was about 3.8kg. A schematic drawing ( see Fig. 21) shows a rigid circular cylinder cantilevered by adapter plates between the cylinder and the load cell.

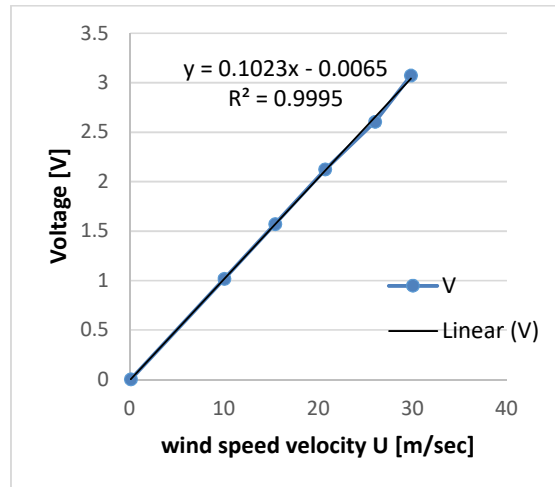


Figure 20 Calibration curve for the velocity Sensor

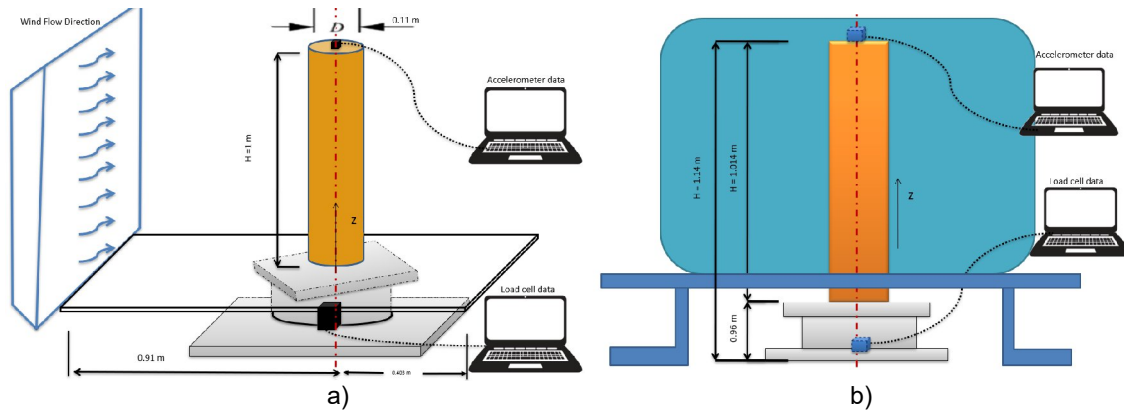


Figure 21 plan view (a) and side view (b) of the experimental setup

A wooden ground plate was installed on the floor of the wind tunnel test section and arranged parallel to the free stream velocity ( $U$ ) to produce a fully developed turbulent boundary layer at the location of the cylinder and to ensure that the specified aspect ratio of ten was maintained for the test cylinder. The boundary layer thickness in the proximity of the model was less than 9% of the model height, ensuring a negligible influence on the vortex shedding frequency and the free end flow [34]. Figure 22 shows the experimental setup and the coordinate system for each sensor.

### 3.2.4 Test procedure and data analysis

The experiments were conducted in the subcritical flow region, where vortex shedding became distinctly turbulent and where three-dimensional features took place in the wake. The Reynolds number ranged from  $3.6 \times 10^4$  to  $3.26 \times 10^5$ , corresponding to the so-called reduced velocity,  $U_r$ , ranging from 1.94 to 18.00. As mentioned this normalized reduced velocity is written as  $U_r = \frac{U}{f_n D}$ , where  $f_n$  is the measured fundamental natural frequency of the cylinder, and  $D$  is the cylinder's diameter. The test duration was approximately ten minutes for each velocity. The

data were processed in a MATLAB environment to obtain the amplitudes of responses and forces and their dominant frequencies. The experimental data were acquired by two data acquisition systems with a sampling rate of 2400Hz. Three channels were used to record the response data of the cylinder and six channels for the forces and moments. The fast Fourier transform (FFT) procedure was applied for the raw signals to analyze the frequency content of the measured time series.

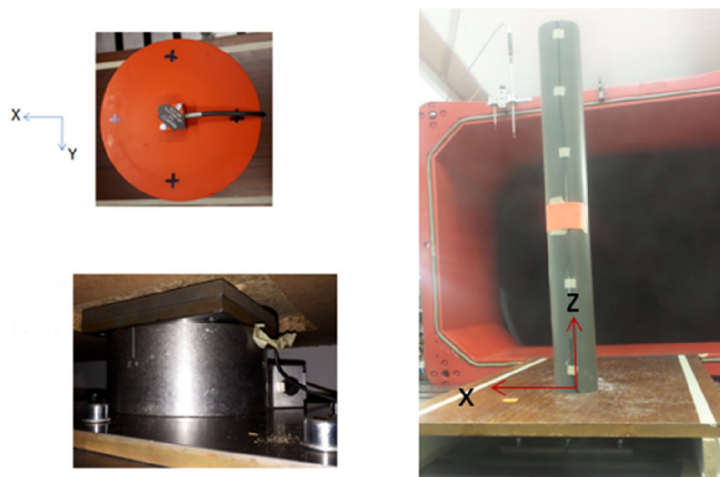


**Figure 22** Experimental setup and the coordinate systems of sensors

For the motion of the cylinder, the measured acceleration was integrated twice to give displacements by a double trapezoidal integration method using the MATLAB program. Two points need to be mentioned before applying the above approach for displacement reconstruction. One is that the accelerometer was composed of two parts, and the used data were obtained by subtracting the offset. The other one is that a bandpass filtering operation should be taken to remove the undesirable frequencies at the Nyquist frequency, 100 Hz. Before integrating the acceleration time series data into the displacement time history, the acceleration data were lowpass filtered to remove their high-frequency noise by a cut-off frequency of 40Hz. As integration reduced the high-frequency vibration and amplified low frequencies, a high pass filter with the same cut-off frequency was used to attenuate low frequencies after integration. A 5th-order Butterworth filter was used due to its maximally flat response in the passband and the filter was applied in both the forward and backward direction in time, resulting in no phase distortion to the acceleration. Both the accelerometer and load cell sensors have been synchronized with the navigation data to allow combining them. The test duration was approximately ten minutes for each velocity. Repeatability tests are completed to estimate the first-order variable uncertainty for the experiments [96]. The data were processed in a MATLAB environment to obtain the amplitudes of responses, velocities, forces, and their dominant frequencies.

The structural damping and natural frequency of the cylinder were evaluated by hammering free decay tests. The natural frequency was determined by applying the Fast Fourier Transform (FFT) procedure for the raw signals from both the accelerometer and load cell sensors. Meanwhile, The logarithmic decrement method was used to calculate the damping ratio for the underdamped system in the time domain. Linear vibration theory proposes a damping coefficient that is directly proportional to the velocity of oscillations. The damping caused by friction between the internal planes that slip or slide as the material deformed is known as hysteresis or structural damping.

For a lightly damped system,  $c/2m < \sqrt{k/m}$ , where  $c$  is the damping constant, and  $k$  is the cylinder stiffness. For any damped system, the damping ratio  $\zeta$  is defined as the ratio of the damping constant to the critical damping constant:

$$\zeta = \frac{c}{4\pi m f_n} \quad (17)$$

The structural damping was measured by perturbing the cylinder from its equilibrium position, in still air, and measuring the decay in amplitude. The damping ratio for the experiments was calculated from the natural log of the ratio of the amplitudes of successive peaks using the logarithmic decrement method. The logarithmic decrement represents the rate at which the amplitude of a free-damped vibration decreases. It is defined as the natural logarithm of the ratio of any two successive amplitudes. the hysteresis logarithmic decrement,  $\delta$ , can be written as follows:

$$\delta = \ln \frac{y_n}{y_{n+1}} = \frac{2\pi\zeta}{\sqrt{1-\zeta^2}} \quad (18)$$

For small damping, the damping coefficient was determined based on the equation:

$$\zeta \cong \frac{\delta}{2\pi} \quad (19)$$

It is noticed that for values up to  $\zeta = 0.3$ , equation 19 could be used instead of equation 17 [97]. Figures 23 and 24 presented the signals before and after filtering, respectively, for a sample test case. The free decay test was repeated five times, and the average values were calculated for each test. It was found that the damping value varied by 1.9% and that the natural frequency was 23.4Hz. The frequency was less than the theoretical calculated due to the effect of the attached mass of the test model setup.

cylinder length = 1000 mm, decaytest in X-dir test no. 0126

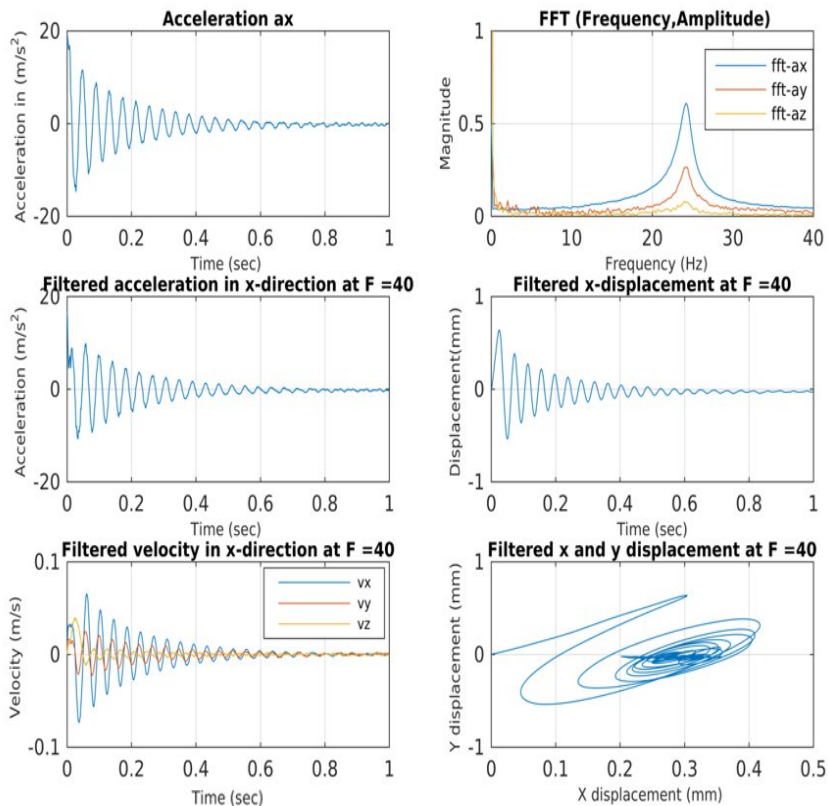


**Figure 23** Recorded data from decay test no. 0126

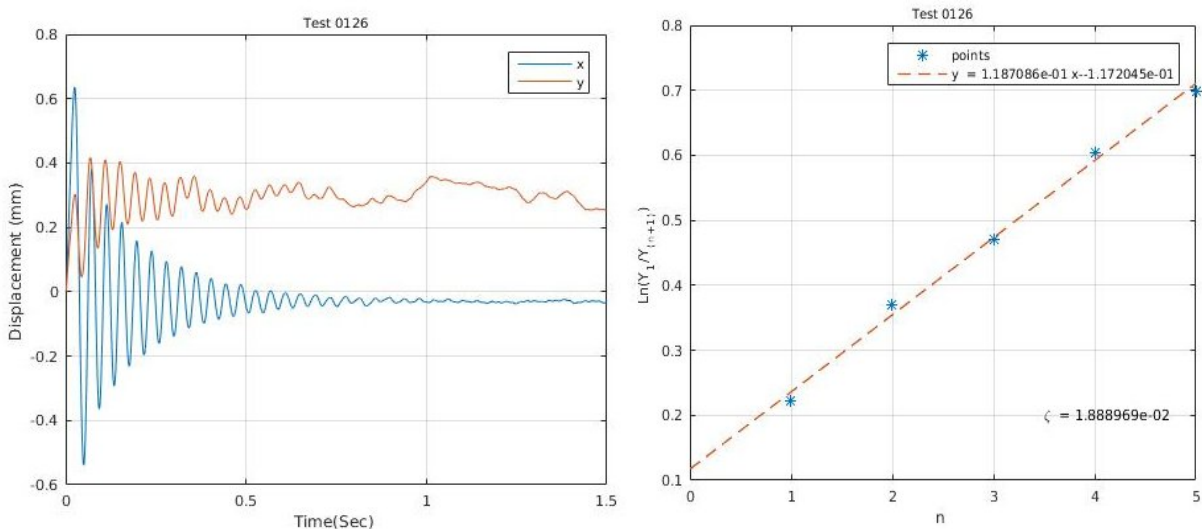


**Figure 24** Analyzing data for a decay test No. 0126 in x-direction; left, Time series output; right, The fitting analysis

## 4. Numerical Methods

The availability of powerful supercomputers recently has allowed users in performing simulations to obtain optimum results as well as in numerical modeling of fluid dynamics. The numerical modeling in fluid dynamics, so-called computational fluid dynamics (CFD), becomes very important in the design process for many purposes as well as in the marine industry.

However, Computational Fluid Dynamics (CFD) has gained momentum and its value in cost-effectiveness could include CFD results enabling the design of smaller and lighter equipment or enabling simpler and cheaper examinations before practical installations. Experiments are sometimes preferable to provide design data and verification. However, offshore structures are constrained by many factors, such as experimental facility availability and capacity limits, model scale limit, the difficulty of current profile generation, and cost and schedule concerns. Under such conditions, CFD simulation provides an attractive alternative to model tests and also provides a cost-effective alternative.

Unlike the model testing facility or experimental laboratory, in CFD simulations there is no need for a big facility. Furthermore, CFD also offers no capacity limit, no model scale limit, and cost and schedule efficiency. Indeed, the advantages of using CFD compared to experiment-based approaches can be concluded as follow:

- a) Ability to assess a system that controls experiments is difficult or impossible to perform (very large system).
- b) Ability to assess a system under hazardous conditions (e.g. safety study and accident investigation).
- c) Gives unlimited detail level of results.

Up to this date, no general solution to the Navier-Stokes equation exists and only for simplified flows such as Stokes flow. This means we need to turn to numerical solutions to achieve an approximate solution to the fluid flow. CFD encompasses a large array of numerical methods for predicting the flow of gas and fluid. The central idea is to take a geometrical representation of a body of interest, discretize the governing equations of fluid flow onto a surrounding computational grid, apply boundary conditions, and solve for the fluid velocities, densities, and pressures in the domain of interest. It is worth noting that Numerical solutions are always approximated values. Even if the equations are precisely solved, the solution will not match reality completely. So, the computation results always need to rely on experimental data for validation.

### 4.1 Flow Model

The commercial CFD code STAR-CCM+ software package developed by CD-adapco has been used. It is a finite volume solver with significant multiphysics capabilities including tools for FSI, rigid body dynamics, and free-surface flow. The main methods used by STAR-CCM+ in the present calculations are described in the following sections. An entire simulation workflow can start and end in STAR-CCM+, however, it is also able to interface with third-party packages and be integrated as a black box CFD solver within an FSI framework.



### 4.1.1 Governing equations

This section introduced the governing equations of fluid dynamics. In fluid dynamics, the flow is described by the conservation of mass, conservation of energy, and conservation of momentum. The fundamental equation for viscous fluid flow is the Navier-Stokes equation. This equation is derived by applying Newton's second law to fluid motion under the assumption that stress in the fluid arises due to the velocity gradient and a pressure term. The equation can therefore describe viscous flow. The solution of this equation can provide the velocity, pressure, density, and temperature in the fluid. It is governed by the following equations of momentum and mass conservations. The conservation principles are written here in differential form using Einstein's notation

$$\frac{\partial \rho}{\partial t} + \frac{\partial(\rho u_i)}{\partial x_i} = 0 \quad (20)$$

The governing equation of momentum conservation is given as

$$\frac{\partial(\rho u_i)}{\partial t} + \frac{\partial(\rho u_i u_j)}{\partial x_j} = \frac{\partial \tau_{ij}}{\partial x_j} + \rho b_i \quad (21)$$

Where  $u_i$  are the velocity components in spatial directions  $x_i$ ,  $\rho$  is the fluid density,  $\vec{b}$  is the body forces acting on the fluid such as gravity or buoyancy, and the Cauchy stress tensor  $\tau$ . In the present thesis, we are only interested in the velocity and pressure, as the density is assumed incompressible and up to this date, the temperature has not been considered relevant. The fluids are assumed Newtonian, therefore, the stress tensor  $\tau_{ij}$  is defined as

$$\tau_{ij} = \mu \left( \frac{\partial u_i}{\partial x_j} + \frac{\partial u_j}{\partial x_i} - \frac{2}{3} \frac{\partial u_k}{\partial x_k} \delta_{ij} \right) - p \delta_{ij} \quad (22)$$

Where  $p$  is the fluid pressure,  $\mu$  is the dynamic viscosity of the fluid, and  $\delta_{ij}$  is the Kronecker delta. With the assumption of an incompressible and isothermal fluid, the time derivative of density in continuity equation (22) vanishes transforming the equation to

$$\frac{\partial u_i}{\partial x_i} = 0 \quad (23)$$

Further, using the continuity equation (22) the divergence term in the definition of shear stress tensor (equation (24)) vanishes, and the momentum equation for an incompressible fluid is written as

$$\frac{\partial(\rho u_i)}{\partial t} + \frac{\partial(\rho u_i u_j)}{\partial x_j} = \frac{\partial}{\partial x_j} \left[ \mu \left( \frac{\partial u_i}{\partial x_j} + \frac{\partial u_j}{\partial x_i} \right) - p \delta_{ij} \right] + \rho b_i \quad (24)$$

Equations (23) and (24) defined the conservation principles for an incompressible, isothermal, and Newtonian fluid motion. These equations defined the fluid subproblem of the coupled fluid-structure interaction study in this work. The incompressible Navier-Stokes equations (23 and 24) were written for an Eulerian frame of reference. The Eulerian formulation of flow field is a way of looking at the fluid motion while focusing on a specific location in space, through which the fluid flows. Therefore, the formulation is not suitable for moving boundaries with body-fitted meshes. In this case, the Arbitrary Lagrangian-Eulerian formulation is used for the solution of conservation equations of the fluid subproblem on moving grids.

The main idea of the ALE approach is that an observer is neither located at a fixed position in space nor moves with the material point, but it can move arbitrarily. To achieve this for the conservation laws already described, a relative velocity is introduced in the convective term. Then the equations were written as

$$\frac{\partial u_i}{\partial x_i} = 0 \quad (25)$$

$$\frac{\partial(\rho u_i)}{\partial t} + \frac{\partial(\rho u_j(u_i - u_i^g))}{\partial x_j} = \frac{\partial}{\partial x_j} [\mu (\frac{\partial u_i}{\partial x_j} + \frac{\partial u_j}{\partial x_i}) - p \delta_{ij}] + \rho b_i \quad (26)$$

The equations are written to account for the motion of the entire grid as a whole (rigid body) or relative to the grid (grid deformation), and therefore  $u_i^g$  is the grid velocity in  $x_i$  direction.

#### 4.1.2 Pressure-velocity coupling

For compressible flows, the continuity equation can be used to determine the pressure and the density based on an equation of state. However, in the case of incompressible flow, A solution of the Navier-Stokes equations is difficult due to the absence of an equation to solve the pressure. To obtain a consistent solution of pressure and velocity, the conservation equations must be reordered to obtain dedicated equations for the velocity and pressure fields.

For this purpose, projection methods that combine the conservation equations eq. (25) and eq. (26) to obtain an explicit equation for the pressure. The most common approaches based on pressure correction equation are SIMPLE (Semi-Implicit Method for Pressure-Linked Equations), Patankar and Spalding [124], and PISO (Pressure-Implicit with Splitting of Operators), Issa [125]. PISO procedure has been successfully adapted for the iterative solution of steady-state problems. it consists of one predictor step and two corrector steps. The SIMPLE algorithm uses an iterative method that satisfies both conservation equations which is described as follow [104]

1. The estimated pressure from the previous iteration or time-step has been used to solve the momentum equation to obtain the velocity field.
2. Using obtained velocities to determine the mass imbalance.
3. Use the mass imbalance to correct the pressure field and again the velocity field.
4. Repeat the processes till the mass and momentum equations get satisfied.

In the solver, discretized continuity and momentum equations are used to derive the pressure correction equation. Each component of momentum is solved to obtain the unknown velocities. The velocities obtained cannot satisfy the continuity equation because the pressure value used during iteration is from a previous time-step or iteration. Then, a correction in velocities as well as correction in pressure obtained from the last time-step satisfying the continuity as well momentum equation is required.

The discretized equation, using an implicit method, for velocities for a new time-step  $n+1$  at node C can be written as

$$A_C^{u_i} u_{i,C}^{n+1} + \sum_l A_l^{u_i} u_{i,l}^{n+1} = Q_{u_i}^{n+1} - \left( \frac{\delta p^{n+1}}{\delta x_i} \right)_C \quad (27)$$

Where  $l$  denotes the neighboring point. During each time-step, an approximation is made because the velocity is not updated, however, the velocity is improved by solving the

momentum equation. Consequently, the pressure correction equation is solved to correct pressure and velocity values to satisfy the mass conservation equation. For an unsteady problem, the repetition of the steps is involved until conservation equations are satisfied with tolerance. The repetition of these steps within each time-step is referred to as outer iteration indexed by  $m$ . Momentum equation solved in  $m$ th outer iteration is

$$A_C^{u_i} u_{i,c}^{m*} + \sum_l A_l^{u_i} u_{i,l}^{m*} = Q_{u_i}^{m-1} - \left( \frac{\delta p^{m-1}}{\delta x_i} \right)_C \quad (28)$$

The coefficients  $A$  and the source term  $Q$  depend on the solution equation that was linearized and the coefficient matrix and source term are based on variable values from the previous iteration. To enforce the continuity constraint, both pressure and velocities are corrected. they need to be corrected and updated as presented

$$u_i^{m**} = u_i^{m*} + u' \quad \text{and} \quad p^{m*} = p^{m-1} + p' \quad (29)$$

Where  $u_i^{m**}$  and  $p^{m*}$  are corrected velocity and pressure respectively. These values must satisfy the linearized momentum and continuity equation. Momentum equation for corrected variables is in SIMPLE defined as

$$A_C^{u_i} u_{i,c}^{m**} + \sum_l A_l^{u_i} u_{i,l}^{m**} = Q_{u_i}^{m-1} - \left( \frac{\delta p^{m*}}{\delta x_i} \right)_C \quad (30)$$

The relation between correction terms for pressure and velocity was determined by subtracting equation 27 from equation 28 and dividing by  $A_p$ . Finally, These lead to the Poisson-like pressure-correction equation

$$\frac{\delta}{\delta x_i} \left[ \frac{\rho}{A_p^{u_i} \left( \frac{\delta p'}{\delta x_i} \right)} \right]_p = \left[ \frac{\delta(\rho u_i^{m*})}{\delta x_i} \right]_p \quad (31)$$

### 4.1.3 Finite volume method

The geometric discretization of the physical domain results in a mesh on which the conservation equations are eventually solved. This requires the subdivision of the domain into discrete non-overlapping cells or elements that completely fill the computational domain to yield a grid or mesh system. One of the popular methods used to approximate the differential equations by a system of algebraic equations and calculate the solution numerically is a Finite Volume Method (FVM). The most advantage of FVM is that there is no restriction on the user over the type of mesh created i.e it is suitable for any type of grid, therefore, it is suitable for complex geometry. This method divides the solution domain into a finite number of contiguous control volumes (CV) enclosed by control volume surfaces (S), and the conservation equations are applied to each CV. The usual approach is to define CVs by a suitable grid and assign the computational node to the CV-centroid. Flow variables like pressure, temperature, velocity, and turbulent kinetic energy (tke) are going to be stored at the cell centroid. These flow variables are assumed to vary linearly across the cell, i.e, between the cell centroid and the various phases of the cell. The finite volume method uses the generic transport equation in an integral form as:

$$\frac{d}{dt} \int_V \rho u_i dV + \int \rho u_i (u_j - u_j^g) \cdot \vec{n} dS = \int_S \mu \left( \frac{\partial u_i}{\partial x_j} + \frac{\partial u_j}{\partial x_i} \right) n_j dS + \int_S p \delta_{ij} n_j dS + \int_V \rho b_i dV \quad (32)$$

$$\int_S u_i n_i dS = 0 \quad (33)$$

If we sum equations for all CVs, we obtain the global conservation equation, since surface integrals over inner control volume faces cancel out and volume integrals add together to the volume integral over the whole domain. Thus global conservation is built into the method and this provides one of its principal advantages.

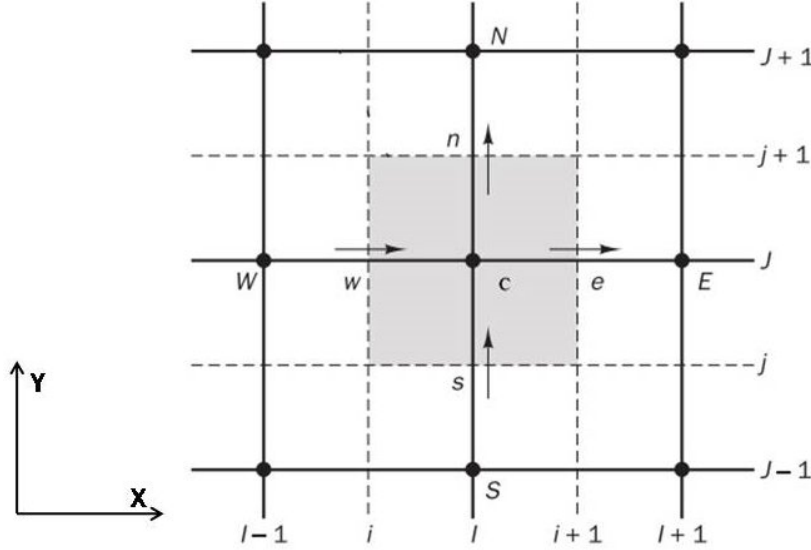


**Figure 25** 2D-view of control volumes with different neighboring cells, C, N, W, E, and S with the interfaces w, e, n, and s

In 3D, the midpoint rule is the simplest second-order approximation. Higher-order approximations, which require the integrand at locations other than the cell-face center (e.g. corners and center of edges) are possible, but they are more difficult to implement. Figure 25 illustrates a 2D-view of control volumes with different neighboring cells, C, N, W, E, and S with the corresponding interfaces w, e, n, and s. According to the linear interpolation, the value of the scalar variable  $\phi$  at the interface w and e can be obtained as follow:

$$\phi_w = f_w \phi_C + (1 - f_w) \phi_W \quad (34)$$

$$\phi_e = f_e \phi_C + (1 - f_e) \phi_E \quad (35)$$

Where  $f_w = \delta x_{wW} / \delta x_{CW}$  and  $f_e = \delta x_{eE} / \delta x_{CE}$  are the interpolation functions which are defined in the interpolation method for a second-order central differencing scheme. To obtain an algebraic equation for a particular CV, the surface and volume integrals need to be approximated using quadrature formulas as illustrated below.

### *Approximation of Surface Integrals*

In 2D Cartesian control volumes, the CV surface consists of four plane faces N(North), S(South), E(East), and W(West) as presented in Fig. 25. Additional two plane faces, T(top) and B(bottom) directions, are added when extending to 3D CV.

The net flux of the convection ( $\rho\phi v \cdot n$ ) or diffusion ( $\Gamma_\phi \nabla\phi \cdot n$ ) term through the CV-boundary equals the sum of integrals over all faces of the control volume; four (in 2D) or six (in 3D) given by

$$\int_S f dS = \sum_k \int_{S_k} f dS \quad (36)$$

where  $f$  is the component of the convection or diffusion flux vector in the direction normal to CV face and  $S_k$  is the area of the projection of cell face  $k$ . It's worth mentioning that the control volume should not overlap and each control volume face is common to the two neighboring control volumes. In order to calculate an integral value of diffusive and convective terms at P, two levels of approximation are needed. The first integral approximation is in terms of the variable values at one or multiple locations on the cell face by using a suitable quadrature formula. Furthermore, the cell-face values are approximated in terms of the CV-center values by a suitable interpolation. An easier way is to apply the midpoint rule for the approximation and approximate as the product of integral at face center and CV face area given by

$$F_e = \int_{S_e} f dS \approx f_e S_e \quad (37)$$

Since the value of the  $f$  is not available as control volume face center  $e$ , which can be obtained by interpolation. The truncation error of this integral approximation is a second-order approximation as it is proportional to the square of the mesh spacing. The values of  $f_w$  need to be calculated with at least second-order accuracy to preserve the accuracy of the midpoint rule. its second-order makes it accurate enough for most engineering applications, and its simplicity makes the implementation in computer code easy. The value of  $f_e$  has to be computed with at least second-order accuracy to preserve the second-order accuracy of the midpoint-rule approximation of the surface integral.

### ***Approximation of Volume Integrals***

Some terms in the transport equations, source term ( $q$ ), require integration over the control volume. The simplest method to approximate a volume integral is again the second-order accurate approximation using the midpoint rule. The volume integral is replaced by the product of the mean value of the integral term and the volume of the control volume is given by:

$$Q_C = \int_V q dV \approx q_C \Delta V \quad (38)$$

Where  $q_C$  is the value at the control volume center  $C$  and  $\Delta V$  is a volume of the control volume. no interpolation is necessary to evaluate the integrand since all variables are available at node  $C$ .

An approximation of higher-order needs the values of  $q$  at more locations than just the control volume center. These values have to be obtained by interpolating nodal values or by using shape functions. The integrand, denoted by  $f$ , involves the product of several variables and/or variable gradients at those locations.

#### 4.1.4 Turbulence model

In laminar flow, fluid can be thought of as flowing in layers parallel to each other as the viscous effects dominate the momentum effects. While the turbulent flow is a flow regime characterized by chaotic and random fluctuating property changes. This includes low momentum diffusion, high momentum convection, and rapid variation of pressure and velocity in space and time. These fluctuations mix transported quantities such as momentum, energy, and species concentration, and cause the transported quantities to fluctuate as well. The fluctuating velocity fields manifest themselves as eddies. The turbulent flow consists of a spectrum of different scales (eddy sizes). The largest eddies are of the order of flow geometry and the smallest eddies are by viscous forces dissipated into internal energy. The largest eddies extract their energy from the mean flow while the small eddies receive the kinetic energy from slightly larger eddies and so on. This process of energy transfer is called the cascade process [126]. In 1941, A. N. Kolmogorov provides two specific, testable results: the 2/3 law which leads directly to the prediction of a  $K^{-5/3}$  decay rate in the inertial range of the energy spectrum, and the 4/5 law that is the only exact results for N-S turbulence at high  $Re$ .

However, laminar flows often permit analytic solutions to N-S equations in simple cases, the presence of turbulence presents many difficulties in obtaining a solution due to its inherently wide range of length and time scales. The smallest dynamically significant scale of turbulent flow is the Kolmogorov scale  $\eta$ , also called the dissipation scale, since scales smaller than  $\eta$  are dominated by viscous rather than inertial forces. The largest scale measuring the size of the largest energy-containing scales is called the integral scale  $l_0$ . For homogenous isotropic turbulent flow, where the turbulent kinetic energy  $K$  is the same in all directions, the smallest and related to the Reynolds number by [127]:

$$\frac{l_0}{\eta} = \mathcal{O}(Re^{\frac{3}{4}}) \quad (39)$$

Therefore,  $\mathcal{O}(Re^{\frac{3}{4}})$  degrees of freedom are needed to represent all the scales of motion in a cube of edge length  $l_0$ .

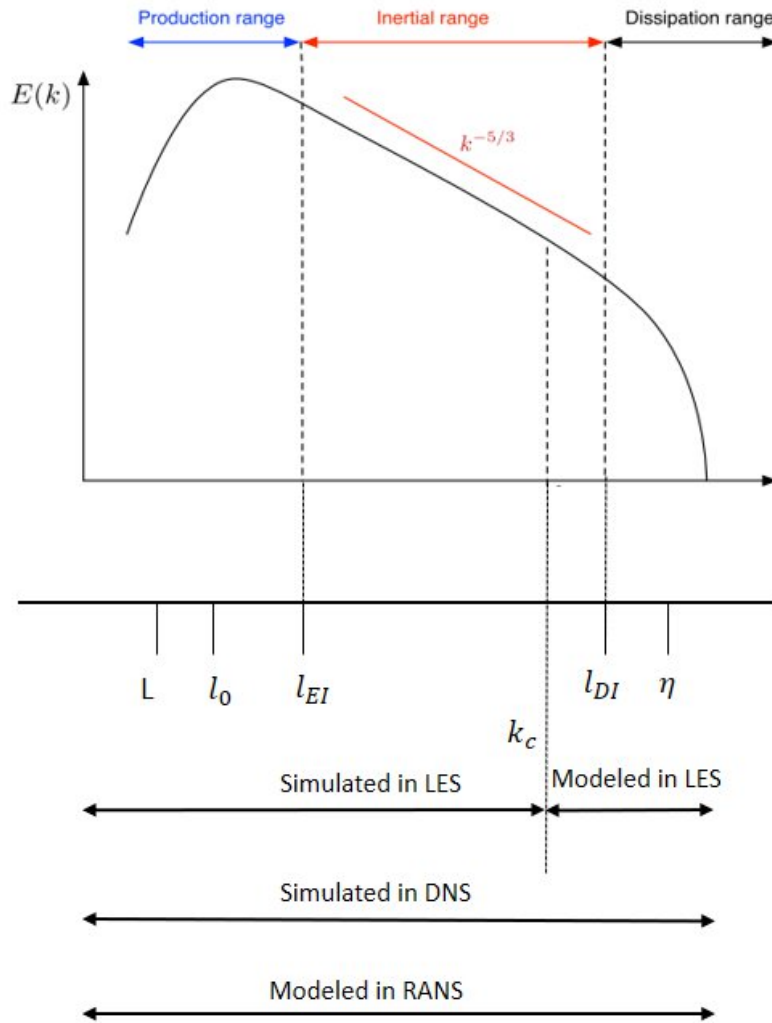


**Figure 26** Energy cascade and different length scales of turbulence

Hence Kolmogorov’s hypothesis of the local isotropy turbulent flow, large-scale turbulence may still be anisotropic.  $l_{EI}$  is the length scale that forms the demarcation between the large scale anisotropic eddies ( $l > l_{EI}$ ) and the small scale isotropic eddies ( $l < l_{EI}$ ).  $l_{EI}$  can be estimated for many high Reynolds number flows as  $l_{EI} \approx l_0/6$  [128]. The size range ( $l < l_{EI}$ ) is referred to as the universal equilibrium range in which the time scales are small compared to Kolmogorov time scale. A new length scale  $l_{DI}$ , approximately  $\approx 60\eta$  for many turbulent high Reynolds number flows, splits the universal equilibrium range into two subranges. The inertial subrange ( $l_{EI} > l > l_{DI}$ ) where the inertial effects on the fluid flow are dominant and the viscous effect is negligible. The other subrange is ( $l < l_{DI}$ ) where the motion experience viscous effects as shown in Fig. 26. Furthermore, the Taylor microscale  $\lambda$ , which falls in between the large-scale eddies and the small-scale eddies, is a measure of the large-scale eddies in the inertial subrange.

Two methods can be used to avoid the need to solve these small scales and high frequencies: filtering and time averaging [129]. Some models for the Navier-Stokes equations that form a hierarchy of approximations to the full multiscale picture of turbulence are presented in the next section.

## Direct Numerical Solution (DNS)

DNS is a method that presents the solution of the discretized Navier-Stokes equations with all scales of the turbulent motions in the flow between  $\eta$  and  $l_0$  resolved and nothing modeled. DNS is a useful tool to examine fine structures of a particular flow of academic interest and to provide reference data for research in turbulence, but it is currently too expensive (in terms of simulation time and computational hardware as well) to use in many practical and industrial problems. It is only possible to be performed at a low Reynolds number problems due to the high number of operations as the number of mesh points is equal to  $Re^3$ . Therefore, the computational cost of DNS is very high even at low  $Re$ .

## Reynolds Averaged Navier-Stokes (RANS)

RANS method is the time-averaged equations of motion of the fluid flow. It governs the transport of the averaged flow quantities, with the complete range of the turbulent scales being modeled and The fluctuating component is included by way of a turbulence model. Therefore, it greatly reduces the required computational effort and resources and is widely adopted for practical engineering applications. RANS' solution is steady-state, i.e. it does not contain any information about transient flow effects which could be important in many engineering problems. RANS models gained widespread popularity and have been used in engineering for decades owing to their low computational requirements and predictable behavior. The requirements for mesh resolution are relatively low because fine turbulent scales do not have to be resolved. Meshes are constrained purely by the requirement to reduce numerical discretization error below a given threshold and geometric accuracy requirements.

The main idea in Reynolds-averaging is that for an unsteady flow, ensemble averaging can be used to write any flow variable in terms of an average value and a fluctuation about that average. For such a flow, a certain value  $\phi$  is expressed as:

$$\phi(x_i) = \bar{\phi}(x_i) + \phi'(x_i, t) \quad (40)$$

This approach is applied to all flow variables in the continuity and momentum equations to remove the rapidly fluctuating components. Through ensemble averaging of nonlinear terms, new terms that involve mean values of the products of rapidly varying quantities is been introduced. Omitting the details of the derivations, the incompressible RANS equations are written in a differential form with tensor notation as:

$$\frac{\partial u_i}{\partial x_i} = 0 \quad (41)$$

$$\frac{\partial u_i}{\partial t} + u_i \frac{\partial u_i}{\partial x_j} = -\frac{1}{\rho} \left( \frac{\partial P}{\partial x_i} \right) + \nu \frac{\partial^2 u_i}{\partial x_j^2} - \frac{\partial \overline{u'_i u'_j}}{\partial x_j} \quad (42)$$

where  $u'_i$  is the fluctuating part of the velocity;  $P$  is the dynamic pressure, and  $\rho$  is the fluid density. These new terms,  $\overline{u'_i u'_j}$ , are known as the Reynolds stresses and must be modeled numerically. These additional terms give additional unknowns in the equations and therefore the equations must be closed by approximating them with a turbulence model, introducing another equation to the system. Turbulence models vary in complexity from one to two-equation models, and various forms of handling the additional terms.

Using the Boussinesq approximation, the Reynolds stress component,  $\overline{u'_i u'_j}$ , is expressed in terms of a turbulent viscosity  $\nu_T$  and the mean flow gradients such as:



$$-\overline{u'_i u'_j} = \nu_T \left( \frac{\partial u_i}{\partial x_j} + \frac{\partial u_j}{\partial x_i} \right) - \frac{2}{3} k \delta_{ij} \quad (43)$$

Where  $\delta_{ij}$  is the Kronecker delta function and  $k$  is the turbulent kinetic energy.

A standard shear-stress transport (SST)  $k$ - $\omega$  turbulence model is used in the present study. In order to close the governing equations, the Shear Stress Transport (SST)  $k$ - $\omega$  turbulence model has been developed by (Menter [130]; Menter et al. [131]). Menter's SST model reduces to a  $k$ - $\omega$  model near solid walls while switches to a  $k$ - $\epsilon$  model away from solid surfaces. The SST  $k$ - $\omega$  model has shown good performance in simulating the boundary layer flows with significant adverse pressure gradient applications where viscous flows need to be well resolved and turbulence models are applied throughout the boundary layer. The model is a combination of a  $k$ - $\epsilon$  model and a  $k$ - $\omega$  model. The standard  $k$ - $\epsilon$  model has the benefits in the free stream, but perform badly in the near-wall region and the opposite is true for the standard  $k$ - $\omega$  model. The model constant in the (SST)  $k$ - $\omega$  turbulence model which used in this study are listed below in table 5.

**Table 5: Parameters of the (SST)  $k$ - $\omega$  turbulence model**

$\beta^*$	$\alpha_1$	$\beta_1$	$\sigma_{k1}$	$\sigma_{\omega1}$	$\alpha_2$	$\beta_2$	$\sigma_{k2}$	$\sigma_{\omega2}$
0.09	5/9	3/40	0.85	0.5	0.44	0.0828	1.0	0.856

### Large-Eddy Simulation (LES)

Large-eddy simulation is based on a space filtering method in CFD. LES is intermediate between RANS and DNS in terms of resolved scales. LES directly computes the large-scale turbulent structures which are responsible for the energy and momentum transfer in the flow while the smaller scale of dissipative and more isotropic structures are being modeled.

The spirit of LES is to explicitly resolve the large scales responsible for the mixing and for determining the dissipation rate while modeling the smallest eddies which are universal and responsible for the final energy dissipation into heat. In order to distinguish between the large and small scales, a filter function is being used in LES. A filter function dictates which eddies are large by introducing a length scale. Scales are resolved as long as they are above a certain size, determined by the filter width, usually denoted as  $\bar{\Delta}$ . LES becomes DNS, in the limit  $\bar{\Delta} \rightarrow \eta$ . Scales that fall below the filter size are parameterized by the LES model using information from the resolved scales and theoretical or empirical arguments. Usually, LES models are performed based on the eddy-viscosity hypothesis.

Many LES models are based upon the assumption that the sub-filter scale obeys the local isotropy hypothesis. In practice, this means that the filter width should be in the inertial subrange. A practical base is that if 80% of the kinetic energy is in the resolved scales, the filter width is small enough and the LES is termed 'well resolved' as stated by S.Pope (2014) [126]. The filter size must satisfy the condition  $\bar{\Delta} \geq \Delta$ , where  $\Delta$  is some metric of the local grid size which requires careful definition on unstructured mesh. The grid has to be fine enough to capture the gradients of the mean flow, which is far less demanding than DNS.

On a practical note, the LES technique is a good compromise between the two extreme approaches DNS and RANS. It provides a good representation of the turbulence and allows to have transient flow information. It requires much less computational resources than the DNS approach however, it can be prohibitively slow to solve due to the requirement to resolve all the scales of turbulence down to a point in the inertial range.

However, LES is capable to solve high Reynolds numbers and more complex geometries problems, the development of robust, accurate, and fast LES models are crucial to meet the needs of the industry. RANS still holds considerable appeal to the industry although advantages can be gained from simulating a problem in greater detail. Nevertheless, there is also a need to simulate ever larger components, or even entire systems, and include extra physical effects such as Fluid-Structure Interaction problems such as VIV phenomena. It is therefore widely acknowledged that a gap exists between RANS and LES, and recently the development of hybrid RANS-LES methods is aimed at addressing this.

### Detached-Eddy Simulations (DES)

Detached Eddy Simulation DES is one of the particular hybrid RANS-LES methods, which shows the greatest promise for widespread practical applications. The goal was to develop a modified version of the Spalart-Allmaras model [132] more practical than LES to deal with high Reynolds numbers in turbulent flows. The original DES concept sketch from the presentation of the 1997 paper is shown in Fig. 27. which illustrates well the envisioned application area of DES. The extensive surface area covered by thin boundary layers can be reliably treated using RANS and would incur unmanageable numerical expense with LES. The separated region of largescale turbulence behind the spoiler contrastingly represents an ideal application region for LES. The onset of this region is needed to be dictated accurately where the separation point would be dictated by the RANS model s a distinct disadvantage.

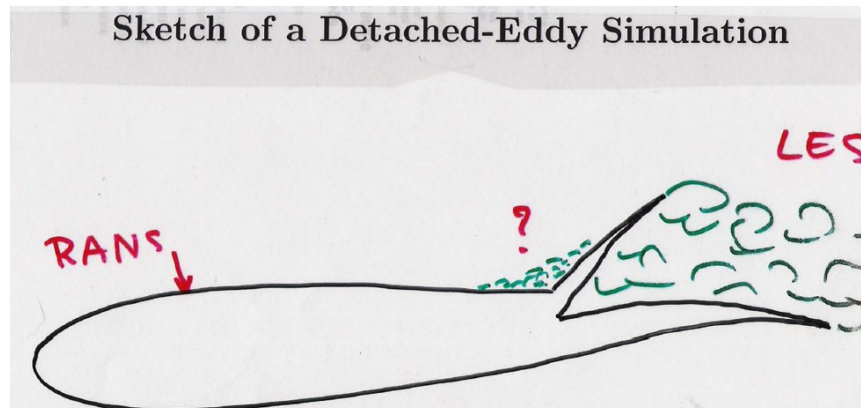


**Figure 27** Original concept sketch of DES [133]

The computing cost problems and the resolution near walls were resolved by using the RANS model within boundary layers and pure LES outside. The DES aims to improve the flow prediction following separation. For a brief treatise on a comprehensive review of prominent application examples and a discussion of the DES state of the art, recourse is sought to the review article of Spalart (2009) [134].

DES is classified as a non-zonal hybrid method which means that the RANS and LES functionality is handled by the same set of model and flow field equations. DES is a 3D unsteady numerical solution using a single turbulence model, which acts as a sub-grid-scale model in regions where the grid density is fine enough for LES and as a RANS model in other regions. Meaning that the fundamental coupling of the RANS and LES activity is corresponding to the local grid resolution.

In the S-A model, the original wall distance is used and the working variable  $\tilde{\nu}$  is used to form the eddy viscosity and its transport equation takes the form Spalart et al. [135]

$$\frac{\partial \tilde{v}}{\partial t} + u \frac{\partial \tilde{v}}{\partial x} + v \frac{\partial \tilde{v}}{\partial y} + \omega \frac{\partial \tilde{v}}{\partial z} = c_{b1} [1 - f_{t2}] \tilde{S} \tilde{v} + \frac{1}{\sigma} \left[ \nabla \cdot \left\{ \left( \frac{1}{R} + \tilde{v} \right) \nabla \tilde{v} \right\} + c_{b2} (\nabla \tilde{v})^2 \right] - \left[ c_{\omega 1} f_{\omega} - \frac{c_{b1}}{\kappa^2} f_{t2} \right] \left( \frac{\tilde{v}}{d} \right) + f_{t1} \Delta U^2 \quad (44)$$

With  $d$  as the wall distance,  $\tilde{S}$  as modified vorticity and an auxiliary function for near-wall behavior  $f_{\omega}$ . The model defines the eddy viscosity field as

$$\nu_t = \tilde{v} f_{v1}, \quad f_{v1} = \frac{\chi^3}{\chi^3 + c_{v1}^3}, \quad \chi = \tilde{v} R \quad (45)$$

The DES formulation is obtained by replacing the distance to the nearest wall in all terms,  $d$ , by distance  $\tilde{d}$  defined as follows:

$$\tilde{d} = \min(d, C_{DES} \Delta) \quad (46)$$

where  $\Delta$  is the largest grid spacing in all directions. In ordinary applications of DES, the wall-parallel grid spacings (e.g., streamwise and spanwise) are typical of the order of the boundary layer thickness, and the S-A RANS model is retained throughout the boundary layer. Consequently, the prediction of boundary layer separation is determined in the RANS mode of the DES model. Away from solid boundaries, the closure is a one-equation model for the subgrid viscosity. When the productive and destructive terms of the model are balanced, the length scale  $d = C_{DES} \Delta$  in the LES region yields a Smagorinsky type eddy viscosity,  $\tilde{v} \propto S \Delta^2$ . Analogous to the classical LES model, with  $\Delta$  small enough to allow the energy cascading down to the grid size, cause this pseudo-Kolmogorov length scale based on the eddy viscosity to be proportional to the grid spacing. We specified a model constant of  $C_{DES} = 0.65$  to ensure a homogeneous turbulent flow and with model parameters given in [132]. Additional features like delayed DES (DDES) are used to prevent the model from generating unphysical separations by switching into the LES mode too early, which usually occurs for ambiguous grids, and low Reynolds number correction for the LES treatment of free shear layers are also available in IDDES formulation of Strelets [136]. The generally high quality of the result obtained gives rise to a high level of optimism that DES could become the future tool in the industrial CFD community.

The simulations in this project are based on the method of Computational Fluid Dynamics (CFD), for the simulation of the interaction between monopile and waves were the FVM-Solver was based on the Reynold-Averaged Navier-Stokes Equations been used, in the following paragraphs were the theoretical backgrounds introduced.

## 4.2 Structural Model

Mechanical systems in general consist of structural components that have distributed mass and elasticity. To the authors' knowledge, only a limited number of studies dealing with the flow past a bluff body used a series of methods to investigate the FSI effects on the structure thus far has been limited to discrete systems that have a finite number of degrees of freedom. Studies [3], [4], and [5] treated the structure as a mass-spring system; labeled described it as a discrete structural simplification with lumped masses and discrete elastic elements governed by a set of second-order ordinary differential equations. Rods, beams, and other structural components on the other hand should be considered as continuous systems that have an infinite number of degrees of freedom, and as a consequence, the vibration of such systems is governed by partial differential equations which involve variables that depend on time as well as the spatial coordinates [137].

This chapter introduces the major concepts involved within structural mechanics, in particular geometrically nonlinear problems and the FEM. The theory covered in this section forms the basis of the finite Starccm+ plugins described in Chapter 7.3. The key concepts are presented, however, numerous textbooks offer more detailed formulations of structural mechanics problems and the FEM [138].

### 4.2.1 Governing equations

Solid mechanics studies the displacement of a solid continuum under applied loads and constraints. The fundamental laws that govern solid mechanics are the same laws that describe fluid mechanics. Applied loads can cause a displacement of the solid structure from an initial configuration to a deformed configuration. Therefore, the total displacement is the sum of rigid body motion  $u(\mathbf{X}, t)$  and its reference configuration,  $\mathbf{X}$ . Thus, the position of the material point in the deformed configuration is defined as:

$$x(\mathbf{X}, t) = \mathbf{X} + u(\mathbf{X}, t) \quad (47)$$

The deformation gradient  $F$  is used to relate the deformation of an element in the current configuration with that in the reference configuration and introduced as:

$$F = \frac{\partial x}{\partial X} = I + \frac{\partial u}{\partial X} = I + \begin{pmatrix} \frac{\partial u_x}{\partial X} & \frac{\partial u_x}{\partial Y} & \frac{\partial u_x}{\partial Z} \\ \frac{\partial u_y}{\partial X} & \frac{\partial u_y}{\partial Y} & \frac{\partial u_y}{\partial Z} \\ \frac{\partial u_z}{\partial X} & \frac{\partial u_z}{\partial Y} & \frac{\partial u_z}{\partial Z} \end{pmatrix} \quad (48)$$

Where  $I$  is the identity matrix, the displacement  $u$  in component form can be expressed as  $u = \{u_x \ u_y \ u_z\}^T$ , and  $X$ ,  $Y$ , and  $Z$  are the Cartesian components of the material point position vector  $\mathbf{X}$ . There are many stress and strain measures formulas are used within structural mechanics, depending on the frame of reference that is used. In the present study, the infinitesimal strain assumption is used to describe the elastic behavior of the structure. In cases of low deformation, the assumption of infinitesimal strain can greatly reduce the computational time required to solve the problem. However, in cases where the body only undergoes rigid-body rotation, the infinitesimal strain measure does not remain zero. In these cases, the Green-Lagrange strain measure is required. The Lagrangian strain measure also referred to as the Green-Lagrange strain tensor, uses the initial undeformed configuration as its reference frame. This strain tensor,  $E$ , measures the difference in the square of the length of an infinitesimal segment in its reference configuration and current configuration as follow:

$$E = \|dx\|^2 - \|d\mathbf{X}\|^2 = \frac{1}{2}(F^T F - I) \quad (49)$$

The present work relied on Cauchy's equilibrium equations to describe the two-degrees-of-freedom (2DOF) motions of the solid prism structure. These equations expressed the conservation of linear momentum for a continuum. Using the Lagrangian approach, we reduced the time derivative of the velocity to obtain the partial second derivative of the displacement described as follows:

$$\rho_0 \ddot{u} + \nabla \cdot \sigma - b = 0 \quad (50)$$

where  $\rho_0$  is the density of the structure,  $b$  is the total body force per unit volume,  $\ddot{u}$  the second time derivative of  $u$  (displacement) and  $\sigma$  is the Cauchy stress tensor or true stress. This equation

is known as the strong form of the conservation equation while the weak form can be obtained by multiplying the equation by a test function  $\delta w$ , integrating the domain, and applying Gauss's theorem. The weak form is also referred to as the principle of virtual work, which states that the sum of the internal work and external work is equal to zero as described below:

$$\delta w = \delta w_{int} + \delta w_{ext} = 0 \quad (51)$$

This equation forms the basis of the computation of structural mechanics problems using the FEM.

## 4.2.2 Finite element method

The Finite Element method is a powerful tool for finding approximate solutions to continuous problems. Similar methodology to other numerical techniques that approximate continuous partial differential equations with discrete algebraic equations. In this section, the relevant formulations and solvers used in the presented finite element models will be described.

The finite elements used to discretize the structural geometry have five aspects that affect the behavior of the element and as a result, the overall solution. The first of these is the element family which describes the type of problem being solved and the level of precision of the model. At the core of finite element analysis is the geometry of interest. The overall geometry is subdivided into a discrete number of finite elements. Major families of elements include 3D continuum, shell, beam, rigid, truss, and membrane elements as shown in Fig. 28.

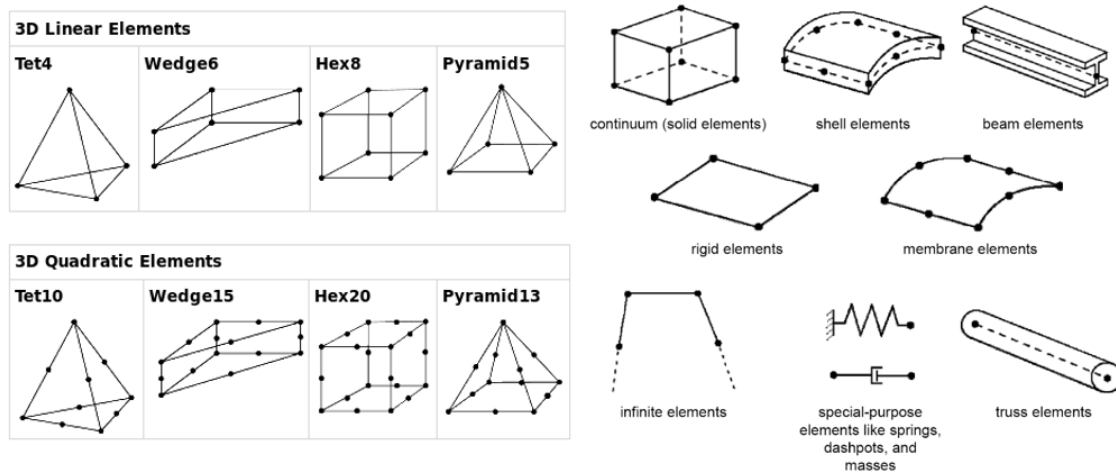


**Figure 28** Major families of elements Used for FEM discretization

The second feature of an element is degrees of freedom because they are the primary solution variables that are being solved for at the nodes of the model.

Each element is comprised of nodes and shares them with other interconnected elements immediately surrounding it. Together, all of the elements and nodes form a grid that defines the discretized structure. The total number of DOF in all the connected elements is dependent on the third feature, the total number of nodes, and the order of interpolation. The solution variables are only solved at the nodes of the model so that obtaining the solution at an arbitrary point requires the interpolation of the nodal solution values to that location. The total number of nodes in the element determines the order of interpolation. There are two primary element types which

are linear (1<sup>st</sup> order interpolation) and quadratic (2<sup>nd</sup> order interpolation). As shown in Fig. 28, for 3D continuum elements, linear elements have 8 nodes and quadratic elements have 20 nodes.

The accuracy of a finite element model depends greatly on the selection of the element and properties concerning the problem of interest. Specifically, in bending-dominated problems, care should be taken to ensure an appropriate number of elements through the thickness to ensure that the bending stresses are resolved. In Starccm+, the only available solid element was the 3D continuum which was used in this work. Due to the solid element would show the bending behavior much stiffer in comparison with the analytical solution(the locking problems) the 3D continuum elements were introduced in the present work for FE with quadratic shape. The quadratic reduced integration elements are generally free of locking and are good general-purpose elements for stress/displacement analysis. It is worth noting here that fully integrated linear 3D elements have eight nodes and eight integration points. Conversely, a fully integrated quadratic element has 20 nodes and 27 integration points. The fourth and fifth features of an element are the elements' formulation and integration.

In each element, the displacement is described locally through the element shape functions

$$\mathbf{u} = \mathbf{N}\mathbf{u}_M \quad (52)$$

where  $\mathbf{N}$  is the element shape functions and  $\mathbf{u}_M$  is the local nodal displacements. Therefore, the derivatives of the variable  $\mathbf{u}$  concerning the undeformed coordinates  $\mathbf{X}$  are related to the nodal quantities  $\mathbf{u}_M$  through

$$\frac{\partial \mathbf{u}}{\partial \mathbf{X}} = \frac{\partial \mathbf{N}_M}{\partial \mathbf{X}} \mathbf{u}_M \quad (53)$$

The relationship between the elemental Green-Lagrange strains and displacements is given by

$$\mathbf{E} = \mathbf{B}\mathbf{u} \quad (54)$$

where  $\mathbf{B}$  is the strain-displacement matrix. Then, the principle of virtual work is discretized using the Finite Element method

$$\delta \Pi = \delta \mathbf{u}_M^T \left[ \int_{V_0} \widehat{\mathbf{B}}_M^T \mathbf{S} \, dV + \int_{V_0} \mathbf{N}_M \mathbf{I} \mathbf{N}_N \rho_0 \ddot{\mathbf{u}}_N \, dV + \int_{V_0} \mathbf{N}_M \mathbf{b} \, dV - \int_{\Gamma} \mathbf{N}_M \bar{\mathbf{t}} \, d\Gamma - \mathbf{f}_M^P \right] = 0 \quad (55)$$

where  $\mathbf{f}_M^P$  was introduced to take into account point forces at node  $M$ . Since  $\mathbf{u}_M$  is zero at the Dirichlet boundaries, but otherwise arbitrary, the expression within brackets must be zero, leading to the discrete equilibrium equations.

$$\mathbf{f}_M^{\text{int}} + \mathbf{M}_{MN} \ddot{\mathbf{u}}_N = \mathbf{f}_M^{\text{ext}} \quad (56)$$

Where Each of the components of Equation 58 can be formulated as follows

$\mathbf{f}_M^{\text{int}}$  is the internal force at node  $M$

$$\mathbf{f}_M^{\text{int}} = \int_{V_0} \widehat{\mathbf{B}}_M^T \mathbf{S} \, dV \quad (57)$$

$M_{MN}\ddot{u}_N$  is the inertial term, with the mass matrix  $M_{MN}$  expressed as

$$M_{MN}\ddot{u}_N = \int_{V_0} N_M I N_N \rho_0 dV \quad (58)$$

$f_M^{\text{ext}}$  is the external force applied at node M:

$$f_M^{\text{ext}} = \int_{V_0} N_M b dV - \int_{\Gamma} N_M \bar{t} d\Gamma - f_M^p \quad (59)$$

For large displacements, the internal forces are a nonlinear function of the displacement. The sensitivity of the internal forces with respect to the displacement is defined by the stiffness matrix

$$K_{MN} = \frac{\partial f_M^{\text{int}}}{\partial u_M}$$

an iterative procedure is required to solve this problem. For each iteration, the incremental displacement is calculated and used to update the total displacement as

$$u^{i+1} + u^i = \delta u^i \quad (60)$$

The dynamic solution must satisfy the equation

$$M\ddot{u}^{i+1} + K\delta u^i + C\dot{u}^i = f_M^{\text{ext}} - f_M^{\text{int}} \quad (61)$$

Standard 2<sup>nd</sup> order Newmark-beta scheme is the time discretization method used within this work. The Newmark-Beta method, with constants  $\gamma$  and  $\beta$ , between time steps  $n$  and  $n + 1$ , rests on the following assumptions

$$\dot{u}_{n+1} = \dot{u}_n + ((1 - \gamma)\ddot{u}_n + \gamma\ddot{u}_{n+1})\Delta t \quad (62)$$

$$u_{n+1} = u_n + \Delta t\dot{u}_n + \Delta t^2 \left( \frac{1-2\beta}{2} \ddot{u}_n + \beta\ddot{u}_{n+1} \right) \quad (63)$$

The constants  $\gamma$  and  $\beta$  are used to control the stability and accuracy of the analysis. The method is 2<sup>nd</sup> order accurate and unconditionally stable when  $\gamma = 0.5$  and  $\beta = 0.25$ .

The material under study in this work was made of Polyvinylchloride (PVC). With only information about its Young's Modulus and density, a linear elastic model is the only option that can be defined directly, however, due to the nature of PVC and the long polymer chains which define its molecular structure, PVC is most likely not isotropic. In the absence of any information pertaining to the directional dependencies of its behavior, an isotropic, linear elastic model was defined in the present work.

### 4.2.3 Fluid-structure interaction

In this thesis, the fluid domain is solved with CFD calculations, while the solid domain is solved with FEA calculations. These two solution domains create the foundation for the numerical fluid-structure interaction analysis. This coupled interaction between the fluid and solid introduces a challenging problem both numerically and computationally. This section is aimed

to describe and how these are dealt with in Starccm+. In this thesis, the FSI study is done solely by the use of Solid stress solver within Starccm+. In the following, some classifications of the interactions and the capabilities that are needed to address FSI problems in Starccm+ are given.

Fluid-structure interaction (FSI), can be grouped into distinct categories:

- “One-way” coupling
- “Two-way” coupling

### ***One-Way coupling***

One-way interaction problems indicate that the fluid may impart some action on the structure but the response of the structure to the fluid loading does little to affect the fluid motion. Take, for example, the analysis of a piston in an internal combustion engine. The piston has a huge impact on the flow in the engine, while the fluid does not deform the piston. A one-way interaction implies that we only send information from one code to another, from CFD solver to FE solver.

### ***Two-way coupling***

A case where the fluid motion and pressure affect the displacement and deformation in the structure (or rigid body motion) and this deformation leads to a change in the fluid flow is referred to as a "two-way" interaction. Two-way interaction implies that we send information between two codes. Vortex-Induced Vibration implies a classical example of strong coupling. The flow past a bluff body exerts oscillating forces when alternate vortices are shed. These oscillating forces generate high response amplitudes in the structure followed by changes in the fluid flow vortices formation. Therefore, oscillating forces have been affected as well.

For strong coupling, the physical coupling is two-way and the coupling between the codes is pronounced. This is associated with dynamic problems where the dynamic loads and the structural velocities change dramatically. An implicit coupling scheme is necessary for this type of problem since the deformations and fluid flow can change dramatically over time to assure the strong coupling we need to perform several exchanges within each time step.

The FSI approach utilized two-way coupling, where the fluid-structure coupling model only accounts for the fluid forces computed by the separated flow. This meant that the mathematical models for the fluid flow and the motion of the solid structure were integrated separately, as schematically illustrated by the flow chart in Fig. 29. The simulation within each time step was initiated by solving the Navier–Stokes equations to obtain the forces on the cylinder. Then, the fluid forces were applied to the solid boundary at the fluid-structure interface, and the forces were transferred to the structural dynamic model to obtain the displacements of the structure. The new mesh configuration was evaluated based on these displacements. The two-way coupling accounted for the effect of the solid structure’s displacement on the fluid flow. All the FSI simulations were initialized from the final flow field obtained for the rigid cases. Figure 29 shows the flow chart of the FSI solution algorithm



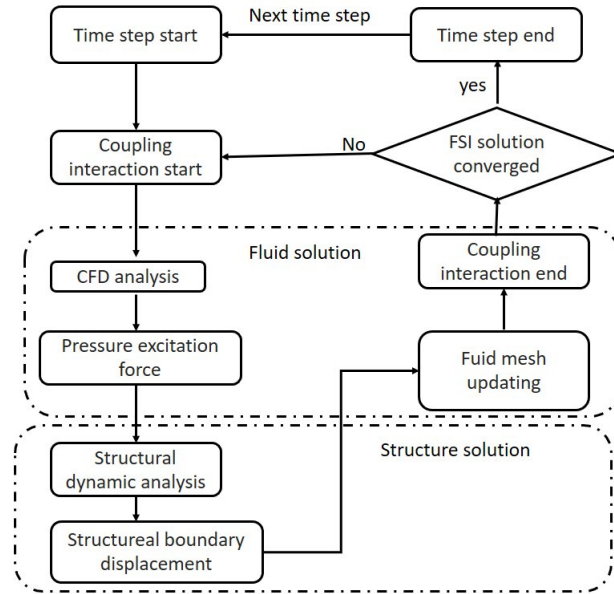


**Figure 29** Flow chart of the FSI solution algorithm

When simulating an FSI case, Starccm is required to account for the changes of shape for the solid structure. FSI simulations with large displacements of the solid structure result in large deformations of the fluid mesh. When these distortions affect the quality of the fluid mesh, a new fluid mesh based on the deformed solid structure is been created. After remeshing, the fluid mesh is based on the new solid part, which represents the deformed structure, while the solid mesh is based on the undeformed part. Due to the deformation of the solid structure as a result of the fluid loads, the new fluid mesh is directly linked to the solution state in the structure at the time of remeshing. Starccm+ stores the solid mesh configuration at the time of remeshing and uses it for all subsequent mapping of data between the fluid and the solid mesh. In this thesis, a morphing of the fluid and solid displacement has been assigned to the structure domain. Morphing is the deformation of the fluid grid by moving the fluid vertices in such a manner as to conform to the solid structure and maintain a reasonable quality fluid grid. This is done by altering the cell shape and at the same time ensuring that all cells maintain the same neighboring cell. To account for the arbitrary motion of the fluid mesh, Starccm+ uses a space conservation law to conservatively and accurately express the transport motion.

When dealing with the FSI problem, due to different discretization techniques applies for the subtasks (finite volumes and finite element), two meshes have existed; one for the fluid domain and one for the structural domain. This difference in the mesh is often due to the difference in physical processes in the fluid and the structure. One challenge in FSI, therefore, is the difference in the resolution between the fluid and the structure mesh. Figure 30 presented an example of a non-matching grid. The challenge subsequently was finding consistent and conservative interpolation methods across these non-matching meshes. The Mapped Contact Interface is an indirect interface type between fluid/solid boundaries that allows for a non-conformal mesh and has been used in the present work. The grid to grid data interpolation steps included the data transfer from fluid loads determined by the CFD solver to the CSD solver, and from the structure displacements predicted by the CSD solver back to the CFD solver. A compact scheme has been used. This scheme builds a connectivity map by finding the nearest neighbor of a face on the opposite side of the interface. After the connectivity map is created, The conservative method based on weighted interpolation, using face area ratios, is defined.

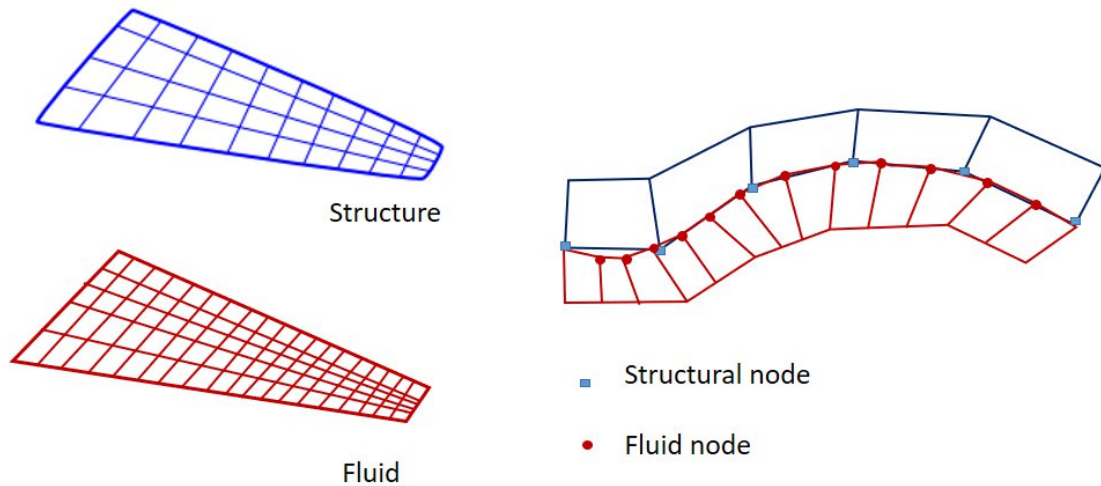


**Figure 30** Example of the interface between non-conformal grids

The forces from the fluid imparted on the structure at its nodal points in two steps. First, the traction at the center of the fluid face is interpolated to the center of the solid face, then the traction at the center of the solid face is converted to a single force vector by multiplying it by the face area and subsequently distributed to the element nodes. The transfer of displacements from the CSD solver back to the CFD solver is completed through a similar process.

### **Grid motion**

The coupled boundaries at the fluid-solid interface are moved according to the displacements calculated by Abaqus. All of the fluid domain grid vertices must also be moved to maintain the quality of the cells in the region surrounding the coupled boundaries and avoid squashed cells. In STAR-CCM+, grid motion is referred to as mesh morphing. The mesh morphing solver collects the displacements of all control points, calculates an interpolation field throughout the domain using multiquadric interpolation theory, and then applies the field to all the vertices to get the new grid. Mesh morphing can also be used in a more general sense to model moving boundary conditions by applying rigid body grid motion to the grid vertices. In the case of the sloshing tank, the rigid body rotation of the tank walls is applied with this solver. The angular displacement time history is input into STAR-CCM+ as a table and then linearly interpolated to determine the angular position at any time within the history.

Together the grid deformation due to the fluid-structure interaction and the rigid body rotation of the tank are superimposed to arrive at the final morphed grid. For large deformations or non-periodic motions, it may be advisable to remesh the fluid domain periodically or use an overset grid combined with mesh morphing.

# 5. Experimental Results

## 5.1 Water Tank Tests Results

### 5.1.1 Smooth cylinder

As seen in Fig. 31, it can be seen that the measured r.m.s. values of motion amplitudes (normalized against  $D$ ) at the top end of the test cylinder in a streamline and transverse directions to the flow are plotted against the reduced velocity,  $U_r$ . This figure depicts also the associated orbital trajectories for the top end of the smooth cylinder. For an elastically mounted cylinder having a low but super-critical mass ratio, the lateral displacement amplitude response was divided into three regimes.

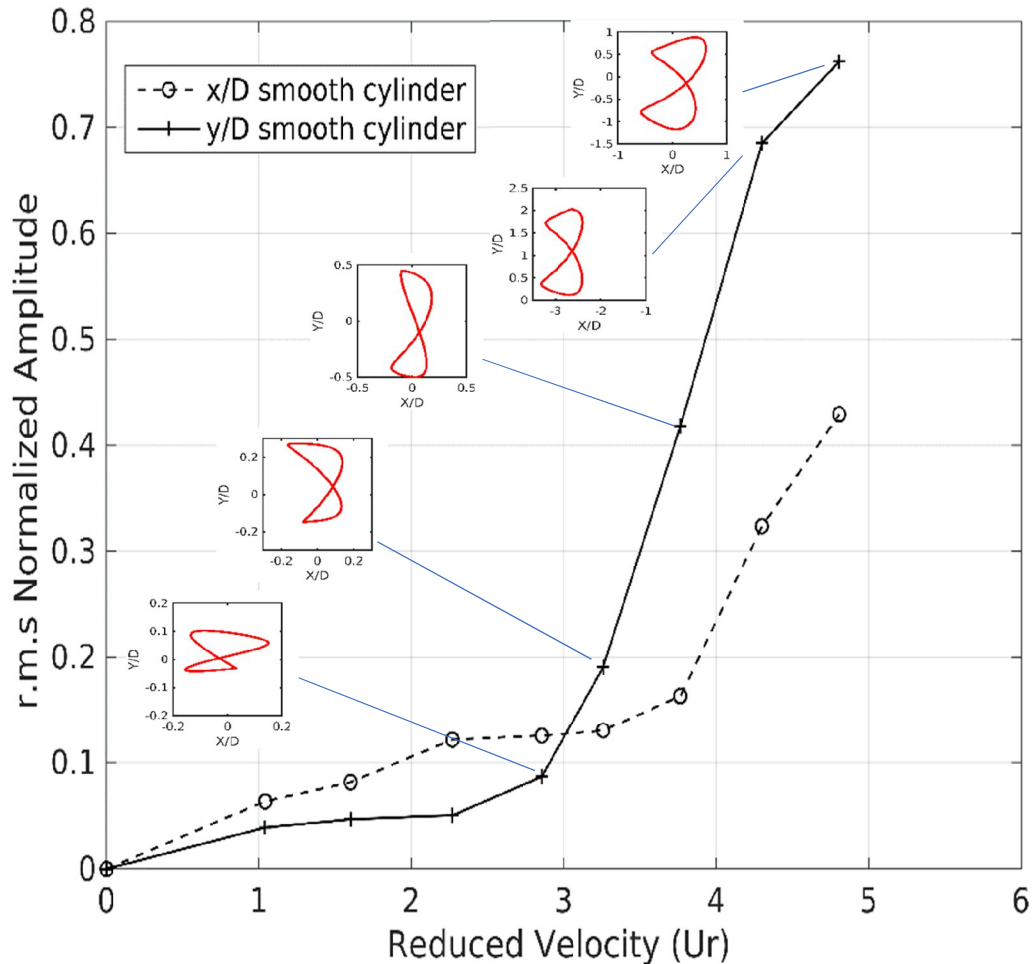


**Figure 31** Root mean square (r.m.s.) values of measured normalized stream-wise ( $x/D$ ) and lateral ( $y/D$ ) top-end displacement amplitudes (and the associated trajectories) vs. reduced velocity ( $U_r$ ) for the smooth cylinder.

First, there was the initial branch at low reduced velocities, characterized by small-amplitude displacements. This is followed by the second regime, consisting of an upper branch in which the displacement amplitudes reached a maximum. The third regime occurred after the lock-in range, where the lateral displacement amplitudes decreased, and this regime was known as the lower branch. For that mass ratio range, two jumps in the displacement response are observed between each branch. From Fig. 31, the smooth cylinder is set into vibration at a reduced velocity of about 1.1 and at  $U_r \approx 3.0$ , the streamline, as well as the transverse amplitudes, starts to increase at a greater rate. Although not shown in this figure, the maximum displacement amplitudes of nearly  $0.8D$  occurred at a reduced velocity of  $U_r \approx 5.0$ . Both the streamline as well as the transverse response characteristics are similar.

Although there does not appear to be a clear amplitude jump distinguishable, a break in the branch around  $U_r \cong 2.8$  has been imposed from the transverse response curve. Then, the amplitude increasing nearly linearly with flow speed before a break in the increasing slope observed at about  $U_r \cong 4.2$ . Unfortunately, the smooth cylinder could not withstand the severe fatigue stress applied at such conditions and it fractured, as shown in Fig. 41, at  $U_r \cong 5$ . Similar behavior for the response of a critical mass ratio of 0.54 has been reported by Leong and T. Wei [100] and Geo et al. [95], and the lower branch can never be reached.

For the inline motion, the amplitudes of the vibrations in the streamline became larger as  $U_r$  increased and, due to the mean drag force effect. Different from the previous note, for  $y/D$ , a large jump in the branch has occurred at  $U_r \cong 3.8$ . However, owing to limitations in the top speed of the water tunnel, it was not possible to ascertain whether the streamwise amplitude keeps increasing or if it approaches an asymptote.

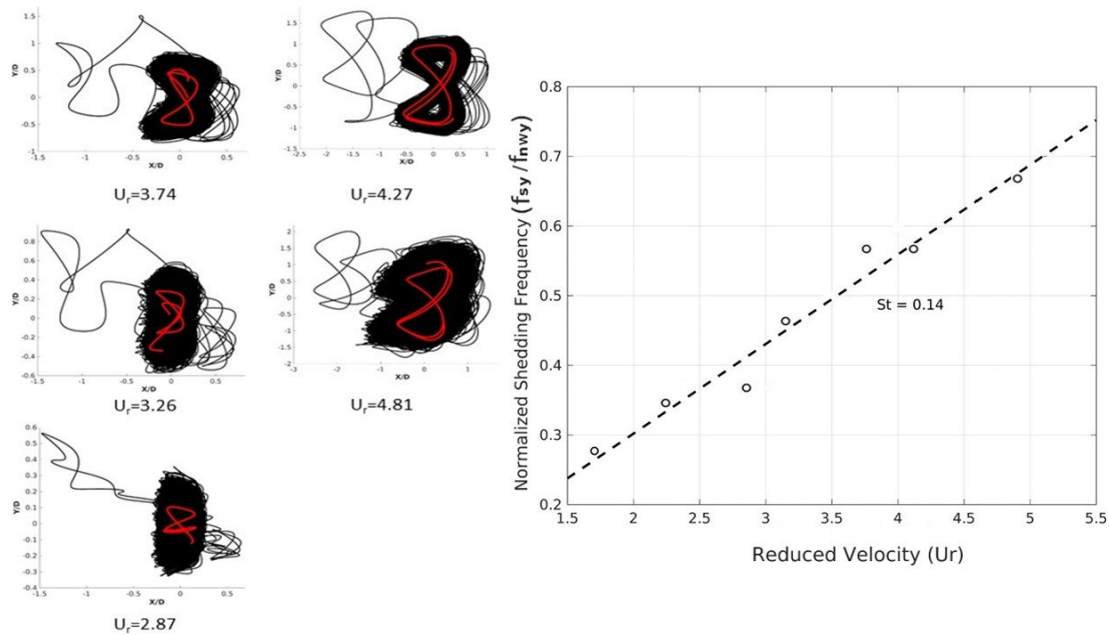


**Figure 32** Motion trajectories of the smooth cylinder's top in flows at different velocities (left), black lines represent trajectories over the entire duration of the experiments; red lines, trajectories obtained over one cycle, and the plot of normalized lateral shedding frequency vs. reduced velocity (right)

Furthermore, one can see that the maximum streamwise amplitude is large,  $A_x = 0.42D$  compared to the value of  $0.3D$  reported in the 2DOF elastically mounted cylinder above critical mass ratio case of Jauvtis & Williamson (2004), principally because of the effect of mass ratio. Figure 32 gives the cross-flow dominant mode measured by LDV and dimensionless fundamental still water natural frequency  $f_{sy}/f_{nwy}$  against the reduced velocity  $U_r$ . The cross-

flow shedding frequency ( $f_{sy}$ ) was determined from the velocity spectra using the Fast Fourier Transform (FFT).

The estimation of power spectra presented in this study was the interpolation of the arbitrarily or randomly sampled LDV data to obtain a uniform velocity over time, which is then resampled in equal steps with a sampling frequency close to the average sampling frequency. Nobach [169] described the details of up-to-date available methods to analyze the frequency spectrum from arbitrarily sampled data acquired by LDV measurements. The dominant peak in each spectrum is assumed to correspond to the vortex shedding frequency ( $f_s$ ).

It may be observed that the cross-flow frequency data, appearing in Fig. 32 as hollow circles, vary linearly with reduced velocity. This trend was well fitted by a linear regression using the least square method, appearing in Fig. 32 as a dashed line. The slope of this fitting line was found to be 0.14 and referring to Strouhal no. Besides, the cylinder motion trajectories corresponding to the cross-flow shedding frequencies were presented at different reduced velocities. Figure 32 (left) Black lines represent trajectories over the entire duration of the experiments; red lines, trajectories obtained over one cycle.

Although a figure eight configuration more or less describes all the motion trajectories shown in the left graph of Fig. 32, the lock-in region was not achieved yet because our experimental setup was unable to generate high enough velocities. For lower reduced velocities, the dominant oscillating frequency was different from the shedding frequency. Here, it is worth emphasizing that, The presence of the cylinder's free end altered the flow structure in the near wake region, thereby affecting the vortex shedding process, the vortex structure itself, and the surface pressure distribution on a cylinder. This may well result in more than one frequency appears. Only the dominant frequency among others has been considered for calculations of the Strouhal number in the present work.

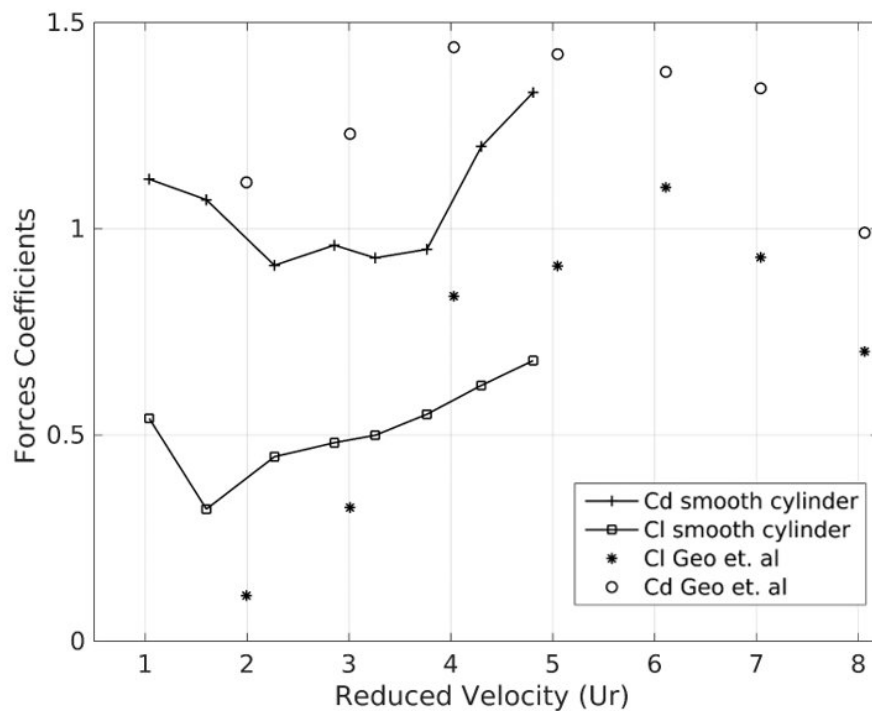


**Figure 33** Drag and lift forces coefficients versus the reduced velocity

The variations of the transverse force (lift) and the streamline force (drag) with the reduced flow speed velocity,  $U_r$  are shown in Fig. 33. In the present work, the drag coefficient and the lift coefficient were determined by taking the r.m.s. values of the measuring forces. The drag and lift coefficients were defined as follows

$$C_d = F_x/(\rho U^2 A/2), \quad C_l = F_y/(\rho U^2 A/2) \quad (64)$$

where  $F_x$  is the drag force in the (streamwise) x-direction, and  $F_y$  is the lift force in the (transverse wise) y-direction obtained by load sensor measurement. The drag coefficient on the bare cylinder increases as the flow speed, as does the in-line deflection. As seen, the mean drag coefficients gradually decrease from a value of  $C_d = 1.1$  at  $U_r = 1.0$  to a value of  $C_d = 0.9$  at  $U_r = 3.45$  and then suddenly increase to a value of  $C_d = 1.4$  at  $U_r = 3.9$ . Figure 33 includes also comparative sample results from VIV experiments of Geo et al. on flexible cylinders with critical mass ratios[95]. However, the drag coefficient observed was smaller than the present study, this may be caused by the difference in their end condition (2D), and the difference in values of aspect ratio (181.8). The lift coefficient  $C_l$  showed a typical behavior as the drag coefficient does. It increased rapidly decrease from a value of  $C_l = 0.5$  at  $U_r = 1.0$  to a value of  $C_l = 0.3$  at  $U_r = 1.6$  and then gradually increase to a value of  $C_l = 0.7$  at  $U_r = 4.9$ .

## 5.1.2 Cylinder with attached fins

### *Amplitude response*

For the cylinders fitted with fin plates, Fig. 34 presents r.m.s. values of measured normalized transverse top-end response amplitudes,  $y/D$ , against reduced velocity,  $U_r$ . Comparative r.m.s. values for the smooth cylinder are also plotted in this figure. As mentioned above, three angular positions have been chosen for the fins' location, and the values corresponding to the three angular positions of 80, 90, and 110deg are indicated in the figure's legend. It is known that in the subcritical range of Reynolds numbers, the boundary layer separation point oscillates at angular positions between 80 and 90deg from the front stagnation point [101] [102]. Besides, the published literature suggests that there is a correlation between the angle of separation and the base pressure coefficient [103].

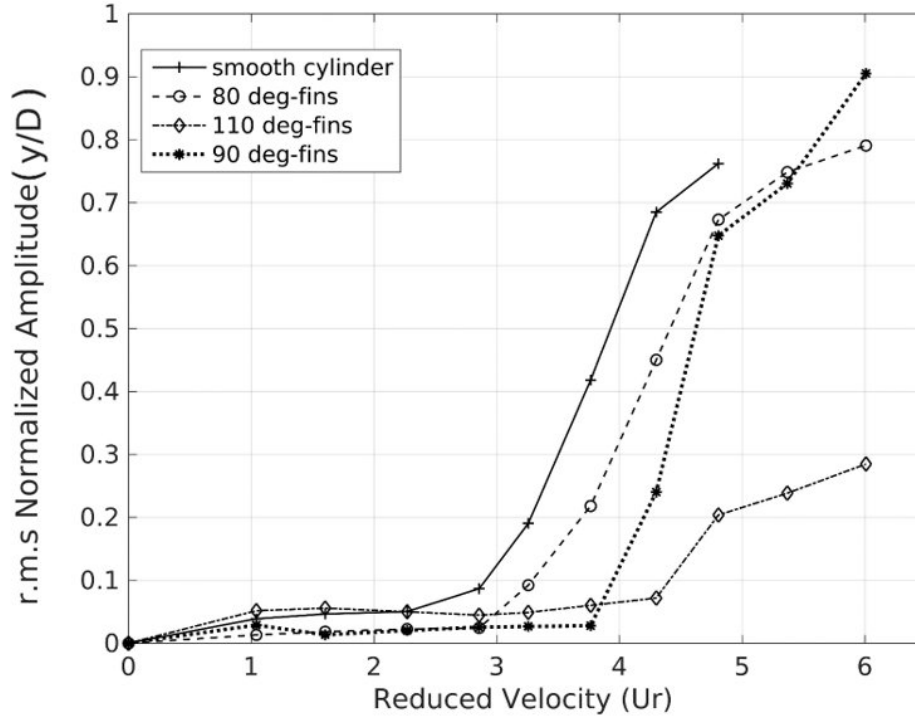


**Figure 34** Comparative r.m.s. amplitudes of normalized lateral top-end amplitude response vs. reduced velocity for the smooth cylinder and the finned cylinder models

One additional location has been examined at angle  $110^\circ$  from the front stagnation point. For the cylinder fitted with fin plates at a radial position of  $110^\circ$ , the vortex shedding process is less pronounced, and the pressure becomes more or less constant and equal to the base pressure [11]. The placement of the fin plates for suppression aims to stretch the shear layer vorticity away from the cylinder wake region before it rolls up into the vortices. Then, the vortex formation length would be increased. This is a matter of finding experimentally the best angle position at which fin plates would be located. More about the fins position and arrangements were discussed in detail later in chapter 6.2.

All cylinders fitted with fin plates show a continuous increase in response as flow speed increases. Cylinders with  $110^\circ$  fin plates show a somewhat steeper response curve when compared with the other tested models, but the response of none of the cylinders represents a resonant behavior typical of VIV.

In fact, the response curves for the  $80^\circ$  and  $90^\circ$  fin plate cases were similar. With the  $90^\circ$  finned cylinder showing the lowest response than the  $80^\circ$  and  $110^\circ$  models at lower reduced velocity till  $U_r = 3.7$ , then it started to jump to higher values of the response.

The plots showed that the fitting of fins caused a significant reduction in transverse response. For the cylinders fitted with fins at 80 and 90 degrees, the transverse response is at  $U_r = 4.25$  is about 35 % less and, for the cylinder fitted with fins at  $110^\circ$ , it is about 88 % less than the response of the smooth cylinder. Owing to the imitated maximum velocity attainable in the water channel in the present tests, for the cylinders fitted with fin plates at 80 and 90 degrees, the synchronization region did not be reached, i.e., the region where the vortex-shedding frequency matches the cylinder's natural frequency. However, for the cylinder fitted with fin plates at  $110^\circ$ , the lock-in region is obtained, as seen by the power spectral density distributions of the wake behind this cylinder presented in Fig. 38. For higher reduced velocities, it may be

expected that the amplitudes will increase monotonically both for the cross-flow and in-line motions and a constant amplitude response would have been observed (seen in  $80^\circ$  and  $110^\circ$  fins response shape), as observed previously by Leong and T. Wei [100]. It seems that each sharp change in the rate of a response manifested a changing wake of vortices and, accordingly, indicates a different vortex branch.

Some significant differences in the finned cylinders' dynamics characteristics from the smooth case were found in the transverse displacement curves. Observe in Fig. 34 that for the cylinder fitted with fins at  $80^\circ$ , the break in the curve, i.e., the steep increase of  $y/D$  values occurred at  $U_r = 2.7$ , while for the cylinders fitted with fins at  $90$  and  $110$  degrees, this steep increase occurred at  $U_r = 3.8$  and  $U_r = 4.27$ , respectively. This indicates that the onset of lock-in for the finned cylinders occurred at higher velocities than for the bare cylinder, i.e., the jump to the upper branch was delayed. This feature was consistent with the remarked conclusion that would be shown later in chapter 5.2 that reported the onset of lock-in occurs at a higher velocity than for the plain cylinder i.e the jump to the upper branch is delayed. This is due to the influence of the location of fin plates on increasing the vortex formation length and then decreasing the vortex strength near the wake region at a low velocity.

It is worth mentioning that cases, when the peak amplitude is suppressed by 30% or more compared to the peak amplitude of the smooth cylinder response, are classified as strong suppression cases [91]. In the present tested tools, all the cylinders models fitted with fins reduced the transverse response by more than 30% at  $U_r = 4.25$  as illustrated.

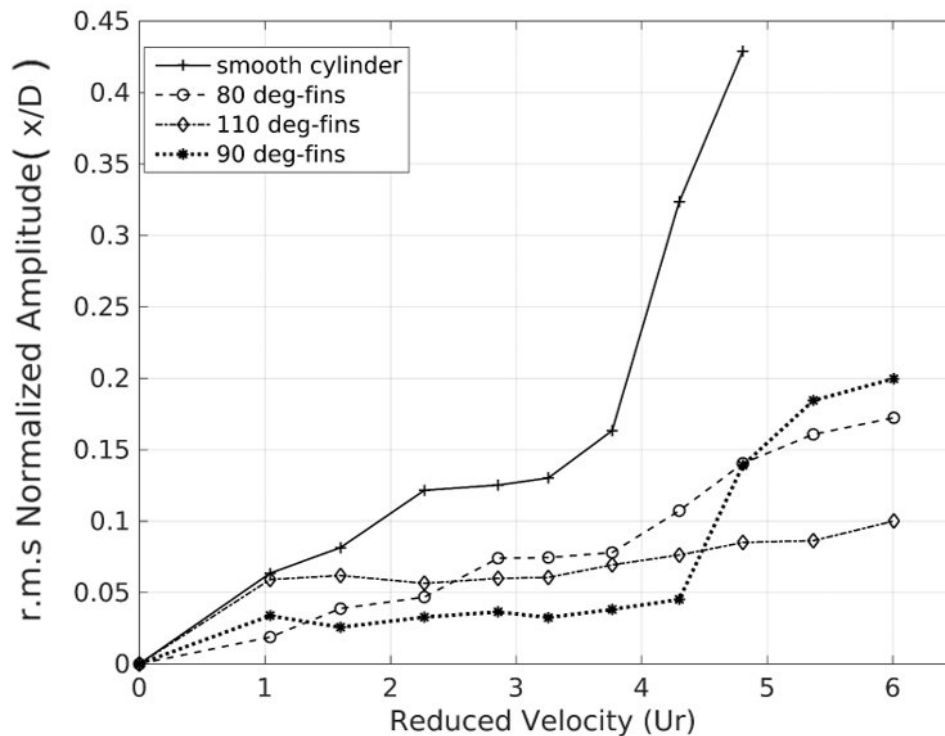


**Figure 35** Comparative *r.m.s.* amplitudes of normalized inline amplitude response vs. reduced velocity for the finned cylinder models and the smooth cylinder

One of the most remarkable features for the cylinders below the critical mass ratio is the severe increase in the inline response amplitude which could reach  $2.5D$ . C. Leong and T. Wei [100] observed that the inline amplitude response keeps increasing and does not approach an asymptote value like its lateral counterpart.



In the present study, the inline response of the cylinders fitted with fins at 80 and 90 degrees was reduced to at least 67%, and the greatest amplitude reduction of nearly 82% was obtained for the cylinder fitted with fins located at 110° from the front stagnation point. Although the slope of the inline amplitudes in Fig. 35 increases at  $U_r = 1.4$  for the cylinder fitted with fins at 80deg and at  $U_r = 4.3$  for the cylinder fitted with fins at 90°, these slopes increase significantly less than the slope for the smooth cylinder. Furthermore, for the cylinder fitted with fins at 110°, there is no sudden increase of the slope of the inline amplitudes, acknowledging the 82% amplitude suppression for  $U_r=4.81$  compared to that of the smooth cylinder. Table 6 presents approximated reduction caused by using these fin plate configurations at different reduced velocities. It is worth recalling that, the smooth cylinder has high fatigue stress and damage occurs at a reduced velocity of about 4.81.

Furthermore, in the third model with 110°, the in-line response presented a first-order linear relation with the increase in the reduced velocity with nearly no slope changes despite the frequencies lock-in, which was reached at a reduced velocity of about 5.0 (see Fig. 38).

**Table 6 Approximated reduction percentage of displacement response for the tested cylinders at different reduced velocities**

<b>Reduced velocity</b>	<b>Reduction percentage in axial displacement</b>			<b>Reduction percentage in lateral displacement</b>		
	<b>Model 80</b>	<b>Model 90</b>	<b>Model 110</b>	<b>Model 80</b>	<b>Model 90</b>	<b>Model 110</b>
<b>At <math>U_r = 3.27</math></b>	44%	71%	57%	53%	75%	90%
<b>At <math>U_r = 3.8</math></b>	50%	72%	62%	53%	87%	96%
<b>At <math>U_r = 4.25</math></b>	66%	85%	77%	35%	68%	88%
<b>At <math>U_r = 4.81</math></b>	67%	67%	81%	12%	15%	75%

### **Forces analysis**

For stationary and flexible cylinders, it was proved that the effect of the fin plates attached to the cylinder is very important on the characteristics of the fluid flow characteristics and, in turn, the drag and lift forces as well as the oscillating cylinder responses. The measured total streamwise (drag force including inertia forces) and lateral forces (lift force including inertia forces) were not increased by the presence of the attached fin plates. The fin plates caused the streamwise force to stay below the streamwise force of the smooth cylinder, despite the fact that the fins slightly increased the cylinders' frontal area.

In VIV, although the lift force is proportional to the strength of the vortices, the drag force acting on the cylinders was not amplified by the presence of the attached fin plates in equivalent ranges of flow velocities. Figure 36 plots comparative r.m.s. values of stream-wise (in-line) force and lateral force versus reduced velocity acting on the smooth cylinder and on the cylinders fitted with fin plates at 80 and 110 degrees. Unfortunately, the load cell signals have been corrupted for the case model 90 deg fined cylinder and they were eliminated from the analysis. However, it is expected to be similar to the behavior of the 80 deg fined model, as do the response features.

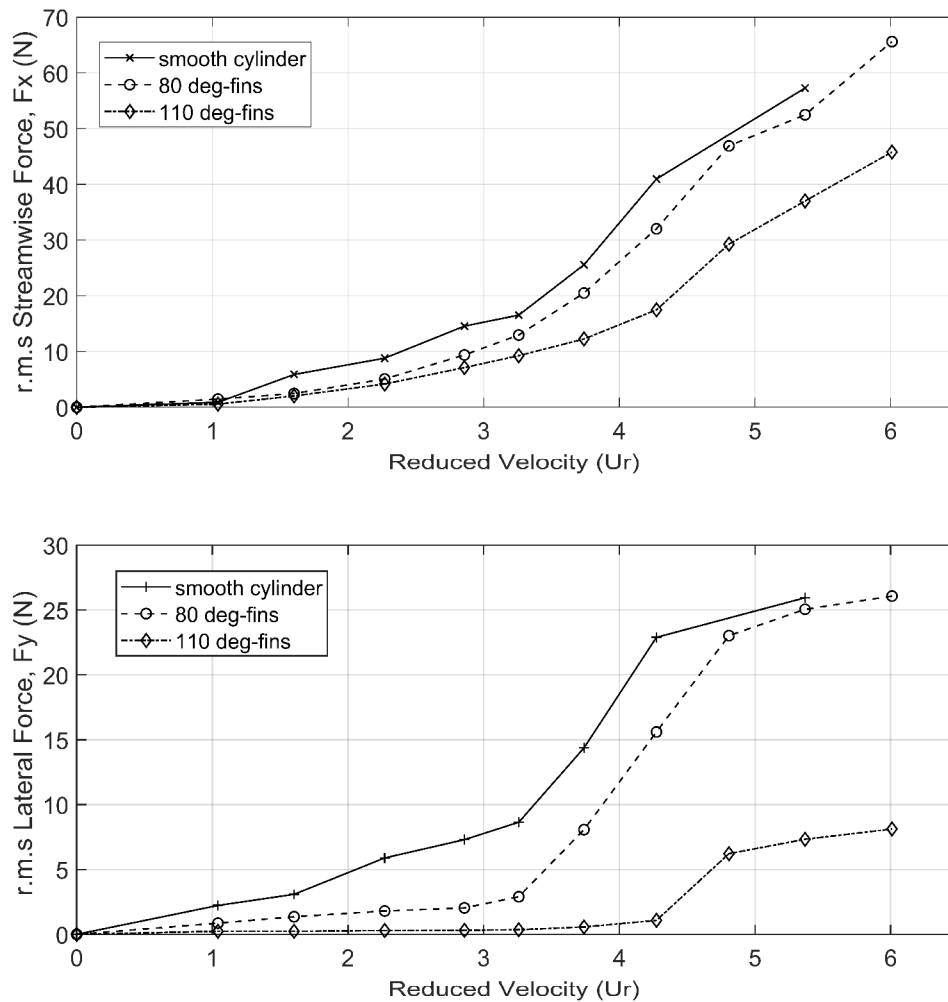


**Figure 36** Comparative r.m.s. amplitudes of stream-wise (top) and lateral forces (bottom) vs. reduced velocity  $U_r$  acting on the smooth cylinder and on the cylinders fitted with fin plates positioned at 80 and 110 degrees.

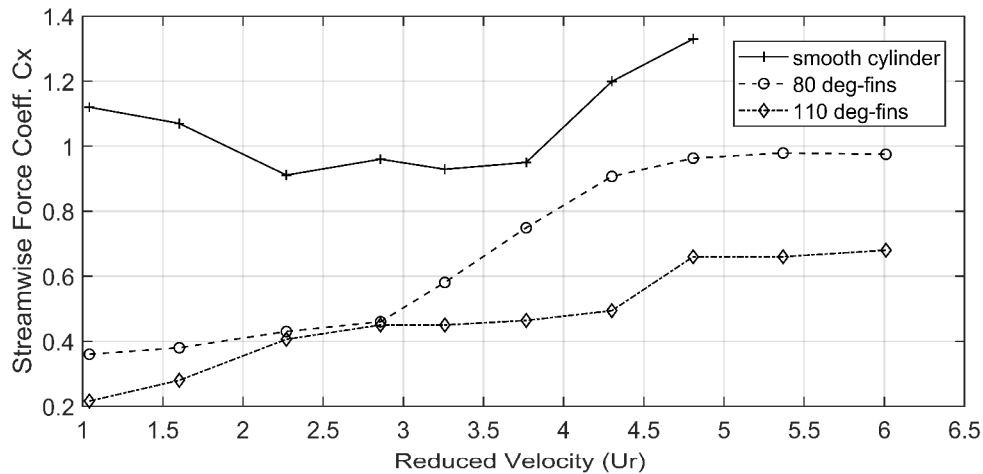
Very interestingly, although the fins increased the cylinders' cross-sectional area, the drag forces on all the finned cylinders were smaller than the drag force on the smooth cylinder. To illustrate, it is worth noting that the flow-induced forces are likely to split into two components: pressure force acting normal to the wall surface ( $F_w^p$ ), and shear force, caused by a wall-normal gradient of wall parallel velocity components, acting tangential to the wall surface ( $F_w^t$ ). Forces that act upon the flow direction is the drag force while the upward forces represent the lift force [104].

$$F_w^p = \int_S p n dS, \quad F_w^T = \int_S \tau_{nt} t dS \quad (65)$$

Where,  $\tau_{nt} = \mu \left( \frac{\partial U_t}{\partial n} \right)_w$  is the shear stress components,  $t$  is a unit vector in the x-direction, and  $n$  is a unit vector in the y-direction. The response reduction of the fined cylinder in the present work lies in the fact that the pressure force acting normal to the wall surface ( $F_w^p$ ),  $F_w^p = \int_S p n dS$ , keeps decreasing with increasing Re due to the fins' effect, accordingly, the drag and lift forces decrease in sequence. The same features are observed in chapter 6.2, as illustrated later, however, the drag forces, in chapter 6.2, have been started with higher values. This seems due to the influence of viscous effect which has been decreased in the present test due to higher Re. It is worth noting that the inertia force is influenced by the cylinder response which is affected by the lift and drag forces applied on the cylinder surface.

Observed that drag continues to drop with increasing the angular position of the attached fin plate's location. This claim remains valid for the entire range of reduced velocities considered in the experiments. The same was verified to occur for the lift force features. Although the cylinders vibrating amplitudes became larger with increasing flow velocity, the fin plates kept the lift force below the lift force of the smooth cylinder. On the contrary to the displacement, there is no pronounced jump of the lift and drag force coefficients at higher reduced velocities; nevertheless, the cylinders with fin plates approached their natural frequencies during the corresponding synchronization range of VIV, which was reached at a reduced velocity of about 5.0 for the cylinder with fin plates located at 110 deg.

However, a break in the slope was observed for all the tested cylinders, including the plain cylinder, at an asymptotic value of  $U_r = 1.8$  for the smooth cylinder and for the cylinder with the fins attached at 110deg, and at an asymptotic value of  $U_r = 3.0$  for the cylinder with fins attached at 80°. No clear explanation could be offered for this kind of behavior because the frequency response showed that at this reduced velocity different shedding frequency has been observed than the oscillating frequency of the cylinder as discussed later. This means that this behavior has not related to the synchronization features. More experiments with visualization tools are needed for more investigation.



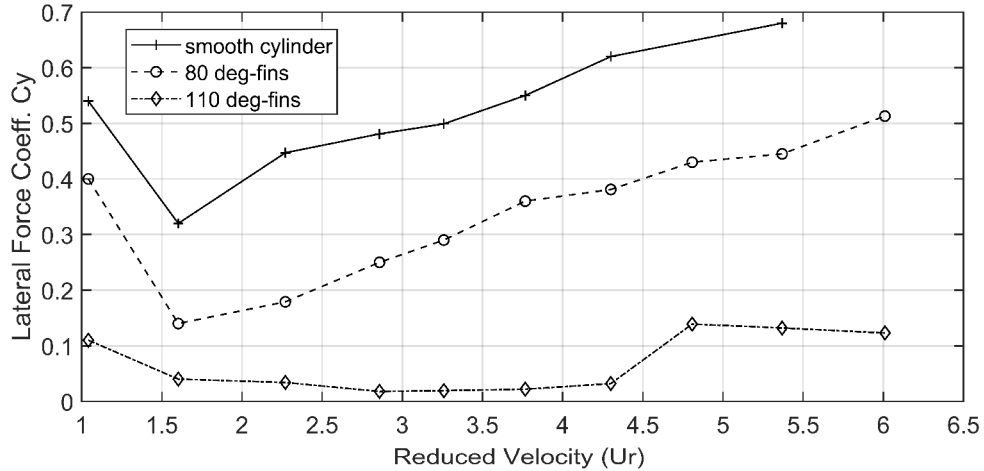


**Figure 37** Comparative *r.m.s.* values of stream-wise (top) and lateral force coefficients (bottom) vs. reduced velocity for the smooth cylinder and for the cylinders fitted with fin plates at 80 and 110 degrees

Nevertheless, for the cylinder with fin plates positioned at  $80^\circ$ , these fin plates reduced the lift and drag force coefficients for  $U_r = 4.8$  by about 30 and 62%, respectively. Similar behavior has been shown for the forces coefficients as depicted in Fig. 37. Using equation 64 to non-dimensional the force quantities and calculate the drag and force coefficients for the different tested models.

For the cylinder with fins attached at  $110^\circ$ , drag and lift force coefficients remained nearly constant after reaching the lock-in condition at the onset of synchronization, which theoretically occurred at  $U_r = 4.81$ , i.e., when the shedding frequency approached the cylinder's wet natural frequency. At  $U_r > 4.81$ , the lift coefficients started to decrease in a non-conventional behavior as the reduced velocity keep increasing up to the limitation of the present study. The drag coefficient was found to be approximately constant after approaching the lock-in region. It seems that the fin plates have a great effect on suppressing VIV features even at the resonance condition.

### ***Frequencies and trajectories***

As mentioned above, the velocity signals, in the cylinders' wake region, captured by LDV from the cylinder wake region were analyzed to investigate the effect of the finned models. Since the vortex shedding frequency was measured at the mid-height of the cylinder, the effects of the wall boundary layer and the horseshoe vortex on the shedding frequency were considered to be very small. Figure 38 plots the comparative normalized frequency ratio,  $f_{sy}/f_{nwy}$ , versus the reduced velocity,  $U_r$ , for the smooth cylinder and for the cylinders fitted with fin plates at 80, 90, and 110 degrees.

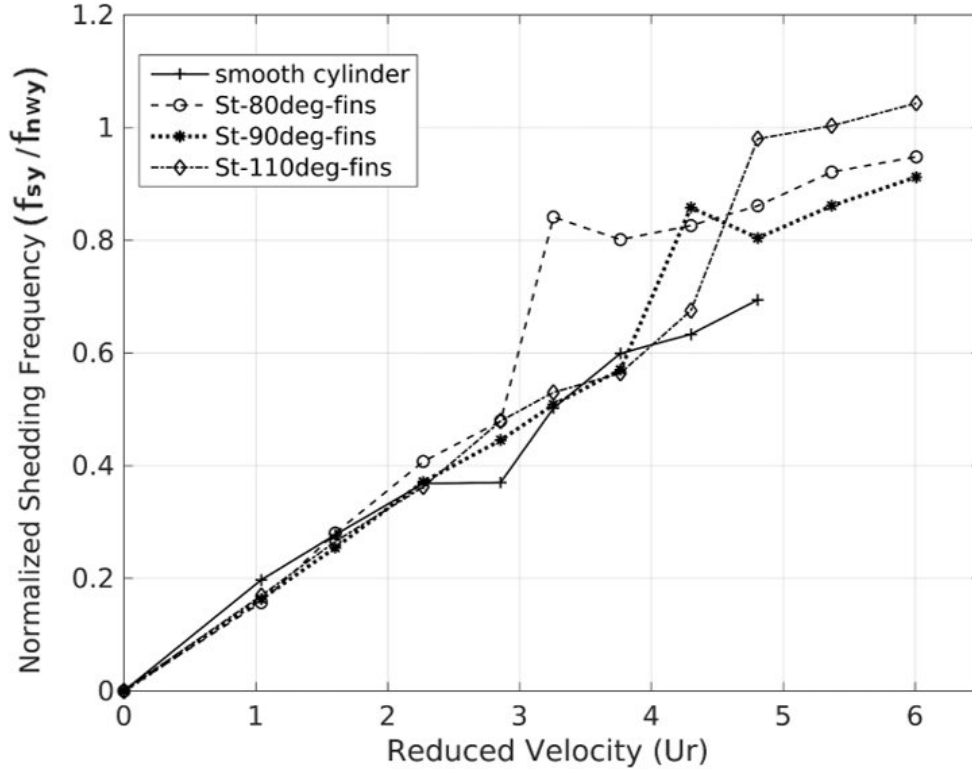


**Figure 38** Comparative shedding frequency ratio vs. reduced velocity for the smooth cylinder and for the cylinders fitted with fin plates positioned at 80, 90, and 110 degrees

Along with the abrupt increase in amplitude observed in Fig. 37, the frequency ratio  $f_s / f_{nw}$ , where  $f_s$  flow shedding frequency also registers a step-increase. Thereafter, the frequency undergoes a steep increase almost linearly to higher velocities values as shown in Fig. 37. All three tested models showed the same features to the smooth cylinder. It is worth noting that, Roshko, in 1961 [105] found for Reynolds' numbers,  $Re > 3.5 \times 10^6$  that there was a regular vortex development in flow past a stationary cylinder characterized by Strouhal numbers with a nearly constant value of 0.26-0.27, but the wake width was less than that at  $R \sim 10^5$ . Also, working from Roshko's concept [56] of a Universal Strouhal number, it was found that, for a stationary cylinder that  $S_t$  at  $Re \sim 10^5$  agreed quite well with  $S_t$  at  $Re \sim 10^7$ , which would imply that vortex development would be similar except for the difference in wake widths causing the lift force coefficient to be somewhat lower at  $R \sim 10^7$  than at  $R \sim 10^5$ . On the assumption that somewhat similar action would occur with an oscillating cylinder and based on the consistent results obtained in chapter 6.2, it was considered that the models would behave in a similar behavior. This means that as the Strouhal number is approximately similar for all the tested models, the vortex development was different in wake widths and lengths because of the attached fin effect resulting in decreasing the lift force coefficient.

It is observed that Strouhal's law behavior in the present experiments could be divided into two distinct regions for each model. They deviated from the smooth cylinder slope at different reduced velocities. It is well known that the vortex shedding frequency very strongly deviates from the Strouhal law at the lock-in velocities range, however, abrupt deviation of the shedding frequency could be seen in Fig. 37 before approaching the coincided point ( $f_{sy} / f_{nwy} = 1$ ). Furthermore, as the frequency response approaches the lock-in, there does not appear to be any dramatic change at the peak response of the upper branch. This confirms the constant monotonic

behavior for the transverse response observed of the upper branch for the subcritical mass ratio cylinders [100].

Even when reaching the synchronization point for the  $110^\circ$  fin positioned model case at reduced velocity  $U_r \cong 5.37$ , the features did not show any distinct behavior and with no synchronization region. Figure 39 presents power spectral density (PSD) distributions of transverse velocity components measured at the cylinders' mid-height downstream locations of  $x/D = 5$ . For this cylinder, the corresponding oscillating frequency was obtained from accelerometer measurements. These distributions indicated that a clear and strong coupling synchronization occurred between fluid and structure. As seen, with an increase of the reduced velocity, the peak amplitude of these distributions become larger, and the frequency approaches the cylinder's natural frequency in the water of ( $f_{nwy} = 11.7$ ).

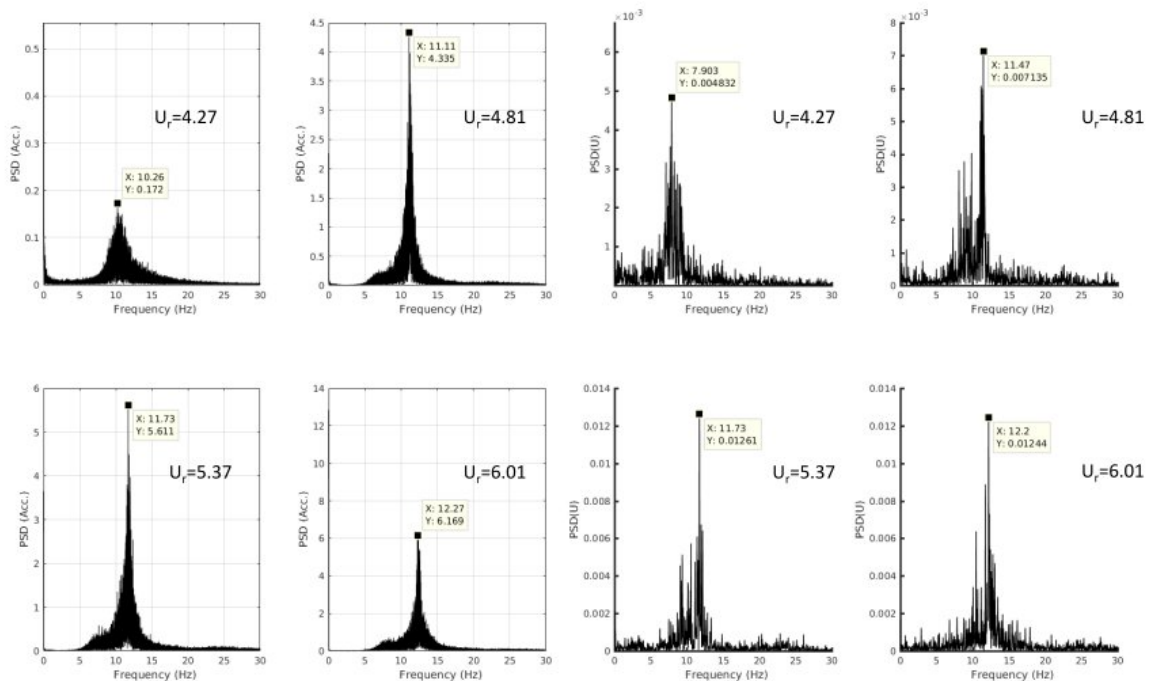


**Figure 39** Comparative power spectral density distributions of lateral acceleration (left) and the lateral velocity of the wake behind the cylinder (right) fitted with  $110^\circ$  fin plates of  $x/D = 5$  and  $y/D = 0$

The data suggest that when the fluid flows past the cylinder attached with fin plates at these specific locations and when the cylinder started to oscillate, the fins broke up the flow and generate vortices at different locations along the cylinders' lengths. These vortices might have been out of phase with one another and, due to a partial cancellation of the out-of-phase lift forces at the different spanwise positions, the lift coefficient for the finned cylinders decreased to values below those for the smooth cylinder. very similar, with the strakes effect on the wake vortices reduction in correlation in previous literature reported data [55]. Further investigations using a DPIV system would have been necessary to examine this aspect. Unfortunately, such a facility was unavailable.

The median and distribution of the data can be determined by a histogram. To demonstrate this, creating a Density histogram has been used to provide a visual representation of data distribution. It is well known that Histograms can display a large amount of data and the frequency of the data values. Histograms provide a visual interpretation of numerical data



The graphs in Fig. 40 depict the limits of these classes, here the maximum normalized responses, and their heights were calculated by dividing the relative frequency by the class width. The resulting heights are called densities; the vertical scale is called the density scale [107]. The sample time series shown in Fig. 40 illustrates that the presence of the fins caused a remarkable reduction of the cylinders' response. Besides, the drop in the r.m.s. amplitudes also reduced the range of maximum oscillations, an aspect of considerable practical significance in that a large oscillation itself may damage a structure rather than fatigue-related synchronization frequencies. These features are common, especially for the light cylindrical structures with mass ratios below the critical mass ratio. This happened with our smooth cylinder as it was too light to withstand the fatigue stresses and, consequently, it was damaged

Figure 41 presented the crack area that occurred with the plain cylinder model at a reduced velocity of about  $U_r \cong 4.81$  due to the fatigue stresses caused by the high range of oscillating displacement before the onset of the synchronization frequencies. Further studies are needed to figure out the correlated changes in vortex modes trying to figure out the feature and improve the reduction percentage. Also, illustrating these attached fin plates with a flexible 2DOF cylinder with a mass ratio above the critical is expected to have an intensive effect in suppressing VIV as well as observed in the present work for cylinder below the critical mass ratio. Varying geometric parameters could be a way for more enhancement studies. One of the simple ways of enhancement is by shaping the free end tip corner smoothly as has been illustrated by Park and Lee 2004 [108]. Additional investigations would have been required to confirm and validate these effects also for flows at higher Reynolds numbers.

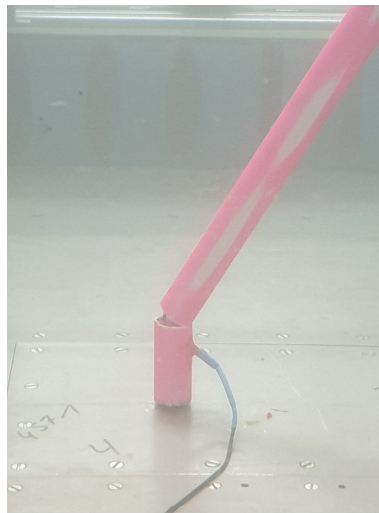


**Figure 41** Structural fatigue damage of the smooth cylinder



## 5.2 Wind Tunnel Tests Results

Researchers are seeking a combined parameter, like Skop and Griffin parameter  $S_G$  or  $m^*\zeta$ , as a universal parameter to couple the effects of both mass and damping on the dynamic response of the cylinder in the VIV problem. Griffin et al. attempted to expand the application of the mass-damping parameter to the prediction of the maximum response amplitude of a wide variety of flexible structures. The Griffin plots showed general trends of agreement between maximum response amplitude and Scruton number but there was lots of scattering to the data. In Figure 42, the data points are overlaid by an empirical curve of Skop & Griffin [10], indicating that this data agreed favorably with past results, deviating by a mere 3.6%. The results are plotted as continuous light lines.

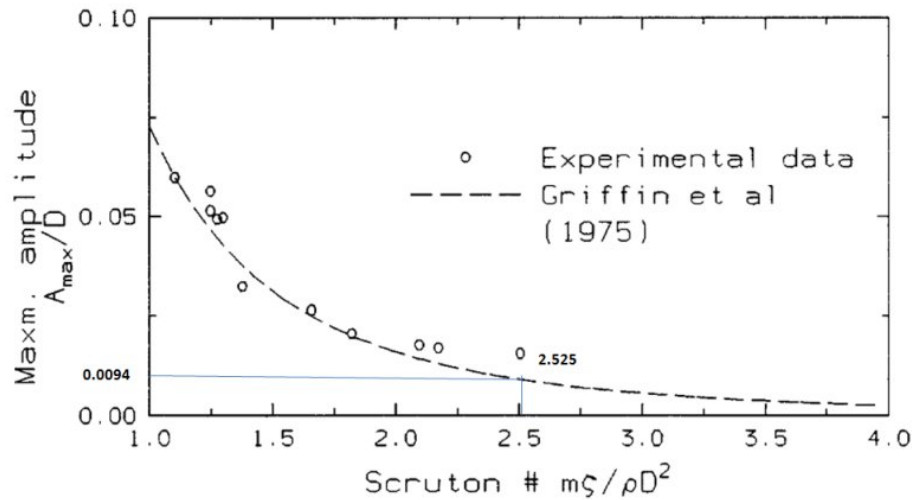
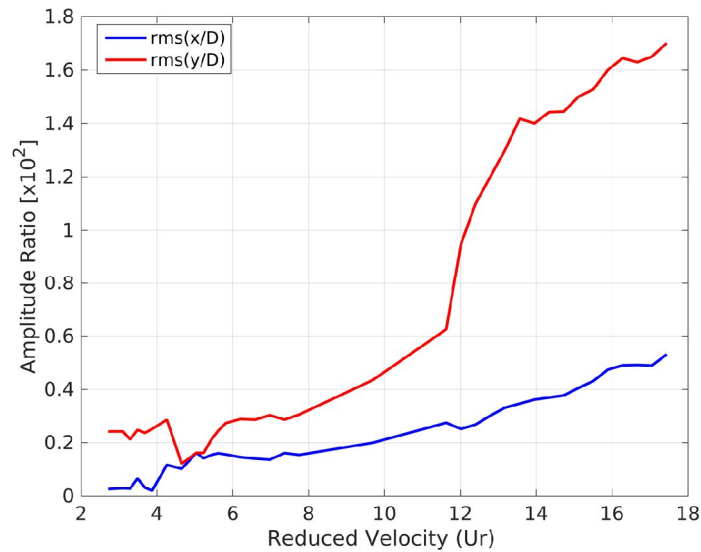


Figure 42 Normalized maximum amplitude vs. Scruton number [111]

### *Amplitude response*

Figure 43 plots measured r.m.s values of motion amplitudes (normalized against  $D$ ) at the top end of the test cylinder in a streamline and transverse directions to the flow against the reduced velocity,  $U_r$ . Root means squares displacement at cylinder top,  $Y_{rms}$ , increased as the reduced velocity increased. However, there is a distinct peak in the  $Y_{rms}$  distribution, which is consistent with the synchronization behavior discussed below. The measurements agreed favorably with the resulting transverse response and with the response of So et. al. [112]. The peak amplitude of the VIV occurred at  $U_r = 4.20$ . Thereafter, the amplitude of the VIV decreased significantly until  $U_r = 4.65$  and then started increasing again until reaching the highest velocity available in this test. On the other hand, the peak in this test was larger than the one obtained by So et al. [22], and this was caused by the higher Reynolds numbers.



**Figure 43** *r.m.s. Values of normalized streamline (x) and lateral (y) top-end motion amplitudes Vs. reduced velocity ( $U_r$ )*

It is clear that the free end had a great influence on the VIV. Although the amplitude of end-cell-induced vibration (ECIV) was unsteady, the VIV remained nearly steady. This was indicated in the time histories at lower values of  $U_r$  as seen in Fig. 44. The amplitude of the model's response due to the ECIV that occurred at a high wind speed was not influenced although the critical damping ratio of the model was higher, whereas the amplitude of the ordinary vortex-induced vibration decreased significantly [113]. It seemed that the increase of the displacement amplitude after the peak occurred was due to the tip vortex, as it was not affected by the high damping ratio of the model

Furthermore, the peak due to ECIV, occurring at a wind speed higher than the ordinary vortex shedding speed, was two times greater than reported by Wootton and 2.9 times greater than reported by Kitagawa et. al. [114]. This could have been due to the higher Reynolds number in these experiments. The ECIV would have occurred at four times higher velocity. For the inline motion at  $U_r = 4.60$ , the amplitudes of the vibrations in the streamline and transverse directions were nearly equal. The streamline amplitudes became larger as  $U_r$  increased and, due to the mean drag force effect, quadratic polynomials approximated their functional relationship quite well.

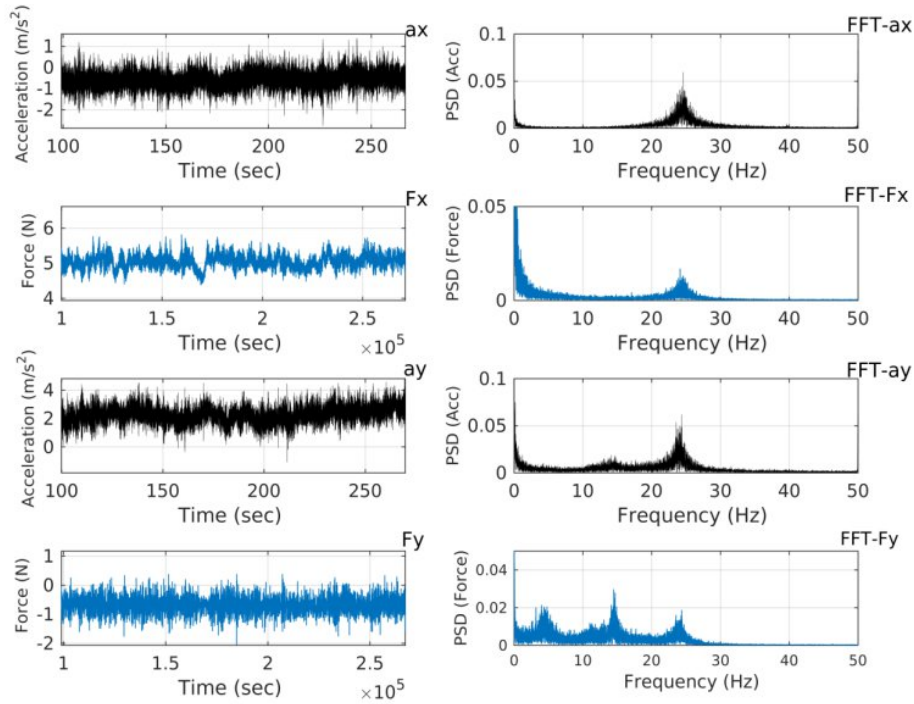


**Figure 44** Time series and frequency plots of inline (X) and transverse (Y) accelerations and forces at a flow velocity of 9.00 m/s

### **Behavior of forces**

The relationships between the reduced wind speed velocity,  $U_r$ , and the transverse force (lift) and the streamline force (drag) are shown in Fig. 45a. Drag forces were related to the drag coefficient as shown in Fig. 45b. The drag coefficient increased by about 30% throughout the range tested although it did not dramatically depend on the Reynolds number. The drag force coefficient, obtained from r.m.s. force values, was consistent with [115], but it decreased to a value of about 0.05 because the surface of the commercial pipes used was smooth. In the subcritical region, the lift force plotted in Fig. 45 increased at higher velocities until near the end of the region. At  $U_r = 15.89$  (Reynolds number =  $2.975 \times 10^5$ ) it began to decrease. As the minimum wake width occurred when the Reynolds number was  $3 \times 10^5$ , it seemed probable that the bubbles separating from the cylinder's surface became unstable and asymmetrical, leading to an angled wake. As with the two-dimensional cylinder, alternating vortex shedding, associated with fluctuating pressures acting on the surface of the cylinder, was responsible for the fluctuating lift force coefficients. The aerodynamic lift coefficients were sensitive to several influences, principally Reynolds number, surface roughness, turbulence scale and intensity, end conditions, and the aspect ratio of the structure. For such a large number of parameters, most experiments dealing with the behavior of lift concentrated on varying only one or two parameters.

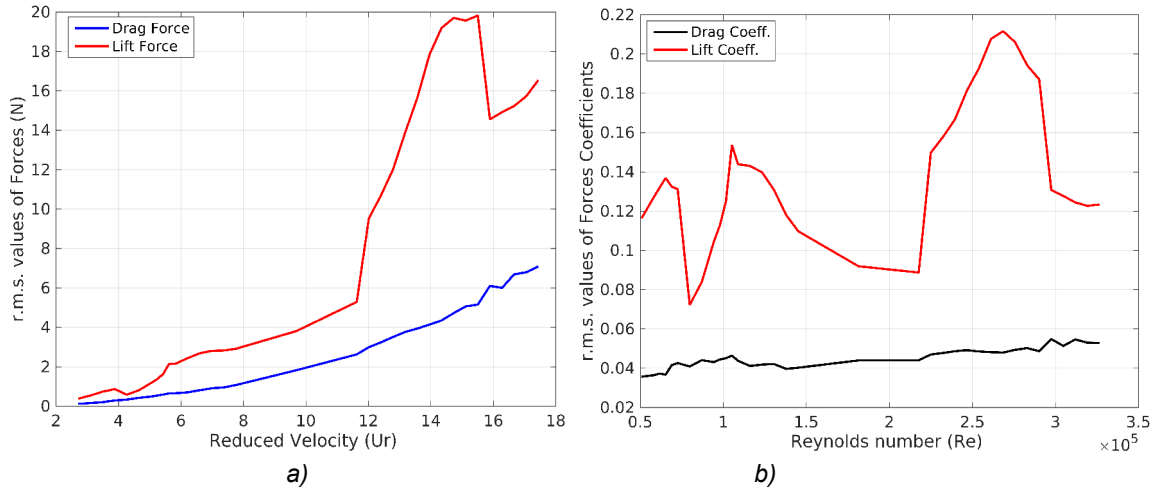


**Figure 45** r.m.s. Values of drag force ( $F_x$ ) and transverse force ( $F_y$ ) (a), and of lift and drag coefficients (b) VS. reduced velocity ( $U_r$ )

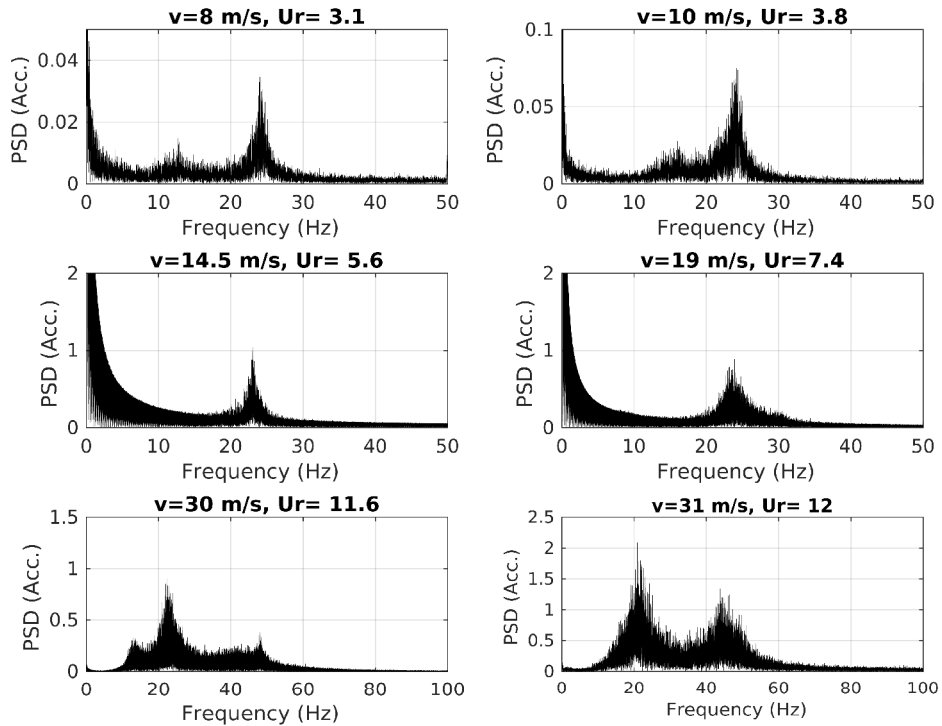
Norberg [116] highlighted his investigations of lift acting on a stationary circular cylinder and presented experimentally obtained lift coefficients at Reynolds numbers ranging from 47 to  $2 \times 10^5$ . He discussed the investigations concerning fluctuating lift and the effect of Reynolds numbers. He found that at higher Reynolds numbers the pressure distribution around the cylinder surface increases. He justified this dramatic flow variation with the appearance of more than one peak occurring near flow separation angles because the shear layer changes and suction peaks appear due to vibration effects. Additionally, investigations of three-dimensional effects are hampered by the relative lack of comparative data. Park & Lee [117] examined circular cylinders with aspect ratios of 6, 10, and 13 at a Reynolds number of  $2 \times 10^4$ . They reported that as the flow approaches the cylinder tip, it accelerates upward and separates from the leading edge of the free end. They detected also a dominant 24Hz signal, which remains constant with aspect ratio. They reported that the increasing pressure away from the tip is due to the decreasing influence of downwash and the dominant vortex shedding from the cylinder sides.

In the present study, the first peak in the lift coefficient diagram identified the tip vortex. It differed from the dominant frequencies at the upper and lower part of the cylinder as shown in Fig. 44. The other peaks were associated with the changing correlation length of the near wake shedding process, which indicated a phase change as illustrated below. The last peak fluctuating point seemed to be due to the beginning of the unstable separation bubbles at the end of the subcritical region.

Khalak & Williamson [25] demonstrated the effect of free end conditions on vortex shedding at Reynolds numbers between 1000 and 20000 by comparing the case of parallel shed vortices and the case of obliquely shed vortices. They also illustrated the characteristics of the shedded forces and their frequencies. Contrary to their experimental results, the lift coefficient is well approximated by a quadratic polynomial function, unlike their obliquely shed vortices case. These results confirmed that the increasing Reynolds number and the changing mass ratio affect the lift coefficient because it depends on Reynolds number and vibratory effects. The same discrepancy occurred for the drag coefficient. The increasing drag occurred in the obliquely shed vortices case, under a condition similar to these experiments, but not in the parallel shed vortices case. At higher Reynolds numbers, the drag coefficient increases by about 55%. With increasing Reynolds number, it seems that in the obliquely shed vortices case characteristics become more pronounced than in the parallel shed vortices case. This suggests that the Reynolds number has a strong effect.

### *Oscillating frequency response*

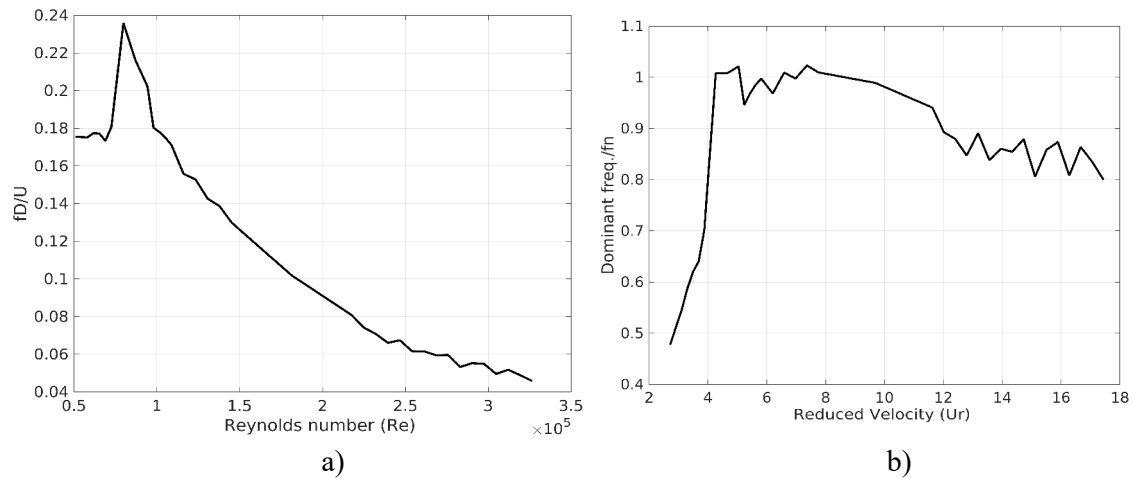
The cylinder frequency was measured directly from two separate sensors attached to the cylinder at its top and bottom. Figures 44 and 46 show data samples of FFT frequency plots that we used to analyze the frequency content of the measured time series. The acceleration frequencies had stronger peaks than the force frequencies. Similar to [118], various frequencies appeared for the transverse direction, whereas in the streamline direction, only one dominant frequency appeared as VIV excited higher harmonic motions. Frequency content in the transverse direction changed from one to two and three components, depending on the velocity, and the curve shape changed as one response component was converted to the other component. At lower velocities ranging from  $U = 5.0$  to  $8.5\text{m/s}$  ( $U_r = 1.94$  to  $3.29$ ), the frequency content consisted of two components. At  $U = 5.0\text{m/s}$ , the second frequency was 2.7 times higher than the first frequency, and, at  $U = 8.5\text{m/s}$ , it decreased until it reached the value of 1.7 for the first frequency, accompanied by a drop of response amplitude. The response amplitude ratio started to increase again at  $U = 9\text{m/s}$  until reaching its peak at  $U = 11\text{m/s}$  ( $U_r = 4.2$ ) at which the frequency ratio (dominant oscillating frequency/natural frequency) equaled 1.008. The dominant frequencies of the lift force spectra, which had the largest peaks, were normalized against flow velocity and cylinder diameter,  $D$ , to neglect the dependency of Reynolds number and facilitate comparing these measurements with those of Khalak and Williamson [115].



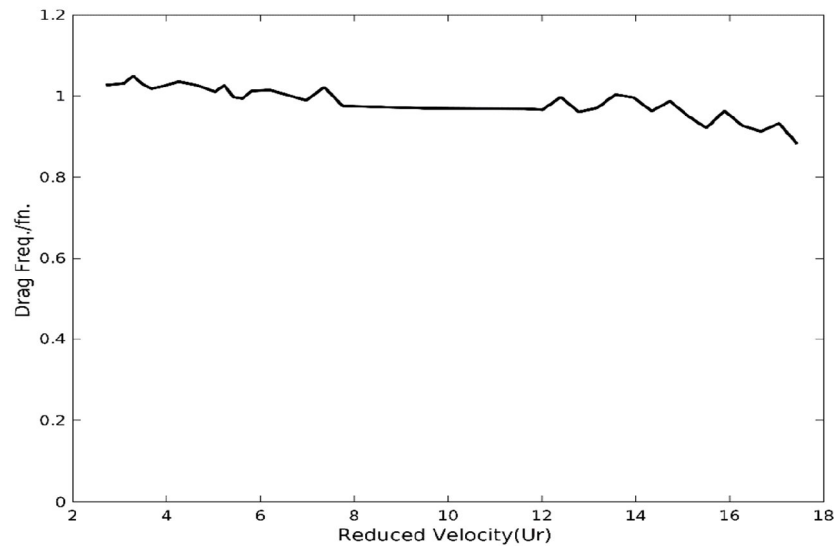
**Figure 46** Power spectral densities (PSD) of transverse accelerations at the bottom-end of the cylinder

These results emphasized again the complicated nature of the obliquely shedding vortices, ECIV, at increasing Reynolds numbers. The associated frequencies reflected the presence of cellular vortex shedding. As seen in Fig. 47a, at the Reynolds number of  $7.982 \times 10^4$  ( $U_r = 4.2$ ), a distinct peak characterizes the normalized frequency response, which rapidly decreases as the

Reynolds number increases. Similar characteristics were seen when comparing the frequency change at increased values of the reduced velocity,  $U_r$ , with those of [112]. These results exhibited a marked agreement of similar response characteristics although the decrease started after the first increase and the jump occurred at synchronization. As  $U_r$  increased, there was generally a decrease in the oscillating frequency, indicating also the effect of cylinder vibrations on vortex shedding and its associated frequency. Figure 47b plots the frequency ratio (dominant frequency of the cylinder obtained from lift force spectra/cylinder natural frequency) against the reduced velocity,  $U_r$ . These characteristics were thought to be due to two effects. First, cylinder vibrations and fluid forces converged to create higher harmonic excitations. Wang et al. [119] analytically demonstrated the occurrence of nonlinear (higher-order) force components, even for a case of relatively weak fluid-structure interaction.



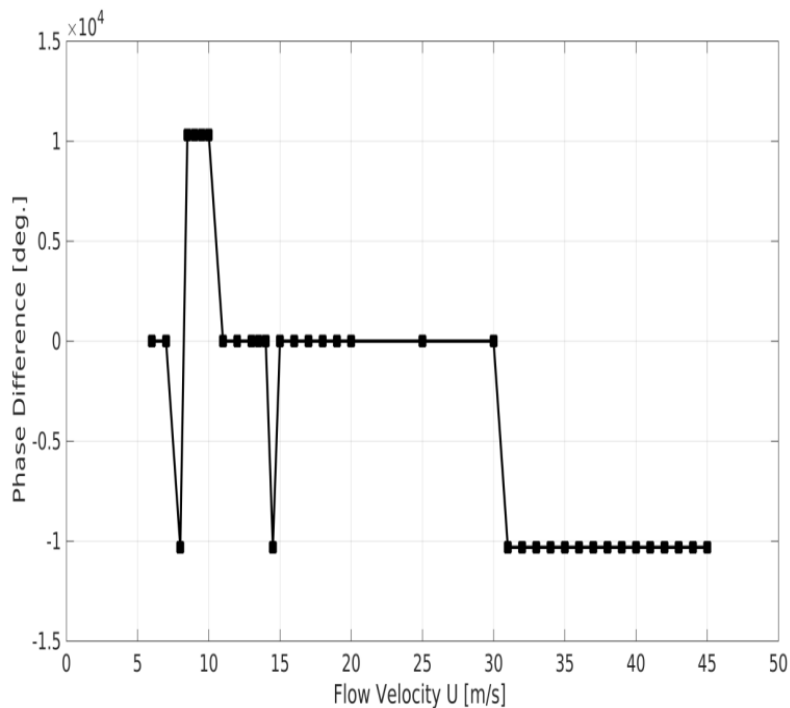
**Figure 47** Dominant frequencies from lift spectra, nondimensionalized by flow speed,  $U$ , and diameter,  $D$ , Vs. Reynolds number (a) and dominant frequency ratio obtained from lift force spectra Vs. reduced velocity (b)



**Figure 48** Drag force frequencies from drag force spectra Vs. reduced velocity

They proved that the free vibration of an elastic cylinder introduces a third and higher harmonic to the transverse fluid force, followed by the displacement response. Second, strong nonlinearities of aerodynamic forces induced the intermittent generation of the tip-associated vortices. This counter-intuitive behavior was related to the change of drag frequency ratio (drag frequency/natural frequency) with velocity. As shown in Fig. 48, the drag frequency seemed to be constant and coincided with the natural frequency. Recall that Alfred & Karancheti [30] investigated the same range of frequency components for descending counter-rotating swirling vortices from the free end of a finite cylinder at Reynolds numbers ranging from  $0.85 \times 10^5$  to  $7.70 \times 10^5$  [101]. Park & Lee [117] also found the same 24Hz frequency characteristics generated at the free end of a finite cylinder at a Reynolds number of 20000. Such a prediction of the tip vortex frequency could not be detached from the measured value of the natural frequency of the model (23.4Hz), which seemed to have occurred coincidentally. This coincidence prevented the streamline frequency to attain a value of twice the transverse frequency causing the VIV characteristics to disappear. However, detailed flow information would have been required to support this hypothesis.

It was of interest to investigate the manner of the vibrating cantilever transitions from one mode of response to another. To provide evidence for mode changes, we had to rely on other than response data. In some cases, the phase of motions and in other cases the phase of fluid forces was an excellent indicator to evaluate these transitions [90]. An important feature of the dynamics of such an elastically mounted cylinder was the jump-in phase,  $\theta$ , between the transverse force and the cylinder displacement, which occurred when the response changed modes.



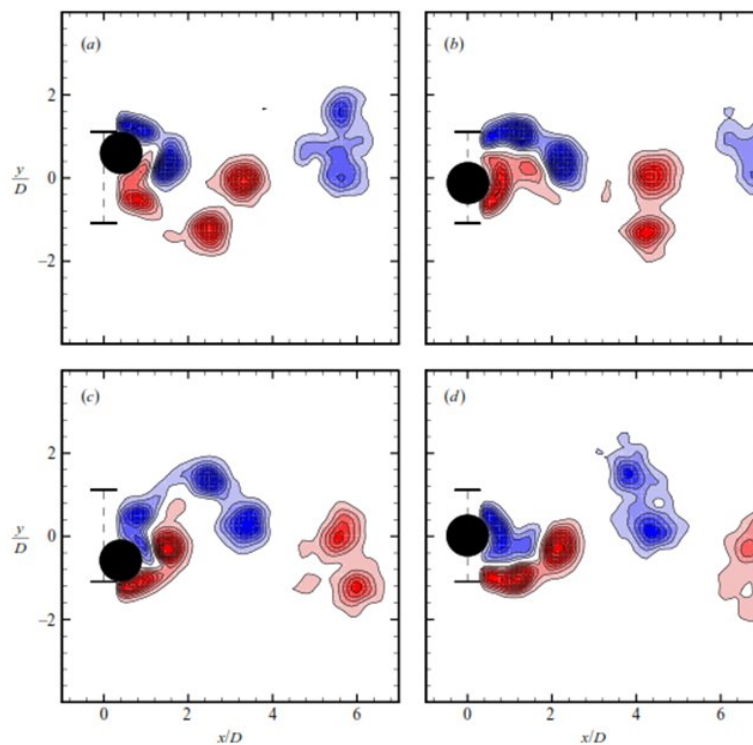
**Figure 49** Phase angle between the transverse force and transverse motion of the cylinder Vs. flow velocity

Figure 49 shows the phase between the transverse force and the transverse cylinder displacement. Of interest was, contrary to Hubert [32], that the phase change occurred suddenly in a distinct manner at many points during synchronization. As velocity increased, the phase

angle between the force exerted on the cylinder by the fluid and its displacement showed a discontinuous jump. This should have been caused by the sudden 180 deg. a phase angle change of vortex shedding [120]. Similar graphs of the phase angle between the streamline and the transverse motion of the cylinder as a function of the reduced velocity,  $U_r$ , and the phase angle,  $\theta$ , of the aerodynamic forces. Hubert [32] investigated the VIV of long flexible cylinders in a water tunnel and found that, in the synchronization range, a phase angle change of about 180deg occurs gradually [121]. To illustrate these changes, we attempted to visualize the vortex modes in each region. Unfortunately, at higher speeds, these attempts failed.

### *Modes of Vortex Formation*

Many vortex formation modes correspond to response branches associated with vortex-induced vibrations. The well-known vortex wake modes comprise the 2S mode, consisting of two single vortices per cycle, and the 2P mode, consisting of two vortex pairs of vortices per cycle. These two modes are common for one and two-degree-of-freedom cylinders. Jauvtis & Williamson [8] investigated the so-called super upper branch mode. The vortex formations corresponded to the 2T mode. They consisted of a triplet of vortices formed per half-cycle. For the lightest bodies, the larger transverse amplitude was found to correspond to a new vortex formation mode defined as the 2C mode, which consisted of two co-rotating vortices per half cycle. Figure 50 visualizes the formation of such a 2C mode during a single cycle.



**Figure 50** Evaluation of the 2C mode in time during one cycle of the tested pivoted cylinder [122]



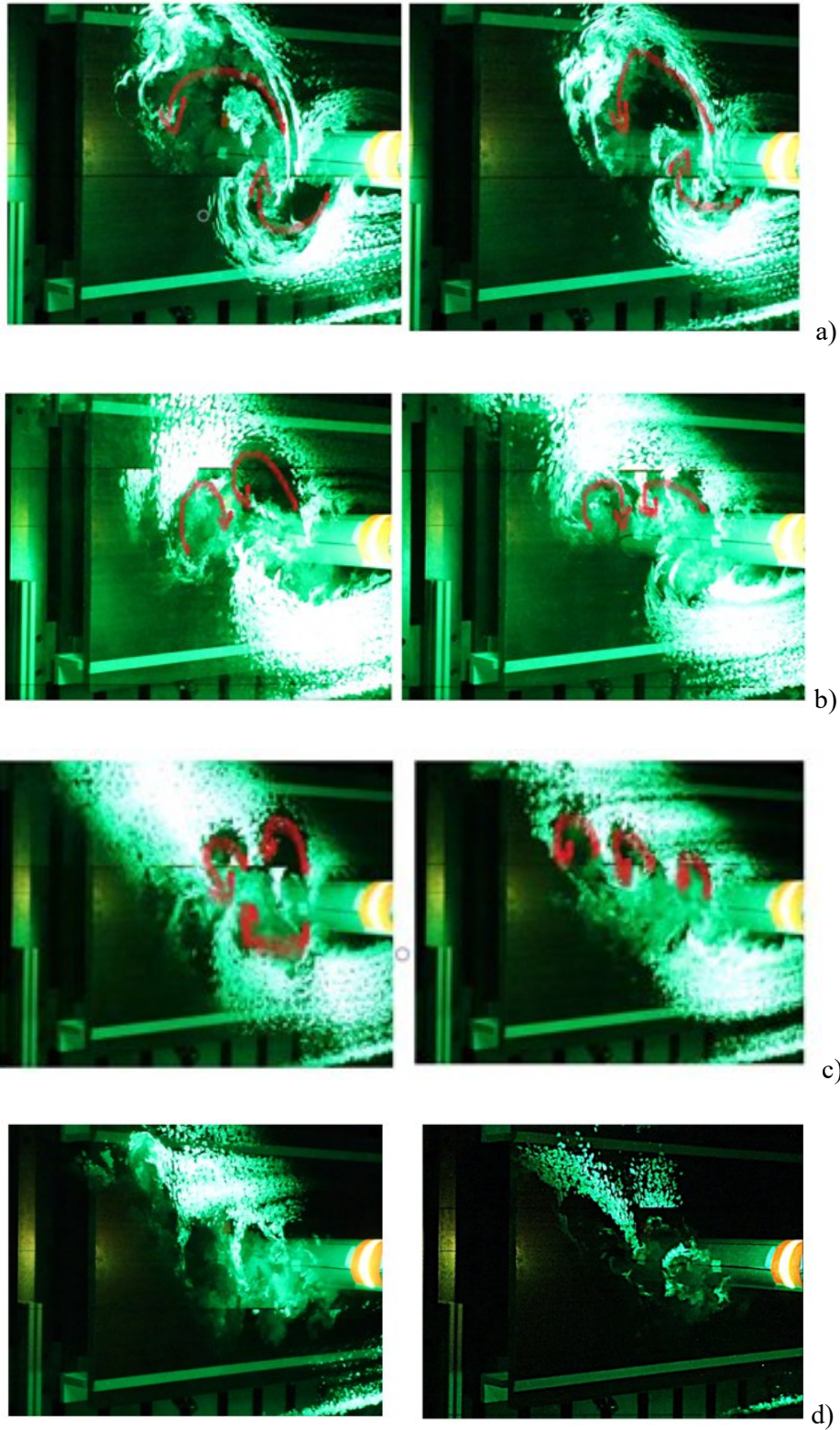


**Figure 51** Visualizations of a variety of vortex formation patterns observed in the wake of the tested cylinder at flow velocities of 5 m/s (a), 10 m/s (b), 17m/S (c), 19 m/s (d), and 25m/s (e)

The formation of such patterns depended on various parameters, such as Reynolds number, cylinder motions, and accelerations, phase angles, etc., that were functionally related to each

other. To visualize the vortex patterns, the smoke wire flow visualization technique is used. A constantan wire, made of copper-nickel alloy, produced dense smoke from burning oil and introduced smoke lines into the flow. Using a cylindrical lens, a beam from an ND-YAG laser source of continuous power output produced pulses of 532nm wavelength. Screenshots were obtained from a Canon EOS 80D digital camera with a resolution of 1600x1200 pixels and a frame rate of 50Hz. Oriented appropriately, it captured the smoke lines at the beginning mode of a vortex formation pattern. Here, the laser sheet illuminated the x-y plane at the midspan of the cylinder ( $z/L = 0.5$ ) to avoid the influence of the free end.

Figure 51 shows flow patterns obtained at different flow velocities. Each velocity corresponded to a different phase region. As shown, each pattern provided evidence for mode changes. At a velocity of 5m/s, the pattern seems to be a 2S vortex mode, while at 10 m/s, it seems to be a 2P vortex mode. The 2C vortex modes are formed at velocities of 17, 19, and 25m/s as they occurred in the same phase region. The 2C vortex modes were not observed before in aerodynamics tests, because the mass ratios were higher than unity. There appeared to be no obvious explanation for the existence of such a pattern, confirming that further investigations would have been necessary. Unfortunately, facilities were unavailable to examine this aspect.

## 5.2.2 Summary and discussion

There is an integrated effect of several parameters combined in the present work, that would have a great influence on the VIV characteristics. Among them, higher mass-damping ratio, higher  $Re$ , and Intermediate aspect ratio which increases the effect of the tip vortex. As mentioned, The VIV phenomena are characterized by the higher amplitude of oscillation, range of synchronization, and oscillation frequency. If the cylinder vibrates at, or near, its structural natural frequencies, then the vibration is initially limited only by the cylinder damping. However, at the moment the amplitude reaches about 1 to 1.5 times the cylinder diameter, the boundary layers are altered enough by the cylinder motion and the vibration becomes self-limiting. If the cylinder does not vibrate at, or near, its structural natural frequencies, then the vibration is a forced vibration and is typically limited to about 0.1-0.2 times the cylinder outside diameter. This was the case in the present work. Thus, because the lift forces were not sufficient to produce larger motions than this. This also might be the reason for decreasing the range of synchronization which seems to be a distinct point. Furthermore, The higher  $Re$  may be the reason for shifting the start of synchronization range to  $U_r = 4.2$  instead of 5. The same effect was found as damping increased by Klamo et al. [43].

In addition, the drag coefficient showed significantly lower values. It is worth noting that the drag coefficient is strongly coupled to displacement, with the smoothest cylinder having the lowest drag. D. W. Allen and D. L. Henning reported that if the cylinder's surface roughness is sufficiently smooth the VIV all but disappears and the drag coefficients are very low [123]. However, their experiments were conducted at the critical and supercritical Reynolds number range. It might be one of the tested parameters that could result in shifting of these features to lower  $Re$ .

One other area of importance is the vibration response frequencies. Of particular significance is axial frequency behavior which seems to be almost constant and coincides with the natural frequency. One could relate this frequency to the tip vortex frequency as it has been seen to have the same value in some previous works of literature as discussed in chapter 2. Besides, Due to additional vortex formation patterns appear depending on the particular cylinder motion and behavior. This could explain some differences being seen in Fig. 45. There have been few studies that have measured the wake velocity field downstream of the cylinder tip.

Further tests with special tools and simulations are needed to investigate the tip vortex frequency and determine its' contributions to VIV especially for this range of aspect ratios and Reynolds numbers.

## 6. Numerical Simulations and Results

As mentioned in the past chapter, numerical simulation is a useful tool to study VIV because it provided a simultaneous vision of the wake patterns, fluid forces, and body responses, which allowed for a coupled analysis of the flow-structure system. However, the numerical simulation of VIV in conditions close to those encountered in nature or in the experimental works remains challenging. Recent studies have shown that with the improvement of numerical methods and the development of computational resources, the investigation of VIV in the turbulent regime via numerical simulation becomes possible [139]. Several approaches have been employed in the field of CFD to study the flow past a cylinder problem. The knowledge and experience found in the literature show that the simulation of flows at high Reynolds number problem in all of its length and time scales would only be completely achieved using direct numerical simulation. However, it requires massive computational resources for a consistent (i.e., time and grid-independent) simulation for high Reynolds numbers and thus stands as a tool used mainly for more fundamental research rather than for engineering applications. This explains why most of the numerical works concerning VIV have been dedicated to low Reynolds number configurations. The numerical study and physical analysis of the pressure and velocity fields in the near wake of a circular cylinder have been investigated by Braza et al [140]. Coutanceau and Defaye have investigated this problem for different Reynolds numbers [141]. The turbulent flow over the cylinder was also investigated by Rai & Moin for high Reynolds number [142].

All of the above numerical studies have solved the unsteady Navier-Stokes Equation in two dimensional. They described the relevant flow by the global parameters such as the Strouhal number as a main feature of the unsteady wake, drag, and lift coefficients in the wall region; nevertheless, poor analysis is provided for the near wake characteristics.

Nowadays it is known that unsteady Reynolds Averaged Navier–Stokes (RANS) models fail to predict proper flow physics in many cases. A step towards the attempts to simplify the numerical approaches, one is naturally led to the large-eddy simulations, which represents a less computational effort at the cost of introducing some modeling in the sub-grid scales. Nevertheless, a full and correct (without near-wall modeling) LES for high Reynolds numbers is still unfeasible due to the approximately same computer requirements as DNS. The detached eddy simulations DES, based on the Spalart-Allmaras one equation turbulence model [132], is a hybrid RANS/LES approach that operates like RANS in the near-wall regions and like LES in separated flow zones. It is particularly attractive because it achieves good results in several conditions with fewer computational resources than standard LES. The performance of DES for a given grid may be less accurate than the performance of DES on a coarser grid. This is because the concept of grid spacing for DES is an ambiguous and crucial requirement of grid spacing, which must be taken into account [143]. However DES & LES have a demand for much greater computer power than RANS methods, they are computing fluctuation quantities resolve shorter length scales than RANS models [104].

As mentioned above, many factors such as Reynolds number, length of the plate, frequency, and amplitude can affect the flow pattern. Recently, a vast amount of studies has been conducted to increase the understanding of different VIV features of the flow past a circular cylinder experimentally, numerically, and theoretically. By contrast, there are very few similar studies found for demonstrating the various method for suppressing. Especially, there is rarely numerical investigation represented the effects and flow features for different suppressing tools, for example, M. Springer et al. [144]. Besides, Ranjith et. al. presented a numerical investigation of the flow around a circular cylinder with and without the helical strakes at

Reynolds numbers 100&28000 has been presented. It is found that at low Reynolds number flows, since the boundary layer thickness is high, the same helical strake of 0.15d in height is not given the same effectiveness in reducing the vortex shedding. A maximum of 19% reduction is possible at Low Reynolds numbers [55]. However, Computational Fluid Dynamics (CFD) has gained momentum and its value in cost-effectiveness could include CFD results enabling the design of smaller and lighter equipment or enabling simpler and cheaper examinations before practical installations.

In the first part of this chapter, Computational Fluid Dynamic (CFD) analysis is performed for a fixed-cylinder case, at Reynolds number  $Re = 7000$ , where different mesh qualities and two different turbulence models have been evaluated. Unsteady Reynolds-averaged Navier–Stokes (URANS) simulations and detached-eddy simulations (DES) were performed of flow around a circular cylinder. The results were compared with experimental results [115]. Secondly, newly developed various fin configurations attached to the plain cylinder surface have been employed to investigate numerically the flow characteristics behind a stationary circular cylinder and illustrate their effect on suppressing VIV. For comparing the various attached structure features, the only focus was on the turbulent flow, thus, the Reynolds number was fixed at  $Re = 5.3 \times 10^3$ . Finally, a new turbulent FSI validation test case is defined based on detailed measurements and the experimental results for the smooth cylinder (chapter 5.1) have been used to validate.

## 6.1 Turbulence Model Assessment

### 6.1.1 Computational domain

The numerical computational domain was defined by a rectangular box. Table 7 lists the dimensions and Fig. 52 presents a top view of the computational domain surrounding the cylinder. The arrows at the left (inlet) side of the domain indicate the flow direction. The inlet boundary was located five-cylinder diameters away from the cylinder axis [145]. The origin of the cartesian coordinate system was located at the center of the top end of the cylinder. Similar to the experiments of Khalak and Williamson [115], a small gap of 0.04D existed underneath the bottom of the cylinder.

**Table 7 Domain and cylinder dimensions**

<b>Geometric parameter</b>	<b>Symbol</b>	<b>Value [m]</b>
<b>Domain length</b>	$L_D$	2.5
<b>Domain width</b>	$W$	0.41
<b>Cylinder diameter</b>	$D$	0.0381
<b>Cylinder length</b>	$L$	0.3810
<b>Domain depth</b>	$H$	0.3830

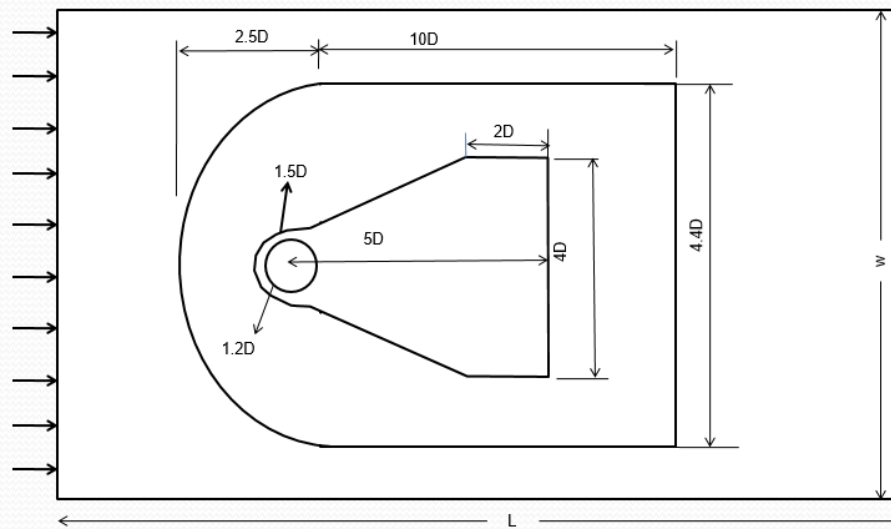


**Figure 52** Top view of the computational domain

## 6.1.2 Grids and boundary conditions

To quantify the dependence of the numerical results on mesh density, numerical simulations on three different grids characterized by successively finer meshes were performed. Mesh 1 described the coarsest grid; mesh 2, the medium grid; mesh 3, the finest grid, and mesh 4, the superfine grid. Table 5 lists the number of cells, the grid spacing  $\Delta x$  in the flow direction, and the time step size  $\Delta t$  of these four grids, and Fig. 53 exemplarily depicts top and side views of the medium grid (mesh 2). and side views of the medium grid (mesh 2). The top graph in this figure includes a zoom-in view of the prism layer surrounding the cylinder, with a total of 120 grid nodes situated along its circumference. As seen in Fig. 53, four refined grid blocks surrounded the cylinder and its wake region to adequately capture high-velocity gradients near the cylinder's surface. Based on previous studies [146], [49], configurations and dimensions of these grid blocks, see Fig. 52, were selected to optimally identify the evolution of vortex structures behind the cylinder. Nonetheless, to improve the computational efficiency, a coarser mesh was specified in regions far away from the cylinder.

The inflow boundary condition represented a uniform velocity profile equal to the free stream velocity. The outflow boundary required more care because it would have been incorrect to specify velocities occurring infinitely far away from the cylinder at the outlet boundary. Therefore, the gradients of the outflow velocity in the streamwise direction were set to zero, and the pressures were assigned a reference value of zero. The outlet was located at the right boundary. On the top and bottom boundaries, a slip condition was assumed; on the side boundaries, a non-slip condition. A non-slip boundary condition was assumed also on the cylinder surface. To improve temporal accuracy and to ensure numerical stability, the wall function's  $y^+$  value always equaled unity, and the Courant-Friedricks-Lewey (CFL) number never exceeded the value of 0.2.

The numerical simulations implemented the SIMPLE algorithm in code Starccm+ to enable utilizing second-order temporal discretizations. As an upwind scheme has limits when performing DES simulations [104], a hybrid second-order upwind/central scheme has been used, where the blending factor was computed to optimally account for the flow features. While the second-order upwind scheme has been used for the calculations using the SST  $k-\omega$  turbulence approach.

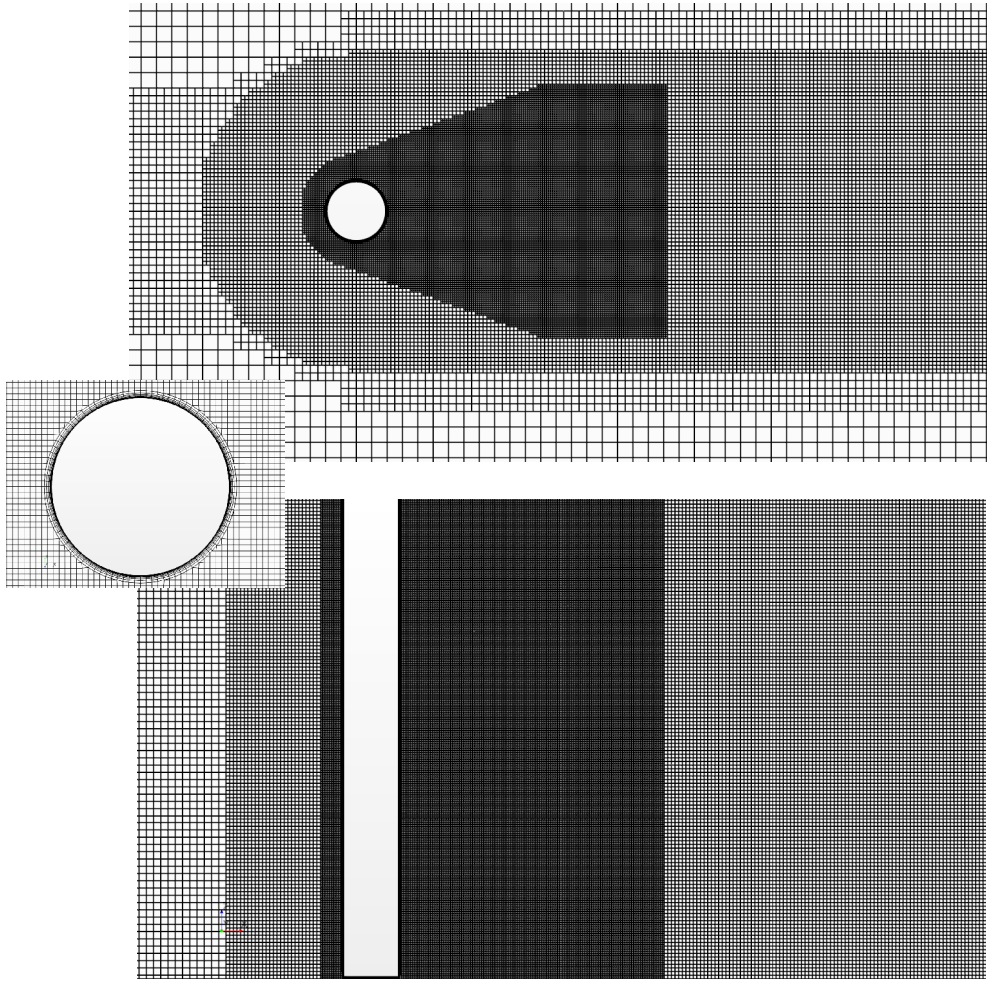


*Figure 53 Top view (top) and side view (bottom) of the computational mesh 2 on the medium grid*

### 6.1.3 Numerical verification and validation

For turbulent flows, it is expected that the major source of modeling error to be caused by the turbulence models. To systematically assess numerical errors, it should be distinguished between modeling errors  $\epsilon_M$ , discretization errors  $\epsilon_d$ , and iteration errors  $\epsilon_I$ . Hence, total computational error  $\epsilon_T$  was obtained from their sum:

$$\epsilon_T = \epsilon_M + \epsilon_I + \epsilon_d \quad (66)$$

Many practical problems of fluid dynamics are currently analyzed by numerical solution of the mathematical models by Computational Fluid Dynamics (CFD). It is no longer enough to produce a solution, this approach is called the “engineering approach”, but rather the credibility of the simulations must be established with the Verification and Validation “scientific approach” [145]. Due to unsteady flow simulations, the numerical results were sensitive to spatial and temporal discretization. According to ITTC guidelines, the total numerical error consists of contributions from incomplete iteration convergence  $\delta_I$ , numerical grid density  $\delta_G$ , time step

size  $\delta_T$ , and other parameters  $\delta_P$ . According to these guidelines, it was also recommended that studying for all input quantities systematically by keeping other parameters fixed [147]. Therefore, the contributions were assumed independent, corresponding to orthogonal dimensions constituting the space of uncertainty, which does not allow for interactions between uncertainty contributions. An alternative approach of Oberhagemann and el Moctar [148], especially suitable for transient problems, was used to estimate the discretization errors. The method required the same refinement factors to be applied to all dimensions and that spatial and temporal refinements be done simultaneously. It is considered a uniform refinement in all directions (space and time) that corresponded to a constant CFL number. The one dimensional CFL number, a reasonable measure for convection dominated flow, was expressed as follows:

$$r = \frac{\Delta x_{i+1}}{\Delta x_i} = \frac{\Delta t_{i+1}}{\Delta t_i} \Rightarrow CFL = u \frac{\Delta t}{\Delta x} = const \quad (67)$$

where  $\Delta x$  and  $\Delta t$  are the spatial and time-step sizes, respectively, the index  $i$  denotes the level of refinement,  $r$  is the refinement factor, and  $u$  is the fluid velocity. In this approach, contrary to Eça and Hoekstra [149], the coarsest grid (mesh 1) was the reference grid, and further grid refinements were made via the refinement factor. A non-dimensional scalar grid refinement ratio,  $Y$ , measured the relative grid resolution as follows:

$$Y_i = \sqrt{\frac{1}{3} \left[ \left( \frac{\Delta x_i}{\Delta x_1} \right)^2 + \left( \frac{\Delta y_i}{\Delta y_1} \right)^2 + \left( \frac{\Delta z_i}{\Delta z_1} \right)^2 \right]} \quad (68)$$

where  $\Delta x_1$ ,  $\Delta y_1$ , and  $\Delta z_1$  are arbitrarily chosen as reference grid spacings. Following this approach,  $Y_\infty = 0$  corresponds to a grid representing infinitely small grid spacing in all directions, which is associated with the grid-independent solution. Then, the discretization error was estimated as a function of  $\gamma$  via Taylor series expansion as follows:

$$\epsilon_d \approx \delta_D = \phi_i - \phi_0 = a_1 Y_i + a_2 Y_i^2 \quad (69)$$

where  $\phi$  is the sought after variable, and  $\phi_i$  is the result obtained on the grid with spacing  $\Delta x_i$ . For second-order approximations, a minimum of three grids was needed to determine the unknown coefficients  $\phi_0$ ,  $a_1$ , and  $a_2$ . Following the least-squares minimization approach of Eça and Hoekstra [149], it is first obtained the grid-independent solution,  $\phi_0$ , and then the following first and second order polynomial formulations of  $\delta_D$ :

$$S_1(\phi_0, a_1) = \sqrt{\sum_{i=1}^{n_g} (\phi_0 - (\phi_0 + a_1 Y_i))^2} \quad (70)$$

$$S_2(\phi_0, a_1, a_2) = \sqrt{\sum_{i=1}^{n_g} (\phi_i - (\phi_0 - (\phi_0 + a_1 Y_i + a_2 Y_i^2)))^2} \quad (71)$$

The order of convergence,  $p$ , was obtained from the solution as follows:

$$p = \frac{\ln\left(\frac{|\phi_3 - \phi_2|}{|\phi_2 - \phi_1|}\right)}{\ln(r)} \quad (72)$$

where  $\phi_1$  is the solution obtained on the grid with the finest mesh.

As of now, the unstructured grids are comprised mainly of hexahedral cells, and an automatic meshing strategy generated these grids. This technique did not allow systematic refinements in a strict sense, due to the unstructured grid point distributions. However, the grid node allocation



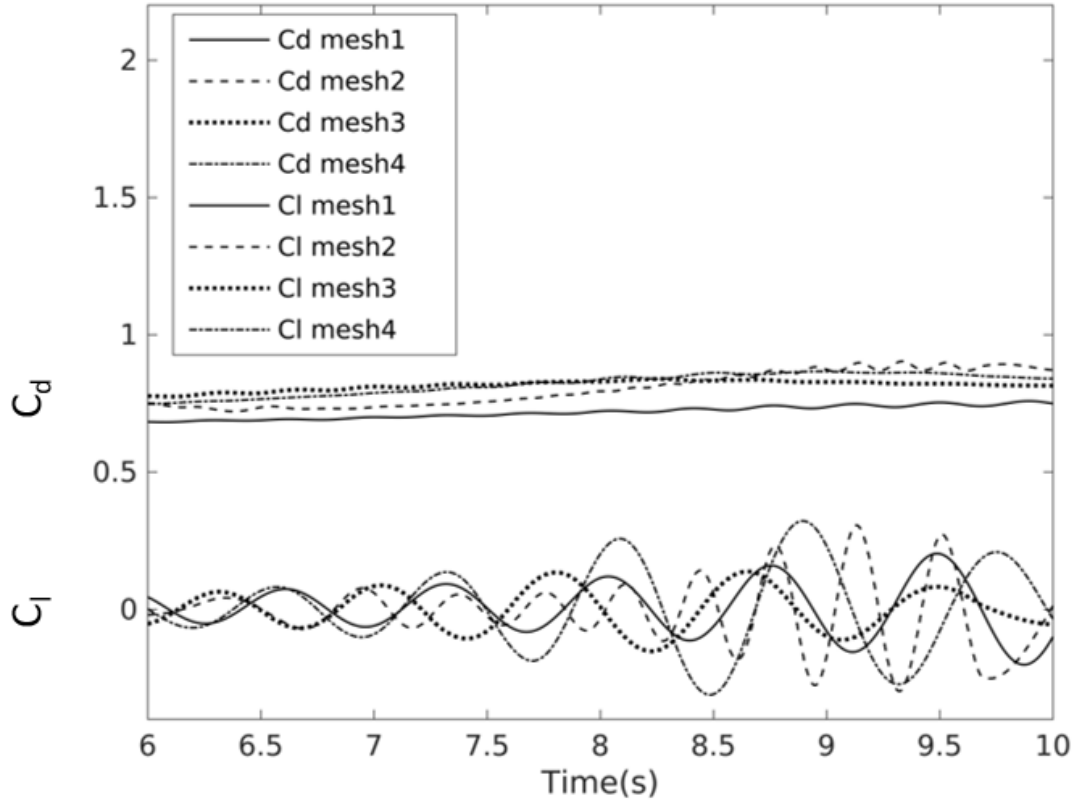
of the hexahedral cells followed the criterion of systematic refinement. The discretization error analysis was carried out with the SST  $k-\omega$  turbulence model; the refinement factor of  $r = \sqrt{2}$  was uniformly specified for all spatial directions and time steps. Generally, the uncertainty of integer quantities, such as the drag coefficient  $C_d$ , was smaller less than the uncertainty of local quantities.

Table 8 lists the solution's corresponding results in terms of r.m.s. values of drag coefficient  $C_d$ , Strouhal number  $S_t$ , and shedding frequency  $f_s$ , of the shed vortices. The fifth row in Table 7 lists the comparative values for the extrapolated grid-independent solution (Extrapol.), for which  $\Delta x = 0$ ; the sixth row, the comparative values of Khalak and Williamson [115]; and the last row, the percentage deviation (Error) of the values obtained on the medium grid (mesh 2) from the values of Khalak and Williamson. The drag and lift force coefficients were defined using equation 17. Where the drag and lift forces, in the (streamwise) x-direction and transverse y-direction respectively, are obtained by integrating pressures and shear stresses acting on the cylinder's surfaces, and  $f_s$  is the dominant frequency of the lift force coefficient obtained by Fast Fourier Transform (FFT) analysis of lift coefficient time histories.

**Table 8 Grid particulars and comparative r.m.s. values of drag coefficient, Strouhal number, and shedding frequency, obtained with the SST  $k-\omega$  turbulence model on different grids, and values of the grid-independent solution, values of [96], and the associated errors**

<b>Grid</b>	<b><math>\Delta x</math> [m]</b>	<b>Cells No. <math>\times 10^6</math></b>	<b><math>\Delta t</math> [s]</b>	<b><math>C_d</math></b>	<b><math>S_t</math></b>	<b><math>f_s</math> [Hz]</b>
<b>Mesh 1</b>	0.126	2.3	1.26x10-3	0.6898	0.26	1.3
<b>Mesh 2</b>	0.1	4.6	0.001	0.8409	0.26	1.3
<b>Mesh 3</b>	0.08	8.9	8x10-4	0.7721	0.23	1.2
<b>Mesh 4</b>	0.063	17.4	6.3x10-4	0.7710	0.23	1.2
<b>Extrapol.</b>	0	–	–	0.8610	–	–
<b>[115]</b>	–	–	–	0.9	0.21	1.05-0.4
<b>Error %</b>	–	–	–	4.3%	9.5%	14.0%

Turbulent modeling errors have been quantified by comparing the drag and lift force coefficients obtained on the fine mesh as shown in Fig. 54. It is known that the drag coefficient is considered to be the least demanding coefficient to assess the discretization error in comparison with the exact solution. Furthermore, the drag coefficient gave a consistent constant value in the range of subcritical Re [105].



**Figure 54** Time histories of the drag force coefficients calculated from different grids

Nevertheless, the computational grids had to provide asymptotically converging discrete solutions and, by definition, these solutions were dominated by truncation errors. As the residual level of the order of  $10^{-1}$  was relatively high, it has been decided to decrease the time step. It is adopted the same refinement factor between grids for the time step study. Table 9 lists the resulting r.m.s. values of drag coefficient  $C_d$ , lift coefficient  $C_l$ , and shedding frequency  $f_s$ , obtained from simulations of 10s duration performed on the medium mesh grid (mesh 2). The last row in table 9 lists the comparative values of Khalak and Williamson [115].

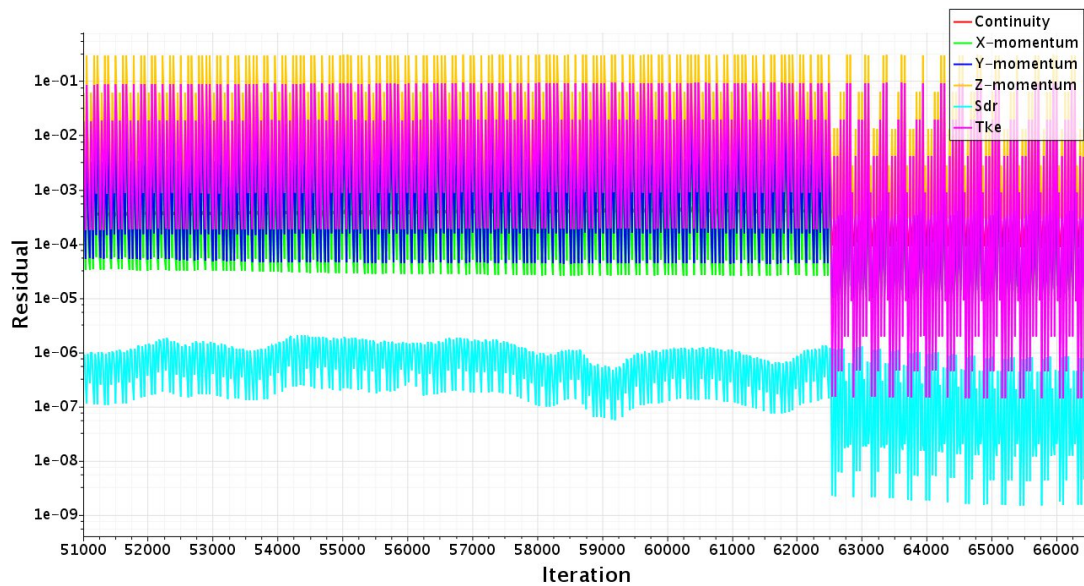
**Table 9** Drag coefficient, lift coefficient, and shedding frequency, obtained with the SST  $k-\omega$  turbulence model on the medium grid (mesh 2) for successively decreasing time steps and comparative values of [96]

<b>Grid</b>	<b><math>\Delta t</math></b>	<b><math>C_d</math></b>	<b><math>C_l</math></b>	<b><math>f_s</math> [Hz]</b>
<b>Mesh 1</b>	0.0010	0.8409	0.0969	1.27
<b>Mesh 2</b>	$8.0 \times 10^{-4}$	0.7998	0.0502	1.30
<b>Mesh 3</b>	$6.3 \times 10^{-4}$	0.8048	0.1679	1.20
<b>[115]</b>	–	0.9000	0.0580	1.05

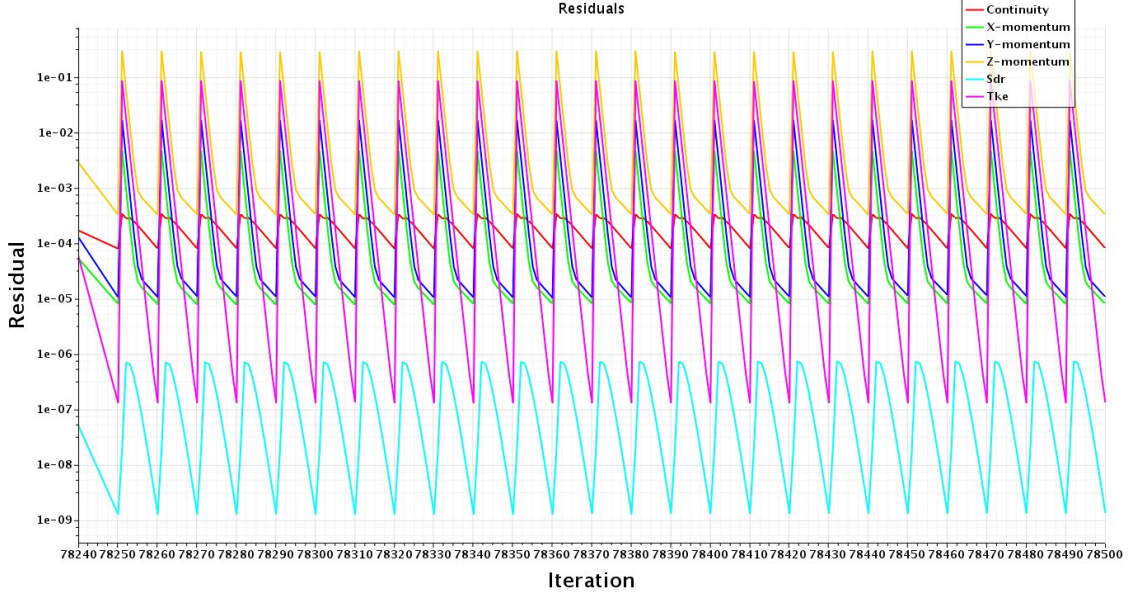
The results listed in Table 8 indicate that the time step did not significantly affect the solutions i.e. the problem is less time-dependent. Recall that the CFL number was always less than 0.2 and, therefore, it has been performed subsequent simulations on the medium grid. Furthermore, decreasing the time step is another way to decrease the iterative errors while the other way is to increase the number of iteration.

Rosetti et al. [145] defined limiting convergence criteria at infinity for iterative residual errors of  $L_\infty \leq 10^{-12}$  for steady simulations and  $L_\infty \leq 10^{-6}$  for unsteady simulations. However, they considered only the two-dimensional flow around a single circular cylinder.

Nevertheless, the plotted in Fig. 55 is presented the residuals obtained versus the number of iterations. These residuals were generated when solving the continuity equation (Continuity) and when computing the horizontal momentum (X-momentum), the transverse momentum (Y-momentum), the vertical momentum (Z-momentum), the Specific dissipation rate (Sdr), and the turbulent kinetic energy (Tke). As seen, the simulations associated with these plots were started at the same order of residuals, which indicated that iterative errors (residuals) did not depend on the number of iterations. Moreover, the variation of the residuals was not large enough to justify differentiating between discretization errors, which meant that the current numerical results may have been subject to modeling errors.



(a)



(b)

**Figure 55** Residuals of computed flow quantities vs. number of iterations; full-time calculations (a), zoom in (b)

### 6.1.4 The DES turbulence model

To compare the use of the DES turbulence model, the same numerical parameters as for the SST  $k-\omega$  turbulence model have been used. Even so, it was important to ensure that the grid’s mesh was adequate for DES solutions. For efficient DES calculations, this meant that the grid spacing should be kept between the Kolmogorov and the Taylor scale. The Taylor micro-scale,  $\lambda$ , defined as the intermediate length scale at which fluid viscosity significantly affects the dynamics of turbulent eddies in the flow, is expressed as follows:

$$\lambda = \left( \frac{v^3}{\beta^* \omega k} \right)^{\frac{1}{4}} \quad (73)$$

where  $k$  is the turbulent kinetic energy, and  $\omega$  is a specific dissipation rate. Larger lengths than the Taylor length are not strongly affected by viscosity. However, with lesser lengths, the turbulent motions are subject to strong viscous forces, and the dissipation of kinetic energy is then governed by the energy cascaded theory and converted to heat [126]. However, at the Kolmogorov scale,  $\eta$ , the smallest turbulence flow scale, viscosity dominates and the turbulent kinetic energy is dissipated into heat. This flow scale is expressed as follows:

$$\eta = \sqrt{10\nu \frac{1}{\beta^* \omega}} \quad (74)$$

For the DES turbulence model, the turbulent modeling error on the fine grid (mesh 3) was quantified by determining the lift and drag coefficients, the boundary-layer separation location, and the Strouhal number. Generally, the lift coefficient for flow around a cylinder is the most troublesome quantity to obtain, yielding the largest errors and uncertainties, even for two-dimensional simulations. In contrast, the drag coefficient is considered the least demanding one in terms of discretization errors to generate the “exact” numerical solution.

Table 9 lists not only the integral flow quantities the results of the verification and validation exercise achieved with the DES turbulence model but also those currently available from the literature. Specifically, this table lists the r.m.s. values of drag coefficient  $C_d$ , lift coefficient  $C_l$ , Strouhal number  $S_t$ , and frequency  $f_s$  obtained on the coarse grid (mesh 1), the medium grid (mesh 2), and the fine grid (mesh 3). Table 10 lists also the comparative values of Khalak and Williamson [115], Lysenko et al. [150], and Norberg [151]. As seen, with increasing grid fineness, the lift coefficient determined with the DES turbulence model converged monotonously towards the experimental lift coefficient of [115], which was not the case with the SST k- $\omega$  (see Table 8).

**Table 10 Drag coefficient, lift coefficient, Strouhal number, and shedding frequency obtained with the DES turbulence model and comparative values of [115], [145], and [144]**

<b>Grid</b>	<b><math>C_d</math></b>	<b><math>C_l</math></b>	<b><math>S_t</math></b>	<b><math>f_s</math> [Hz]</b>
<b>Mesh 1</b>	0.7747	0.0407	0.26	1.3-0.79
<b>Mesh 2</b>	0.7869	0.0461	0.23	1.2-0.69
<b>Mesh 3</b>	0.8002	0.0562	0.23	1.2-0.72
<b>[115]</b>	0.90	0.058	0.21	1.05-0.4
[151]	0.98	–	–	–
[150]	1.18	0.44	0.19	–

As seen, the drag and lift coefficients obtained with the DES model underestimated the experimental values, even the ones determined on the fine grid (mesh 3). These results were inconsistent with those of D' Alessandro et al. [152] as they associated this behavior with the nature of the DES model for near-wall URANS flow simulations. Recall that conditions near the cylinder's surface corresponded closely to subcritical flow conditions [105].

### 6.1.5 Comparative flow characteristics

Employing the two turbulence models resulted in different flow characteristics. This is best seen in Figs. 56 and 57, depicting, respectively, time series of lift force coefficient and time-averaged streamlines of flow on the cylinder's horizontal mid-span plane obtained with the SST k- $\omega$  turbulence model and the DES turbulence model and the corresponding frequencies.

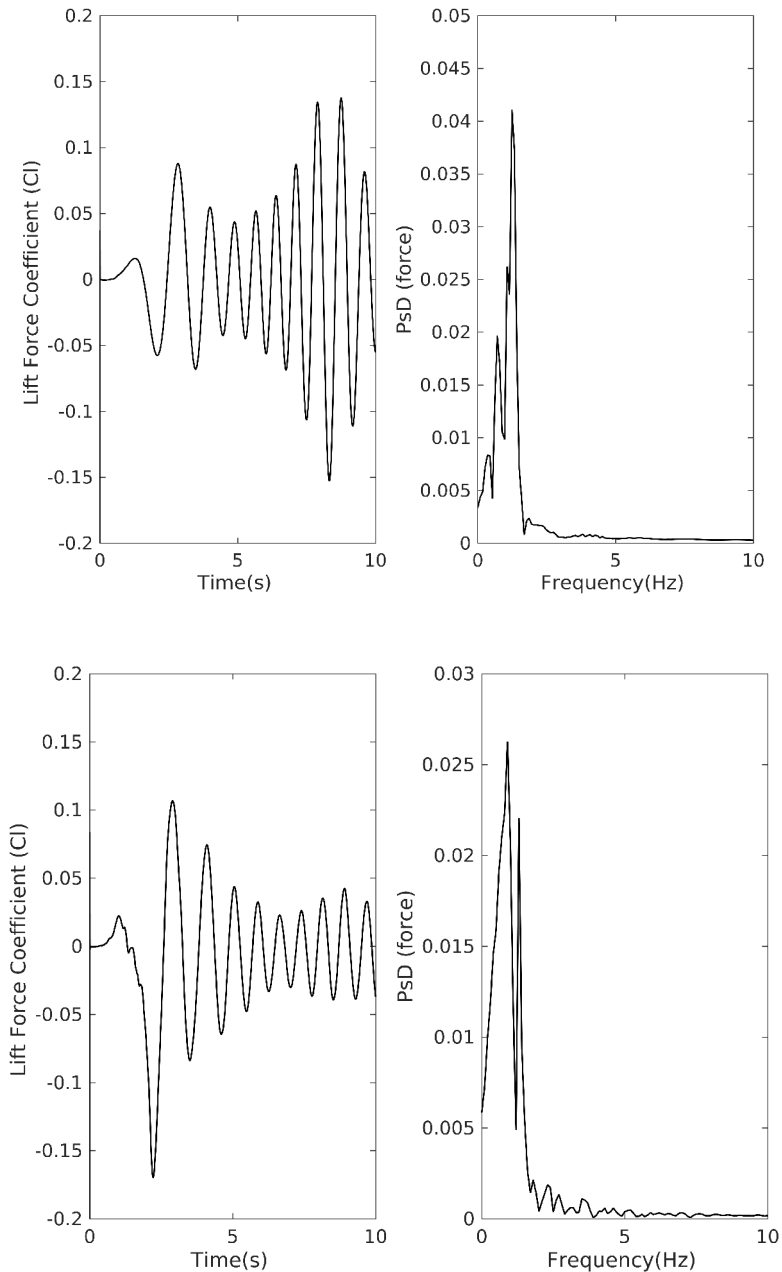
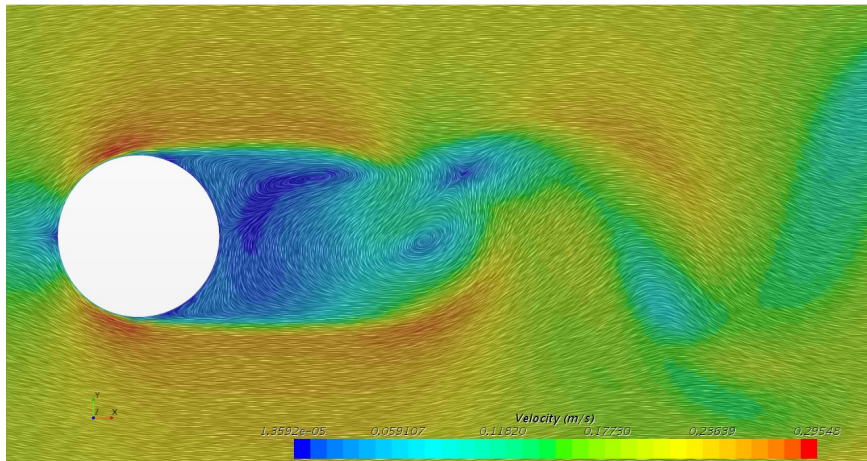
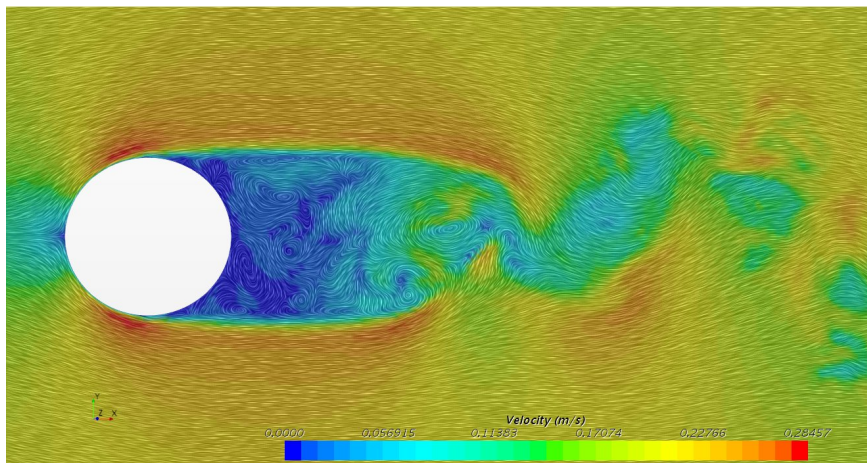


**Figure 56** Time series of lift coefficient obtained with the SST  $k-\omega$  (top) and the DES (bottom) turbulence model

With the SST  $k-\omega$  turbulence model, the flow past the cylinder was characterized by parallel shed vortices; with the DES model, the more complex flow was characterized by obliquely shed vortices. The simpler frequency content of the parallel shed vortices obtained with the SST  $k-\omega$  turbulence model was dominated by a single peak, whereas the obliquely shed vortices obtained with the DES turbulence model consisted of two dominant peaks, as shown by the lift coefficient's power spectral density obtained with the DES turbulence model presented in Fig. 56. This two-peaked power spectral density was similar to the comparative experimentally determined spectral density of Khalak & Williamson [115].



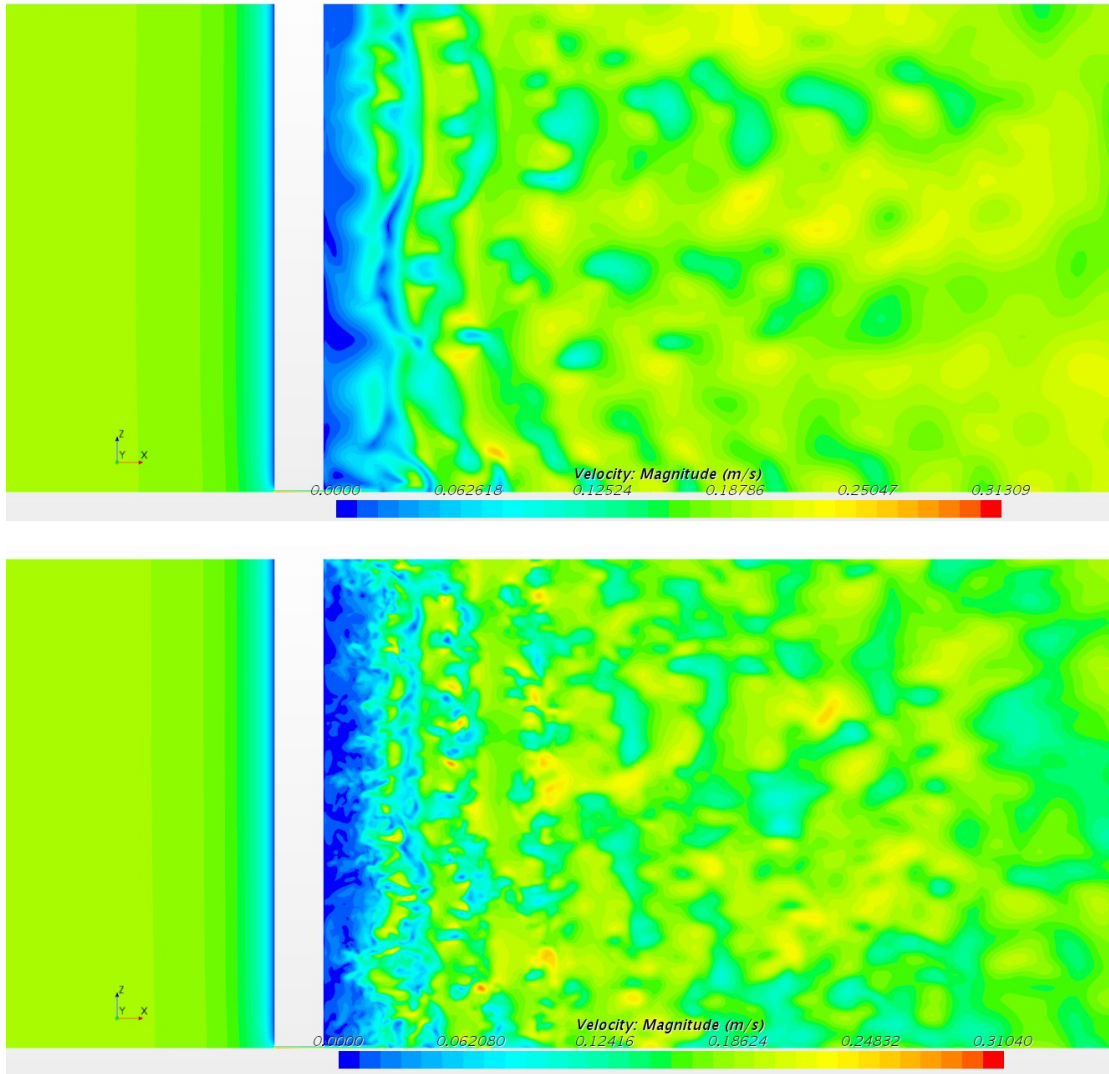
RANS



DES

**Figure 57** Time-averaged streamlines on the horizontal mid-span plane of the cylinder obtained with the SST  $k-\omega$  (top) and the DES (bottom) turbulence models

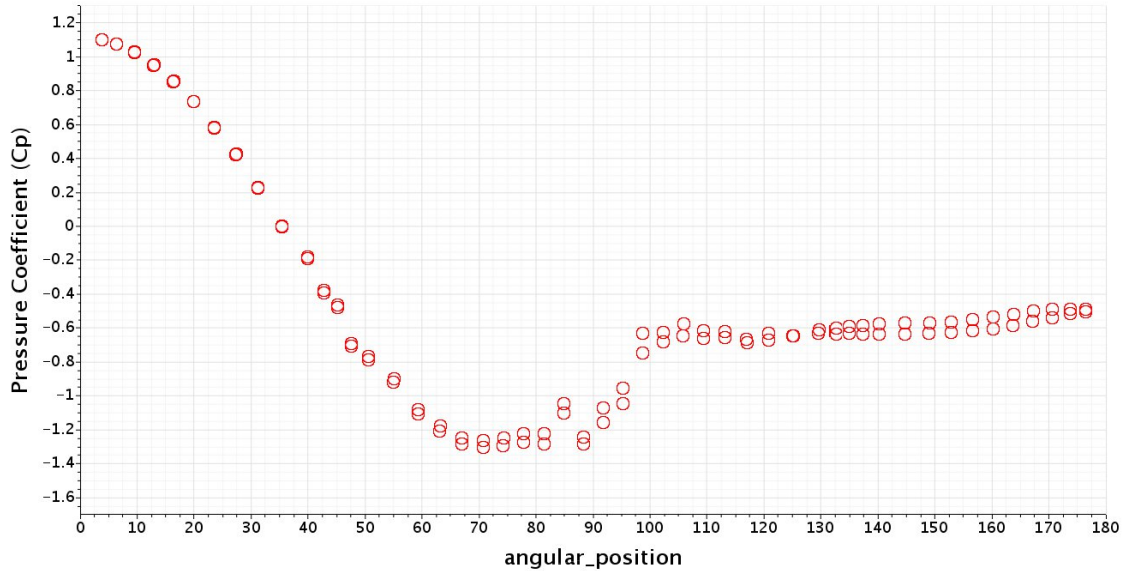
Although the gap between the cylinder's end and the bottom of the computational domain was small, it caused a slight downwash flow that led to obliquely shed vortices with more than one single frequency, which were captured obviously with the DES model. Overall, the DES model was found to be more successful in terms of detecting small-scale vortex shedding eddies in the near wake region. This became more evident when examining the asymmetric vortex distributions shown by the time-averaged streamlines on the cylinder's vertical symmetry plane shown in Fig. 58.



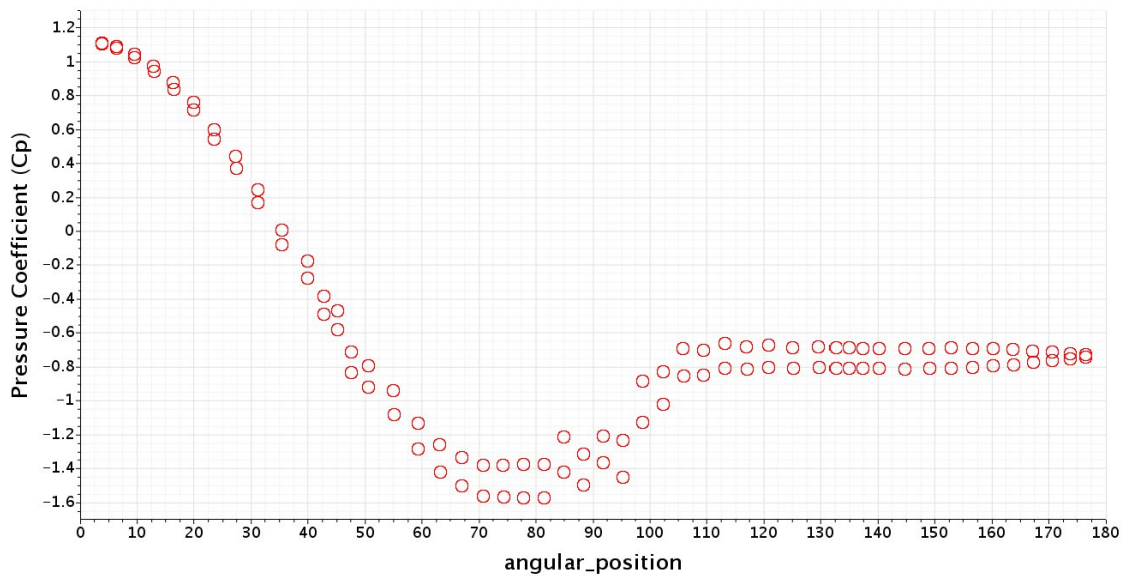
**Figure 58** Time-averaged streamlines on the cylinder's vertical symmetry plane obtained with the SST  $k-\omega$  (top) and the DES (bottom) turbulence model

Figure 59 plots the associated average pressure coefficient,  $C_p$ , versus angular position around the cylinder's circumference. For the sake of comparison, only the pressures computed on the fine grid (mesh 3) were considered. The predictions show a similar shape of the  $C_p$  obtained with SST  $k-\omega$  and the DES turbulence models. However, the value of  $C_{p,b}$  obtained with the DES model were underestimated to the experimental pressures of Lysenko et al. [150] and Norberg [151]. These results correlate with the nature of the DES approach, in that using the RANS technique in the near-wall region may give rise to inaccurate wall data a priori.





DES



RANS

**Figure 59** Mean pressure coefficient vs. angular position around the cylinder's circumference obtained with the SST  $k-\omega$  (top) and the DES (bottom) turbulence models

To determine the flow separation point, the plotted in Fig. 60 illustrated the shear stress distributions on the cylinder obtained with the SST  $k-\omega$  and the DES turbulence models. As known that in the subcritical range of Reynolds numbers the boundary layer's separation point oscillates between 80 and 90deg from the cylinder's front stagnation point [101]. Based on these plotted stress distributions, the flow separation occurred at an angle of  $\theta_{sep} = 87.4\text{deg}$ , a result that correlated favorably with DES calculations of Luo et al. (86.4deg) [153] and LES investigations of Kravchenko and Moin (88.0deg).

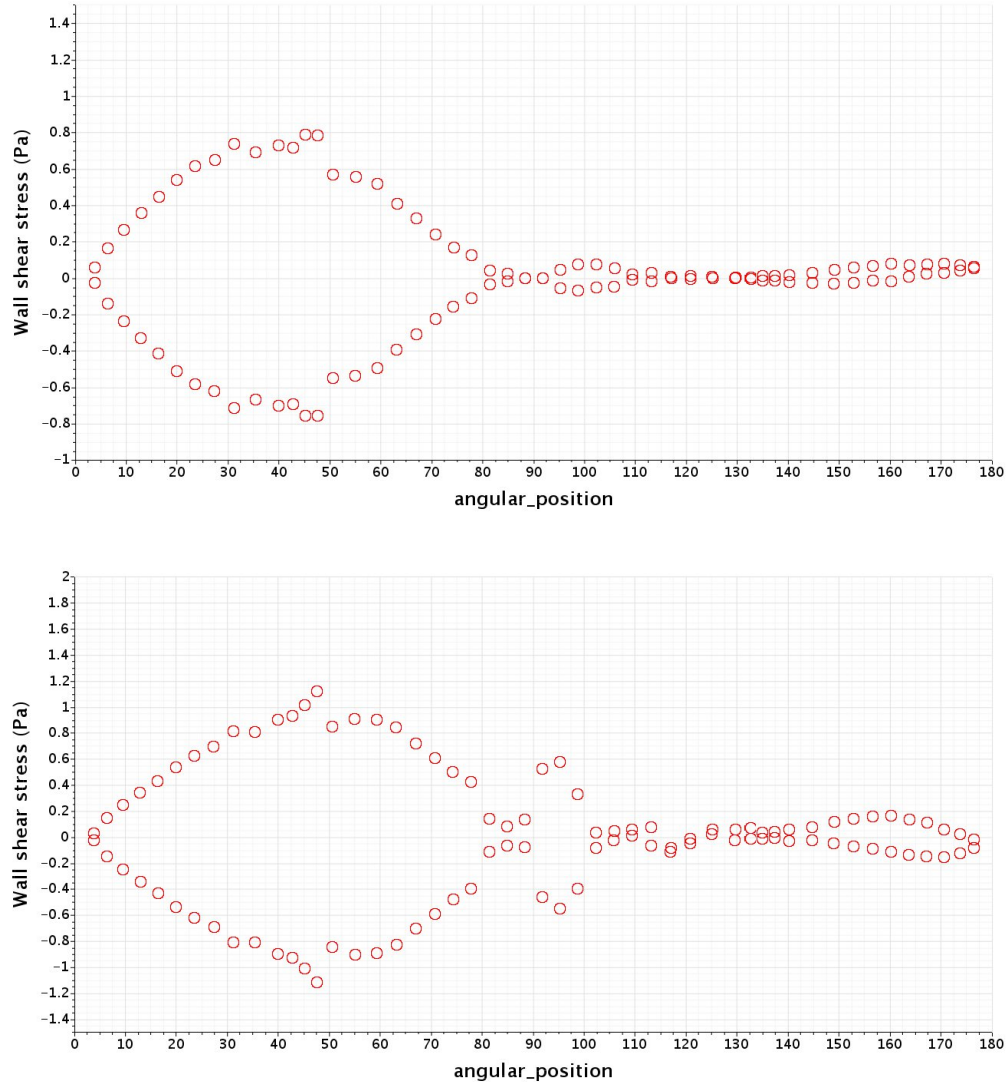


**Figure 60** Shear stress distribution on the cylinder wall obtained with the SST  $k-\omega$  (top) and the DES (bottom) turbulence models

It is noted that the level of residuals with both turbulence models remained nearly the same, even when refining the grid size, whereby the Courant number for all the calculations was kept constant.

## 6.2 Suppressing Using Attached Structures

There are very few studies that demonstrated the various method for VIV suppressing. Especially, there is rarely numerical investigation represented the effects and flow features for different suppressing tools, for example, M. Springer et al. [144] and Ranjith et al. [55]. However, Computational Fluid Dynamics (CFD) has gained momentum and its value in cost-effectiveness could include CFD results enabling the design of smaller and lighter equipment or enabling simpler and cheaper examinations before practical installations.

In this second part, the newly developed various fin configurations attached to the plain cylinder surface have been employed to investigate numerically the flow characteristics behind a stationary circular cylinder using a detached eddy simulation turbulent approach. For

comparing the various attached structure features, the focus only on the turbulent flow, the Reynolds number, based on the free stream velocity and the diameter of the cylinder, was fixed at  $Re = 5.3 \times 10^3$ . In the following, the problem definition and numerical validation were presented at first. a brief description of the tested models is followed. After that, a detailed numerical study of flow over a stationary circular cylinder with fin plates was given. From the comparison results, The mean drag coefficients and the root mean square (r. m. s.) values of lift coefficient for a plain cylinder were compared with the same range of data results reported from previous Khalak and Williamson research in Fig. 61. It can be seen that the present smooth cylinder data fairly agree well. It is illustrated that the model established in the present study can be used to investigate different VIV suppressing tools attached to the smooth circular cylinder.

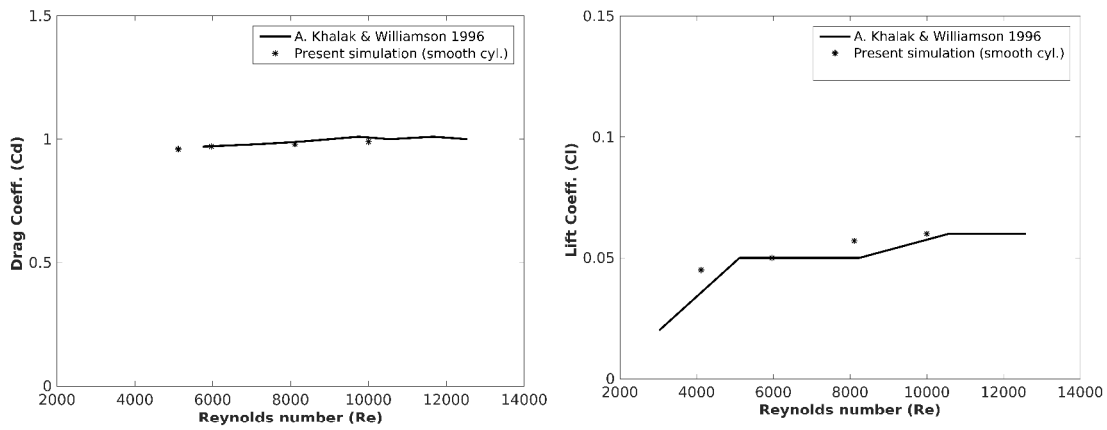


**Figure 61** Drag coefficients for the bare cylinder compared with data from published work by Khalak and Williamson 1996.

Figure 62 presents time-averaged streamlines and pressure contours on the midspan plane for the rigid cylinder. As seen, the flow pattern behind the rigid cylinder generated an asymmetrical vortex pair, an asymmetrical von Kármán vortex, and strong negative pressure behind the cylinder has been observed. Next, the influence of the attached fins on the velocity and pressure contours will be examined at the same time step.

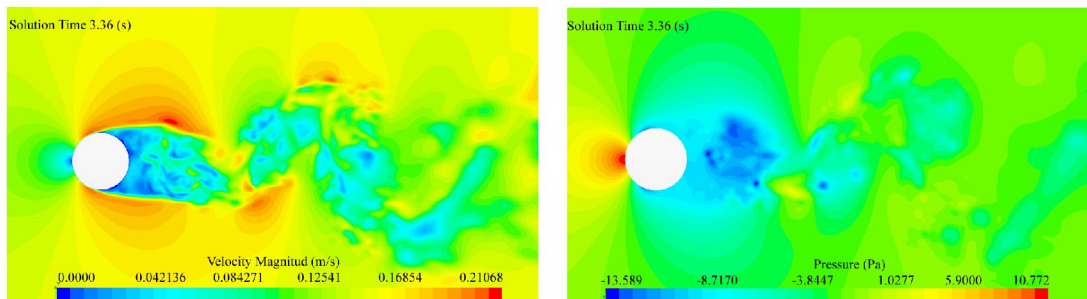


**Figure 62** Time-averaged streamlines and pressure contours on the horizontal midspan plane for the plain cylinder

## 6.2.1 Models description

Gartshore et al. [59], placed straight fins on the sides of the cylinder, rather than at the front and back of a smooth cylinder. Their effect was to increase the maximum amplitudes of response in a smooth and turbulent flow. This may be due to sharp edges near the top and/or bottom of the cylinder causing galloping which means, this increase is due to a combination of galloping and vortex excitation.

Instead of straight fins tested by Gartshore et al. [59], thought of equal distances discrete straight fins along the cylinder span with equal spaces in between along the cylinder model as shown in Fig. 63. Various straight fin lengths have been examined for the shown model A in Fig. 63. As shown in Fig. 63, at the bottom boundary layer, a double space distance has been chosen as two different boundary layers from the two opposite directions of the bottom surface boundary condition, and the last fins' end is supposed to be performed. Besides, due to the tip vortex at the top of the cylinder which attenuates the ordinary vortex strength, the fins location has been shifted from the top location to the lower one. In order to decrease the effect of straight fins sectional area on the drag, a  $45^\circ$  inclination angle of the fins has been tested in models shown in Fig. 63 B and C.

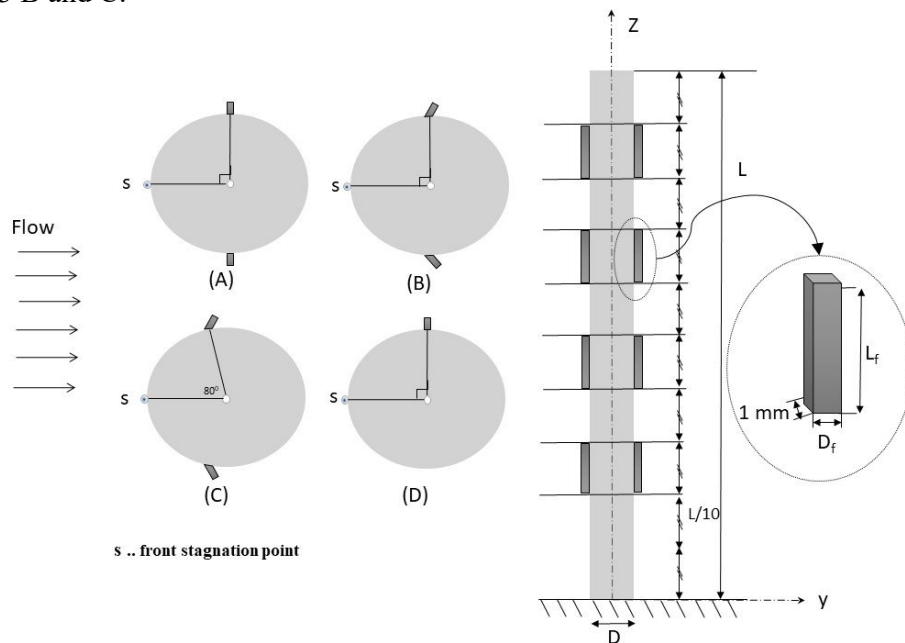


**Figure 63** Schematics of the cylinder with attached fin plates in frontal view; and the cross-sectional view of different tested model; (A) straight fin plates, (B) 90 deg fin plates, (C) 80 deg fin plates, and (D) asymmetric straight fin plates model

Furthermore, It was reported in pieces of literature that the cause of VIV was thought to be; the presence of a bluff body, symmetric cross-section, and separation angle [30], [154], however, Bearman explained that primarily responsible for vortex shedding is the presence of two shear layers rather than the bluff body itself [6]. In the present study, the factors of symmetry cross-section and separation angle have been examined. It is well-known that in the subcritical range of Reynolds number, the boundary layer's separation point oscillates between  $80^\circ$  and  $90^\circ$  from the front stagnation point [101]. Thus it is very likely that in the  $90^\circ$  positions the fin plates had a particularly disturbing effect on the flow (Fig. 63 B). Furthermore, another model (Fig. 63 C) has been tested to demonstrate the effect of disturbing the range of the separation angle on VIV. In addition, model 6 (Fig. 63 D) has been used to test the effect of asymmetry cross-section on VIV. Two non-dimensional parameters are used to describe the fin plates.

The ratio between the length of the fin plate in the radial direction and the diameter of the cylinder is defined as  $R = \frac{D_f}{D}$ , where  $D_f$  is the length of the fin plate in the radial direction of the cylinder. The fin plate aspect ratio which could be defined as  $A_f = \frac{D_f}{L_f}$ , where  $L_f$  is the height of the fin plate in the vertical direction. In the case study,  $R = 0.05, 0.1,$  and  $0.2$  have been used with  $A_f = 0.1$  for all the models with thickness 1 mm to avoid the effect of galloping which is expected to happen with thick plates as observed by A. Vinod et al. when using thick strips attached to the cylinder surface [155]. The models description has been represented in table 11.

**Table 11 Specification of different tested models**

<b>Model</b>	<b>Description</b>	<b>location</b>	<b>R</b>
<b>Model 1</b>	Cylinder with straight fins located at 90° from the stagnation point	Two sides symmetry	0.05
<b>Model 2</b>	Cylinder with straight fins located at 90° from the stagnation point	Two sides symmetry	0.1
<b>Model 3</b>	Cylinder with straight fins located at 90° from the stagnation point	Two sides symmetry	0.2
<b>Model 4</b>	Cylinder with 45° inclined fins located at 90° from the stagnation point	Two sides symmetry	0.1
<b>Model 5</b>	Cylinder with 45° inclined fins located at 80° from the stagnation point	Two sides symmetry	0.1
<b>Model 6</b>	Cylinder with straight fins located at 90° from the stagnation point	one sides asymmetry	0.05

The same mesh configuration parameters have been used for numerical solutions for each tested model. The only difference was the change in the number of prism layers to enhancements the sharp changes in the circular geometry. The first layer thickness has been kept with the same value to ensure the  $y^+$  criteria for all the numerical models. Figure 64 presents examples of the mesh patterns used for different models.

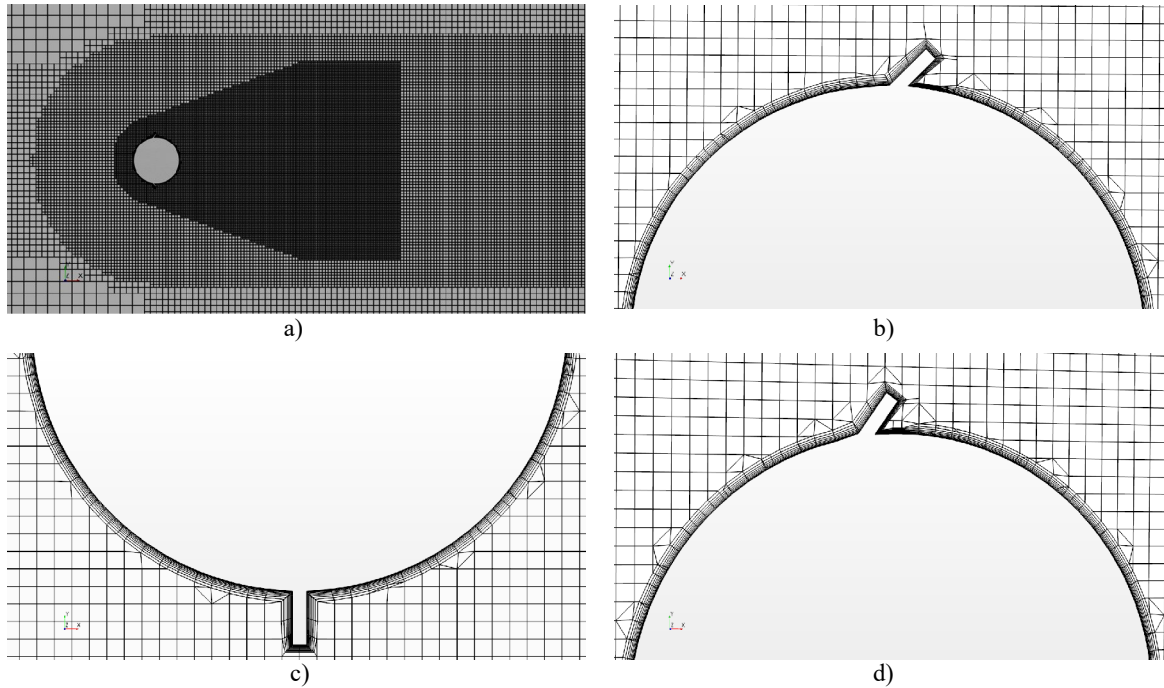


**Figure 64** Top view of the computational meshes for each study case; a) total computational domain, b) 80 deg fins, c) straight fins, d) 90 deg fins

## 6.2.2 Attached structures results

### *Analysis of wake flow*

Before going through the results of the suppressing tool, it is needed to figure out some features of the wake flow to understand how these tools are supposed to work. The mechanism of the vortex formation region is with the growing vortex continues to be fed by circulation from the shear layer until the vortex becomes strong enough to draw the other shear layer across the wake. The fluid is drawn across the wake by the action of the growing vortex on the other side. when the irrotational flow is beginning to cross the wake axis, the flow is separated into three different paths [156], [157]. It is partly entrained by the growing vortex and partly by the shear layer upstream of the vortex. Some of this fluid will also find its way into the interior of the formation region. The size of the formation region could be determined by the balance between entrainment into the shear layer and the replenishing of fluid by the induced reversed flow described above. As the Re number increases, the turbulence of the shear layer increased. there will be more diffuse in the region of interaction [158]. When the layer is diffused it will take longer for a sufficient concentration of vorticity to be carried across the wake and initiate shedding. On the same reasoning, the greater diffusion of the vorticity would result in less entrainment into the growing vortex, hence a higher value of the vortex strength at a high Reynolds number. In this case, there would be an effective cancellation of circulation in the interior of the formation region.

So, the idea here of using the straight fins is to increase the thickness of the shear layer by making the shedding vortices unable to roll from one side to the other side along the cylinder's rear surface easily due to the fin plate's prevention. Thus they are forced to process downstream. Therefore, with the existence of the fin plate, the shear layer is greatly influenced and extended. Figure 65 represents the flow pattern behind the stationary cylinder generated vortices for each model case at approximately the same time step.

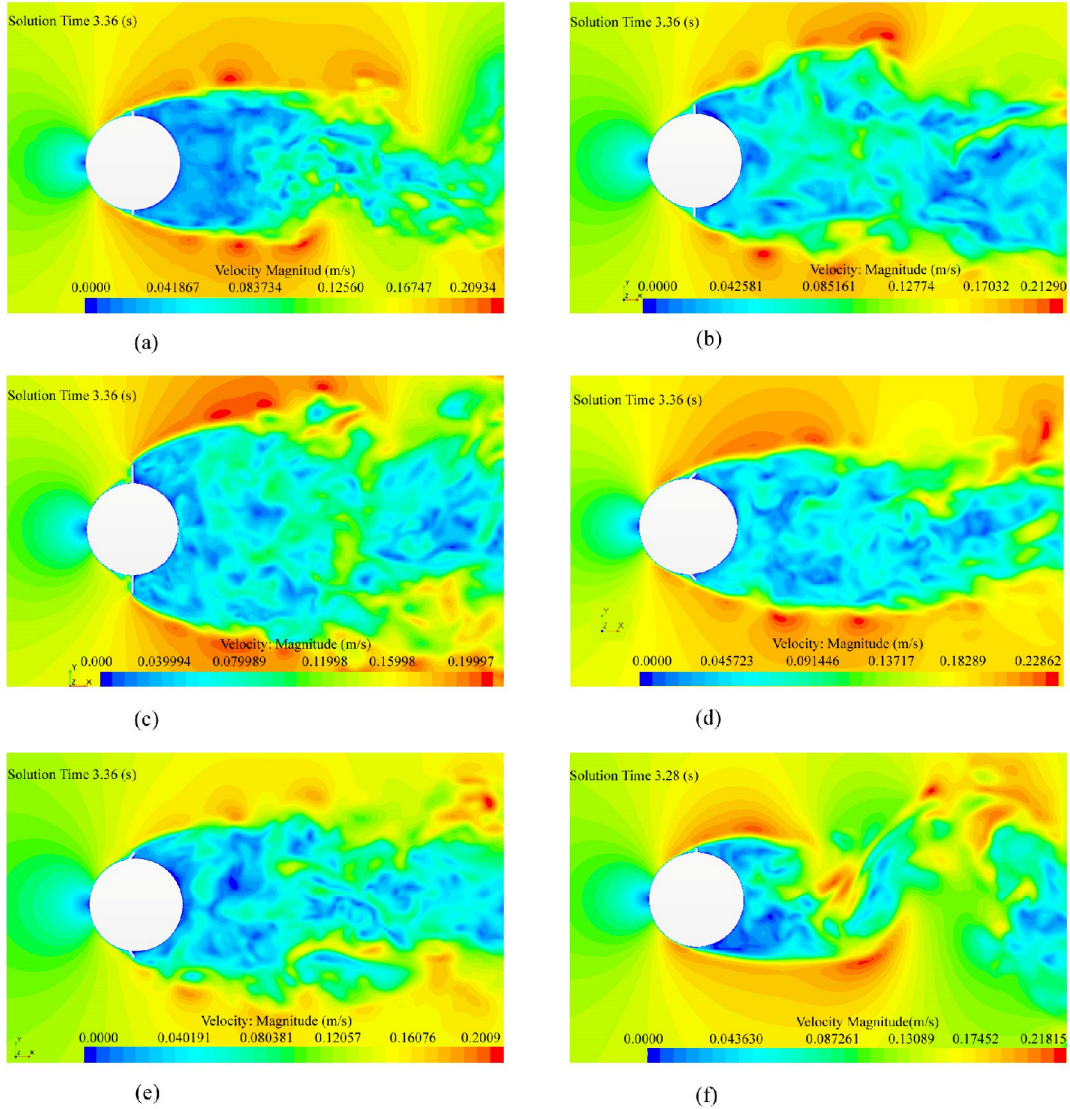


**Figure 65** Time-averaged streamlines on the horizontal midspan plane presented the variation of the vortex formation length and vortex thickness for each case at the same time step; model 1 (a), model 2 (b), model 3 (c), model 4 (d), model 5 (e), model 6 (f)

Due to the existence of the fin plates, it can be found that the separation bubble size becomes larger as compared to the case of the plain cylinder, as they make the vortex shedding slower. To be explained, the entrainment fluid by the growing vortex increased and the diffusion part becomes very weak and the vortex strength decreased. This is obvious as the length of the fin plates increased from 0.05, 0.1, and 0.2 (see Fig. 65 a), b), and c) respectively). Such stream flow pattern is similar to that could be seen in the inclined fins 80 deg (Fig. 65d)), and 90 deg (Fig. 65 e). In contrast, in the asymmetric cylinder, the shrinking of the separation bubble is observed, increasing the vortex strength.

In order to show the variation of the wake structure at different design parameters, pressure contours on the horizontal midspan plane are presented in Fig. 66 in comparison to each simulated case. The maximum negative pressure is obviously greater for the case of the asymmetric model than that shown in other simulation cases, resulting in higher difference pressure zones and higher vortex strength and lift force affecting the cylinder as well. In that case, during the flow oscillation, the vortex remains close to the cylinder as it forms and grows, even closer in fact than the smooth surface cylinder model even the different cells performed

along with the cylinder due to the separate spaces between the fins did not play a significant role in suppressing VIV for such case.

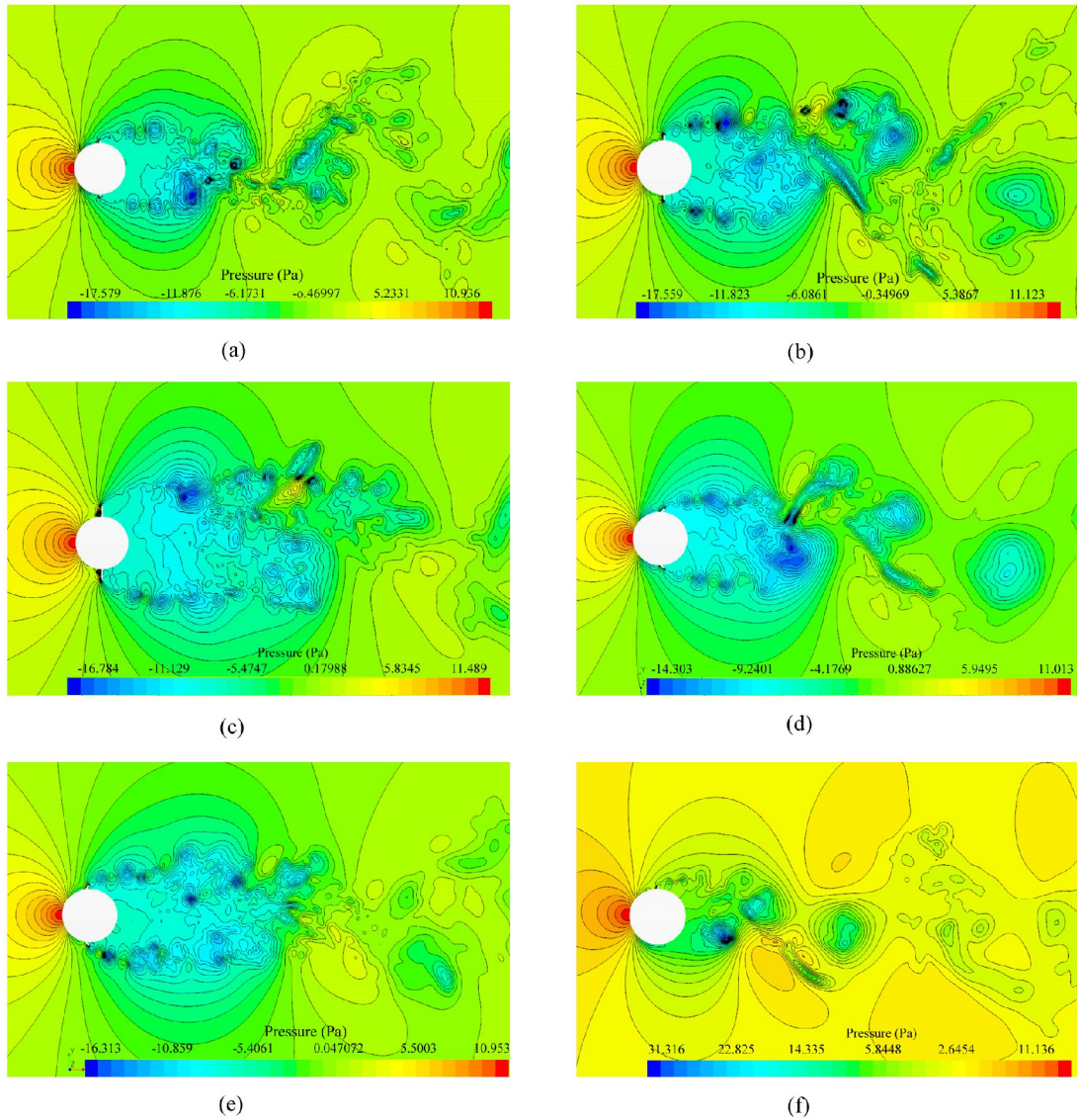


**Figure 66** pressure contours on the horizontal midspan plane variation for each case at the same time step; model 1 (a), model 2 (b), model 3 (c), model 4 (d), model 5 (e), model 6 (f)

Except for the asymmetry case, all other tested models have approximately the same pressure variations. The pressure contours distributions also illustrate the different categories of eddies that correspond to the vortex-shedding phenomenon. The pressure contours also show that the development of the streamwise interval of the vortex shedding is clearly becoming large as a result of the attached structures. It has been seen that for the 80 deg fins model and 0.2 straight fin two sides plates, forming a vortex seemed difficult as illustrated in Fig. 66. Besides, it can be found that the variation of the average base pressure coefficient distribution,  $C_p$ , is obtained for the asymmetric model has a larger value, about 1.1, however, the mean and variations of pressure distributions become relatively stable for all the tested cases and the lowest value can be found in the 90° two sides case for about 0.4.



It is worth noting here that, one of the negative effects of the splitter plate is that the shedding vortices cannot attach to the plate for  $L \leq 1D$ . Additionally, the reattachment of shedding vortices on the longer splitter leads to a counterflow along its surfaces, which also contributes to a larger negative-pressure region and the higher pressure difference between two surfaces [159]. In this suppressing method, this behavior does not exist.

Another remarkable influence where the fin plate locations are supposed to play a role is during the vortex formation along with the cylinder length. The pattern of the projecting fin induces a spanwise motion for the fluid while it flows around the fined attached cylinder. This will produce a swirling motion in the wake region and disrupt the spanwise vortex formation.

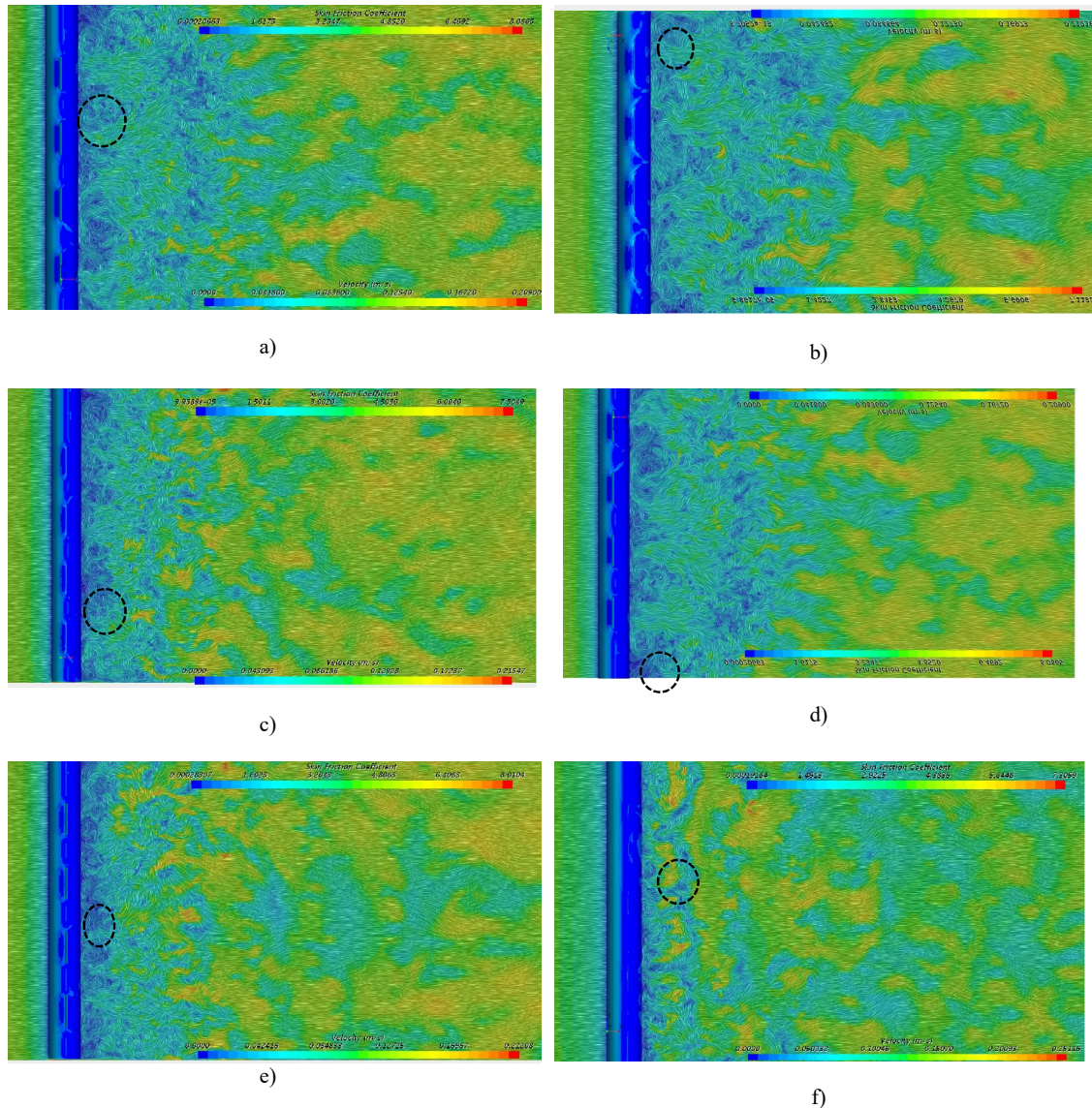


**Figure 67** Time-averaged streamlines on the vertical symmetry plane and the skin friction coefficients for different cases; bare cylinder (top), mode 2 (a), model 3 (b), model 1 (c), model 5 (d), model 4 (e), model 6 (f)

Also, the flow motion in the vertical direction along the cylinder would be disturbed as well because of the difference in the shear layer existence between the fined surface and unfined beneath one, causing the vortex shedding does not occur uniformly along the length of the

cylinder, but rather in cells similar to the effect of tip vortex for the finite cylinder [160]. These cells have a remarkable effect on the shedding vortices' synchronization behavior. As a result, the applied force will not be uniformly distributed along with the cylinder as represented in Fig. 67 where the dashed lines indicated examples to identify the different cells along with the cylinders. As explained by Mukundan [161], for a flexible structure to be excited, it is not sufficient to simply excite a natural frequency; the force must have a spatial distribution in sympathy with the associated mode. The corresponding streamlines on the symmetry plane ( $Y=0$ ) for each model along the cylinder have been illustrated in Fig. 67. Besides, The predictions of the skin friction coefficient,  $C_f = \frac{\tau}{0.5\rho U^2}$ , where  $\tau$  is the tangential wall shear stress, are shown in Fig. 67 for  $Re= 5.3 \times 10^3$ .

### ***Drag and lift forces due to fin plates***

The mean drag of the smooth cylinder and each model case are compared. As expected, the main drawback of using straight fins 0.05, 0.1, and 0.2 is the increase of the drag coefficient with the addition of the fins, however, there was no significant change for fin plates with  $R=0.05$ . In contrast, by using one side fins with  $R=0.05$ , the drag coefficient had a lower value. While inclined fins presented a remarkable effect in decreasing the drag coefficient, the fins location at  $90^\circ$  from the stagnation point has a better influence. This might be caused due to the flow separation that has been performed before  $90^\circ$  while at  $80^\circ$ , the flow stream kept attached to the cylinder surface. The comparisons between the numerical investigation of the drag and lift forces coefficient for the flow around a circular cylinder with and without the different attached fin plates at Reynolds numbers,  $Re = 5.3 \times 10^3$  have been presented in table 12.

**Table 12 A comparison between the smooth cylinder and fined cylinders**

<b>Reynolds Number</b>	<b>Parameter</b>	<b>smooth Cylinder</b>	<b>Fined cylinder</b>					
			<b>Model 1</b>	<b>Model 2</b>	<b>Model 3</b>	<b>Model 4</b>	<b>Model 5</b>	<b>Model 6</b>
<b><math>5.3 \times 10^3</math></b>	<b><math>C_d</math></b>	0.9648	0.9643	1.2756	1.5472	1.083	1.126	0.941
	<b><math>C_l</math></b>	0.0532	0.0287	0.0415	0.0155	0.023	0.0198	0.227
	<b><math>f_s</math></b>	0.078/ 0.5468	0.6636	0.5294	0.089	0.6428/ 0.1428	0.285/ 0.7114	0.7341

On the other hand, the lift coefficient has been decreased for all the tested models except for the asymmetric one. For two sides fined cylinder wake, the two shear layers do not interact with each other, resulting in the absence of the oscillating wake in the downstream region near the cylinder. The choice of test the inclined fin on the parameters of model 2 was to examine how much it would be effective. Again, the inclined fins showed a remarkable influence on the lift forces as well as they had for the drag forces. Generally, the lowest reduction in the lift forces was found in model 2 by approximately 25%, however, by using inclined fins, the reduction increased significantly to about 65%. The maximum reduction was at model 3 by nearly 75% however highest drag was associated with this model due to the larger frontal area.

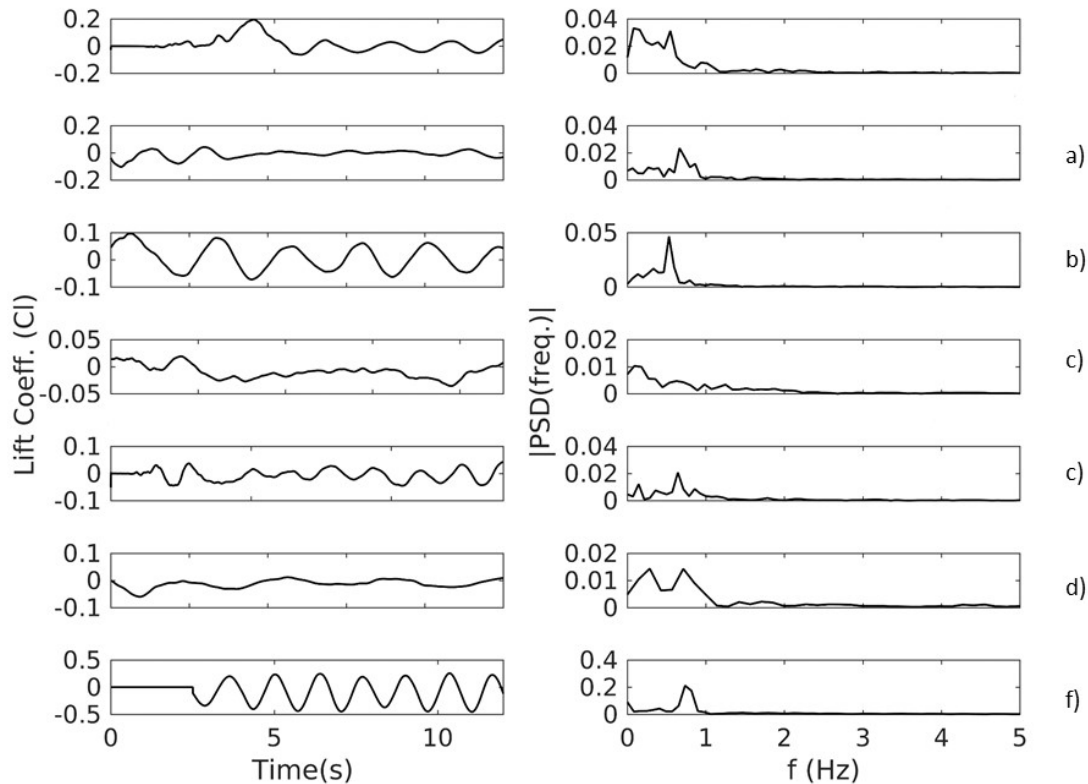


**Figure 68** Time series and frequency plots for for different tested cases; bare cylinder (top), mode 1 (a), model 2 (b), model 3 (c), model 4 (d), model 5 (e), model 6 (f)

As indicated, this high reduction is owing to the separation size which becomes the largest among the other models ( $R=0.2D$  two sides) as compared to the case of the plain cylinder, which makes the vortex shedding formation slower. Besides, the power spectrum shows great attenuation and presents the lowest value. As a result, a high reduction in the vortices' strength and the values of the lift forces have been remarkably obtained. we could see from Fig. 68, the frequency content of the smooth cylinder has two dominant peaks similar to the reported from literature, as a result of the oblique shedding from the free end condition. This leads to a more complicated time trace as shown in Fig.68. For the 80 deg attached fins (model 5), the frequency content shows two dominant peaks while for the 90 deg attached fins (model 4) the second frequency has a much lower value than the dominant one. Except for models 4 and model 5, it seems that the second frequency has been attenuated. The power spectrum densities have approximately the same range except for the asymmetric case in model 6 in which the value has been nearly a ten-fold rise corresponding to 0.7341 Hz frequency. Due to increasing in shedding frequency ( $f_s$ ), the change of vortex strength is significant, and enhanced strength has been obtained. A very periodic lift force has been represented with this model, however, this behavior is normally indicated for that the parallel-shedding (2D cylinder), while the oblique-shedding case time traces is not so simple [109]. This confirms the negative effect of a certain small asymmetric shape on the VIV suppressing.

### 6.2.3 Case study -model 5

The case study of model 5 has been selected for further investigation to examine the results over the range of  $Re$  similar to [115]. For the particular case study, drag and lift coefficients have been plotted, to illustrate the change with the Reynolds number, against the experimental

and numerical results for the smooth cylinder as shown in Fig. 69. Along with the increase in Reynolds number, it has been found that the lift forces decrease. The same behavior has been observed to the drag force with the increasing flow stream velocity with the consideration that the value of the drag force is higher than the bare cylinder case due to the cross-section influence. Furthermore, an increase in the forces was accompanied by a further increase in the flow stream velocity. The reduction of the lift forces by about 70% has been achieved with the maximum Reynolds no in the specific range of the experiment conducted in his study. More experiments are needed for further studies and illustrating the behavior with a higher Reynolds number range.

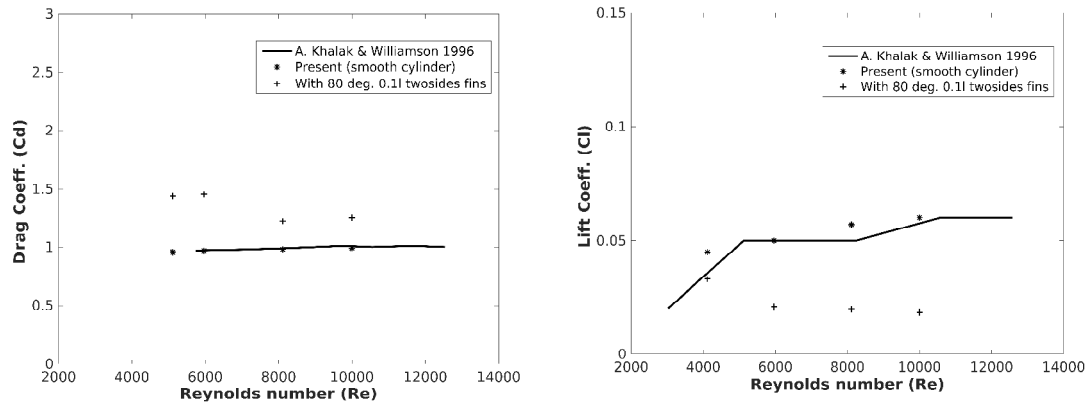


**Figure 69** The mean Drag coefficients and r.m.s. Lift Coefficient for the case study of model 6 in comparison with numerical and experimental results for the bare cylinder

To demonstrate this behavior, as mentioned in chapter 5.1 that the flow-induced forces could be split into two components: pressure force acting normal to the wall surface ( $F_W^P$ ), and shear force, caused by a wall-normal gradient of wall parallel velocity components, acting tangential to the wall surface ( $F_W^T$ ) as illustrated in equation 18. The force in the flow direction is the drag force however the lift force represents the upward forces [162].

Due to the water viscosity, the shear stress components have a small influence and could be negligible compared with the pressure force, furthermore, with Re increases, the viscous effect decreases. These results confirm that the pressure variations and wake vortex strength keep decreasing with increasing Re as a result of using this fin configuration; at least until the limitation of the experimental data is reported.

Bloor & Girrard in 1966 [157] found that the proportionality does approximately exist between the rate of turbulent entrainment and the change in vortex strength. Thus it is shown that the changes in the strength of the vortices with Reynolds number can be attributed to the variation of entrainment of vorticity bearing fluid by the turbulent part of the shear layer. As shown in Fig. 70, there are insignificant changes that take place in the formation region than shown in Fig. 65d as the Reynolds number is increased.

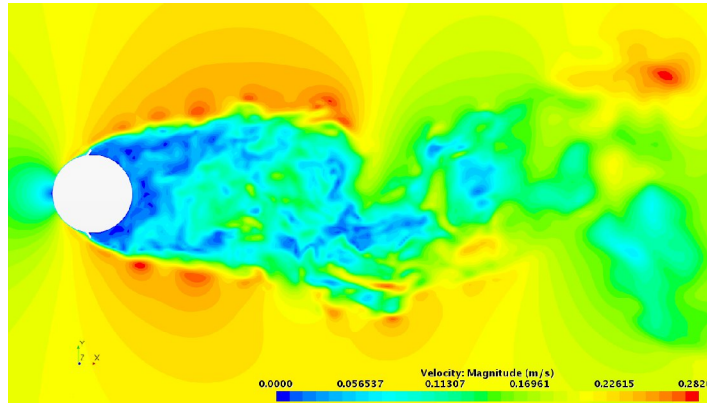


**Figure 70** Time-averaged streamlines on the horizontal midspan plane of model 6 at  $Re = 10^4$

In this case, the entrainment of fluid bearing vorticity from the other shear layer decreased with the Reynolds number. The formation region is maintained in large length which is consistent with the reduction in the strength of the vortices as indicated in the lift and drag forces behavior seen in Fig.69. Another important characteristic is the frequency variations. It has been reported that the frequency increases if the scale of the formation region is reduced[163], however, two major factors determine the frequency of vortex shedding that has been postulated by J. Gerrard [158].

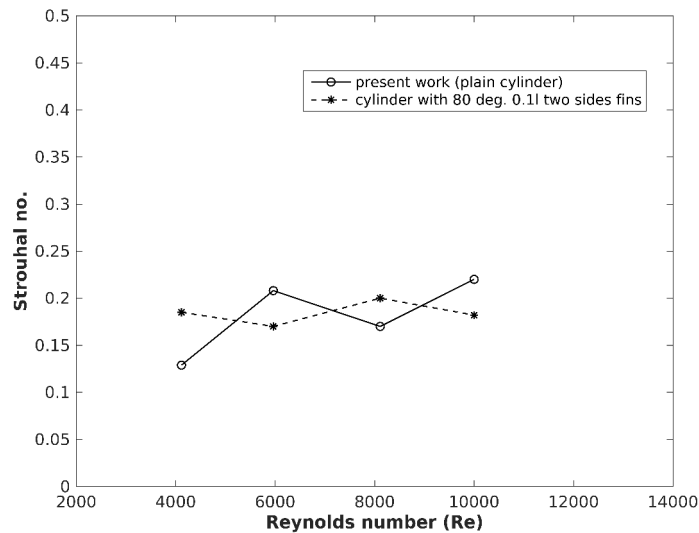


**Figure 71** Dominant frequencies from lift force (FFT), nondimensionalized by flow speed,  $U$ , and diameter,  $d$  for bare and case study numerical data

These factors are the scale of the formation region, where the frequency increases when the scale of the formation region is reduced, and the other is the thickness of the shear layer. It could be seen from Fig. 68, the frequency content of this case is found to have two dominant peaks that nearly have the same power density at frequencies of 0.285 Hz and 0.7114 Hz. However, this frequency behavior did not change by increasing  $Re$  where the two dominants, nearly the same intensity, with values 0.228 Hz and 0.9131 Hz keep existing. It seems that the lower frequency does not change with  $Re$ . More detailed experimental measurements are needed to illustrate this behavior.

The relative constancy of the Strouhal number over the whole experimental Reynolds number range has been illustrated in Fig. 71. Similar behavior to that found by A. Khalak and Williamson [115], who reported that the frequency characteristics do not depend upon Reynolds number when nondimensionalized by the flow stream velocity and the cylinder diameter.

## 6.3 Numerical Validation of FSI Test

Although a CFD analysis is subject to certain limitations, such as complex flow dynamics, the high computational cost to simulate practical three-dimensional flows still relies on the selection of a proper turbulent model, and adding FSI requires more computing resources and time. However, continued advances in computational capabilities, proper simplification techniques, and the availability of comparatively inexpensive turbulent models increase the reliability and accuracy of numerical simulation tools. To date, limited numerical simulations have been performed to predict VIV characteristics especially for cylindrical structures at high Reynolds number flows such as M. Ong et. al [164] and Fluid-structure coupling between the flow and the bluff body.

In several fields, such as aerodynamics, hydrodynamics, biomechanics, and flow control, FSI is considered a vital issue. Despite FSI manifold forms of appearance, it is a topic of major interest in many fields of engineering. Tight coupled FSI approach where a simultaneous solving and satisfaction between fluid and structure governing equations is one of the challenges that need to be accomplished. Moreover, the flexible cylinder supporting is another important factor that affects coupled flow-structural characteristics, for example, For a flexible cylinder VIV, the cable like and beam-like structures are two generally accepted structural systems. If the tension dominates, it is termed a cable, while if the bending rigidity dominates, it is termed a beam [165].

Based on enhanced numerical algorithms and increased computational resources, numerical simulations have become a valuable and important tool for solving this kind of problem within the last decade. As reviewed above, few studies have been conducted to explore the flow mechanism associated with 3D flexible cylinder VIV. Limited studies on flexible cylinders are focused on the vibrating response rather than the flow characteristic in the oscillating cylinder

The overall aim of the present subsection is to provide one of the first comparisons of computational and experimental results for a high- Reynolds number, three-dimensional FSI case. A new turbulent FSI validation test case is defined based on detailed measurements and the experimental results for the smooth cylinder in the circulating water tank have been used to validate

### 6.3.1 Problem description

The fluid flow is predicted by a detached-eddy scheme simulation technique. The numerical simulations were conducted for an elastically mounted circular cylinder with the same parameters tested in the experimental investigation in chapter 3. The computational model was based on the geometric configuration of the circulating water tank. The (streamwise) length and (spanwise) height of the computational domain were, respectively,  $L_D = 35 D$ , and  $H =$  water tank height (0.7 m). It should be noted that a distance of  $5 D$  between the cylinder surface and the inflow boundary was used for all the grids; in the wake region the domain develops for  $30 D$  behind the cylinder's surface while the concern was with the wake region near the cylinder and the generating hydrodynamic forces applied on the cylinder, domain width has been set to  $5D$ . The junction section between the center of the smooth cylinder and the bottom wall was centered at the origin of the coordinate system within the domain. To adequately capture the high-velocity gradients near the cylinder, the same refinement blocks used in section 5.2 surrounded the wake region as shown in Fig. 72. To improve computational efficiency, a coarser grid idealized the region far away from the cylinder.

Before VIV simulations are conducted, it is important to ensure that the mesh, initial and boundary conditions used to produce accurate results. The outlet was located at the right boundary, the gradients of the outflow velocity in the streamwise direction were set to zero, and the pressures were assigned a reference value of zero. On the top and bottom boundaries, a slip condition was assumed; on the side boundaries, a non-slip condition. A non-slip boundary condition was assumed also on the cylinder surface. In order to quantify the dependence of the numerical results on mesh density, again the approach of Oberhagemann and el Moctar has been employed. The numerical simulations were performed on three different grids characterized by successively finer meshes with a refinement factor of  $c = 1.25$  uniformly specified for all spatial directions and time steps. Mesh 1 described the coarsest grid; mesh 2, the medium grid; and mesh 3, the fine grid was well-matched with the factor. Table 12 lists, among other things, the number of cells, the spacing  $\Delta x$  in the flow direction, and the time step size  $\Delta t$  of these three grids, and Fig. 72 exemplarily depicts top and side views of the medium grid (mesh 2). and side views of the medium grid (mesh 2) with a total of 120 grid nodes situated along its circumference.

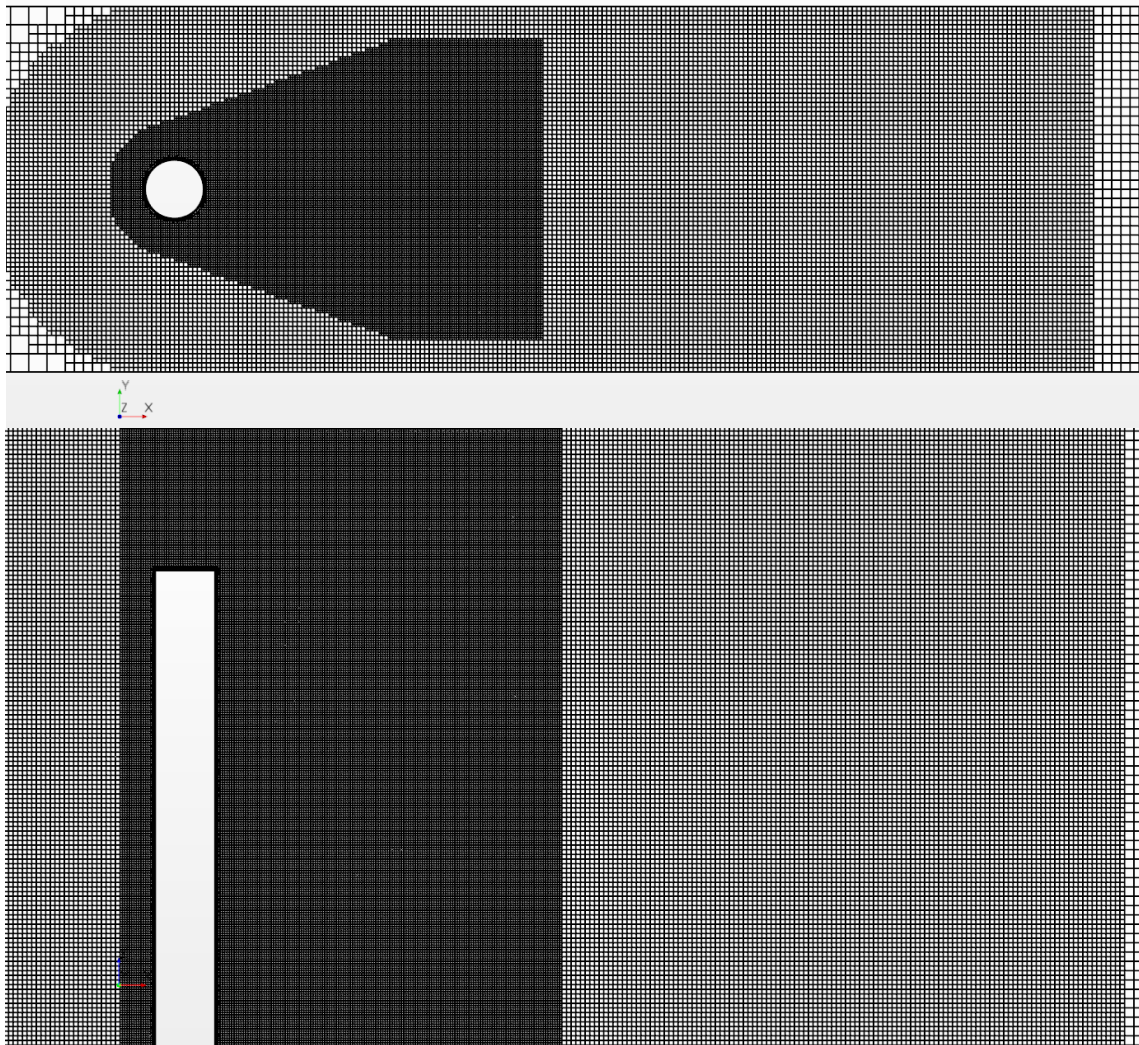


**Figure 72** Top view (top) and side view (bottom) of the computational mesh 2 on the fine grid



Moreover, in Starccm+, the SIMPLE algorithm has been applied and used the second-order time discretization. A higher-order relaxation term was used to simultaneously solve the momentum and pressure-based continuity equations. The convection terms were determined using a second-order upwind scheme. However, due to the limitation of using an upwind scheme when performing DES simulations [104], a hybrid second-order upwind/central scheme has been used, where the blending factor was computed to comply with the flow features. To improve temporal accuracy and to ensure numerical stability for all cases, the  $y^+$  value equaled unity, and the Courant-Friedricks-Lewey (CFL) number was always less than 0.2.

Table 13 shows the results for the verifications exercise concerning the drag and lift coefficients besides the shedding frequency and corresponding Strouhal number calculations achieved by the DES model for a stationary cylinder at a Reynolds number of about  $5.1 \times 10^4$ .

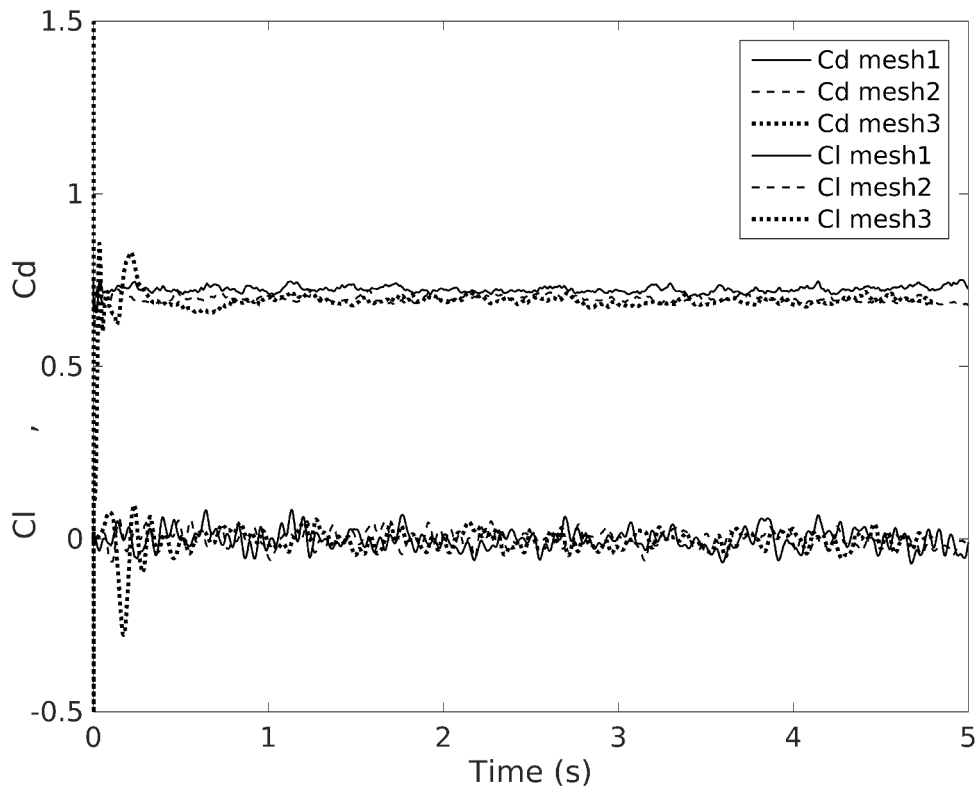


**Figure 73** Time histories of the force coefficients on a stationary cylinder calculated from the different grid meshes

**Table 13** Verification and grid convergence for a stationary cylinder obtained from different grids

<i>Element</i>	$\Delta x$ [m]	No. of cell $\times 10^6$	$\Delta t$ [sec]	$C_d$	$C_l$	$f_s$ [Hz]	$S_t$
<b>Coarse</b>	0.1	7.882	$1.0 \times 10^{-3}$	0.7169	0.037	3.2/17.3	0.13
<b>Medium</b>	0.08	15.269	$8.0 \times 10^{-4}$	0.6996	0.028	2.6/19.5	0.16
<b>Fine</b>	0.063	30.563	$6.3 \times 10^{-4}$	0.6929	0.035	2.3/16.7	0.15
<b>extrapolate</b>	-----			0.7322	0.0296		

For the sake of saving computational cost, simulations with the medium grid were carried out for further validation in this work with an estimated error of about 4.4% as indicated from table 12. In this section, computational simulations were carried out for the flexible vertical cylindrical cantilever. Three values of free stream velocities have been considered for the validation test. The velocities of 0.85, 1.6, and 1.8 m/s have been selected for the mentioned smooth cylinder case experiment.

### 6.3.2 Fluid and structure properties

The values and geometry have been determined depending on the experimental data described in detail in chapter 3.1. the commercial density for the used flexible PVC material is  $\rho_s = 1380 \text{ kg/m}^3$ , the young modulus  $E = 1200 \text{ GPa}$  and the Poisson ratio  $\nu_s = 0.34$ . Three different structural meshes have been created with the natural frequency response to investigate element types and grid size as illustrated in table 14. the cylinder has meshed with 3D quadratic hexahedral elements. The difference can be expected to be small due to less sensitivity to grids for FEM.

**Table 14 The cylinder natural frequency, for the different FE meshes**

<b>FE Grid</b>	<b>No. of elements</b>	<b>Natural Frequency</b>
<b>Coarse</b>	6750	20.253
<b>Medium</b>	18000	19.802
<b>Fine</b>	27000	19.647
<b>Experiment</b>		20.01

### 6.3.3 Results and discussion

Flow around circular cylinders at high Reynolds number is quite well documented and results from the experimental investigation are compared with results from 3D numerical analysis.

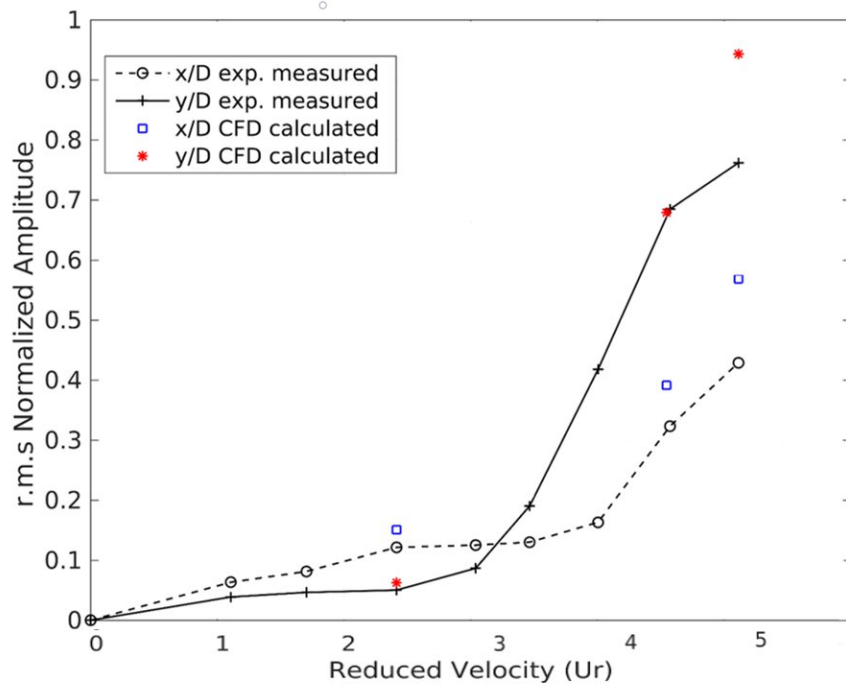
#### *Amplitude response, and motion trajectory*

The experimental results testified the validity of the numerical model used in this study in the simulation of VIV of a circular cylinder in a steady flow. In this section, the variation of the response amplitudes with the reduced velocity is explicated as presented in table 15. The calculated amplitudes and frequencies of the response showed a good agreement with the measured data. In Figure 71 the numerically calculated data points are overlaid by the shapes of the response curves in the present experimental study, indicating that the data that achieved are qualitatively similar. Here, it is worth reminding that at the free stream velocity of  $U=1.8 \text{ m/s}$ , the smooth cylinder could not withstand the fatigue stresses acted upon and it cracked.

**Table 15** The present results of inline response, transverse response, and the dominant oscillating frequency in the transverse direction compared to the experimental result

Flow velocity (m/s)	x-displ. (mm)		y-displ. (mm)		Oscillation frequency in y-dir	
	CFD	Exp.	CFD	Exp.	CFD	Exp.
0.85	4.80	3.82	1.92	1.58	3.73	16.63
1.6	11.09	10.16	19.47	21.50	7.02	7.32
1.8	14.43	13.47	28.79	23.93	7.49	8.14

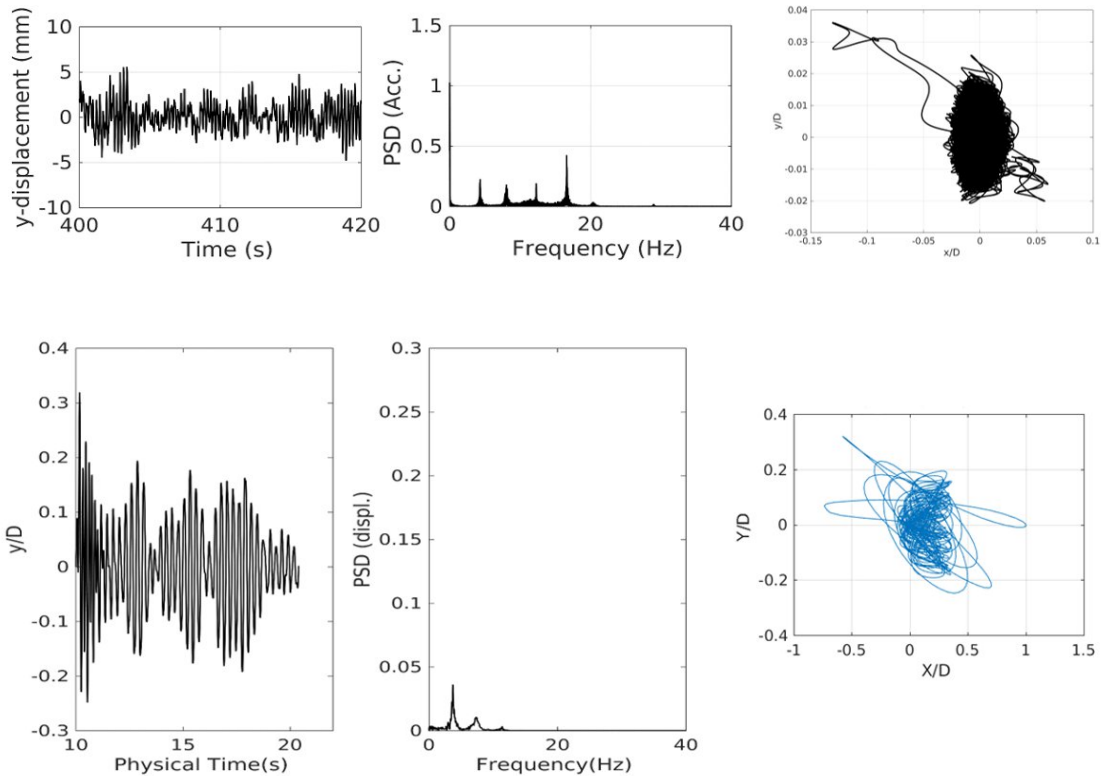
In addition, the time series at this specific speed showed the maximum measuring level of the accelerometer sensor (20 g) in the transverse direction. This could explain the overestimated variation of the cylinder transverse response obtained from CFD than that from the experimental data at this velocity. This test case demonstrates that the present numerical methods are capable of accurately predicting 2 dof VIV response of an elastically mounted circular cylinder at early subcritical Reynolds numbers.



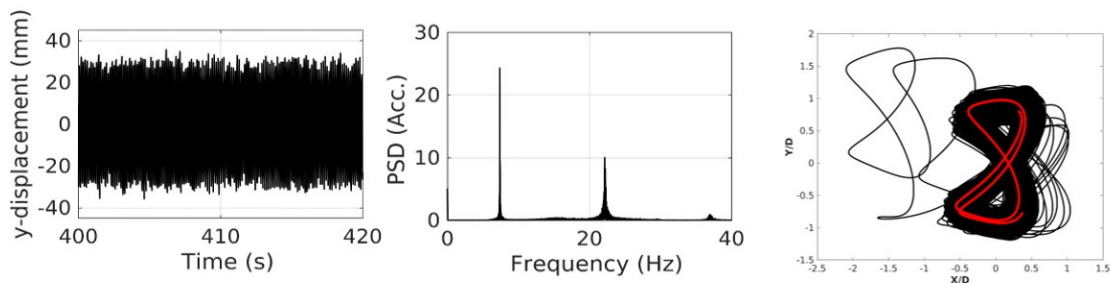
**Figure 74** Comparison of amplitude response curves between the present simulation and the experimental data measurements

Figures 75 -77 show the XY-trajectories of the displacement of the smooth cantilever cylinder, normalized by the cylinder diameter, compared with the experimental measuring data obtained for  $U_r = 2.27, 4.27,$  and  $4.81$  respectively. The 8 figure-mode was observed at high reduced velocities ( $4.27$  and  $4.81$ ) as well as occurred in the experimental tests. However similar trajectory mode shape could be seen between the numerical and experimental results, there are some differences in the shape behavior. This also could be seen from the response time series small differences.

The cause of that could be illustrated by the aid of the PSD distributions of displacement components measured and calculated from experimental and numerical investigations respectively. As shown from figures 75 -77, although the dominant frequency was approximately the same for the case of reduced velocities 4.27 and 4.81, the other frequencies associated with the dominant one do not appear in the numerical results. This was due to the difference between the experimental setup condition and the numerical one. As mentioned, some attached tools have been used to set up the smooth cylinder vertically which did not need to be represented in the numerical approach. More detail about the experimental setup had been illustrated in chapter 5.1.



**Figure 75** Comparison of amplitude response curves between the experimental data measurements (top) and the present simulation (bottom) at  $U_r = 2.27$



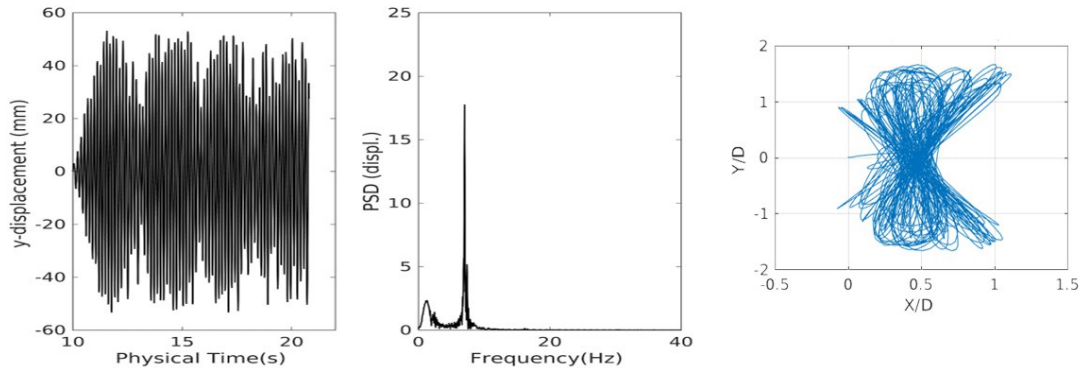


**Figure 76** Comparison of amplitude response curves between the experimental data measurements (top) and the present simulation (bottom) at  $U_r = 4.27$

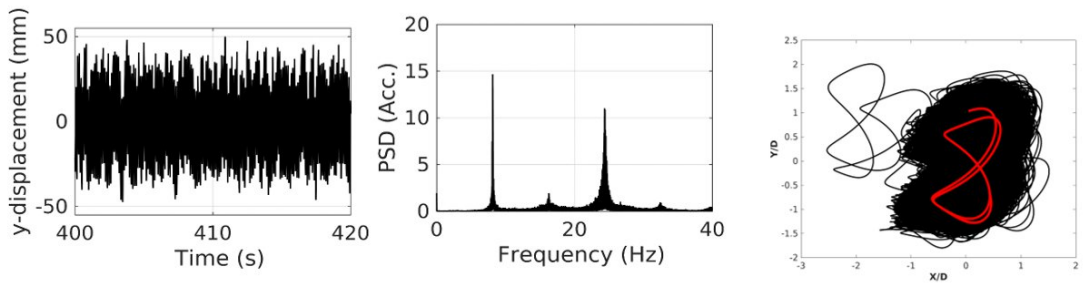


**Figure 77** Comparison of amplitude response curves between the experimental data measurements (top) and the present simulation (bottom) at  $U_r = 4.81$

### Frequency response

Another remarkable feature was the variation between the value of the dominant oscillating frequency of the numerical calculations from that obtained from experimental measurements at a lower reduced velocity value of about  $U_r = 2.27$  as presented in Fig. 75. This was a very interesting point. It was found that the dominant oscillating frequency in the transverse direction obtained from the numerical calculation is quite similar to the frequency obtained from FFT of LDV measured data from the cross-stream velocity (see Fig. 78) which represented the shedding frequency.

As shown in Fig. 75, the shedding frequency value has approximately the same value as the numerical one tabulated in table 14. This confirms that the shedding frequency is equal to the structure transverse oscillating frequency calculated from the numerical calculation even at lower velocities, however, this is not the case in the experimental tests. This could be illustrated with the aid of the power spectral density function which is a very useful tool that tells us at which frequency ranges variations are strong. At lower velocities, the shedding frequency has lower power as shown in the power spectrum density figures 75 and 77. The shedding frequency has a lower strength and influence at lower velocities and due to the experimental setup components and other components such as sensors, the shedding frequency would not be the dominant one. In the numerical investigation, only the effect of the shedding acted on the cylinder was presented despite its lower strength as shown in Fig. 75. Therefore, the following conclusion may be drawn, The shedding frequency could be obtained from the numerical calculations of the oscillating transverse frequency for all the range of velocities, however, this is not valid for the experimental measurements unless the shedding frequency is strong enough to control the motion of the cylinder. This could take place when the flow frequency approaches the structures' natural frequency. Then, most other studies assumed that transverse oscillating frequency was equal to shedding frequency [24] at lower velocities was not accurate.

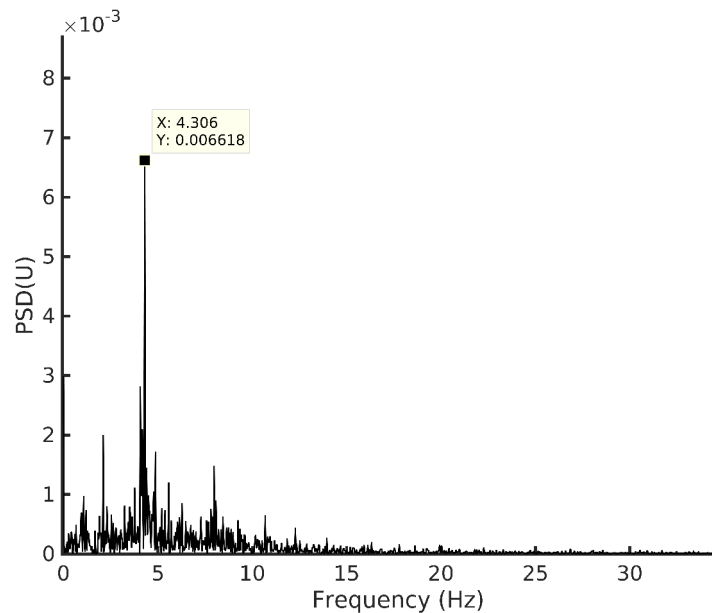


**Figure 78** Power Spectrum Density (PSD) for the flow velocity transverse flow velocity at  $U_r = 2.27$  measured by LDV.

It might be expected now that the Strouhal number be the same as measured from the flow velocity. Figure 79 presented the calculated points from the numerical investigation overlaid by the LDV measuring data. The Figure indicated that the achieved data agreed well with the past results.

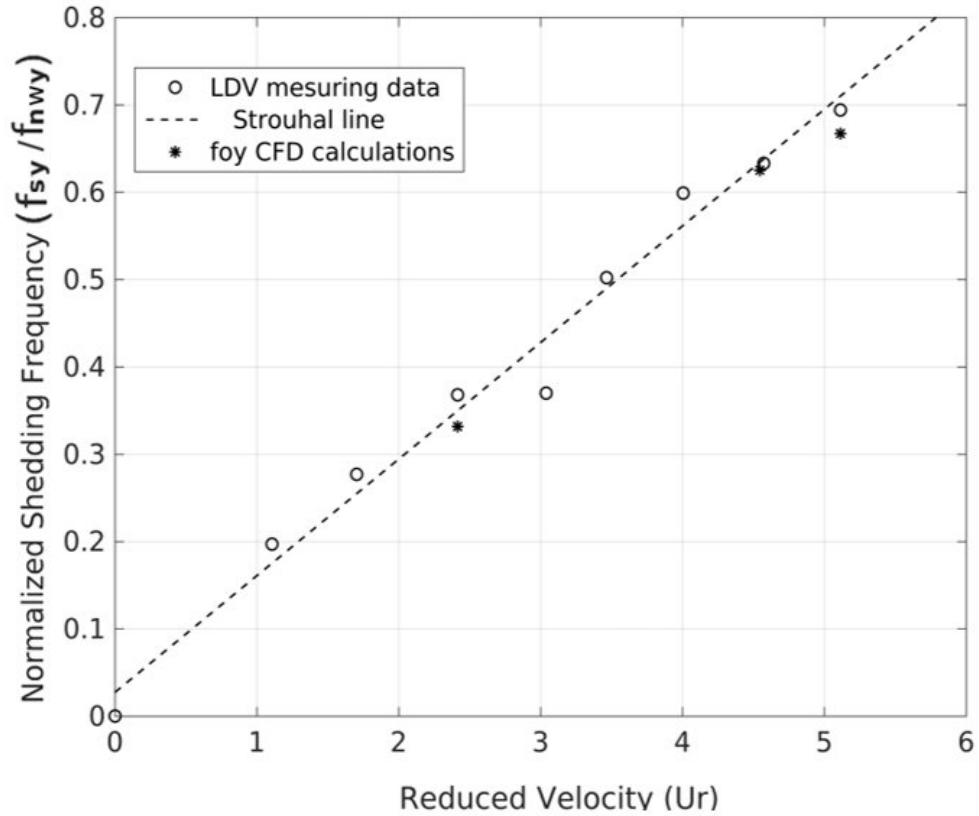


**Figure 79** Shedding frequency normalized by natural frequency against reduced velocity

Furthermore, a comparison between the values of drag and lift forces calculated from the numerical and experimental investigations respectively has been presented in table 16.

**Table 16** The present results of the drag forces, and the lift forces compared to the experimental result

Item	CFD		Exp.	
	$F_x$	$F_y$	$F_x$	$F_y$
$U=0.85$ m/s	8.64	3.63	8.72	3.96
$U=1.6$ m/s	21.5	15.34	40.66	21.09
$U=1.8$ m/s	28.03	17.66	57.11	26.04

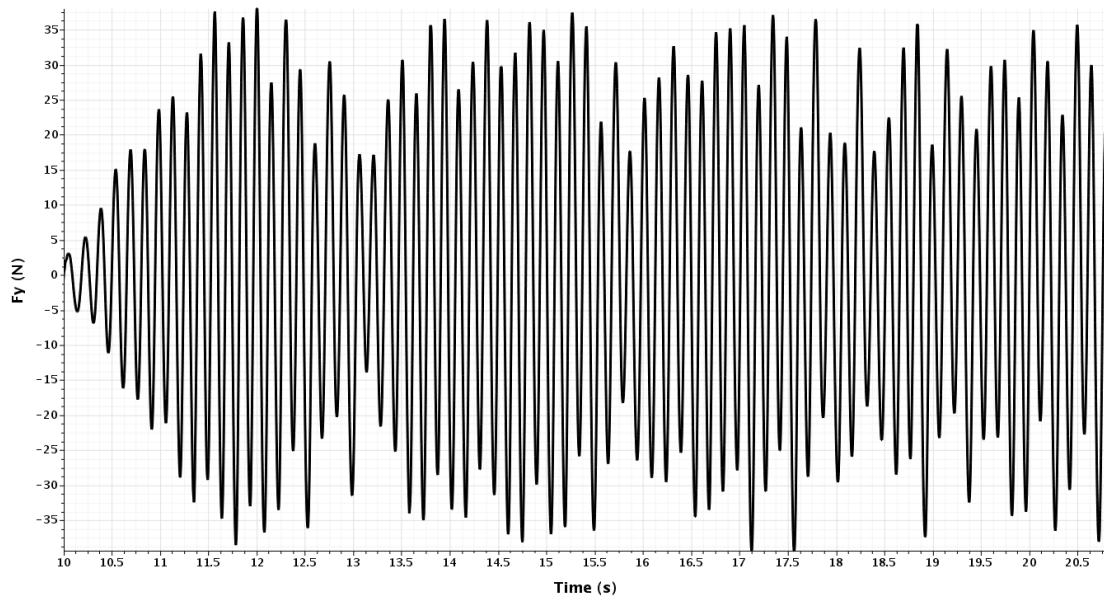
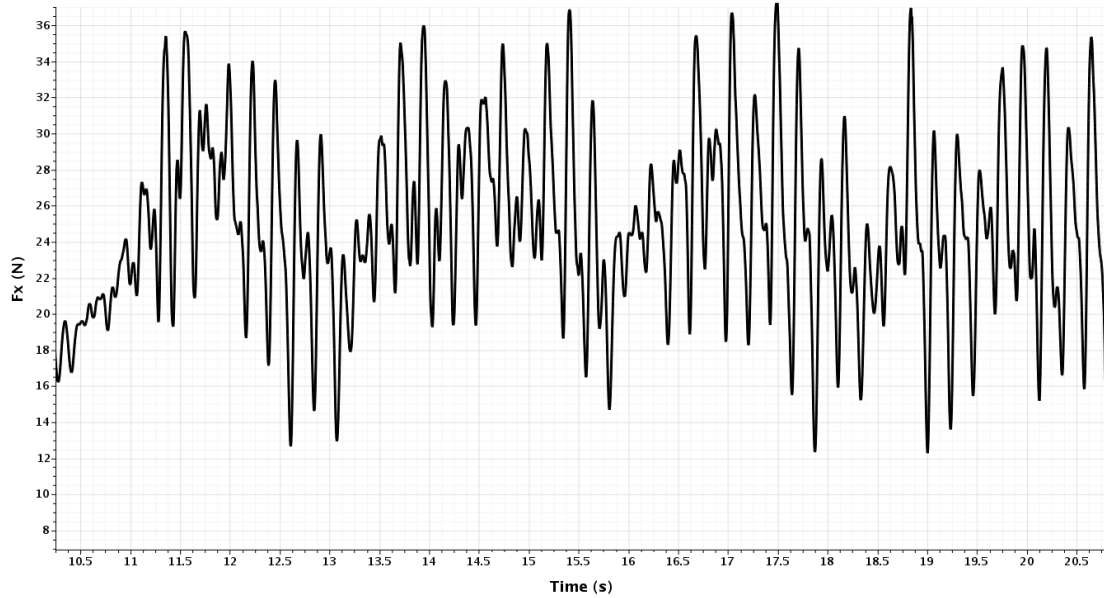


**Figure 80** Forces time histories ( medium grids) at  $U=1.6$  m/s; drag force, top; lift force, bottom

Figure 80 provided a sample of the time series histories for both the drag and lift forces of a flexible cylinder. It is worth noting here that similar characteristics corresponding to experimental forces responses have been presented in the numerical results. Although the lift forces have lower values than observed for the drag forces in both cases, however, the responses in the transverse direction were larger. Thus due to that, the lift forces were applied on an approximately quarter-elliptic shape beam tends to a straight cantilever beam as a result of the applied drag forces and the mechanical characteristics of the light cylindrical model. Studying the bending of beams, the deflection for this standard case founded much larger than a straight cantilever beam loaded by the same force [166].

In the present section comparison of before and after structure interaction has been illustrated. Figure 81 presented the time-averaged velocity streamlines on the x-y plane (Fig. 81 top), and on the x-z plane (Fig.81 bottom) at a symmetry plane ( $Y = 0$ ) for the flexible and rigid cases at



flow velocity 1.6 m/s. The vibrating movements decreased the vortex formation length near the cylinder wake region. As shown in Fig. 81 top, a non-symmetry two distinct spiral nodes are being observed in the rigid case (left) however, the flexible case shows two distinct non-symmetrical spiral nodes but near the wake, region than found in the rigid case. The dominant spiral nodes that exist in the flexible case are caused by dominant Von Kármán vortex sheets that are shed from the cylinder. It appears that the flow has wrapped around onto the back of the cylinder before separating and moving downstream.

It is noted that the high Re number leads to a stronger negative pressure behind the cylinder. Besides, the recirculation region downstream from the tip of the cylinder and the corresponding downwash was created due to the turning of flow towards the bottom wall.

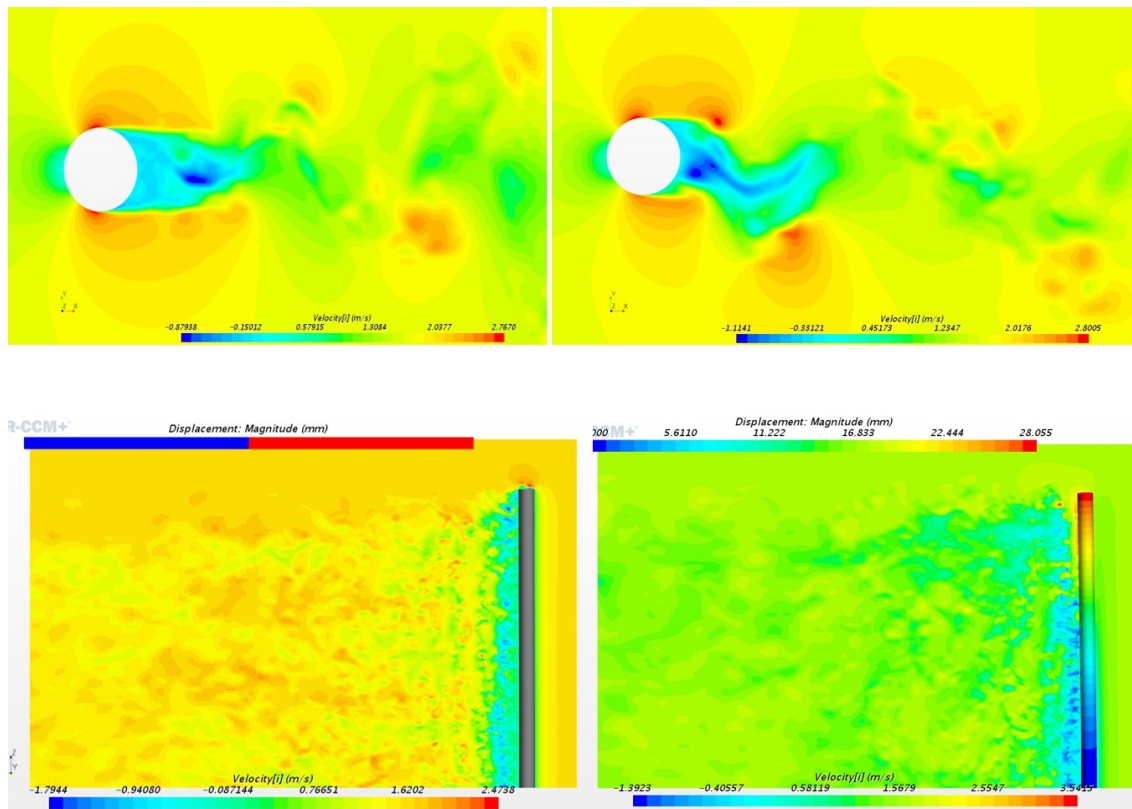


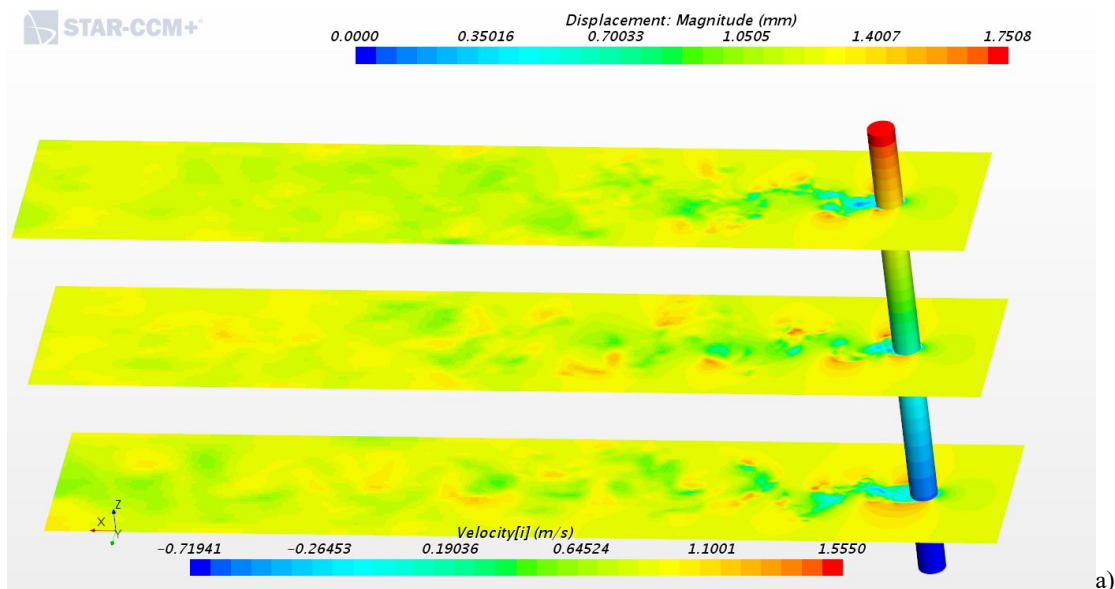
**Figure 81** Direct comparison between the stream-lines of the mean velocity, at the midspan, between the rigid cylinder (left) and the flexible cylinder (right), in an x-y plane (top), and, in an x-z plane (bottom)

Due to the high strength of this tip vortex, the downwash flow from the tip reaches the ground. On the contrary, the vertical dimension of the upwash recirculation region has been observed and monotonically decreased for the flexible case as shown in Fig.81 bottom. Moreover, the curvature of the cylinder, caused by the flexible case, results in a marginal shift in the downwash recirculation region center and the impingement point where the upwash and downwash meet. The differences between the mean flow for the rigid and flexible case have a significant effect on the mean drag over the cylinder. The value of the mean drag has been increased from a value of 0.688 to a value of 1.0313. The increase of the drag was probably due to the increase of the projected area of the flexible cylinder in one vibrating period.

In order to understand well the dynamic response of a flexible cylinder, 3D simulations of the flow past a flexible circular cylinder at the three tested flow velocities were carried out for comparison.

Compared to the rigid case, the flexible cylinder shows its shape deformation due to the unsteady forces related to vortex shedding. With closer observation, three sections of the cylinder along the spanwise direction were picked out for comparison. They are  $z/L = 0.2, 0.5$  and  $0.8$  as shown in Fig. 82. While the wake of the rigid cylinder maintained the ordinary Kármán vortex and a small quantity of stream-wise vortex pairs, the wake along the span-wise direction of the flexible cylinder was disordered. The vortex structure exhibited much more 3D instability.

This 3D instability was due to two main reasons. The first reason, the vibrating movements of the flexible cylinder, therefore, the wake patterns were expected to vary in different sections along the cylinder length as presented for each flow velocity in Fig. 82. The same characteristic has been observed by Flemming and Williamson (2005) [90] and J. Huera Huarte [167]. They also showed a 2P mode with two vortex pairs per cycle in the wake of the vibrating flexible cylinder especially at the middle section and down to the cylinder end support, the 2P mode changed into a 2S mode with a single vortex per cycle. These characteristics were not very clear in the test cases due to the light structure parameters of the cylinder and the effect of the free end condition. Three vortex pairs per cycle could be seen especially at the mid-span section for the tested case which increased with the flow velocity. The second reason was the influence of the free end condition of the cantilever cylinder model. The strength of the downwash flow from the cylinder tip increased with the flow velocity. This could be seen in the mid-span section at  $z/D = 0.8$  for each flow velocity case. These end vortex cells distorted the ordinary vortex shedding patterns along the vertical length of the cylinder. They normally attenuate the vortex pairs per cycle near the top and down corresponding to their strength.



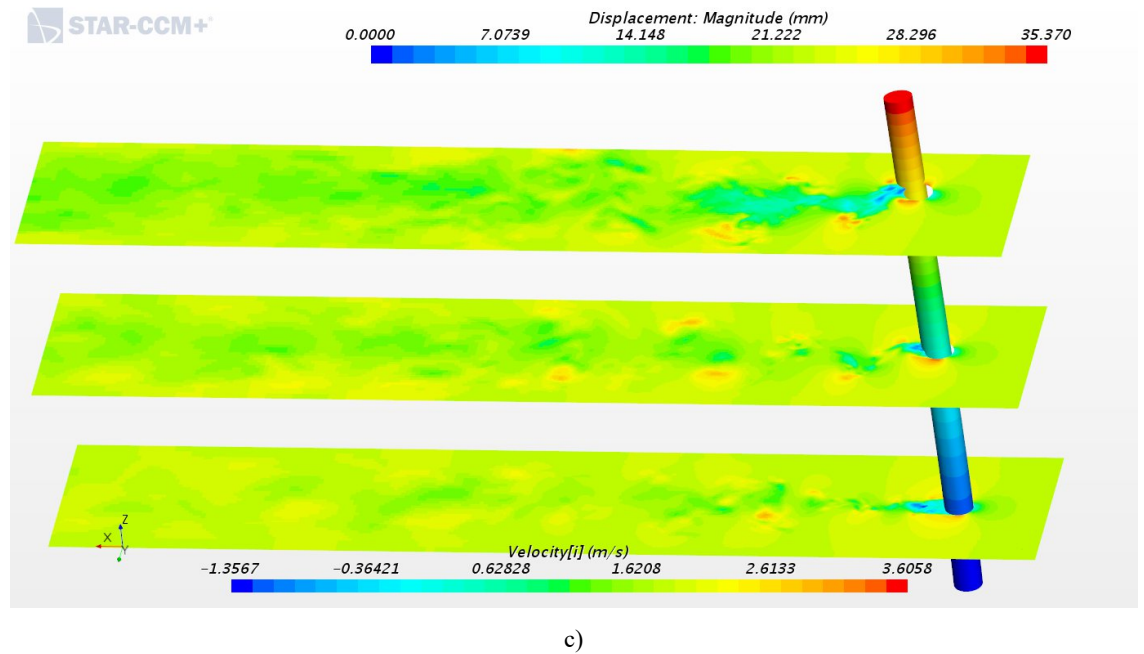
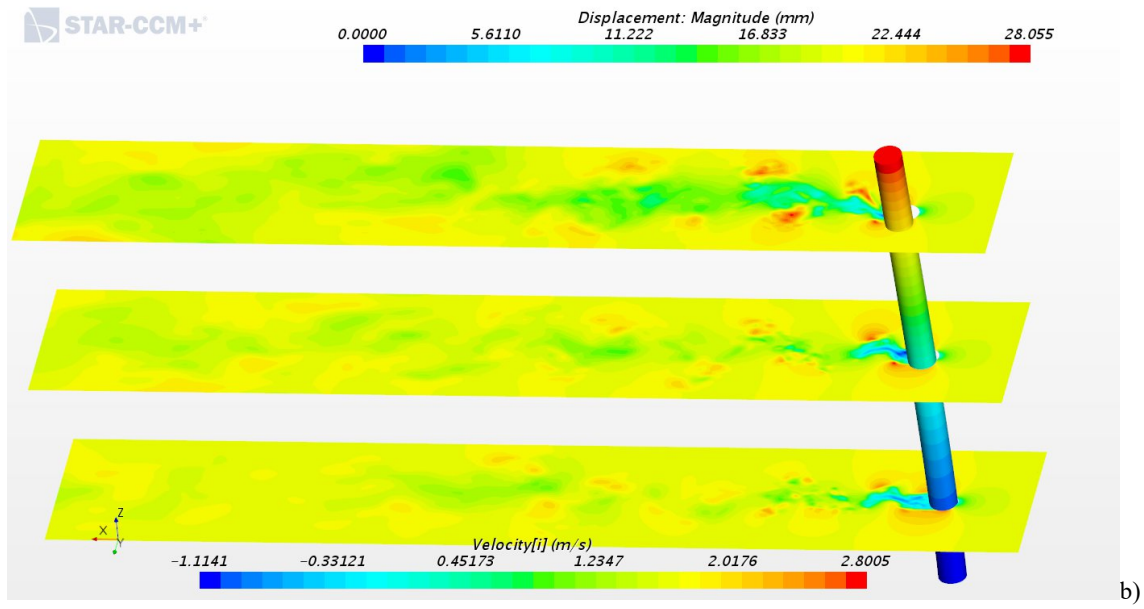


**Figure 82** Instantaneous mean velocity at different z-position: a) at  $U=0.85$  m/s, b) at  $U=1.6$  m/s, and c) at  $U=1.8$  m/s.

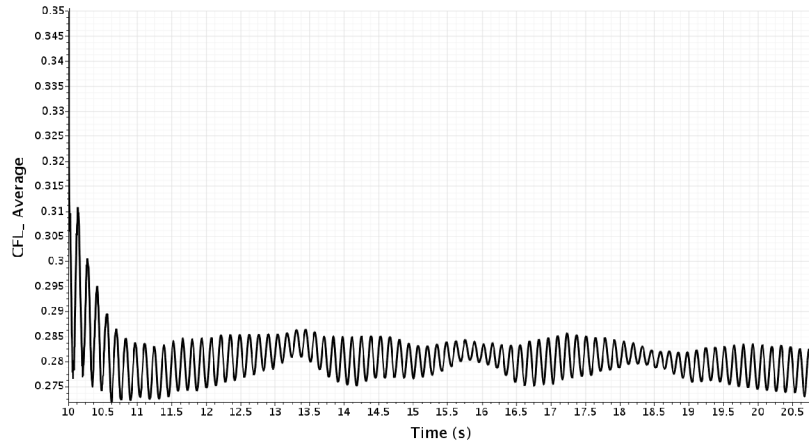


**Figure 83** Average Courant- Friedrichs-Lewey (CFL) number for numerical calculations at  $U=0.85$

During the flexible cylinder numerical calculations, the Courant- Friedrichs-Lewey (CFL) number with lower values was maintained. Besides,  $y^+$  value was equal approximately to unity to improve both the temporal accuracy and the numerical scheme stability, in all case studies.

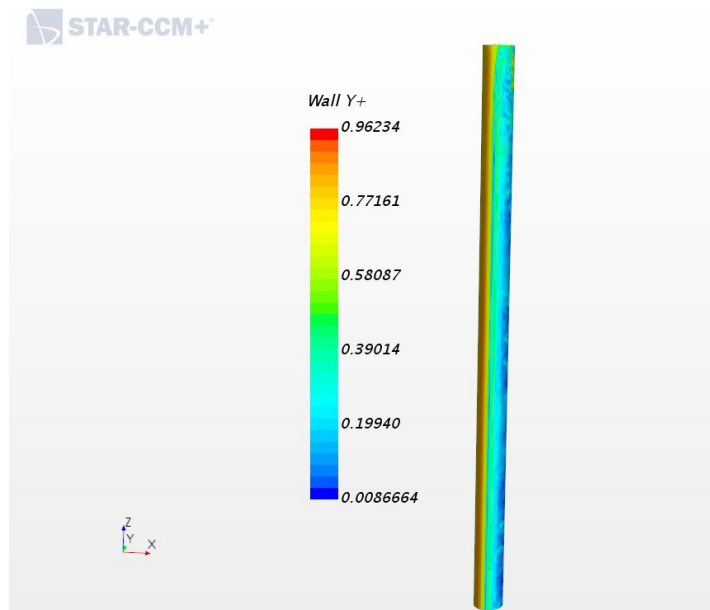


**Figure 84**  $y^+$  ranges on the cylinder for the numerical calculations at  $U= 1.6$

Furthermore, The level of residuals has shown the same criteria, as observed in Fig. 55, through all of the flexible numerical cases in the present study. This confirms that the high level of residuals indicates that the  $10^{-6}$  limits as an acceptable level of residuals, for the case of unsteady flow a round cylinder, does not more valid and needs further review for the case of the high level of turbulence in case of three-dimensional calculations. Further investigations are needed for detailed study of such types of problems.

## 7. Conclusions

Based on the experimental and numerical results, the present study has introduced a novel technique that could be used to conservatively suppress VIV for a circular cylinder of at least the subcritical  $Re$  ranges. Besides, throughout this thesis, the fundamentals of VIV were investigated through a model test experimental study and numerical simulations of FSI problems to verify and validate a commercially available FSI numerical code with the experimental data.

In the experiments, each model case was tested for comparison to the response amplitudes, frequency response, and acting forces by an accelerometer, and 6DOF loadcell. In the numerical investigation, 3D simulations of the flow around a circular cylinder with and without different attached fin plate locations were presented. In addition, the mutual effect of the hydrodynamic loads acting on the structure and the effect of the displacement response on the fluid was presented, and 3D simulations were developed into a self-consistent experimental-numerical investigation. The following conclusions may be drawn

### Experimental Work

Although it is difficult to achieve a fully suppressed VIV response below the critical mass ratio, in the present investigation, strong suppression was obtained. No clear jump in response amplitudes occurred; however, a delay in the onset of the abrupt change in the slope of response behavior was observed for all the tested models at different velocities.

The cylinder model with fin plates located at  $110^\circ$  from the front stagnation point showed a strong VIV suppression reduction percentage in both in-line and transverse response amplitudes by 82% and 75%, respectively. It appears that  $110^\circ$  fin plates have a profound effect on the VIV characteristics even during synchronization, which was reached at a reduced velocity of approximately 5 for this  $110^\circ$  attached fin plate model without any remarkable influence. The  $110^\circ$  location may cause out-of-phase vortices, leading to weakness of the shedding vortex with a negligible effect on the structure. Further studies are planned using DPIV to consider the effects on vortex formations and modes.

Furthermore, the  $80^\circ$  and  $90^\circ$  attached fin plates showed a similar reduction effect, with approximately 32.4% in the transverse direction and about 67% for the in-line direction. At a reduced velocity of  $U_r = 3$ , significant features took place, causing the drag forces and lift forces to change their slope abruptly for all the models, although no remarkable change could be observed in the response behavior. Further investigations with special visualization tools are needed to study this behavior.

Besides, the use of this fin plate configuration that reduced the response amplitudes also limited the range of these oscillations, which is of considerable practical significance in that large oscillation itself may damage a structure rather than fatigue related frequencies, particularly for light-weight cylindrical structures

In summary, these fin plate arrangements may result in different vortex shedding modes along the span of the cylinder, resulting in strong VIV suppression, at least for the subcritical range that was tested in this study (Reynolds numbers ranged between  $1.4 \times 10^4$  and  $8.0 \times 10^4$ ).

Apart from the structural parameters, the influence of tip vortex frequency on VIV and its correlation with vortex shedding requires further investigation. Results, presented in chapter 5.2, revealed that the root mean squares displacement at the cylinder top increased with higher

values of the reduced velocity. However, a distinct peak appeared at a frequency ratio equal to unity, demonstrating the effect of the tip vortex in reducing the synchronization range frequencies.

The further increase in displacement at higher frequencies is thought to be due to the free end flow conditions, represented ECIV, which confirmed the independence of the cylinder damping characteristic. Furthermore, measurements of the oscillating frequency in the transverse direction of the cylinder showed that various frequencies depended on the reduced velocity. This could have been caused by end effects at higher Re values and the associated tip vortices. The axial frequency seemed to coincide with its natural frequency in all the test domains, which meant that in the streamline direction, the cylinder was in the lock-in region.

The discrepancy of the lift coefficient and the discontinuous jumps at phase changes between vibration oscillations in the streamline and transverse directions and the associated aerodynamic forces represented the nonlinearity in the FSI process. The flow visualizations confirmed these features and showed the generation of different vortex wake modes. These results are caused by the integration of large damping ratios, higher Re values, and free end flow conditions.

### **Numerical Work**

First, 3D URANS numerical flow simulations of a fixed circular cylinder subject to VIV were performed to assess the capability of the SST  $k-\omega$  and DES turbulence models. The simulations were performed for different grid sizes of uniform refinements in all directions (space and time) at a constant Courant number and then compared with the experimental results of Khalak and Williamson [1].

Obtained r.m.s. values of drag and lift coefficients,  $S_t$  values, the boundary-layer separation angle, and field plots. These results were compared with experimental and numerical results from the literature. The objective was to demonstrate, in some detail, the capabilities and flaws of these two turbulence models. The results indicated that although the numerical solutions with the SST  $k-\omega$  model provided fairly good results, simulations with the DES turbulence model correlated more closely to experimental measurements. However, neither space nor the time step sizes were thought to be fine enough for an accurate DES-based prediction of this flow. Nevertheless, the results from the DES model were consistent and compared favorably to those documented in the literature as they captured the alternating shedding frequencies, which were not predicted with the SST  $k-\omega$  model.

Furthermore, the residual levels, calculated to evaluate iterative errors, were affected neither by the variation of the different grid and time step sizes nor by the turbulence models. The level of residuals was nearly the same throughout all of the numerical calculations conducted here. Indeed, the residuals were acceptable for URANS simulations of the flow around the cylinder.

Second, a numerical analysis of the 3D flow simulations of a stationary circular cylinder subject to VIV was performed using DES turbulence models. The results were compared with experimental and numerical results from the literature. The results show that for engineering design purposes, They presented a satisfactory qualitative agreement with the published experimental data and numerical results in the supercritical flow regimes for Re 2,000–14,000. The detailed numerical study of flow over a stationary circular cylinder with six newly developed VIV suppression methods was then tested. Several conclusions can already be drawn.

Except for the asymmetric case (model 6), the remarkable features were as follows:

- The shedding vortices cannot roll from one side to the other side along the cylinder's rear surface due to prevention by the fin plate, and thus they are forced to process along the path downstream. Therefore, with the fin plate, the shear layer is greatly influenced and extended.
- If the cylinder is provided with the straight attached fin plates, then the plate height will control the shear layer separation, and the vortices will interact at a greater distance from the cylinder body than the smooth cylinder. However, greater drag will occur as a result of the larger cross-section.
- Using inclined fins has a remarkable effect than the larger frontal area on decreasing the drag force when compared with the same plate length. Furthermore, suppressing lift force was observed to have a profound effect.
- It was of interest to investigate the influence of the separated equidistance spaces between the fin plates along with the cylinder. The vortex shedding does not occur uniformly along the length of the cylinder, but rather in cells, and the resultant force acting on the cylinder over its total length would not be uniformly distributed.
- Furthermore, the computed drag and lift coefficients decreased slightly as  $Re$  increased throughout the case study range. This behavior is due to the presence of fin plate specifications and their effect on the vortex formation mechanism as  $Re$  increases. Further experimentation is needed for the higher range.

For the asymmetric model, although the plate length was very small, a significant increase in pressure and lift force coefficient associated with higher frequency intensity was been observed.

The present results presented a reliable and useful engineering assessment tool for the design of VIV for a flexible cylinder using such models. These models are expected to influence the vortex formation mechanism and loads on the cylindrical structure; at the least, it will result in a delay of the onset of the vibration due to the decrease in vortex strength.

Finally, one of the most important areas for future research is dynamic validation. In the present work, a new turbulent FSI validation test case was presented. A detailed analysis of the FSI for a 3D finite smooth cylinder, based on experimental data, was performed by treating the structure as a flexible, continuous object. Results of the investigation agreed with experiments, both qualitatively and quantitatively. Numerical results were able to predict the hydrodynamic forces and the corresponding structure responses in both directions. Furthermore, to visually present details of VIV features and flow patterns. FSI numerical investigation also provides the capabilities and flaws of these features of vortex shedding from a fixed rigid and flexible cylinder. One key point is to distinguish between shedding and oscillating frequency. Based on numerical and experimental investigation, the shedding frequency could be obtained from the numerical calculations of the oscillating transverse frequency for the full range of velocities. However, this is not valid for the experimental measurements unless the shedding frequency is strong enough to control the motion of the cylinder. This can take place when the flow frequency approaches the structure's natural frequency.

### **Outlook and Recommendations**

Based on the present study and literature review done on the VIV for different aspect ratios, several recommendations for future work can be drawn as below:

1. Demonstrating alternative geometrical parameters would have much interest in recent times.
2. Further investigations with special visualization tools are needed to study this behavior.

3. Further experimental studies have been planned to consider the effects of using these models in a wide range of Reynolds numbers.
4. Furthermore, a numerical validation for the introduced VIV suppression device is highly recommended. Such validation will play two main roles in terms of validation of the presented solver as well as developing tests for new VIV suppression devices.



## 8. Bibliography

- [1] J. B. V. Wanderley, G. H. B. Souza, S. H. Sphaier, and C. Levi, “Vortex-induced vibration of an elastically mounted circular cylinder using an upwind TVD two-dimensional numerical scheme,” *Ocean Eng.*, vol. 35, no. 14–15, pp. 1533–1544, 2008.
- [2] M. Zhao, L. Cheng, and H. An, “Numerical investigation of vortex-induced vibration of a circular cylinder in transverse direction in oscillatory flow,” *Ocean Eng.*, vol. 41, pp. 39–52, 2012.
- [3] E. Wang, Q. Xiao, and A. Incecik, “Three-dimensional numerical simulation of two-degree-of-freedom VIV of a circular cylinder with varying natural frequency ratios at  $Re=500$ ,” *J. Fluids Struct.*, vol. 73, pp. 162–182, 2017.
- [4] N. B. Khan, Z. Ibrahim, L. T. T. Nguyen, M. F. Javed, and M. Jameel, “Numerical investigation of the vortex-induced vibration of an elastically mounted circular cylinder at high Reynolds number ( $Re = 104$ ) and low mass ratio using the RANS code,” *PLoS ONE*, vol. 12, no. 10, 2017.
- [5] R. Jin, M. Liu, B. Geng, X. Jin, H. Zhang, and Y. Liu, “Numerical investigation of vortex induced vibration for submerged floating tunnel under different Reynolds numbers,” *Water (Switzerland)*, vol. 12, no. 1, 2020.
- [6] P. Bearman, “Vortex Shedding from Oscillating Bluff Bodies,” *Annu. Rev. Fluid Mech.*, vol. 16, no. 1, pp. 195–222, 1984.
- [7] P. D. dos S. Conceição, “Numerical simulation of two-degree-of-freedom vortex induced vibration in a circular cylinder with OpenFOAM,” NOVA University of Lisbon, 2016.
- [8] R. King, “A review of vortex shedding research and its application,” *Ocean Eng.*, vol. 4, no. 3, pp. 141–171, 1977.
- [9] T. Sarpkaya, “A critical review of the intrinsic nature of vortex-induced vibrations,” *J. Fluids Struct.*, vol. 19, no. 4, pp. 389–447, 2004.
- [10] R. A. Skop and O. M. Griffin, “On a Theory for the Vortex-Excited,” *J. Sound Vib.*, vol. 41, no. 3, pp. 263–274, 1975.
- [11] C. Norberg, “An experimental investigation of the flow around a circular cylinder: Influence of aspect ratio,” *J. Fluid Mech.*, vol. 258, no. January 1994, pp. 287–316, 1994.
- [12] C. H. K. Williamson, “The existence of two stages in the transition to three-dimensionality of a cylinder wake,” *Phys. Fluids*, vol. 31, no. 11, p. 3165, 1988.
- [13] C. H. K. Williamson and R. Govardhan, “Vortex-Induced Vibrations,” no. *Annu. Rev. Fluid Mech.* 2004. 36:413–55, 2004.
- [14] B. M. Sumer and J. Fredsoe, *Hydrodynamics Around Cylindrical Structures*, vol. 26. World Scientific Publishing Co. Pte. Ltd, 2006.
- [15] S. Chen, *Flow-Induced Vibration Of Circular Cylindrical Structures*, Argonne National Laboratory, 1985.
- [16] K. Kaja and Y. Xiang, “Vortex-Induced Vibrations of Circular Cylinders in Steady and Oscillatory Flow,” Western Sydney University, 2015.

- [17] X. K. Wang, C. Wang, Y. L. Li, and S. K. Tan, "Flow patterns of a low mass-damping cylinder undergoing vortex-induced vibration : Transition from initial branch and upper branch," vol. 62, pp. 89–99, 2017.
- [18] V. Strouhal, "Ueber eine besondere Art der Tonerregung," *Ann. Phys.*, vol. 241, no. 10, pp. 216–251, 1878.
- [19] F. S. Hover and M. S. T. High, "High Harmonic Forces and Predicted Vibrations from Forced In-line and Cross-flow Cylinder Motions," 2015.
- [20] K. Vikestad, "Multi-frequency Response of a Cylinder Subjected to Vortex Shedding and Support Motions," Faculty of Marine Technology Norwegian University of Science and Technology, 1998.
- [21] K. Y. Billah and R. H. Scanlan, "Resonance, Tacoma Narrows bridge failure, and undergraduate physics textbooks," *Am. J. Phys.*, vol. 59, no. 2, pp. 118–124, 1991.
- [22] M. Matsumoto, H. Shirato, T. Yagi, R. Shijo, A. Eguchi, and H. Tamaki, "Effects of aerodynamic interferences between heaving and torsional vibration of bridge decks: The case of Tacoma Narrows Bridge," *J. Wind Eng. Ind. Aerodyn.*, vol. 91, no. 12–15, pp. 1547–1557, 2003.
- [23] G. Moe and Z. Wu, "The Lift Force on a Cylinder Vibrating in a Current," *J. Offshore Mech. Arch. Eng.*, vol. 112, pp. 297–303, 1990.
- [24] A. Khalak and C. H. K. Williamson, "Motions, Forces And Mode Transitions In Vortex-Induced Vibrations At Low Mass-Damping," *J. Fluids Struct.*, vol. 13, no. 7–8, pp. 813–851, 1999.
- [25] S. A. Hall, "Vortex-induced vibrations of structures.," *Struct. Eng. world Congr.*, pp. 2–7, 1981.
- [26] R. Govardhan and C. H. K. Williamson, "Modes of vortex formation and frequency response for a freely-vibrating cylinder," *J. Fluid Mech.*, vol. 420, no. 420, pp. 85–130, 2000.
- [27] N. M. R. Shaharuddin and I. Z. Mat Darus, "Experimental study of vortex-induced vibrations of flexibly mounted cylinder in circulating water tunnel," *Acta Mech.*, vol. 226, no. 11, pp. 3795–3806, 2015.
- [28] A. Ñ. Laneville, "On vortex-induced vibrations of cylinders describing X – Y trajectories," vol. 22, pp. 773–782, 2006.
- [29] C. H. K. Williamson and A. Roshko, "Vortex Formation In The Wake Of An Oscillating Cylinder," *J. Fluids Struct.*, vol. 2, pp. 355–381, 1988.
- [30] D. Jeon and M. Gharib, "On Circular Cylinders Undergoing Two-Degree-Of-Freedom Forced MotionS," *J. Fluids Struct.*, vol. 15, pp. 533–541, 2001.
- [31] N. Jauvtis and C. H. K. Williamson, "Vortex-induced vibration of a cylinder with two degrees of freedom," *J. Fluids Struct.*, vol. 17, no. 7, pp. 1035–1042, 2003.
- [32] N. Jauvtis and C. H. K. Williamson, "The effect of two degrees of freedom on vortex-induced vibration at low mass and damping," *J. Fluid Mech.*, vol. 509, no. 509, pp. 23–62, 2004.
- [33] R. Govardhan and C. H. K. Williamson, "Critical mass in vortex-induced vibration of a cylinder," *Eur. J. Mech. B/Fluids*, vol. 23, no. 1, pp. 17–27, 2004.

- [34] R. Govardhan and C. H. K. Williamson, "Resonance forever: Existence of a critical mass and an infinite regime of resonance in vortex-induced vibration," *J. Fluid Mech.*, vol. 473, no. 473, pp. 147–166, 2002.
- [35] J. M. Dahl, F. S. Hover, and M. S. Triantafyllou, "Two-degree-of-freedom vortex-induced vibrations using a force assisted apparatus," *J. Fluids Struct.*, vol. 22, no. 6–7, pp. 807–818, 2006.
- [36] T. L. Morse and C. H. K. Williamson, "The effect of Reynolds number on the critical mass phenomenon in vortex-induced vibration," *Phys. Fluids*, vol. 21, no. 4, 2009.
- [37] J. M. Dahl, F. S. Hover, M. S. Triantafyllou, and O. H. Oakley, "Dual resonance in vortex-induced vibrations at subcritical and supercritical Reynolds numbers," *J. Fluid Mech.*, vol. 643, pp. 395–424, 2010.
- [38] R. D. Blevins and C. S. Coughran, "Experimental Investigation of Vortex-Induced Vibration in One and Two Dimensions With Variable Mass, Damping, and Reynolds Number," *J. Fluids Eng.*, vol. 131, no. 10, pp. 101202-1 :101202-7, 2009.
- [39] N. Srinil, H. Zanganeh, and A. Day, "Two-degree-of-freedom VIV of circular cylinder with variable natural frequency ratio: Experimental and numerical investigations," *Ocean Eng.*, vol. 73, pp. 179–194, Nov. 2013.
- [40] A. Modir, M. Kahrom, and A. Farshidianfar, "Mass ratio effect on vortex-induced vibration of a flexibly mounted circular cylinder, an experimental study," *Int. J. Mar. Energy*, vol. 16, pp. 1–11, 2016.
- [41] M. Venugopal, "Damping and Response Prediction of a Flexible Cylinder in a Current," Ph.D. thesis, Ocean Engineering Department, MIT, 1996.
- [42] K. Vikestad, C. M. Larsen, and J. K. Vandiver, "Norwegian Deepwater Program: damping of vortex-induced vibrations," *Proc. Annu. Offshore Technol. Conf.*, vol. 2, pp. 577–583, 2000.
- [43] J. T. Klamo, A. Leonard, and A. Roshko, "The effects of damping on the amplitude and frequency response of a freely vibrating cylinder in cross-flow," *J. Fluids Struct.*, vol. 22, no. 6–7, pp. 845–856, 2006.
- [44] M. H. Bahmani and M. H. Akbari, "Effects of mass and damping ratios on VIV of a circular cylinder," *Ocean Eng.*, vol. 37, no. 5–6, pp. 511–519, 2010.
- [45] J. K. Vandiver, "Damping Parameters for flow-induced vibration," *J. Fluids Struct.*, vol. 35, pp. 105–119, 2012.
- [46] E. Garcia, C. Chang, H. Park, and M. Bernitsas "Effect of Damping on Variable Added Mass and Lift of Circular Cylinders in Vortex-Induced Vibrations," 2014 *Ocean. - St. John's*, no. Viv, pp. 1–5, 2014.
- [47] J. Kim Vandiver and Z. Rao, "Omae2015-41296 Estimation of the Damping Parameter Governing the Viv of Long Flexible," pp. 1–7, 2015.
- [48] K. Raghavan and M. M. Bernitsas, "Experimental investigation of Reynolds number effect on vortex induced vibration of rigid circular cylinder on elastic supports," *Ocean Eng.*, vol. 38, no. 5–6, pp. 719–731, 2011.
- [49] J. Carberry, J. Sheridan, and D. Rockwell, "Controlled oscillations of a cylinder: Forces and wake modes," *J. Fluid Mech.*, vol. 538, no. September, pp. 31–69, 2005.

- [50] T. Kokkinis, R. E. Sandstrom, H. T. Jones, H. M. Thompson, and W. L. Greiner, "Om Ae2004-51546 Development of a Stepped Line Tensioning Solution for Mitigating Vim Effects in Loop Eddy Currents," *Response*, pp. 1–10, 2004.
- [51] Vandiver, "Dimensionless parameters important to the prediction of vortex-induced vibration of long, flexible cylinders in ocean currents," *Fluids Struct.*, vol. 7, pp. 423–455, 1993.
- [52] M. M. Zdravkovich, "Review and classification of various aerodynamic and hydrodynamic means for suppressing vortex shedding\*," *Wind Eng. Ind. Aerodyn.*, vol. 7, pp. 145–189, 1981.
- [53] D. Livanos, "Investigation of Vortex-Induced Vibrations on Wind Turbine Towers," Delft University of Technology, 2018.
- [54] B. J. Vickery and R. D. Watkins, *Flow-induced vibration of cylindrical structures*, vol. ed. R. Sil. Pergamon Press LTD, 1964.
- [55] E. R. Ranjith, A. S. Sunil, and L. Pauly, "Analysis of flow over a circular cylinder fitted with helical strakes," *Procedia Technol.*, vol. 24, pp. 452–460, 2016.
- [56] A. Roshko, "On the Wake and Drag of Bluff Bodies," *J. Aeronaut. Sci.*, vol. 22, no. 2, pp. 124–132, 1955.
- [57] C. J. Apelt, G. S. West, and A. A. Szewczyk, "The effects of wake splitter plates on the flow past a circular cylinder in the range  $104 < R < 5 \times 10^4$ ," *J. Fluid Mech.*, vol. 61, no. 1, pp. 187–198, 1973.
- [58] K. Kwon, And, and H. Choi, "Control of laminar vortex shedding behind a circular cylinder using tabs," *J. Mech. Sci. Technol.*, vol. 28, no. 5, pp. 1721–1725, 2014.
- [59] I. S. Gartshore, J. Khanna, and S. Laccinole, "The Effectiveness Of Vortex Spoilers On A Circular Cylinder In Smooth And Turbulent Flow," *Wind Eng. Proc. Fifth Int. Conf. Fort Collins, Color. USA, July 1979*, pp. 1371–1379.
- [60] Y. Qiu, Y. Sun, Y. Wu, and Y. Tamura, "Effects of splitter plates and Reynolds number on the aerodynamic loads acting on a circular cylinder," *J. Wind Eng. Ind. Aerodyn.*, vol. 127, no. April, pp. 40–50, 2014.
- [61] I. Ayoub, J. Lu, B. Dutta, K. Elliot, B. Stappenbelt, and J. Pan, "Acoustics 2008 Acoustics and Sustainability: How should acoustics adapt to meet future An Experimental Study of the Effect of Splitter Plates on Vortex Induced Vibration," *Acoustics*, no. April, 2008.
- [62] S. Liang, J. Wang, B. Xu, W. Wu, and K. Lin, "Vortex-induced vibration and structure instability for a circular cylinder with flexible splitter plates," *J. Wind Eng. Ind. Aerodyn.*, vol. 174, no. December 2017, pp. 200–209, 2018.
- [63] P. J. Strykowski and K. R. Sreenivasan, "On the formation and suppression of vortex 'shedding' at low Reynolds numbers," *J. Fluid Mech.*, vol. 218, pp. 71–107, 1990.
- [64] A. Dipank, T. K. Sengupta, and S. B. Talla, "Suppression of vortex shedding behind a circular cylinder by another control cylinder at low Reynolds numbers," *J. Fluid Mech.*, vol. 573, pp. 171–190, 2007.
- [65] J. Y. Hwang and K. S. Yang, "Drag reduction on a circular cylinder using dual detached splitter plates," *J. Wind Eng. Ind. Aerodyn.*, vol. 95, no. 7, pp. 551–564, 2007.

- [66] V. Bianchi, L. S. P. Silva, F. Cenci, S. Hirabayashi, H. Suzuki, and R. T. Gonçalves, “Spoiler plate effects on the suppression of vortex-induced motions of a single circular cylinder,” *Ocean Eng.*, vol. 210, no. April, p. 107569, 2020.
- [67] A. S. Chan, P. A. Dewey, A. Jameson, C. Liang, and A. J. Smits, “Vortex suppression and drag reduction in the wake of counter-rotating cylinders,” *J. Fluid Mech.*, vol. 679, no. July, pp. 343–382, 2011.
- [68] M. Carini, J. O. Pralits, and P. Luchini, “Feedback control of vortex shedding using a full-order optimal compensator,” *J. Fluids Struct.*, vol. 53, pp. 15–25, 2015.
- [69] Z. Li, I. M. Navon, M. Y. Hussaini, and F. X. Le Dimet, “Optimal control of cylinder wakes via suction and blowing,” *Comput. Fluids*, vol. 32, no. 2, pp. 149–171, 2003.
- [70] Y. Sung, W. Kim, M. G. Mungal, and M. A. Cappelli, “Aerodynamic modification of flow over bluff objects by plasma actuation,” *Exp. Fluids*, vol. 41, no. 3, pp. 479–486, 2006.
- [71] H. Choi, W. P. Jeon, and J. Kim, “Control of flow over a bluff body,” *Annu. Rev. Fluid Mech.*, vol. 40, pp. 113–139, 2008.
- [72] R. Gopalkrishnan, M. S. Triantafyllou, G. S. Triantafyllou, and D. Barrett, “Active vorticity control in a shear flow using a flapping foil,” *J. Fluid Mech.*, vol. 274, pp. 1–21, 1994.
- [73] M. Bergmann, L. Cordier, and J. P. Brancher, “On the generation of a reverse von Kármán street for the controlled cylinder wake in the laminar regime,” *Phys. Fluids*, vol. 18, no. 2, 2006.
- [74] P. Bearman, “Vortex Shedding from Oscillating Bluff Bodies,” *Annu. Rev. Fluid Mech.*, vol. 16, no. 1, pp. 195–222, Jan. 2002.
- [75] T. L. Morse and C. H. K. Williamson, “The effect of Reynolds number on the critical mass phenomenon in vortex-induced vibration,” *Phys. Fluids*, vol. 21, no. 4, 2009.
- [76] F. S. Hover, A. H. Techet, and M. S. Triantafyllou, “Forces on oscillating uniform and tapered cylinders in crossflow,” *J. Fluid Mech.*, vol. 363, pp. 97–114, 1998.
- [77] F. S. Hover, J. T. Davis, and M. S. Triantafyllou, “Three-dimensionality of mode transition in vortex-induced vibrations of a circular cylinder,” vol. 23, pp. 29–40, 2004.
- [78] G. R. S. Assi and P. W. Bearman, “Vortex-induced vibration of a wavy elliptic cylinder,” *J. Fluids Struct.*, vol. 80, pp. 1–21, 2018.
- [79] Y. Nakamura, K. Hirata, and K. Kashima, “Gallop of a circular cylinder in the presence of a splitter plate,” *Journal of Fluids and Structures*, vol. 8, no. 4, pp. 355–365, 1994.
- [80] C. Mannini, T. Massai, A. Maria Marra, and G. Bartoli, “Interference of Vortex-Induced Vibration and Galloping: Experiments and Mathematical Modelling,” *Procedia Eng.*, vol. 199, pp. 3133–3138, 2017.
- [81] R. Mills, J. Sheridan, and K. Hourigan, “Particle image velocimetry and visualization of natural and forced flow around rectangular cylinders,” *J. Fluid Mech.*, no. 478, pp. 299–323, 2003.
- [82] C. Mannini, A. M. Marra, and G. Bartoli, “VIV-galloping instability of rectangular cylinders: Review and new experiments,” *J. Wind Eng. Ind. Aerodyn.*, vol. 132, pp. 109–

124, 2014.

- [83] A. Simpson, “Determination of the natural frequencies of multiconductor overhead transmission lines,” *J. Sound Vib.*, vol. 20, no. 4, pp. 417–449, 1972.
- [84] G. R. S. Assi and P. W. Bearman, “Transverse galloping of circular cylinders fitted with solid and slotted splitter plates,” *J. Fluids Struct.*, vol. 54, pp. 263–280, 2015.
- [85] H. Zheng and J. Wang, “Gallop oscillation of a circular cylinder firmly combined with different shaped fairing devices,” *J. Fluids Struct.*, vol. 77, pp. 182–195, 2018.
- [86] G. V. Parkinson and M. A. Wawzonek, “Some considerations of combined effects of galloping and vortex resonance,” *J. Wind Eng. Ind. Aerodyn.*, vol. 8, no. 1–2, pp. 135–143, 1981.
- [87] R. King, “Vortex Excited Structural Oscillations of a Circular Cylinder in Steady Currents,” *Offshore Technol. Conf.*, 1974.
- [88] C. P. Pesce and A. L. C. Fuarra, “Vortex-Induced Vibrations and jump phenomenon: Experiments with a clamped flexible cylinder in water,” *Int. J. Offshore Polar Eng.*, vol. 10, no. 1, pp. 26–33, 2000.
- [89] A. Khalak and C. H. K. Williamson, “Fluid forces and dynamics of a hydroelastic structure with very low mass and damping,” *J. Fluids Struct.*, vol. 11, no. 8, pp. 973–982, 1997.
- [90] F. Flemming and C. H. K. Williamson, “Vortex-induced vibrations of a pivoted cylinder,” *J. Fluid Mech.*, vol. 522, pp. 215–252, 2005.
- [91] H. Park, R. Ajith Kumar, and M. M. Bernitsas, “Suppression of vortex-induced vibrations of rigid circular cylinder on springs by localized surface roughness at  $3 \times 10^4 \leq Re \leq 1.2 \times 10^5$ ,” *Ocean Eng.*, vol. 111, pp. 218–233, 2016.
- [92] G. S. West and C. J. Apelt, “The effects of tunnel blockage and aspect ratio on the mean flow past a circular cylinder with Reynolds numbers between 104 and 105,” *J. Fluid Mech.*, vol. 114, no. January, pp. 361–377, 1982.
- [93] J. Zhao, “Flow-Induced Vibration of Circular and Square Cylinders with Low Mass and Damping,” *Monash University*, 2012.
- [94] N. C. Shapley, “Laser Doppler velocimetry measurements of particle velocity fluctuations in a concentrated suspension,” *Ph.D. thesis, Massachusetts Institute Of Technology*, 1993.
- [95] X. Gao, Z. Xu, W. Xu, and M. He, “Cross-flow vortex-induced vibration (VIV) responses and hydrodynamic forces of a long flexible and low mass ratio pipe,” *J. Mar. Sci. Eng.*, vol. 7, no. 6, 2019.
- [96] S. M. Sayeed-Bin-Asad, T. S. Lundström, and A. G. Andersson, “Study the flow behind a semi-circular step cylinder (Laser Doppler Velocimetry (LDV) and Computational Fluid Dynamics (CFD)),” *Energies*, vol. 10, no. 3, 2017.
- [97] S. S. Rao, *Mechanical Vibrations*, Fifth. Prentice Hall, 2012.
- [98] G. R. S. Assi, P. W. Bearman, and J. R. Meneghini, “Unsteady Force Measurements on a Responding Circular Cylinder in the Wake of an Upstream Cylinder,” 2009, no. January, pp. 633–639.

- [99] R. J. Moffat, "Describing the uncertainties in experimental results," *Exp. Therm. Fluid Sci.*, vol. 1, no. 1, pp. 3–17, 1988.
- [100] C. M. Leong and T. WEI, "Two-degree-of-freedom vortex-induced vibration of a pivoted cylinder below critical mass ratio," no. May, pp. 2907–2927, 2008.
- [101] A. Alfred and K. Karamcheti, "An experiment on the flow past a finite circular cylinder at high subcritical and supercritical Reynolds numbers," *J. Fluid Mech.*, vol. 118, pp. 1–26, 1982.
- [102] C. Norberg, "Pressure Distributions around a Circular Cylinder in Cross-Flow," (2002) Symposium on Bluff Body Wakes and Vortex-Induced Vibrations (BBVIV3) p.1-4.
- [103] R. I. Basu, "Aerodynamic forces on structures of circular cross-section. Part 2. The influence of turbulence and three-dimensional effects," *J. Wind Eng. Ind. Aerodyn.*, vol. 24, no. 1, pp. 33–59, 1986.
- [104] Joel H. Ferziger and Milovan Peric, *Computational Methods for Fluid Dynamics*, 3 rd. Springer Science & Business Media, ISBN 3642560261, 2003
- [105] A. Roshko, "Experiments on the flow past a circular cylinder at very high Reynolds number," *J. Fluid Mech.*, no. 1924, pp. 345–356, 1961.
- [106] T. J. Ulrich, "Envelope Calculation from the Hilbert Transform Envelope calculation from the Hilbert transform," no. March 2006, 2006.
- [107] D. Zwillinger, *Standard Mathematical Tables and Formulae*, 31 st. CRC press LLC, 2003.
- [108] C. W. Park and S. J. Lee, "Effects of free-end corner shape on flow structure around a finite cylinder," *J. Fluids Struct.*, vol. 19, no. 2, pp. 141–158, 2004.
- [109] D. Sumner, "Flow above the free end of a surface-mounted finite-height cylinder," *J. Fluids Struct.*, vol. 8, pp. 41–63, 2013.
- [110] D. Sumner, N. Rostamy, D. J. Bergstrom, and J. D. Bugg, "Influence of aspect ratio on the flow above the free end of a surface-mounted finite cylinder," *Int. J. Heat Fluid Flow*, vol. 56, pp. 290–304, 2015.
- [111] B. I. Goswami, "vortex-induced vibration of circular cylinders. I: Experimental Data," *J. Eng. Mech.*, vol. 119, no. 11, pp. 2270–2287, 1994.
- [112] R. M. C. So, Y. Zhou, and M. H. Liu, "Free vibrations of an elastic cylinder in a cross flow and their effects on the near wake," *Exp. Fluids*, vol. 29, no. 2, pp. 130–144, 2000.
- [113] T. Kitagawa, K. Kimura, and Y. Fujino, "Effects Of Free-End Condition On End-Cell-Induced Vibration," *J. Fluids Struct.*, pp. 499–518, 1999.
- [114] J. Tetsuya Kitagawa " ", Toshihiro Wakahara b, Yozo Fujino u, Kichiro Kimura b, "wind engineering An experimental study on vortex-induced vibration of a circular cylinder tower at a high wind speed" *J. Wind Eng. Ind. Aerodyn.*, vol. 71, pp. 731–744, 1997.
- [115] A. Khalak and C. H. K. Williamson, "Dynamics Of A Hydroelastic Cylinder With Very Low Mass And Damping," *Fluids Struct.*, vol. 164, no. 4179, pp. 455 – 472, 1996.
- [116] C. Norberg, "Fluctuating lift on a circular cylinder: Review and new measurements," *J. Fluids Struct.*, vol. 17, no. 1, pp. 57–96, 2003.

- [117] C. W. Park and S. J. Lee, "Free end effects on the near wake flow structure behind a finite circular cylinder," *J. Wind Eng. Ind. Aerodyn.*, vol. 88, no. 2–3, pp. 231–246, 2000.
- [118] R. W. Prastianto, K. Otsuka, and Y. Ikeda, "Vortex-induced Vibration of a Flexible Free-hanging Circular Cantilever," *ITB J. Eng. Sci.*, vol. 41, no. 2, pp. 111–125, 2009.
- [119] X. Q. Wang, R. M. C. So, and K. T. Chan, "A non-linear fluid force model for vortex-induced vibration of an elastic cylinder," *J. Sound Vib.*, vol. 260, no. 2, pp. 287–305, 2003.
- [120] M. M. Zdravkovich, "Different modes of vortex shedding: An overview," *J. Fluids Struct.*, vol. 10, no. 5, pp. 427–437, 1996.
- [121] D. F. Hubert, "Vortex-Induced Vibrations Of Long Flexible Cylinders With and Without Wake Interference" Doctoral Thesis, Department of Mechanical Engineering, Universitat Rovira-i-Virgili 2015.
- [122] K. O. & Y. I. R. W. Prastianto<sup>1</sup>, "Vortex-induced Vibration of a Flexible Free-hanging Circular Cantilever," 2009.
- [123] D. W. Allen and D. L. Henning, "Surface Roughness Effects on Vortex-Induced Vibration of Cylindrical Structures at Critical and Supercritical Reynolds Numbers," *Offshore Technol. Conf.*, pp. 1–10, 2001.
- [124] S. V. Patankar and D. B. Spalding, "A calculation procedure for heat, mass and momentum transfer in three-dimensional parabolic flows," *Int. J. Heat Mass Transf.*, vol. 15, no. 10, pp. 1787–1806, 1972.
- [125] R. J. Issa, "Solution of the Implicitly Discretized Fluid-Flow Equations by Operator-Splitting," *Comput. Phys.*, vol. 26, no. 62, pp. 40–65, 1985.
- [126] S. B. Pope, *Turbulent Flows*, vol. 13, no. 2. Cambridge University Press, 2014.
- [127] D. C. Wilcox, *Turbulence Modelling for CFD*, 2nd ed., vol. 53, no. 9. California 91011: DCW Industries, Inc., La Canada, California, 1994.
- [128] A. Bakker, "Lecture 9 - Kolmogorov 's Theory Applied Computational Fluid Dynamics," *Fluid Dynamics*, 2006. .
- [129] J. R. Bull, "Turbulence Models with Adaptive Meshing for Industrial CFD," Ph.D. thesis, Department of Earth Science and Engineering Imperial College London, p. 325, 2013.
- [130] F. R. Menter, "Two-equation eddy-viscosity turbulence models for engineering applications," *AIAA J.*, vol. 32, no. 8, pp. 1598–1605, 1994.
- [131] R. Menter, F.R.; Kuntz, M.; Langtry, "Ten Years of Industrial Experience with the SST Turbulence Model," *Turbul. Heat Mass Transf.* 4, pp. 625–632, 2003.
- [132] P. R. Spalart and S. R. Allmaras, "One-equation turbulence model for aerodynamic flows," *Rech. Aerosp.*, no. 1, pp. 5–21, 1994.
- [133] C. Mockett, "A comprehensive study of detached-eddy," Von der Fakultät V – Verkehrs- und Maschinensysteme der Technischen Universität Berlin, 2009.
- [134] P. R. Spalart, "Detached-eddy simulation," *Annual Review of Fluid Mechanics* 2009, 41:1, 181-202.
- [135] K. D. Squires, J. R. Forsythe, and P. R. Spalart, "Detached-eddy simulation of the



- separated flow over a rounded-corner square,” *J. Fluids Eng. Trans. ASME*, vol. 127, no. 5, pp. 959–966, 2005.
- [136] A. K. Travin, M. L. Shur, P. R. Spalart, and M. K. Strelets, “Improvement of delayed detached-eddy simulation for LES with wall modelling,” *Proc. Eur. Conf. Comput. Fluid Dyn. (ECCOMAS CFD 2006)*, vol. 47, no. 2, pp. 345–360, 2006.
- [137] and M. S. Stefan Turek, Jaroslav Hron, Mudassar Razzaq, Hilmar Wobker, “Numerical Benchmarking of Fluid-Structure Interaction: A comparison of different discretization and solution approaches,” *Lect. Notes Comput. Sci. Eng.*, vol. 73 LNCSE, no. September, pp. 413–424, 2010.
- [138] K. J. Bathe, “*Finite Element Procedures*”. 2nd edition, Prentice-Hall, Englewood Cliffs, 1996.
- [139] S. Gsell, R. Bourguet, and M. Braza, “Two-degree-of-freedom vortex-induced vibrations of a circular cylinder at  $Re=3900$ ,” *J. Fluids Struct.*, vol. 67, pp. 156–172, 2016.
- [140] M. Braza, P. Chassaing, and H. Ha Minh, “Numerical study and physical analysis of the pressure and velocity fields in the near wake of a circular cylinder,” *J. Fluid Mech.*, vol. 165, pp. 79–130, 1986.
- [141] M. Coutanceau and J. Defaye, “Circular cylinder wake configurations: A flow visualization survey,” *Appl. Mech Rev.*, vol. 44, no. 6, pp. 255–305, 1991.
- [142] M. Rai and P. Moin, “Direct Numerical Simulation Of Transition And Turbulence In A Spatially Evolving Boundary Layer,” *J. Comp. Phys.*, vol. 109, no. 2, pp. 169–192, 1993.
- [143] Shamooun Jamshed, *High Reynolds number flows*. Elsevier Inc., 2015.
- [144] M. Springer, R. K. Jaiman, S. Cosgrove, and Y. Constantinides, “Numerical modeling of vortex-induced vibrations of two flexible risers,” *Proc. Int. Conf. Offshore Mech. Arct. Eng. - OMAE*, vol. 5, pp. 749–756, 2009.
- [145] G. F. Rosetti, G. Vaz, and A. L. C. Fajarra, “URANS calculations for smooth circular cylinder flow in a wide range of Reynolds numbers: Solution verification and validation,” *J. Fluids Eng. Trans. ASME*, vol. 134, no. 12, pp. 1–18, 2012.
- [146] C. Williamson and R. Govardhan, “Mean And Fluctuating Velocity Fields In The Wake Of A Freely-Vibrating Cylinder,” *J. Fluids Struct.*, vol. 15, pp. 1031–1060, 2001.
- [147] ITTC., “Uncertainty Analysis in CFD Verification and Validation Methodology and Procedures,” *ITTC – Recomm. Proceed. Guidel.*, 2017.
- [148] J. Oberhagemann, “On prediction of wave-induced loads and vibration of ship structures with finite volume fluid dynamics methods,” *Univ. Duisburg-Essen*, pp. 1–214, 2017.
- [149] L. Eça and M. Hoekstra, “A procedure for the estimation of the numerical uncertainty of CFD calculations based on grid refinement studies,” *J. Comput. Phys.*, vol. 262, pp. 104–130, 2014.
- [150] D. A. Lysenko, I. S. Ertesvåg, and K. E. Rian, “Large-eddy simulation of the flow over a circular cylinder at reynolds number 3900 using the openfoam toolbox,” *Flow, Turbul. Combust.*, vol. 89, no. 4, pp. 491–518, 2012.
- [151] C. Norberg, “An experimental investigation of the flow around a circular cylinder: Influence of aspect ratio,” *J. Fluid Mech.*, vol. 258, pp. 287–316, 1994.

- [152] V. D'Alessandro, S. Montelpare, and R. Ricci, "Detached-eddy simulations of the flow over a cylinder at  $Re = 3900$  using OpenFOAM," *Comput. Fluids*, vol. 136, pp. 152–169, 2016.
- [153] D. Luo, C. Yan, H. Liu, and R. Zhao, "Comparative assessment of PANS and DES for simulation of flow past a circular cylinder," *J. Wind Eng. Ind. Aerodyn.*, vol. 134, pp. 65–77, 2014.
- [154] S. Rashidi, M. Hayatdavoodi, and J. Abolfazli, "Vortex shedding suppression and wake control: A review Vortex shedding suppression and wake control: A review," no. October 2017, 2016.
- [155] A. Vinod, A. Auvil, and A. Banerjee, "On passive control of transition to galloping of a circular cylinder undergoing vortex induced vibration using thick strips," *Ocean Eng.*, vol. 163, no. October 2017, pp. 223–231, 2018.
- [156] H. Schlichting, *Boundary- Layer Theory*, Ninth. Springer Berlin Heidelberg, 2017.
- [157] M. Bloor and J. Gerrard, "Measurements on turbulent vortices in a cylinder wake," *R. Soc. Publishing*, vol. 294, no. 1957, p. 24, 1966.
- [158] Gerrard, J. H., "The mechanics of the formation region of vortices behind bluff bodies," *J. Fluid Mech.*, vol. 25, no. 02, pp. 401–413, 1966.
- [159] X. An, B. Song, W. Tian, and C. Ma, "Design and CFD simulations of a Vortex-Induced Piezoelectric Energy Converter (VIPEC) for underwater environment," *Energies*, vol. 11, no. 2, pp. 1–15, 2018.
- [160] J. W. Kamphuis, "Hydrodynamics around cylindrical structures," *Coast. Eng.*, vol. 33, no. 1, p. 69, Mar. 1998.
- [161] H. Mukundan, "Vortex-Induced Vibration of Marine Risers: Motion and Force Reconstruction from Field and Experimental Data by," *Massachusetts Institute Of Technology*, 2008.
- [162] L. Zeng, F. Najjar, S. Balachandar, and P. Fischer, "Forces on a finite-sized particle located close to a wall in a linear shear flow," *Phys. Fluids*, vol. 21, no. 3, 2009.
- [163] G. Buresti, "Vortex Shedding from Bluff Bodies," *Wind Eff. Build. Struct.*, no. November, pp. 61–95, 1998.
- [164] M. C. Ong, T. Utnes, L. E. Holmedal, D. Myrhaug, and B. Pettersen, "Numerical simulation of flow around a smooth circular cylinder at very high Reynolds numbers," *Mar. Struct.*, vol. 22, no. 2, pp. 142–153, 2009.
- [165] F. Xie, J. Deng, Q. Xiao, and Y. Zheng, "A numerical simulation of VIV on a flexible circular cylinder," *Fluid Dyn. Res.*, vol. 44, no. 4, 2012.
- [166] T. Dahlberg, "Procedure to calculate deflections of curved beams," *International Journal of Engineering Education*, vol. 20, no. 3. pp. 503–513, 2004.
- [167] F. J. Huera-Huarte, "Multi Mode Vortex induced Vibration of a Flexible Cylinder," *Imperial College, University of London*, 2006.
- [168] Neil Schlager. *When technology fails: Significant technological disasters, accidents, and failures of the twentieth century*. 1994.

- [169] Nobach, H. Present Methods to Estimate the Cross-Correlation and Cross-Spectral Density for Two-Channel Laser Doppler Anemometry. In Proceedings of the 18th International Symposium on the Application of Laser and Imaging Techniques to Fluid Mechanics, Lisbon, Portugal, 4–7 July 2016.